Dissertation
zur Erlangung des Doktorgrades
der Naturwissenschaften (Dr. rer. nat.)
im Fachbereich Geowissenschaften
der Freien Universität Berlin

Modelling of the Magnetic Field Induced by Ocean Circulation

Jan Dostal

Berlin, 2014

Institut für Meteorologie
Freie Universität Berlin

1. Gutachter: Prof. Dr. Maik Thomas

2. Gutachter: Prof. Dr. Zdeněk Martinec

Tag der Einreichung: 29.1.2014

Tag der mündlichen Prüfung: 25.11.2014

Abstract

This work is concerned with the forward modelling of ocean-induced magnetic fields on a global scale as the first step needed for the identification of the ocean-induced magnetic signals in the recently launched satellite mission Swarm and coastal-site magnetometers. The aim is at developing a numerical model for the estimation and evaluation of the magnetic field constituents generated by ocean flow dynamics. As an example of the input data, the strong semidiurnal M_2 tide with the period of 12 h 42 min is applied. Moreover, static main magnetic field of the Earth and a realistic distribution of the electrical conductivity in radial direction are considered. Three different solution methods for the Earth approximated by a spherically layered model are developed. For this purpose a magnetic induction equation in the form of the Helmholtz equation is derived. The analytical solution in the Fourier frequency domain in classical (strong) sense is found by using the spherical Bessel functions. The second method makes use of weak formulation of the induction equation where the spectral-finite element approach in Fourier frequency domain is later applied. The third method is used to solve for the toroidal magnetic field in time domain. The complex input ocean velocity field is discretized at individual time instants and the spectral-finite element approach is applied in time domain. The ocean-induced magnetic field in this work is split into toroidal and poloidal modes that are calculated separately. Additionally, the secondary poloidal magnetic field generated by the lateral conductivity contrast due to the ocean-continent boundary, the so-called coastal effect, is estimated. As the magnetic field is calculated for the identical input data sets and parametrization, the numerical results of the three methods are compared. Additionally, the behaviour of the calculated magnetic field is examined with respect to the variations of different input parameters. The results of the individual magnetic field constituents are compared in magnitude and spatial distribution.

Kurzzusammenfassung

Diese Arbeit beschäftigt sich mit der Vorwärtsmodellierung ozeaninduzierter Magnetfelder auf globalen Skalen als eine Voraussetzung für die Identifizierung solcher Magnetfeldsignale in der vor Kurzem gestarteten Satellitenmission Swarm und küstennahen Magnetometern. Das Ziel ist die Entwicklung eines numerischen Modells für die Schätzung des Magnetfeldanteils, der durch die ozeanische Dynamik induziert wird. Als Eingangsdaten für die ozeanische Strömungen wird die stärkste halbtägliche M_2-Tide benutzt. Weitere Eingangsparameter der Modellierung bilden ein statisches Hintergrundmagnetfeld der Erde und eine realistische radiale Verteilung der elektrischen Leitfähigkeit der Erde. In der Arbeit werden drei verschiedene Lösungsmethoden entwickelt bei denen die Erde durch eine Kugel aproximiert ist. Um dieses Ziel zu erreichen wird eine Induktionsgleichung in Form der Helmholtzgleichung hergeleitet. Bei der ersten Methode wird die Induktionsgleichung mit einer analytischen Lösung in klassischer (starker) Formulierung im Fourier-Frequenzbereich mit Hilfe von spherischen Bessel-Funktionen gelöst. Bei dem zweiten Ansatz ist das Induktionsproblem in schwacher Formulierung, mit Hilfe der sogenannten Spektral-Finite-Element Methode, im Fourier-Frequenzbereich gelöst. Bei der dritten Methode wird die Lösung des toroidalen Magnetfeldanteils im Zeitbereich gesucht. In diesem Fall werden die komplexen Eingangsgrößen des periodischen Tidensignals in einzelne Zeitschritte diskretisiert und die Spektral-Finite-Element Methode ist im Zeitbereich angewandt. Das generierte Magnetfeld ist in einen toroidalen und einen poloidalen Anteil getrennt und diese werden separat berechnet. Neben dieser zwei primär induzierten Magnetfeldanteile wird zusätzlich der sogenannte Küsteneffekt, ein sekundär induzierter poloidaler Magnetfeldanteil, der aufgrund des lateralen elektrischen Leitfähigkeitskontrastes zwischen Kontinent und Ozean induziert wird, geschätzt. Da die Berechnungen des Magnetfeldes bei allen drei Methoden mit identischen Eingangsgrößen und Parametrisierung durchgeführt werden, können die resultierenden Magnetfeldanteile untereinander verglichen werden. Zusätzlich wird die Sensitivität des induzierten Magnetfeldes bezüglich der wichtigsten Parameter untersucht und das magnetische Signal in Bezug auf seine Größe und räumliche Verteilung diskutiert.

Acknowledgements

First and foremost, I am deeply grateful to my supervisor Prof. Dr. Zdeněk Martinec who accompanied me continuously over the whole time working on the PhD project. His scientific expertise as a geophysicist and modeller, didactic skills and kindness create an excellent mixture, I constantly profited from his advising, teaching and offering a help. I also appreciated very much his psychological support, patience and encouraging, even more as the contact between us has been limited mostly to internet phone calls and emails. I further thank Prof. Dr. Maik Thomas, the head of the Earth System Modelling section at GFZ, for his supervision and necessary support, enabling the realisation of the project. I am also thankful to all my colleagues at the GFZ, especially Dr. Jan Hagedoorn for many helpfull discussions about the electromagnetic induction, to Dr. Volker Klemann for many advices on numericall modelling. Furthermore, to Dr. Henryk Dobslaw and Dr. Irina Rogozhina for proof reading and other support, Dr. Ingo Wardinski for discussions on the Earth's magnetic field and, definitely, to Inga Bergmann-Wolf who contributed significantly to a friendly and pleasant working athmosphere in the office we have shared for the most time of my PhD project.

'Theres this farmer, and he has these chickens, but they wont lay any eggs. So, he calls a physicist to help. The physicist then does some calculations, and he says, um, I have a solution, but it only works with spherical chickens in a vacuum.'
(The Big Bang Theory, Season 1, Episode 9)

'Magnus magnes ipse est globus terrestris.'
William Gilbert, De Magnete (1600)

Contents

List of Figures

Introduction

The question about motional induction driven by ocean flow has attracted scientists for a long time. The idea about the motionally induced electric currents by water flow and their usage as indicators for water transport in the river Thames was first suggested by Faraday (1832). The electric field variations induced by oceanic tidal motion were identified by submarine telegraph cables already in 1850's, but the observed lunar magnetic variations have been an object of discussion for a long time ever since. With the exception of van Bemmelen (1912, 1913) who expected that the tidal magnetic variation have a source in both, internal and external fields, the majority of the researchers at the time (Chapman, 1919; Chapman and Bartels, 1962) believed that the lunar magnetic variations were dominated by external sources. Larsen (1968) revealed the tidal signal in the electric field and magnetic declination from sea floor, coastal- and island-side observations and concluded on the dependence of the signal to the distribution of tidal currents and electrical conductivity beneath the ocean with the hint that if either would be known perfectly, the measurements would serve to give a precise information about the other.

The electromagnetic induction in the ocean as a separate scientific subject was introduced by works of Stommel (1948), Longuet-Higgins (1949) and Longuet-Higgins et al. (1954). One of the fundamental theoretical study for using electric fields for monitoring the in-situ oceanic transport has been carried out by Sanford (1971). In the following theoretical studies by Chave (1983) and Chave and Luther (1990a) the magnetic field was divided into toroidal and poloidal part according to the Helmholtz decomposition and the differences in the behavior of the two modes were discussed. Chave (1983) in his theory confirmed the idea of Larsen (1968) that the crust and mantle as electrical conductors were coupled to the ocean conductively and inductively. Therefore, the low-frequency electromagnetic field observations with the oceanic origin contain an information about the electrical conductivity and the circulation of the ocean. Hereby, from the geomagnetic point of view, the dynamo interaction of the ocean flow with the background magnetic field forms an additional natural source beside of geomagnetic field variations. Finally, he suggested the use of tidally induced electromagnetic fields with their high sensitivity to lithospheric electrical conductivity in toroidal mode to probe the Earth's conductivity structures. The precondition for interpretation of the electromagnetic records is the numerical modelling which is in case of electromagnetic fields generated by ocean flow a complex mathematical problem requiring specific solutions approaches. All theoretical studies tend to reduce the complexity using various approximations depending on specific applications, mostly involving interpretation of observational records and feasibility of numerical calculations.

Today the applications involving oceanic contribution to the electromagnetic fields can be separated in two groups, the geomagnetic and oceanographic ones. The geomagnetic applications are more general and concentrate on estimation and extraction of the individual constituents of different origins from the superposition of the Earth's magnetic field signal (see section Global Geomagnetic field constituents). For example, a correction of magnetic data for tidal signals increases the accuracy of other field components, especially the lithospheric field (Friis-Christensen et al., 2006; Maus et al., 2006; Manoj et al., 2006) and vice versa. Besides the identification and extraction of the electromagnetic signals from the observational records, the primary oceanographic application is to gain an additional, independent and complementary indicator for determining the oceanic flow by observations of the ocean-induced electric and magnetic fields and their variations.

In-situ observations of electric and magnetic signals are obtained using different techniques, like submarine cables, sea floor sensors and mobile devices including vertical profilers and floating platforms (Lilley et al., 2004). While in situ observations by submarine cables or bottom electrometers are suitable for monitoring the integrated water transport (Luther et al., 1991), other techniques like floating vertical profilers are used for measuring vertical profiles with a high resolution (Lilley et al., 2001). Present day interpretations of in-situ electric field measurements in terms of oceanic transport study also the influence of small horizontal velocity gradient of the flow or the sloping topography (Szuts, 2010a,b), but often neglects global (non-local) effects (Szuts, 2008). One of the advantages of remote magnetic sensing is its capability of measuring the integrated ocean flow also in ice covered regions (Friis-Christensen et al., 2006). Observation techniques and numerical models are also chosen depending on the investigated oceanic dynamics. This can be either a steady state flow with small time variations but strong velocity decay with depth similar to investigations of the Golf stream in the area of Cape Hatteras (Szuts, 2012), time-variable flow constant over the whole ocean layer depth (oceanic tides) (Tyler et al., 2003; Maus and Kuvshinov, 2004), or individual events like tsunami waves registered by sea floor geomagnetic observatories (Toh et al., 2011; Manoj et al., 2011, 2010). Besides local terrestrial and marine observations, an additional possibility of surveying the Earth's magnetic field on a global scale is offered by satellite missions over the last two decades.

The new generation of space-born magnetometers starting from Østred (launched in February 1999), followed by CHAMP (launched in July 2000) and SAC-C (launched in November 2000) provide with high-precision data of uniform quality and excellent spatio-temporal coverage (Kuvshinov, 2008). As electric fields from internal sources can not be observed from the space, the global oceanic induction remains focused on magnetic field. High-resolution observations from the single satellite CHAMP observations made it possible to identify the strong semidiurnal M_2-tide signal by comparing the magnetic records with numerical simulations (Tyler et al., 2003). The satellite mission Swarm, consisting of three identical satellites, launched in November 2013, promises with single satellite requirements for magnetic field magnitude of 0.15 nT and for magnetic field vector of 0.5 nT an accuracy in the range of ocean-induced magnetic signals. Identifying the ocean circulation by its magnetic signature is one of the research objectives of the Swarm mission (ESA_SP-1279-6, 2004). Space-born measurements provide among others the possibility to detect depth-integrated magnetic field variations. Therefore, magnetic field caused by tidal flow with well known periodicity is suitable for identification in the Swarm magnetic records. Golubev (2011, 2012) studied the potential of a mathematical algorithm for extracting the ocean-induced signals from the satellite geomagnetic measurement that are approximately 4 orders smaller than the main magnetic field. Such challenging task can be approached using numerical forward modelling on a global scale.

Besides the theoretical studies that are mostly intended to interpret measurements or estimate the electric and magnetic fields by in-situ ocean flow, in recent years, being motivated by global observations from CHAMP satellite, an interest in modelling global electromagnetic induction in ocean has arisen. As only the poloidal magnetic field is measurable outside the ocean, present-day global models reduce the ocean layer to a thin sheet approximation with depth-integrated velocities as input data which allows consideration only of primary induced horizontal electric currents. Such thin sheet models has been published by Tyler et al. (2003), who consider the space beneath this thin sheet as insulator, or in an other approach from Kuvshinov et al. (2002) who places the ocean as a thin sheet atop of global 3D conductivity distribution of the Earth. This model, based on an integral equation approach, has been published also in Kuvshinov and Olsen (2005), Vennerstrom et al. (2005b) and Vennerstrom et al. (2005a). The results of the two models for the M_2 tide have been compared in Vennerstrom et al. (2005b) and Vennerstrom et al. (2005a) and found to agree well in magnitude and global distribution. Besides the global modelling of tidal flow, predictions for the general (termohaline and wind driven) circulation on a global scale have been studied for a thin sheet approximation by Manoj et al. (2006) and for the Antarctic Circumpolar Current by Vivier et al. (2004). Summarized results of the ocean-induced magnetic field on a global scale from the geomagnetic point of view have been reviewed by Kuvshinov (2008). In another global study for motional induction, Tyler et al. (1997a) focus on non-local effects of the electromagnetic fields inside the ocean and point out the importance of sophisticated models with realistic conductivity distribution beneath the ocean when considering non-local electric currents.

An accurate prediction based on numerical forward modelling, especially for small magnetic field constituents, is a precondition for their identification and correct interpretation in the Earth's magnetic field. Therefore, the following thesis present a spherical model with an ocean as a layer of finite thickness, beneath which an electric conductive space with realistic radial conductivity distribution in finite layers are considered. This model implicitly includes also the influence of mutual induction by large-scale poloidal magnetic signals discussed already by Sanford (1971). In addition, a spherical model consisting of layers of finite thickness enables a calculation of the toroidal magnetic field and study of its sensitivity to the velocity field decay with depth and lithospheric structure. Already Chave (1983) pointed out that modelling the ocean as a thin sheet with insulating boundaries causes large errors in calculated seafloor electromagnetic fields. Consideration the toroidal part of the magnetic field is also a condition for studying coastal effects - magnetic field induction due to ocean-continent conductivity contrast. Without accounting for these effects the magnetic records in vicinity of coastal sites or small islands cannot be properly interpreted (Manoj et al., 2006). Driven by a velocity field with well known periodicity and global extent the semidiurnal M_2 tide used for the study in this thesis forms an ideal input for the prediction of the magnetic signal on a global scale. In addition, a periodical signal offers the possibility of solutions in Fourier frequency domain which in turn allows using different mathematical approaches so that the obtained results can be mutually validated. Also, the known periodicity facilitates an identification of such tidal signal variations in magnetic records.

Organization of the dissertation

In chapter 1, the phenomenon of the motional induction and the separation in two modes, namely toroidal and poloidal, are explained and the induction equation is derived. In chapter 2, the input data for the modelling experiments are introduced and a source term based on realistic input data is calculated. In chapter 3, we present an analytical solution for the toroidal and poloidal magnetic field in Fourier frequency domain. The results from chapter 3 are reproduced in chapter 4 where we solve the motional induction using a numerical spectral-finite elements approach for both, the toroidal and poloidal modes. In the last chapter 5 we present a solution for the toroidal field in time domain using the method from chapter 4 and compare the result with the solutions in Fourier domain.

Global geomagnetic field constituents

The observed magnetic field near the Earth surface represents a superposition of magnetic field constituents of different origins. The intention of this section is to give an overview of the diversity of magnetic field sources and their contributions to the Earth's magnetic field as they are important indicators for geological structure and dynamic processes in the Earth system.

Traditionally, the lower atmosphere (troposphere) is treated as an insulator. The magnetic field constituents whose sources are placed in the electric conductive space above the lower atmosphere are referred to as external, whereas the sources from the conductive space beneath, within the solid Earth, as internal sources. Over 90 % of the magnetic field observed near the Earth surface is generated by the geodynamo in the outer core (Mandea and Thebault, 2007) and is referred to as the main field. The outer core consists of liquid iron and its flow induces magnetic field that reaches the magnitudes of up to 60000 nT for the radial component in polar regions (Figure 2.4). As the flow of the fluid iron evolves with time, the main field experiences spatial and temporal variations on different scales. These secular variations can be among others related to torsional oscillations, core-mantle interaction or geomagnetic jerks. The induced main field passes through the electrical conductive mantle on its way to the Earth surface. Although the mantle is not considered as a source of magnetic field, its electrical conductivity and especially the conductivity inhomogeneities perturb the magnetic signal by up to ± 200 nT for the observed poloidal part on the Earth surface. The lithosphere and crust overlying the mantle carry both the induced and remanent magnetization with magnitudes of up to ± 1000 nT. The remanent magnetization is formed by rock cooling and depends on the chemical composition, crystal conformation of the rocks and is influenced by the main magnetic field at the time of the crystallization. The lithospheric magnetic constituent below degree 14 of spherical harmonic series is masked by the core field (Friis-Christensen et al., 2006). Another source of magnetic field at the Earth surface comes from the ocean dynamics. This constituent of the magnetic field is the main topic of this thesis and will be discussed later in more detail.

The external sources of the magnetic field lie above the solid Earth and are predominantly influenced by the solar activity. The sun's magnetic activity, which experiences an 11-year periodicity known as the solar cycle, causes a stream of small particles, namely neutral hydrogen atoms, protons and electrons. This so-called solar wind streams at high speed towards the Earth where the magnetosphere, at a height of about 10 to 20 Earth's radii, builds a protective shield that hinders by deflection the penetration of these particles into the atmosphere. The deflection of such electric charges in the magnetosphere forms a complicated system of electric currents. One of the dominant parts of this current system is the equatorial circulation, the ring current, that contributes to the Earth magnetic field and can be observed at the Earth surface. An another example with a longitudinal character are the field-aligned currents. The sun influences also the ionosphere, the outer atmosphere beneath the magnetosphere, at heights between about 50 and 600 km above the Earth surface. The ultraviolet radiation ionizes atmospheric atoms whose electric currents induce magnetic field reaching the values of up to 80 nT. As the sunlight is the origin of the ionization process, the ionosphere experiences strong daily variations. As a result the sunlit hemisphere is much more electrically conductive then the nighttime one. In addition, the flow of electrically charged particles in the atmosphere follows the gravitation forces and therefore the magnetic field contribution from the ionosphere experiences variations due to tidal signatures. Irregularity in the sun activity causes high energetic processes called geomagnetic storms. Here the solar wind-magnetosphere interaction at auroral latitudes complemented by strong ionospheric currents in these regions manifests in well known polar auroras. Ionospheric currents at mid- and low latitudes are primarily driven by high-altitude wind system. The Figure 1 and the corresponding Table 1 show the time, spatial and signal range for the individual magnetic field components at 400 km altitude as they are expected for the Swarm satellite mission for internal and external sources.

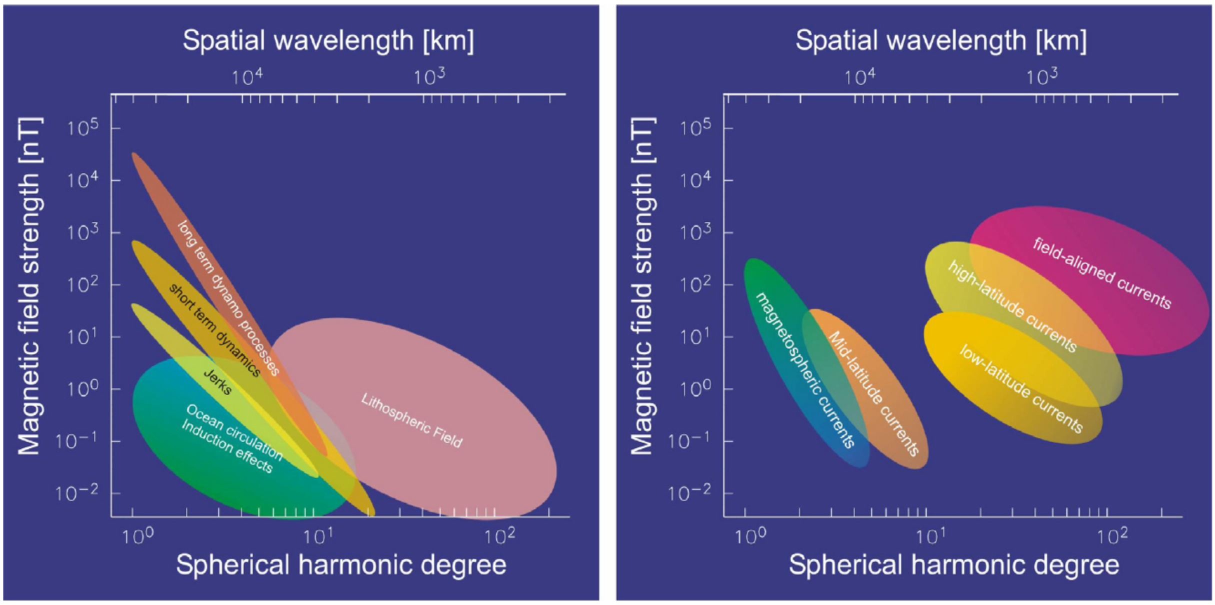

Figure 1: Amplitude of magnetic field constituents at 400 km (Swarm orbit) attitude as a function of space scale separated according to the source origin. Source terms from within the Earth (internal sources) and ocean (left) and external sources (right). Taken from ESA_SP-1279-6 (2004).

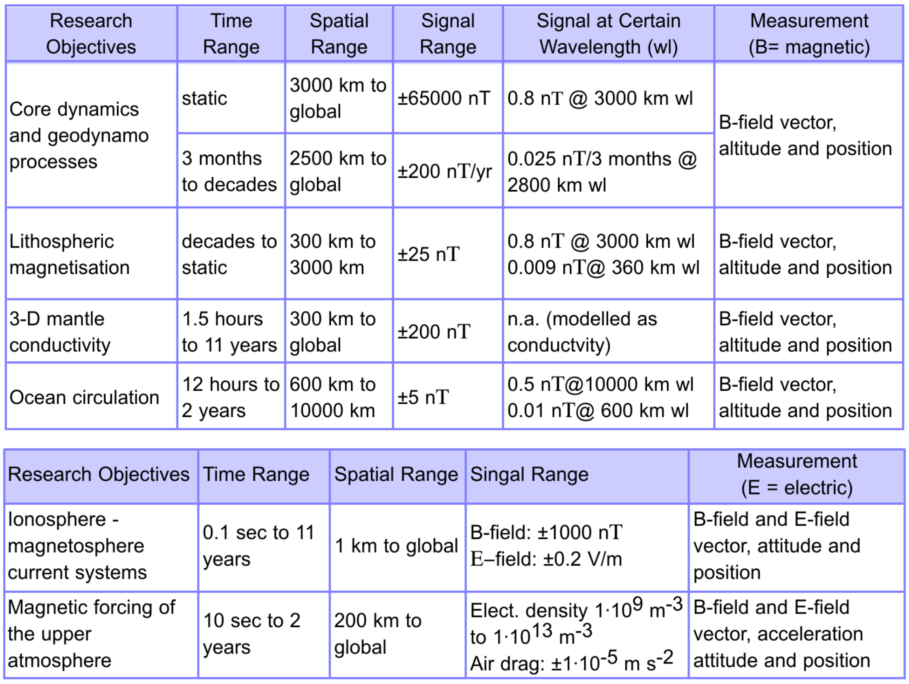

Research Objectives	Time Range	Spatial Range	Signal Range	Signal at Certain Wavelength (wl)	Measurement (B= magnetic)
Core dynamics and geodynamo processes	static	3000 km to global	±65000 nT	0.8 nT @ 3000 km wl	B-field vector, altitude and position
	3 months to decades	2500 km to global	±200 nT/yr	0.025 nT/3 months @ 2800 km wl	
Lithospheric magnetisation	decades to static	300 km to 3000 km	±25 nT	0.8 nT @ 3000 km wl 0.009 nT@ 360 km wl	B-field vector, altitude and position
3-D mantle conductivity	1.5 hours to 11 years	300 km to global	±200 nT	n.a. (modelled as conductvity)	B-field vector, altitude and position
Ocean circulation	12 hours to 2 years	600 km to 10000 km	±5 nT	0.5 nT@10000 km wl 0.01 nT@ 600 km wl	B-field vector, altitude and position

Research Objectives	Time Range	Spatial Range	Singal Range	Measurement (E = electric)
Ionosphere - magnetosphere current systems	0.1 sec to 11 years	1 km to global	B-field: ±1000 nT E–field: ±0.2 V/m	B-field and E-field vector, attitude and position
Magnetic forcing of the upper atmosphere	10 sec to 2 years	200 km to global	Elect. density $1\cdot10^9$ m^{-3} to $1\cdot10^{13}$ m^{-3} Air drag: $\pm1\cdot10^{-5}$ m s^{-2}	B-field and E-field vector, acceleration attitude and position

Table 1: Expected magnetic signals to internal (upper) and external field (lower). Taken from ESA_SP-1279-6 (2004).

Chapter 1

The motionally induced magnetic field

This chapter focuses on the description of the physical phenomenon of the electromagnetic induction in the ocean. We introduce some basic terminology, derive the induction equation in forms used in the calculus and design a model for which the induction equation will be solved. These descriptions are intended for introducing the strategy of numerical solutions in the following chapters.

1.1 Electromagnetic induction in the ocean

Sea water contains a high concentration of dissolved salts. Therefore, the ocean acts as an ionic fluid where the electric charges are carried by dissolved cations and anions, making sea water highly conductive. As oceans flow through the Earth's main magnetic field, the ion content in the oceans induces electric currents. As these electric currents flow around the globe, they in turn generate secondary magnetic fields, which evolve in terms of both magnitude and geometry through time. This effect, called motional induction, depends on the geometry and spatial scales of the ocean flow, as well as the electrical conductivity of sea water and the Earth's underlying crust and mantle (Sanford, 1971)

The ocean-induced, that is motionally induced, magnetic field can be decomposed into its poloidal and toroidal components based on the Helmholtz representation of a solenoidal vector field. The poloidal magnetic field component results from toroidal electric currents flowing in horizontal planes, while the toroidal magnetic field component is generated by the spheroidal electric currents flowing in vertical planes (Chave, 1983; Chave and Luther, 1990b). An overview of ocean-induced magnetic fields separated in toroidal and poloidal mode according to toroidal and spheroidal electric currents is shown in the Figure 1.1. Both magnetic field modes depend on sea water transport, but respond in different ways to the ocean flow velocity structure. The poloidal magnetic component is predominantly sensitive to the depth integrated ocean velocities weighted by the ocean's electrical conductivity (Sanford, 1971), while the toroidal magnetic component is largely sensitive to the vertical gradient of ocean flow velocities (Chave, 1983). The toroidal magnetic field component can only be detected inside the oceans, e.g., at the sea floor, since it vanishes at the ocean surface, while the poloidal magnetic field component is observable also outside the oceans by land observatories and satellites.

Figures 1.2 and 1.3 display the individual modes of the magnetic fields in more detail. In an example for the toroidal mode (Figure 1.2) we assume an oceanic circle flow ($\boldsymbol{u}$, in blue) and a homogeneous main (background) magnetic field ($\boldsymbol{B}_{\mathrm{E}}$, in green). The acting Lorentz force separates the positive (cations) and negative (anions) electrical charges , positive on one side of the flow circle and negative on the other, and built electric fields ($\boldsymbol{E}_{\mathrm{L}}$, in red). The electric fields attempt to discharge in short-circuit currents in the conductive space. Because the electrical field can not discharge at the same place where they are generated due to acting Lorentz force, the (spheroidal) electric currents find their way in dependency on the conductivity distribution in radial direction and, therefore, discharge in the vertical planes ($\boldsymbol{J}$, in brown). These electric currents in turn induce the toroidal magnetic field ($\boldsymbol{b}$, in green) that is constrained by the electric currents to the electric conductive space. The distribution of the electric currents in respect to the depth is governed by the electric conductivity profile in and beneath the ocean layer which explains the high sensitivity of the toroidal magnetic field to the lithospheric electrical conductivity.

The second mode – the poloidal magnetic field (Figure 1.3) requires toroidal electric currents. To fulfill this condition, the electric field has to discharge in the horizontal planes. In the previous example we considered homogeneous ring flow through a homogeneous ambient (background) magnetic field. Such idealistic symmetric case does not allow horizontal electric currents. To break this symmetry we consider now an inhomogeneous background magnetic field and oceanic flow. The inhomogeneity by the oceanic transport, different directions of the flow or horizontal gradient in the flow promote the conditions for induction of the poloidal magnetic field. As shown in the cartoon, the poloidal magnetic field induced by horizontal electric currents emanate the electric conductive space and can be measured in the atmosphere. The horizontal electric currents cause that the poloidal magnetic field is less sensitive in respect to radial conductivity profile. This property justifies a crude approximation of thin sheet models with vertical integrated oceanic transport, where the thin sheet is considered to have a uniform electrical conductance. Nevertheless, more sophisticated models shows the influence of the radial distribution of the Earth's electrical conductivity on the poloidal magnetic field. Also, even by a high resistivity of the crust and lithosphere, a mutual induction for non-local electric currents by increasing electrical conductivity with the depth should be taken in account. Therefore, the horizontal electric currents are often separated into local and non-local by the ratio of the horizontal scale of flow to the electromagnetic skin depth of the mantle (Sanford, 1971). As we are interested in global magnetic fields generated by tidal flow, a realistic radial conductivity profile should be included.

But not only the radial conductivity profile influences the resulting magnetic field. In a medium with uniform electrical conductivity, the toroidal and poloidal modes do not influences mutually and can be treated separately. In 3D conductive medium a conversion (so called coupling) between the two magnetic modes occurs. Besides the radial electric conductivity distribution, represented by spherical layers with uniform properties, the largest impact on the ocean-induced magnetic field is given by conductivity differences in lateral direction due to the ocean-continent border. This effect is illustrated in Figure 1.4. Besides the toroidal and primary poloidal magnetic fields induced directly by flow in the oceans (described above), the induction of the secondary ocean-induced poloidal magnetic field occurs. The generated toroidal magnetic field (green horizontal arrows) hits the continents with at least 3 order of magnitude smaller electrical conductivity. Thereby the toroidal magnetic field (1) is disturbed, new horizontal electric currents are generated (2) and a secondary poloidal magnetic field (3) is induced.

This example shows that a precise determination of the ocean-induced contribution to the geomagnetic field can be achieved only with 3D conductive models that include the toroidal part of the magnetic signal. We may, therefore, also conclude that the toroidal component of the ocean-induced magnetic field can indirectly be observed outside the ocean. In particular, a non-trivial contribution of the secondary poloidal magnetic signals to the geomagnetic field at ground-based magnetic observatories situated close to the oceanic shorelines necessitates accounting for it in geomagnetic coastal-effect modelling. Without accurate estimation of this contribution, the coastal magnetic records can not be interpreted reliably.

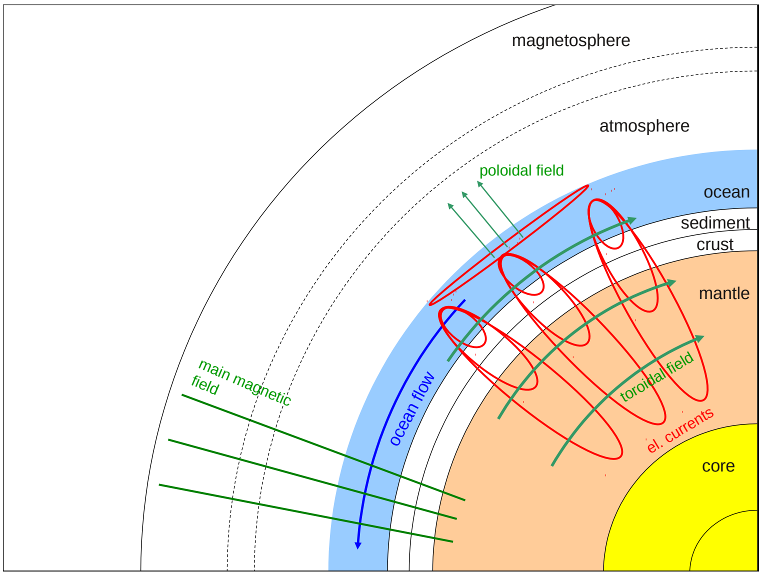

Figure 1.1: Scheme of spherical layered model with ocean-induced magnetic field. The ocean-flow containing electrical charges (in upper most layer) moves relatively to the main magnetic field and induces electric currents in horizontal and vertical planes. Consequently, the electric currents generate the toroidal and poloidal ocean-induced magnetic field.

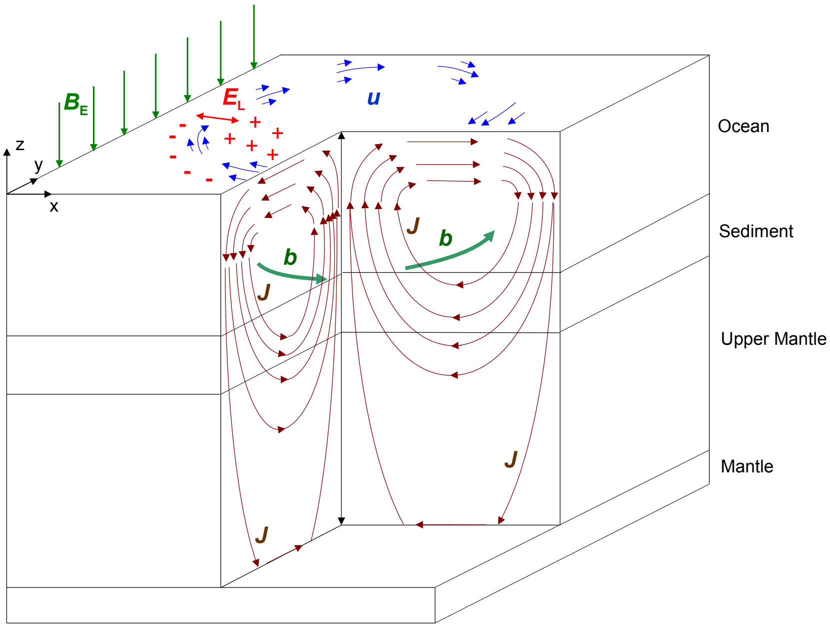

Figure 1.2: Induction of the toroidal magnetic field ***b*** by ocean currents ***u***. Based on Tyler et al. (1997b).

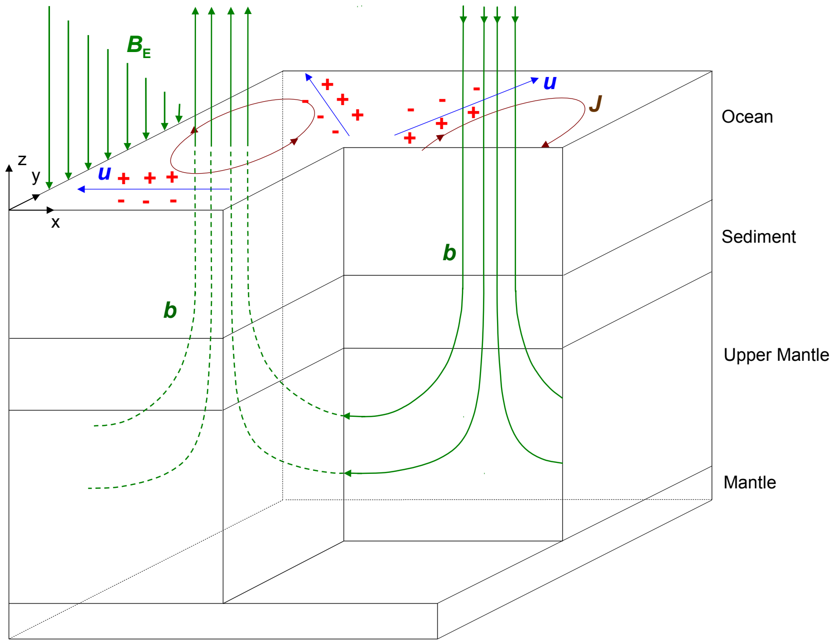

Figure 1.3: Induction of the poloidal magnetic field $\boldsymbol{b}$ by ocean currents $\boldsymbol{u}$. Based on Tyler et al. (1997b).

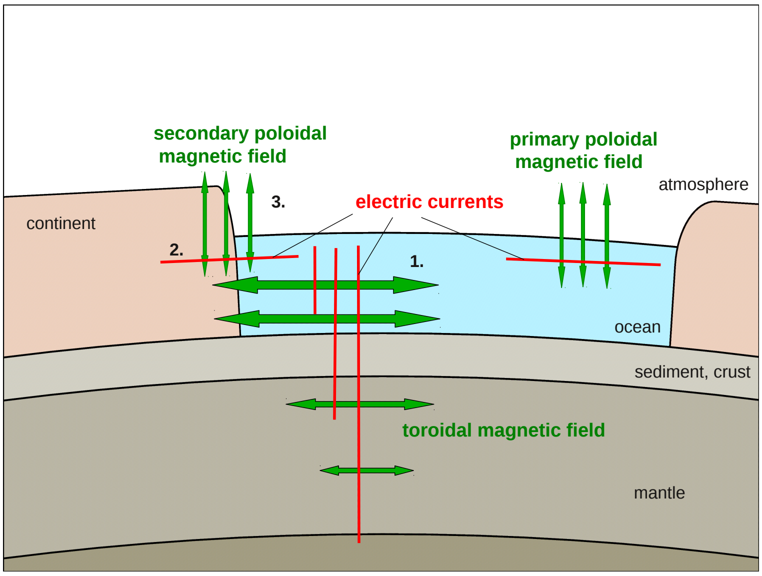

Figure 1.4: Splitting the ocean-induced magnetic field in the toroidal, primary and secondary poloidal constituents. The secondary field: The toroidal magnetic field (1) induces a toroidal electric currents (2) on the conductivity jump between ocean and continent. These currents in turn induce a secondary poloidal magnetic field (3).

1.2 Derivation of the induction equation

The electromagnetic induction is governed by **Maxwell's equations**, that is a set of four partial differential equations (Stratton, 1941) of the form

$$\operatorname{curl} \boldsymbol{B} = \mu_0 \left(\boldsymbol{j} + \frac{\partial}{\partial t} \boldsymbol{D} \right) , \tag{1.1}$$

$$\operatorname{div} \boldsymbol{B} = 0 , \tag{1.2}$$

$$\operatorname{curl} \boldsymbol{E} = -\frac{\partial}{\partial t} \boldsymbol{B} , \tag{1.3}$$

$$\operatorname{div} \boldsymbol{D} = \rho , \tag{1.4}$$

where $\boldsymbol{B}$ stands for magnetic field, $\boldsymbol{E}$ for electric field, $\boldsymbol{j}$ for electric current density, $\boldsymbol{D}$ for displacement field, μ_0 for permeability of vacuum and ρ for total electric charge density. The electromagnetic induction caused by ocean flow is a slow process where the displacement field $\boldsymbol{D}$ can be neglected. This reduces equation (1.1) to the Ampère's circuital law

$$\operatorname{curl} \boldsymbol{B} = \mu_0 \boldsymbol{j} \tag{1.5}$$

and the Maxwell's equations take the **quasi-stationary** form. The following **material equations** supplement Maxwell's equations,

$$\boldsymbol{B} = \mu_0 \mu_r \boldsymbol{H} , \tag{1.6}$$

$$\boldsymbol{D} = \epsilon_0 \epsilon_r \boldsymbol{E} , \tag{1.7}$$

where $\boldsymbol{H}$ is magnetic field intensity, μ_r permeability coefficient, ϵ_0 permittivity for vacuum and ϵ_r permittivity coefficient. The third material equation is the Ohm's law. In a electric conductive, source-free medium (in our case without ocean currents), it is of the form

$$\boldsymbol{j} = \sigma \boldsymbol{E} . \tag{1.8}$$

The Lorentz force acting on the electrical charges moving with the ocean flow of velocity $\boldsymbol{u}$ through the background magnetic field $\boldsymbol{B}_{\mathrm{E}}$ leads to an additionally term in the Ohm's law,

$$\boldsymbol{j} = \sigma (\boldsymbol{E} + \boldsymbol{u} \times \boldsymbol{B}_{\mathrm{E}}) . \tag{1.9}$$

The first summand describes the conduction and the second the advection part of the electric current density. Using this basic electromagnetic relations we derive the **induction equation** that will be later solved in different ways. We substitute equation (1.9) for $\boldsymbol{E}$ in Faraday's law (eq. 1.3) and get the form

$$\operatorname{curl} \left(\frac{1}{\sigma} \boldsymbol{j} - \boldsymbol{u} \times \boldsymbol{B}_{\mathrm{E}} \right) = -\frac{\partial}{\partial t} \boldsymbol{B} . \tag{1.10}$$

Further we substitute Ampère's law (eq. 1.5) for $\boldsymbol{j}$ in eq. (1.10) and get the final form of the induction equation

$$\frac{1}{\mu_0} \operatorname{curl} \left(\frac{1}{\sigma} \operatorname{curl} \boldsymbol{B} \right) + \frac{\partial}{\partial t} \boldsymbol{B} = \operatorname{curl} (\boldsymbol{u} \times \boldsymbol{B}_{\mathrm{E}}) , \tag{1.11}$$

an approximation where the self-induction ($\boldsymbol{u} \times \boldsymbol{B}$) is not considered. It is a non-homogeneous partial differential equation for the magnetic signal $\boldsymbol{B}$ generated by ocean flow with the right hand side given by input signals. In the source-free part of the solution space – the electric conductive space beneath the ocean layer where $\boldsymbol{u} = 0$ – we apply the Ohm's law in the form of eq. (1.8) and get a homogeneous form of the induction equation

$$\frac{1}{\mu_0} \operatorname{curl} \left(\frac{1}{\sigma} \operatorname{curl} \boldsymbol{B} \right) + \frac{\partial}{\partial t} \boldsymbol{B} = 0. \tag{1.12}$$

We intend to calculate magnetic fields generated by partial tidal forcing with a particular angular frequency ω. This allows a solution of the induction equation in **Fourier frequency domain** (chap. 3 and chap. 4). To be able to do this we will assume that the ocean responds to the tidal forcing by a steady-state periodic circulation with an ocean velocity field $\boldsymbol{u}$ whose temporal variations are represented by the time-harmonic dependency $e^{i\omega t}$, that is $\boldsymbol{u}(\boldsymbol{r},t) = \boldsymbol{u}(r)e^{i\omega t}$, where $\boldsymbol{r} = (r,\Omega)$, $\Omega = (\vartheta,\varphi)$ and $i = \sqrt{-1}$. Consequently, the induced magnetic field will be expressed in the form $\boldsymbol{B}(\boldsymbol{r},t) = \boldsymbol{B}(r)e^{i\omega t}$. Approximating the Earth by a conducting sphere of radius $r = a$ with a spherically symmetric distribution of electrical conductivity and dividing the spherical conductor into a number of homogeneous layers, each of which is characterized by a constant electrical conductivity σ we write

$$\operatorname{curl}\operatorname{curl}\boldsymbol{B} + i\omega\mu_0\sigma\boldsymbol{B} = \mu_0\sigma\operatorname{curl}(\boldsymbol{u}\times\boldsymbol{B}_{\mathrm{E}})\ . \tag{1.13}$$

Considering the vector identity $\operatorname{curl}\operatorname{curl} = \operatorname{grad}\operatorname{div} - \nabla^2$ and that the magnetic field is divergence free (eq. 1.2), the magnetic induction equation within a homogeneous layer transforms to Helmholtz equation

$$\nabla^2\boldsymbol{B} + k^2\boldsymbol{B} = -\mu_0\sigma\operatorname{curl}(\boldsymbol{u}\times\boldsymbol{B}_{\mathrm{E}})\ , \tag{1.14}$$

where k is the wave number, $k^2 = -i\omega\mu_0\sigma$. For the **time domain** solution in chapter 5 we discretize the periodical circulation of the tidal flow in a finite number of time steps, so we can express the time dependent term in the induction equation as

$$\frac{\partial\boldsymbol{B}}{\partial t} = \frac{\boldsymbol{B}^{i+1} - \boldsymbol{B}^{i}}{\Delta t}\ . \tag{1.15}$$

where index i marks the time instant and Δt is time step. Finally, the induction equation in time domain takes the form

$$\frac{1}{\mu_0}\operatorname{curl}\left(\frac{1}{\sigma}\ \operatorname{curl}\boldsymbol{B}^{i+1}\right) + \frac{\boldsymbol{B}^{i+1} - \boldsymbol{B}^{i}}{\Delta t} = \operatorname{curl}(\boldsymbol{u}_{i+1}\times\boldsymbol{B}_{\mathrm{E}})\ . \tag{1.16}$$

1.3 Magnetic field decomposition

An arbitrary vector field $\boldsymbol{f}$ can be generally decomposed in toroidal $\boldsymbol{f}_{\mathrm{T}}$ and spheroidal $\boldsymbol{f}_{\mathrm{S}}$ part

$$\boldsymbol{f} = \boldsymbol{f}_{\mathrm{S}} + \boldsymbol{f}_{\mathrm{T}}\ . \tag{1.17}$$

The divergence free part of the spheroidal field is called poloidal ($\operatorname{div}\boldsymbol{f}_{\mathrm{P}} = 0$). According to Maxwell equation (1.2), the magnetic field is divergence free and therefore the nonpoloidal part of the spheroidal magnetic field is always zero. The decomposition of magnetic field can, therefore, be described by

$$\boldsymbol{B} = \boldsymbol{B}_{\mathrm{P}} + \boldsymbol{B}_{\mathrm{T}}\ . \tag{1.18}$$

The formulation for the toroidal field is implicitly divergence free, while the formulation for the poloidal magnetic field does not guarantee a divergence-free solution. This condition must be either explicitly included into model equations, or the poloidal magnetic field is expressed in terms of a toroidal magnetic potential (the case used in this thesis). The relation between the magnetic potential and magnetic induction is (Stratton, 1941)

$$\boldsymbol{B} = \operatorname{curl}\boldsymbol{A}\ . \tag{1.19}$$

In particular, poloidal magnetic field $\boldsymbol{B}_{\mathrm{P}}$ is generated by toroidal magnetic potential $\boldsymbol{A}_{\mathrm{T}}$ as

$$\boldsymbol{B}_{\mathrm{P}} = \operatorname{curl}\boldsymbol{A}_{\mathrm{T}}\ . \tag{1.20}$$

1.4 Induction equation represented in magnetic potential $\boldsymbol{A}$

We present here the induction equation for poloidal magnetic field $\boldsymbol{B}_\mathrm{P}$ expressed in terms of toroidal magnetic potential $\boldsymbol{A}_\mathrm{T}$. Using the induction equation (1.3) for $\boldsymbol{B}_\mathrm{P}$ and the relation (1.20) we write

$$\operatorname{curl}\boldsymbol{E}_\mathrm{S} = -\frac{\partial}{\partial t}\operatorname{curl}\boldsymbol{A}_\mathrm{T}\ . \tag{1.21}$$

As has been used by Martinec (1997) and derived by Souček et al. (2011) for a homogeneous induction equation, under the condition of spherically symmetric model, that means $\sigma(r)$, holds the relation

$$\boldsymbol{E}_\mathrm{S} = -\frac{\partial}{\partial t}\boldsymbol{A}_\mathrm{T}\ . \tag{1.22}$$

We extend this relation for the source term and get from equation (1.10)

$$\frac{1}{\sigma}\boldsymbol{j} - \boldsymbol{u}\times\boldsymbol{B}_\mathrm{E} = -\frac{\partial}{\partial t}\boldsymbol{A}_\mathrm{T}\ . \tag{1.23}$$

Using the Ampère's law (eq. 1.5) we obtain the induction equation for $\sigma(r)$

$$\operatorname{curl}\operatorname{curl}\boldsymbol{A}_\mathrm{T} + \mu_0\sigma\frac{\partial}{\partial t}\boldsymbol{A}_\mathrm{T} = \mu_0\sigma\left[\boldsymbol{u}\times\boldsymbol{B}_\mathrm{E}\right]_\mathrm{T}\ . \tag{1.24}$$

1.5 Modelling approach and approximations

State of the art

Primarily motivated by interpretation of magnetic records from satellite observations, present-day global models of electromagnetic induction are commonly reduced to thin sheet approximation to provide the possibility to calculate primary poloidal ocean-induced magnetic fields. The thin sheet approximations consist of a plain of ocean areas with water flow as radially integrated value moving through only the radial component of the Earth's magnetic field. Conductivity beneath the ocean layer is either neglected (Tyler et al., 2003), or added in the form of conductance as by Tyler et al. (1997a) or the source thin sheet layer is placed atop of the conductivity distribution of the Earth as in Kuvshinov and Olsen (2005). The horizontal electrical currents are constraint to a ocean areas and the secondary effects of the poloidal magnetic field, given by lateral conductivity variations, can not be estimated in such models. As explained above, the magnitude and spatial distribution of the magnetic field induced by ocean flow are largely influenced by the surrounding electric conductive space. Therefore, an accurate prediction can be achieved only by thick layer approximation considering the surrounding electric conductive space, where the toroidal part of the magnetic field is not neglected.

Spherically symmetric layered model

The spherically symmetric layered model presented in this thesis is considered as the first step on the way to the 3D conductive model for electromagnetic induction with its source in the ocean. We represent the Earth by a spherically symmetric model of electrical conductivity. Dividing the Earth in spherical finite layers allows variations of the conductivity in radial direction, where each layer is represented by a constant conductivity. The magnetic fields in individual spherical layers are then connected using boundary conditions. The source term for the electromagnetic induction is placed in the upper most layer(s) representing the ocean. The atmosphere above the Earth is considered as an insulator. (See cartoon in Figure 1.1.) The subdivision of the sphere into layers with constant electrical conductivities and the electromagnetic field decomposition in toroidal and poloidal modes makes the solution of the induction equation for a radial conductivity profile mathematically and numerically feasible. In addition, the use of identical source terms for both modes allows studying differences in the behaviour of the two modes. The magnetic field is parametrized in lateral direction using vector spherical harmonics. For radial direction, we use two different methods. Following the classical approach described in chapter 3, the diffusion of the magnetic signal with depth is solved analytically using the spherical Bessel functions as the solution of the Helmholtz equation. In chapter 4, alternatively, a weak formulation of the induction equation is formulated and magnetic field in radial direction is parametrized by finite elements. One of the advantages of our model is, that under the premise of numerical feasibility, the model with its parametrization allows arbitrary discretization in a radial direction and, dependent on cut-off degree and order, an arbitrary resolution in a lateral direction.

Source term

The source term for the forward modelling consists of horizontal ocean velocities $\boldsymbol{u}$ and background magnetic field $\boldsymbol{B}_{\mathrm{E}}$ comprising all three vector components. Both vectors are represented in horizontal direction by vector spherical harmonic series. The source term, the right hand side of the induction equation, takes in dependency on the calculated case different forms, like shown in equations (1.11), (1.16) or (1.24). As the model consists of thick layers, a volume source in the ocean can be applied in one or several layers with different electrical conductivities. This enables us to include a radial conductivity profile through the ocean. Besides the water flow as a source of energy for the motional induction, temporal variations of the background magnetic field in electrically conductive ocean induce secondary magnetic fields. Especially, fast changes of the ambient magnetic field caused, for example, by magnetic storms induce an additional constituent of magnetic field generated in the ocean. This effect is not considered in this work and the background magnetic field is therefore considered to be static. The results of existing models show that the induced magnetic field is 4 orders of magnitudes smaller than the background magnetic field. This fact leads to the assumption that the self-induction, an effect where the induced magnetic field is considered to be a part of the background magnetic field, does not significantly affect the resulting magnetic field. Therefore, the effect of self-induction is not considered in this work. Also, the feed back coupling in the magnetohydrodynamics, that is the influence of magnetic field on the oceanic dynamics is considered to be negligible. Such a model can be called as a one-sided dynamo.

Limitations

On the one hand, the analytical approach delivers a confident solution of the mathematical problem that can be used for validation of the numerical (approximate) solution. On the other hand, the strong (analytic) solution incorporates numerical limitations that can be overcome by the weak (numerical) solution. In this respect, the analytical solution requires the thicknesses of the conductive layer to be relatively large with relatively large values of electrical conductivity, whereas for the weak solution, a dense discretization is preferable due to the linear approximation of a solution between the neighboring nodes. In addition, a finer lateral resolution results in numerical limitations of the analytical approach. Moreover, the analytical solution of the Helmholtz equation, defined by the spherical Bessel functions can be performed in a Fourier frequency domain only, whereas the numerical solution of the induction equation can be also obtained in a time domain (chapter 5). The tidal dynamics with one particular frequency for each partial tide are, therefore, well suited for the solution in a Fourier frequency domain. The strong (classical) solution discussed in chapter 3, that is based on the matrix-propagator method, serves, therefor, as a reference for the internal validation of the approximate method presented in chapter 4.

Some other aspects such as, for example, the resolution of the spatial discretization can also influence the obtained results. In the case of low lateral resolution, the kinematic energy included in small-scale features like oceanic eddies can not be accounted and thus reduces the magnetic field on small scales. Given the global oceanic tidal flow used in our modelling, small-scale features can affect the signal in shallow coastal regions where the flow becomes turbulent. The spherically symmetric approximation of the Earth and the separation of the calculus into toroidal and poloidal modes have advantage that it makes the induction equation feasible, but does not allow to use 3D conductivity structures. Therefore, lateral inhomogeneities in electrical conductivity such as at the continent-ocean interface or by a depth-dependent bathymetry can not be included in the model. The area of the ocean is defined only by a ocean velocity field, however, not by the conductivity differences between oceans and continents. To obtain an estimate of the secondary magnetic field induced at the ocean-continent boundary (see sec. 3.3), at the forward modelling stage we calculate the spheroidal electric field $\boldsymbol{E}_S$ from the spherically symmetric model, which is then applied as an input datum for calculations of magnetic field in a model with a lateral conductivity mask distinguishing between the ocean and the continent areas.

Chapter 2

Representation of the magnetic source

The Lorentz force acting on the electric charges moving with the ocean flow of velocity $\boldsymbol{u}$ on the background magnetic field $\boldsymbol{B}_{\mathrm{E}}$ is the source and response into ocean-induced magnetic field. In this chapter the source term in vector spherical harmonics is expressed in terms of the toroidal and poloidal modes. This representation will be used for all later solutions in this thesis. The source term is given by the right hand side of the induction equation (1.11) and (1.24) for the toroidal magnetic field and the toroidal magnetic potential, respectively.

2.1 Source term $\boldsymbol{F}$ for the toroidal magnetic field

We denote the right hand side of the induction equation (1.11) as

$$\boldsymbol{F} := \mathrm{curl}(\boldsymbol{u} \times \boldsymbol{B}_{\mathrm{E}}) \ . \tag{2.1}$$

Since $\boldsymbol{F}$ is a vector field, it can be represented in terms of vector spherical harmonics in the form

$$\boldsymbol{F} = \sum_{jm\ell} F^{\ell}_{jm}(r) \boldsymbol{Y}^{\ell}_{jm}(\Omega) \ , \tag{2.2}$$

where $\boldsymbol{Y}^{\ell}_{jm}(\Omega)$ stands for the basis function of the vector spherical harmonics (Varshalovich et al., 1988). The summation in eq. (2.2) runs over $j = 1, 2, \ldots, \infty$, $m = -j, -j+1, \ldots, j-1, j$, and $\ell = j-1, j, j+1$. In section 2.5 we will show that $\boldsymbol{F}$ can be expressed in the form

$$\boldsymbol{F}(r, \Omega) = \sum_{jm\ell} \left[{}^{(1)}F^{\ell}_{jm} \left(\frac{r}{a}\right)^{\ell} + {}^{(2)}F^{\ell}_{jm} \left(\frac{a}{r}\right)^{\ell+1} \right] \boldsymbol{Y}^{\ell}_{jm}(\Omega) \ , \tag{2.3}$$

where the expansion coefficients ${}^{(1)}F^{\ell}_{jm}$ and ${}^{(2)}F^{\ell}_{jm}$ are given by eq. (2.42). By this, a particular solution of the inhomogeneous Helmholtz equation (1.14) in Fourier frequency domain is searched by the ansatz

$$\boldsymbol{B}_{\mathrm{part}}(r, \Omega) = \sum_{jm\ell} \left[{}^{(1)}b^{\ell}_{jm} \left(\frac{r}{a}\right)^{\ell} + {}^{(2)}b^{\ell}_{jm} \left(\frac{a}{r}\right)^{\ell+1} \right] \boldsymbol{Y}^{\ell}_{jm}(\Omega). \tag{2.4}$$

Substituting this ansatz to eq. (1.14) and realizing that functions $r^{\ell}\boldsymbol{Y}^{\ell}_{jm}(\Omega)$ and $r^{-\ell-1}\boldsymbol{Y}^{\ell}_{jm}(\Omega)$ are harmonic, we obtain $k^2 \boldsymbol{B}_{\mathrm{part}} = -\mu_0 \sigma \boldsymbol{F}$, which yields the solution for the coefficients ${}^{(\alpha)}b^{\ell}_{jm}$,

$${}^{(\alpha)}b^{\ell}_{jm} = -\frac{i}{\omega} \ {}^{(\alpha)}F^{\ell}_{jm}(a), \tag{2.5}$$

$\alpha = 1, 2$. The complete solution of the inhomogeneous Helmholtz equation (1.14) in Fourier frequency domain is given by the sum of a homogeneous solution $\boldsymbol{B}_{\mathrm{hom}}$, expressed by eq. (3.2), and the particular solution $\boldsymbol{B}_{\mathrm{part}}$, expressed by eq. (2.4), that is $\boldsymbol{B} = \boldsymbol{B}_{\mathrm{hom}} + \boldsymbol{B}_{\mathrm{part}}$.

2.2 Source term $\boldsymbol{G}$ for the poloidal magnetic field

To describe the source term for the poloidal magnetic field let us denote the cross product of $\boldsymbol{u}$ and $\boldsymbol{B}_{\mathrm{E}}$ on the right hand site of the induction equation (1.24) for the magnetic potential $\boldsymbol{A}$ as

$$\boldsymbol{G} := \boldsymbol{u} \times \boldsymbol{B}_{\mathrm{E}} \ . \tag{2.6}$$

Similar to the decomposition in eq. (2.2), we can write

$$\boldsymbol{G} = \sum_{jm\ell} G_{jm}^{\ell}(r) \boldsymbol{Y}_{jm}^{\ell}(\Omega) \ . \tag{2.7}$$

In contrast to the ansatz (2.3) for the toroidal magnetic field, in the case of the poloidal magnetic field we assume that the horizontal ocean flow $\boldsymbol{u}$ does not change with depth. In such a case, it is sufficient to describe $\boldsymbol{G}$ by only one set of spherical harmonic coefficients G_{jm}^{ℓ},

$$\boldsymbol{G}(r,\Omega) = \sum_{jm\ell} G_{jm}^{\ell}(a) \ \left(\frac{r}{a}\right)^{\ell} \ \boldsymbol{Y}_{jm}^{\ell}(\Omega) \ . \tag{2.8}$$

By this, the partial solution of the inhomogeneous Helmholtz eq. (1.24) is

$$\boldsymbol{A}_{\mathrm{part}}(r,\Omega) = \sum_{jm\ell} p_{jm}^{\ell} \left(\frac{r}{a}\right)^{\ell} \boldsymbol{Y}_{jm}^{\ell}(\Omega) \ , \tag{2.9}$$

where eq. (1.24) reduces to $k^2 \boldsymbol{A}_{\mathrm{part}} = -\mu_0 \sigma \boldsymbol{G}$. This yields the solution for the coefficients p_{jm}^{ℓ},

$$p_{jm}^{\ell} = \frac{-\mu_0 \sigma}{k^2} \ G_{jm}^{\ell}(a) = -\frac{i}{\omega} \ G_{jm}^{\ell}(a). \tag{2.10}$$

2.3 Representation of ocean velocities $\boldsymbol{u}$

To represent the source terms $\boldsymbol{F}$ and $\boldsymbol{G}$ in the term of vector spherical harmonic series, the ocean velocities $\boldsymbol{u}$ and the main magnetic field $\boldsymbol{B}_{\mathrm{E}}$ need to be specified in an explicit way. As a matter of fact, the radial component of ocean flow generated by tidal forcing is significantly smaller in comparison to the horizontal velocity components. We will therefore approximate the ocean flow velocity $\boldsymbol{u}$ by its horizontal components u_{ϑ} and u_{φ} only,

$$\boldsymbol{u} = u_{\vartheta} \boldsymbol{e}_{\vartheta} + u_{\varphi} \boldsymbol{e}_{\varphi}, \tag{2.11}$$

where $\boldsymbol{e}_{\vartheta}$ and $\boldsymbol{e}_{\varphi}$ are unit base vectors in the co-latitude and longitude directions, respectively. The velocity $\boldsymbol{u}$ can alternatively be represented as a series of vector spherical harmonics,

$$\boldsymbol{u}(r,\Omega) = \sum_{jm\ell} u_{jm}^{\ell}(r) \boldsymbol{Y}_{jm}^{\ell}(\Omega). \tag{2.12}$$

Appendix A presents the least-squares method for estimating the coefficients $u_{jm}^{\ell}(r)$ from gridded ocean velocities $(u_{\vartheta}, u_{\varphi})$. To examine the sensitivity of induced toroidal magnetic field on the radial changes of $\boldsymbol{u}$, we assume, without loss of generality, that the flow $\boldsymbol{u}$ can be a linear function of r without a change in flow direction with depth. In the case where $\boldsymbol{u}$ is a more complex function of r, the source term may be discretized into a set of layers analog to the parameter of radial conductivity profile (sec. 3.1.1) in each of which $\boldsymbol{u}$ can be represented as a linear function of r. Hence, we write

$$u_{jm}^{\ell}(r) = g_{jm}^{\ell} + h_{jm}^{\ell} \, r \tag{2.13}$$

for $r_\mathrm{b} \leq r \leq r_\mathrm{a}$, where r_a and r_b are the radii of the ocean surface and bottom, respectively. The coefficients g^ℓ_{jm} and h^ℓ_{jm} can be determined from the ocean flow model.

As the constant and linear functions are not orthogonal to each other and therefore not independent from each other, in the case of over the depth constant ocean flow the radial dependent coefficient h^ℓ_{jm} can not be omitted and the ansatz must be used still in the form of eq. (2.13). As discussed in section 2.2 for the poloidal magnetic field we assume that ocean velocities do not change with depth, and are then represented by coefficient $u^\ell_{jm}(r)$ only.

2.4 Representation of the background magnetic field $\boldsymbol{B}_\mathrm{E}$

The Earth's magnetic field may be described in terms of spherical harmonic series. In the atmosphere ($\sigma = 0$) this representation is given by spheroidal vector spherical harmonics in the form

$$\begin{aligned} \boldsymbol{B}_\mathrm{E}(\boldsymbol{r},\Omega) = -\sum_{j=1}^{\infty}\sum_{m=-j}^{j} \Bigg[& \sqrt{j(2j+1)}\left(\frac{r}{a}\right)^{j-1} G^{(e)}_{jm}\, \boldsymbol{Y}^{j-1}_{jm}(\Omega) \\ & + \sqrt{(j+1)(2j+1)}\left(\frac{a}{r}\right)^{j+2} G^{(i)}_{jm}\, \boldsymbol{Y}^{j+1}_{jm}(\Omega) \Bigg] , \end{aligned} \tag{2.14}$$

where then Gauss coefficients $G^{(e)}_{jm}$ and $G^{(i)}_{jm}$ describe the magnetic fields of external and internal origins, respectively. In the case of ocean-induced magnetic field, we consider the background magnetic field $\boldsymbol{B}_\mathrm{E}$ as the main magnetic field of the Earth

$$\boldsymbol{B}_\mathrm{E}(r,\Omega) = -\sum_{j=1}^{j_\mathrm{main}}\sum_{m=-j}^{j} \sqrt{(j+1)(2j+1)}\left(\frac{a}{r}\right)^{j+2} G^{(i)}_{jm}\, \boldsymbol{Y}^{j+1}_{jm}(\Omega), \tag{2.15}$$

where $G^{(i)}_{jm}$ are the internal Gauss coefficients truncated at degree j_main. Moreover, we assume that $G^{(i)}_{jm}$ are time independent. To simplify the notation, we introduce

$$B^{j+1}_{\mathrm{E},jm}(r) = B^{j+1}_{\mathrm{E},jm}(a)\left(\frac{a}{r}\right)^{j+2}, \qquad B^{j+1}_{\mathrm{E},jm}(a) = -\sqrt{(j+1)(2j+1)}\; G^{(i)}_{jm}. \tag{2.16}$$

It is common in the magnetic community to describe the magnetic field by spherical harmonics expressed in the Schmidt semi-norm. The calculus in this thesis is carried out according to the norm given in Varshalovich et al. (1988) (eqs D.20 and D.8). The conversion between the two normalizations is as follow. The Schmidt semi-normalized associated Legendre functions (Winch et al., 2005) are given by

$$\hat{P}^m_j(\cos\vartheta) = \sqrt{(2-\delta_{m0})\frac{(j-m)!}{(j+m)!}}\, P_{jm}(\cos\vartheta) , \tag{2.17}$$

where $P_{jm}(\cos\vartheta)$ stands for associated Legendre functions and δ_{m0} is the Kronecker delta symbol here distinguishing the zonal case. On the other hand, the fully-normalized Legendre functions are

$$P^m_j(\cos\vartheta) = \sqrt{\frac{2j+1}{4\pi}\,\frac{(j-m)!}{(j+m)!}}\, P_{jm}(\cos\vartheta) . \tag{2.18}$$

Therefore, the background magnetic field expressed in the Schmidt semi-normalized coefficient g_{jm} and in fully normalized Gauss coefficient G_{jm} has the forms that equals to each other,

$$G_{jm}\sqrt{\frac{2j+1}{4\pi}\,\frac{(j-m)!}{(j+m)!}}\, P_{jm}(\cos\vartheta) = g_{jm}\sqrt{(2-\delta_{m0})\,\frac{(j-m)!}{(j+m)!}}\, P_{jm}(\cos\vartheta) . \tag{2.19}$$

This yields the relation between the Schmidt semi-normalized coefficients g_{jm} and fully normalized coefficients G_{jm}

$$G_{jm} = \sqrt{(2-\delta_{m0})\,\frac{4\pi}{2j+1}}\; g_{jm}\; . \tag{2.20}$$

2.5 Representation of the source terms of $\boldsymbol{F}$ and $\boldsymbol{G}$

Having represented ocean velocities $\boldsymbol{u}$ and the main magnetic field $\boldsymbol{B}_{\mathrm{E}}$ in terms of vector spherical harmonics, we aim now to express the source terms $\boldsymbol{F}$ and $\boldsymbol{G}$ in the form of the ansatz by eq. (2.3) and (2.8), respectively. We will do this for the case when the background magnetic field $\boldsymbol{B}_{\mathrm{E}}$ is characterized by *one* individual coefficient $B^{j_2+1}_{\mathrm{E},j_2m_2}(r)$ only. Hence, we assume for the moment that

$$\boldsymbol{B}_{\mathrm{E}}(r,\Omega) = B^{j_2+1}_{\mathrm{E},j_2m_2}(r)\boldsymbol{Y}^{j_2+1}_{j_2m_2}(\Omega), \tag{2.21}$$

where the indexes j_2 and m_2 are fixed through the following derivation. Since the source term is linear with respect to the background magnetic field $\boldsymbol{B}_{\mathrm{E}}$, the complete representation of $\boldsymbol{F}$ and $\boldsymbol{G}$ will be given by the sum of the representations of the individual contributions (eq. 2.21). The cross-product of $\boldsymbol{u}$ and $\boldsymbol{B}_{\mathrm{E}}$ reads as

$$\boldsymbol{u}\times\boldsymbol{B}_{\mathrm{E}} = \sum_{j_1m_1\ell_1} u^{\ell_1}_{j_1m_1}(r)B^{j_2+1}_{\mathrm{E},j_2m_2}(r)\left(\boldsymbol{Y}^{\ell_1}_{j_1m_1}(\Omega)\times\boldsymbol{Y}^{j_2+1}_{j_2m_2}(\Omega)\right), \tag{2.22}$$

where the cross-product of two vector spherical harmonics can be expressed as a finite sum of vector spherical harmonics (Varshalovich et al., 1988)

$$\boldsymbol{Y}^{\ell_1}_{j_1m_1}(\Omega)\times\boldsymbol{Y}^{j_2+1}_{j_2m_2}(\Omega) = \sum_{jm\ell} V^{jm\ell}_{j_1m_1\ell_1,j_2m_2}\boldsymbol{Y}^{\ell}_{jm}(\Omega) \tag{2.23}$$

with the expansion coefficients given by equation (D.27)

$$V^{jm\ell}_{j_1m_1\ell_1,j_2m_2} = i\sqrt{\frac{3}{2\pi}(2j_1+1)(2j_2+1)(2\ell_1+1)(2j_2+3)}\begin{Bmatrix} j_1 & \ell_1 & 1\\ j_2 & j_2+1 & 1\\ j & \ell & 1\end{Bmatrix} C^{\ell 0}_{\ell_1 0 j_2+1 0}\, C^{jm}_{j_1m_1j_2m_2}\; . \tag{2.24}$$

Here, the curl brackets stand for Wigner's $9-j$ symbols and $C^{jm}_{j_1m_1j_2m_2}$ are the Clebsch-Gordan coefficients. The source term $\boldsymbol{G} = \boldsymbol{u}\times\boldsymbol{B}_{\mathrm{E}}$ can now be represented as a series of vector spherical harmonics

$$\boldsymbol{G}(r,\Omega) = \sum_{jm\ell} G^{\ell}_{jm}(r)\boldsymbol{Y}^{\ell}_{jm}(\Omega)\; , \tag{2.25}$$

where

$$G^{\ell}_{jm}(r) = \sum_{j_1m_1\ell_1}\sum_{\ell_3} V^{jm\ell_3}_{j_1m_1\ell_1,j_2m_2}\, u^{\ell_1}_{j_1m_1}(r)\, B^{j_2+1}_{\mathrm{E},j_2m_2}(r). \tag{2.26}$$

Applying the differential operator *curl* to eq. (2.22) and making use of the identity $\mathrm{curl}(f\boldsymbol{v}) = f\,\mathrm{curl}\boldsymbol{v} + \mathrm{grad}f\times\boldsymbol{v}$, where f and $\boldsymbol{v}$ are scalar and vector differentiable functions, respectively, we obtain

$$\begin{aligned}\mathrm{curl}(\boldsymbol{u}\times\boldsymbol{B}_{\mathrm{E}}) = \sum_{j_1m_1\ell_1} &\Big\{u^{\ell_1}_{j_1m_1}(r)B^{j_2+1}_{\mathrm{E},j_2m_2}(r)\,\mathrm{curl}\left(\boldsymbol{Y}^{\ell_1}_{j_1m_1}(\Omega)\times\boldsymbol{Y}^{j_2+1}_{j_2m_2}(\Omega)\right)\\ &+\frac{d}{dr}\left(u^{\ell_1}_{j_1m_1}(r)B^{j_2+1}_{\mathrm{E},j_2m_2}(r)\right)\boldsymbol{e}_r\times\left(\boldsymbol{Y}^{\ell_1}_{j_1m_1}(\Omega)\times\boldsymbol{Y}^{j_2+1}_{j_2m_2}(\Omega)\right)\Big\}.\end{aligned} \tag{2.27}$$

By eq. (2.23) and the differential relation for the *curl* of $\boldsymbol{Y}^{\ell}_{jm}(\Omega)$ (see eqs D.32 - D.34),

$$\operatorname{curl}\boldsymbol{Y}^{\ell}_{jm}(\Omega) = \frac{1}{r}\sum_{\ell_3}\alpha^{\ell_3}_{\ell}\,\boldsymbol{Y}^{\ell_3}_{jm}(\Omega), \tag{2.28}$$

where the coefficients $\alpha^{\ell_3}_{\ell}$ vanish unless

$$\begin{aligned}
\alpha^{j}_{j-1} &= -i\sqrt{\frac{j+1}{2j+1}}\,(j-1)\,, &\qquad \alpha^{j}_{j+1} &= i\sqrt{\frac{j}{2j+1}}\,(j+2)\,,\\
\alpha^{j-1}_{j} &= i\sqrt{\frac{j+1}{2j+1}}\,(j+1)\,, &\qquad \alpha^{j+1}_{j} &= -i\sqrt{\frac{j}{2j+1}}\,(j),
\end{aligned} \tag{2.29}$$

the first term in eq. (2.27) can be written as

$$\operatorname{curl}\Big(\boldsymbol{Y}^{\ell_1}_{j_1m_1}(\Omega)\times\boldsymbol{Y}^{j_2+1}_{j_2m_2}(\Omega)\Big) = \frac{1}{r}\sum_{jm\ell}\sum_{\ell_3}V^{jm\ell_3}_{j_1m_1\ell_1,j_2m_2}\,\alpha^{\ell}_{\ell_3}\,\boldsymbol{Y}^{\ell}_{jm}(\Omega). \tag{2.30}$$

Likewise, by eq. (2.23) and the relation for the cross product of $\boldsymbol{e}_r$ with $\boldsymbol{Y}^{\ell}_{jm}(\Omega)$, see eqs (D.38 - D.40),

$$\boldsymbol{e}_r\times\boldsymbol{Y}^{\ell}_{jm}(\Omega) = \sum_{\ell_3}\beta^{\ell_3}_{\ell}\,\boldsymbol{Y}^{\ell_3}_{jm}(\Omega), \tag{2.31}$$

where the coefficients $\beta^{\ell_3}_{\ell}$ vanish unless

$$\begin{aligned}
\beta^{j}_{j-1} = \beta^{j-1}_{j} &= i\sqrt{\frac{j+1}{2j+1}},\\
\beta^{j}_{j+1} = \beta^{j+1}_{j} &= i\sqrt{\frac{j}{2j+1}}.
\end{aligned} \tag{2.32}$$

we find that the second term in eq. (2.27) is

$$\boldsymbol{e}_r\times\Big(\boldsymbol{Y}^{\ell_1}_{j_1m_1}(\Omega)\times\boldsymbol{Y}^{j_2+1}_{j_2m_2}(\Omega)\Big) = \sum_{jm\ell}\sum_{\ell_3}V^{jm\ell_3}_{j_1m_1\ell_1,j_2m_2}\,\beta^{\ell}_{\ell_3}\,\boldsymbol{Y}^{\ell}_{jm}(\Omega). \tag{2.33}$$

The source vector $\boldsymbol{F} = \operatorname{curl}(\boldsymbol{u}\times\boldsymbol{B}_{\mathrm{E}})$ can now be represented as a series of vector spherical harmonics

$$\boldsymbol{F}(r,\Omega) = \sum_{jm\ell}F^{\ell}_{jm}(r)\boldsymbol{Y}^{\ell}_{jm}(\Omega) \tag{2.34}$$

with the expansion coefficients

$$F^{\ell}_{jm}(r) = \sum_{j_1m_1\ell_1}\sum_{\ell_3}V^{jm\ell_3}_{j_1m_1\ell_1,j_2m_2}\Big[\alpha^{\ell}_{\ell_3}\frac{1}{r}\,u^{\ell_1}_{j_1m_1}(r)\,B^{j_2+1}_{\mathrm{E},j_2m_2}(r) + \beta^{\ell}_{\ell_3}\,\frac{d}{dr}\Big(u^{\ell_1}_{j_1m_1}(r)\,B^{j_2+1}_{\mathrm{E},j_2m_2}(r)\Big)\Big]. \tag{2.35}$$

Substituting for the radial dependence of $u^{\ell}_{jm}(r)$ and $B^{j_2+1}_{\mathrm{E},j_2m_2}(r)$ from eqs (2.13) and (2.16), respectively, we find, after some algebraic manipulations, that

$$F^{\ell}_{jm}(r) = \Big(D_{jm\ell,j_2m_2} + \frac{1}{r}E_{jm\ell,j_2m_2}\Big)\Big(\frac{a}{r}\Big)^{j_2+2}, \tag{2.36}$$

where

$$\begin{aligned}
D_{jm\ell,j_2m_2} &= B^{j_2+1}_{\mathrm{E},j_2m_2}(a)\sum_{j_1m_1\ell_1}\sum_{\ell 3}V^{jm\ell_3}_{j_1m_1\ell_1,j_2m_2}\Big(\alpha^{\ell}_{\ell_3} - (j_2+1)\beta^{\ell}_{\ell_3}\Big)h^{\ell_1}_{j_1m_1},\\
E_{jm\ell,j_2m_2} &= B^{j_2+1}_{\mathrm{E},j_2m_2}(a)\sum_{j_1m_1\ell_1}\sum_{\ell 3}V^{jm\ell_3}_{j_1m_1\ell_1,j_2m_2}\Big(\alpha^{\ell}_{\ell_3} - (j_2+2)\beta^{\ell}_{\ell_3}\Big)g^{\ell_1}_{j_1m_1}.
\end{aligned} \tag{2.37}$$

Finally, comparing the coefficients at $\boldsymbol{Y}^{\ell}_{jm}(\Omega)$ in the ansatz (2.3) with eq. (2.36), we obtain

$$ {}^{(1)}F^{\ell}_{jm}\Big(\frac{r}{a}\Big)^{\ell} + {}^{(2)}F^{\ell}_{jm}\Big(\frac{a}{r}\Big)^{\ell+1} = \Big(D_{jm\ell,j_2m_2} + \frac{1}{r}E_{jm\ell,j_2m_2}\Big)\Big(\frac{a}{r}\Big)^{j_2+2} \tag{2.38}$$

for all eligible indexes j, m and ℓ, but fixed indexes j_2 and m_2. The last condition should hold at any point of radius r inside the ocean layer, that is for $r_{\mathrm{b}} \leq r \leq r_{\mathrm{a}}$. Considering the thickness of ocean layer being much smaller than the mean radius of the Earth, the powers $(r/a)^{\ell}$ and $(a/r)^{\ell+1}$, divided by power $(a/r)^{j_2+2}$, can be approximated within the ocean layer by $1/r$ by applying the binomial theorem,

$$\Big(\frac{a}{r}\Big)^{k} = \Big(\frac{r+a-r}{r}\Big)^{k} = \Big(1+\frac{a-r}{r}\Big)^{k} = 1 + k\Big(\frac{a-r}{r}\Big) + O\Big(\frac{a-r}{r}\Big)^{2} \doteq 1 - k + k\Big(\frac{a}{r}\Big), \tag{2.39}$$

where the higher-order expansion terms can be safely neglected. In particular, for $k = -\ell - j_2 - 2$ and $k = \ell - j_2 - 1$, it holds that

$$\begin{aligned} \Big(\frac{r}{a}\Big)^{\ell+j_2+2} &= \ell + j_2 + 3 - (\ell + j_2 + 2)\Big(\frac{a}{r}\Big), \\ \Big(\frac{a}{r}\Big)^{\ell-j_2-1} &= -\ell + j_2 + 2 + (\ell - j_2 - 1)\Big(\frac{a}{r}\Big). \end{aligned} \tag{2.40}$$

Substituting eq. (2.40) into eq. (2.38) and comparing the constant terms and the coefficients at $1/r$, we find

$$\begin{aligned} (\ell + j_2 + 3)\, {}^{(1)}F^{\ell}_{jm} - (\ell - j_2 - 2)\, {}^{(2)}F^{\ell}_{jm} &= D_{jm\ell,j_2m_2}, \\ -(\ell + j_2 + 2)\, {}^{(1)}F^{\ell}_{jm} + (\ell - j_2 - 1)\, {}^{(2)}F^{\ell}_{jm} &= \frac{1}{a}E_{jm\ell,j_2m_2}. \end{aligned} \tag{2.41}$$

The solution of eq. (2.41) is therefore

$$\begin{aligned} {}^{(1)}F^{\ell}_{jm} &= \frac{1}{2\ell+1}\Big[(\ell - j_2 - 1)\, D_{jm\ell,j_2m_2} + (\ell - j_2 - 2)\frac{1}{a}E_{jm\ell,j_2m_2}\Big], \\ {}^{(2)}F^{\ell}_{jm} &= \frac{1}{2\ell+1}\Big[(\ell + j_2 + 2)\, D_{jm\ell,j_2m_2} + (\ell + j_2 + 3)\frac{1}{a}E_{jm\ell,j_2m_2}\Big], \end{aligned} \tag{2.42}$$

by which the coefficients ${}^{(\alpha)}F^{\ell}_{jm}$ of the source term $\boldsymbol{F}$ are expressed in terms of the coefficients $D_{jm\ell,j_2m_2}$ and $E_{jm\ell,j_2m_2}$ of $\boldsymbol{u}$ and one individual coefficient $B^{j_2+1}_{\mathrm{E},j_2m_2}(a)$ of the background magnetic field $\boldsymbol{B}_{\mathrm{E}}$. The complete representation of $\boldsymbol{F}$ is given by the sum of the individual contributions (2.42) for $j_2 = 1, \ldots, j_{\mathrm{main}}$, and $m_2 = -j_2, \ldots, j_2$.

2.6 Input data

2.6.1 Ocean velocities

The input ocean velocities are generated by the Ocean Modell for Circulation and Tides (Thomas (2002); Dobslaw (2007)) over a regular (ϑ, φ) grid with a grid size of 1.875° in latitude and longitude. The model has been derived from The Hamburg Ocean Primitive Equation Modell (HOPE; Drijfhout et al. (1996) and Wolff et al. (1997)). Thereby, the original model has been adapted for studying short-term mass variations in ocean caused by lunisolar tides and general circulation. For this purpose, the OMCT model has been coupled with ephemeris module for tides which allows the determination of tidal lunisolar gravitation potential differences. Using temporally high resolution atmospheric data adapted for short-time weather scales, the general circulation in the OMCT is composed of thermohaline, wind driven and pressure driven circulation. As input for our modelling, the OMCT model provides depth-integrated velocity field of barotropic horizontal ocean circulation flow $\boldsymbol{u}$ driven by the lunar semidiurnal tide M_2 with a period of 12 h and 42 min,

$$\boldsymbol{u}_{\mathrm{int}} = \int_{h_{\mathrm{bath}}}^{0} \boldsymbol{u} \, dr \ , \tag{2.43}$$

where h_{bath} stands for the bathymetry shown in Figure 2.3. An identical depth integrated velocity field has been used also for the thin sheet approximation in Dostal (2009) where a good agreement of the amplitude and global distribution of the radial component of the generated magnetic field in comparison to the results by Tyler et al. (2003) and Maus and Kuvshinov (2004) has been presented. This data set is used as the input of all numerical experiments carried out in this thesis. Dividing the depth integrated velocity field $\boldsymbol{u}_{\mathrm{int}}$ by ocean depth h_{ocean} ,

$$\boldsymbol{u}(\vartheta, \varphi) = \frac{\boldsymbol{u}_{\mathrm{int}}(\vartheta, \varphi)}{h_{\mathrm{ocean}}(\vartheta, \varphi)} \tag{2.44}$$

we obtain a realistic velocity distribution $\boldsymbol{u}$ (in the units of m/s). In dependence on h_{ocean}, we can study two different effects of the ocean-induced magnetic field.

In the first case we scale $\boldsymbol{u}_{\mathrm{int}}$ with the ocean depth given by the bathymetry field $h_{\mathrm{ocean}}(\vartheta, \varphi) = h_{\mathrm{bath}}(\vartheta, \varphi)$. The resulting data are the average tidal velocities $\boldsymbol{u}_{\mathrm{avg}}$. This velocity field includes the whole ocean areas and equals to ocean flow close to a sea surface. The average velocities enable $\boldsymbol{u}_{\mathrm{avg}}$ us to study the influence of the M_2 tidal wave on the generated magnetic field, given by large ocean velocities in shallow-water coastal regions. The fast moving electrical charges are particularly important for the induction of the toroidal and poloidal magnetic field. In addition, in the locations close to the coast, the secondary poloidal magnetic field can be generated due to the electrical conductivity contrast between ocean and continent. The areas of interest in this case are shallow coastal regions. Not overestimate the generated magnetic field by using the average velocity field $\boldsymbol{u}_{\mathrm{avg}}$, we reduce the depth of the spherically symmetric ocean layer to $h = 1$ km.

In a second case, where we calculate the ocean induced magnetic field generated by the whole transport of the M_2 tide, we apply the integrated velocity field $\boldsymbol{u}_{\mathrm{int}}$ on a layer of average ocean thickness equal to the ocean depth of $h_{\mathrm{ocean}} = 4$ km. Dividing the integrated velocity field by constant ocean layer depth reduces the value of the flow velocity in shallow regions and increases the velocity in deeper regions. This weighing guarantees that the whole oceanic transport is considered without overestimation or underestimation in shallow or deeper oceanic regions, respectively.

The gridded velocity field is described by the amplitude $u_\alpha^A(\vartheta, \varphi)$ and spatial phase-shift $u_\alpha^\phi(\vartheta, \varphi)$ for the horizontal components $(\boldsymbol{u})_\vartheta$ and $(\boldsymbol{u})_\varphi$. For each velocity component we introduce a complex quantity $u_\alpha = u_\alpha^{\mathrm{real}} + i \, u_\alpha^{\mathrm{imag}}$ by the relations

$$u_\alpha^{\mathrm{real}}(\vartheta, \varphi) = u_\alpha^A(\vartheta, \varphi) \, \cos u_\alpha^\phi(\vartheta, \varphi) \ , \tag{2.45}$$

and

$$u_\alpha^{\mathrm{imag}}(\vartheta, \varphi) = u_\alpha^A(\vartheta, \varphi) \, \sin u_\alpha^\phi(\vartheta, \varphi) \ , \tag{2.46}$$

where label $\alpha = (\vartheta, \varphi)$ stands for the two horizontal velocity components ϑ and φ. For a solution in time domain (chap. 5) we discretize the tidal wave by the time step Δt and have discrete values of velocities in time

$$u_\alpha^i(\vartheta, \varphi) = u_\alpha^A(\vartheta, \varphi) \, \cos[u_\alpha^\phi(\vartheta, \varphi) + i \, \Delta t] \qquad\qquad i = 1, 2, \dots \ . \tag{2.47}$$

with i as a index for a time instant. The least-squares method (presented in the Appendix A) is then applied to gridded ocean velocities (u_ϑ, u_φ), to each time instant to compute the least-squares estimate $\hat{u}^\ell_{jm}$ of the spherical harmonic expansion coefficients u^ℓ_{jm} of horizontal ocean velocity $\boldsymbol{u}$. For a grid-step size of 1.875°, the angular degree $j = 95$ is the highest degree for which the discrete velocity data can unambiguously be represented by spherical harmonic series in eq. (2.12). To achieve reliable results, we represent the ocean velocity by the vector spherical harmonic series, see eq. (2.12), cut off at degree $j_{\max} = 48$. In addition, to mitigate the effect of the Gibbs phenomenon, the series in eq. (2.12) is weighted by the Lanczos η_j coefficients (Duchon, 1979). In summary, the horizontal ocean velocities are represented in the form

$$\boldsymbol{u}(r, \vartheta, \varphi) = \sum_{j=1}^{j_{\max}} \sum_{m=-j}^{j} \sum_{\ell=j-1}^{j+1} \eta_j \, \hat{u}^\ell_{jm}(r) \boldsymbol{Y}^\ell_{jm}(\vartheta, \varphi). \tag{2.48}$$

Figure 2.1 shows the real and imaginary parts of the ϑ and φ components of the average ocean velocities synthesized from the spherical harmonic coefficients $\hat{u}^\ell_{jm}$ according to eq. (2.48). We can see large-scale spatial patterns of the ocean velocities over deep-water open ocean areas and rather short-wavelength spatial patterns over shallow-water coastal regions. Due to the truncation of the spherical harmonic series in eq. (2.48), the modeled ocean velocities are slightly extended over continental coastal regions. This will not, however, affect our estimates of the size and scale of the induced magnetic field, but it would be a limitation when the observed magnetic field is interpreted in terms of ocean velocities. The synthesized velocity of the oceanic transport are presented in Figure 2.2. Comparing them with the average velocities (Figure 2.1) we recognize again the large-scaled patterns over oceanic basins, but the weighting by constant ocean depth thickness reduces the influence of the small-scaled features in coastal regions given by large velocities in shallow water. Consider the different scale in both Figures.

2.6.2 Background magnetic field

For the Earth's background magnetic field $\boldsymbol{B}_{\mathrm{E}}$, which is considered constant over time, we apply the POMME-6 model from Maus et al. (2010). The magnetic dipole term has the dominant influence on the magnitude and spatial patterns of the ocean-induced magnetic field. For the poloidal mode the background field is represented by dipole term only. The model for the toroidal magnetic field has been designed also for higher degrees (non-dipole) of spherical harmonic coefficients of the background magnetic field. Including higher-degree spherical harmonic coefficients allows to locate the geographic position to the magnetic poles. This causes minor changes in the magnitudes of the induced magnetic field, in particular, the magnetic field is slightly weakened around New Zealand. Including spherical harmonic coefficients higher than degree and order 6 has no significant influence on the induced magnetic field. Hence, the magnetic field $\boldsymbol{B}_{\mathrm{E}}$ is truncated at degree and order 6 in numerical computations. The three components of the main magnetic field used for generating the toroidal magnetic field are shown in Figure 2.4.

2.6.3 Radial profile of electrical conductivity

A conductive spherical earth model consists of two regions. A highly conductive ocean, where the ocean velocities induce the magnetic field, and a source-free, less conductive mantle beneath the ocean. For modelling the induced toroidal magnetic field, the ocean is divided into several spherical layers with different electrical conductivities. In this thesis, we use 6-layer ocean where the conductivity is piecewise constant and varies from $\sigma_{\mathrm{o}} = 4.7\ \mathrm{Sm}^{-1}$ at the sea surface to $\sigma_{\mathrm{o}} =$

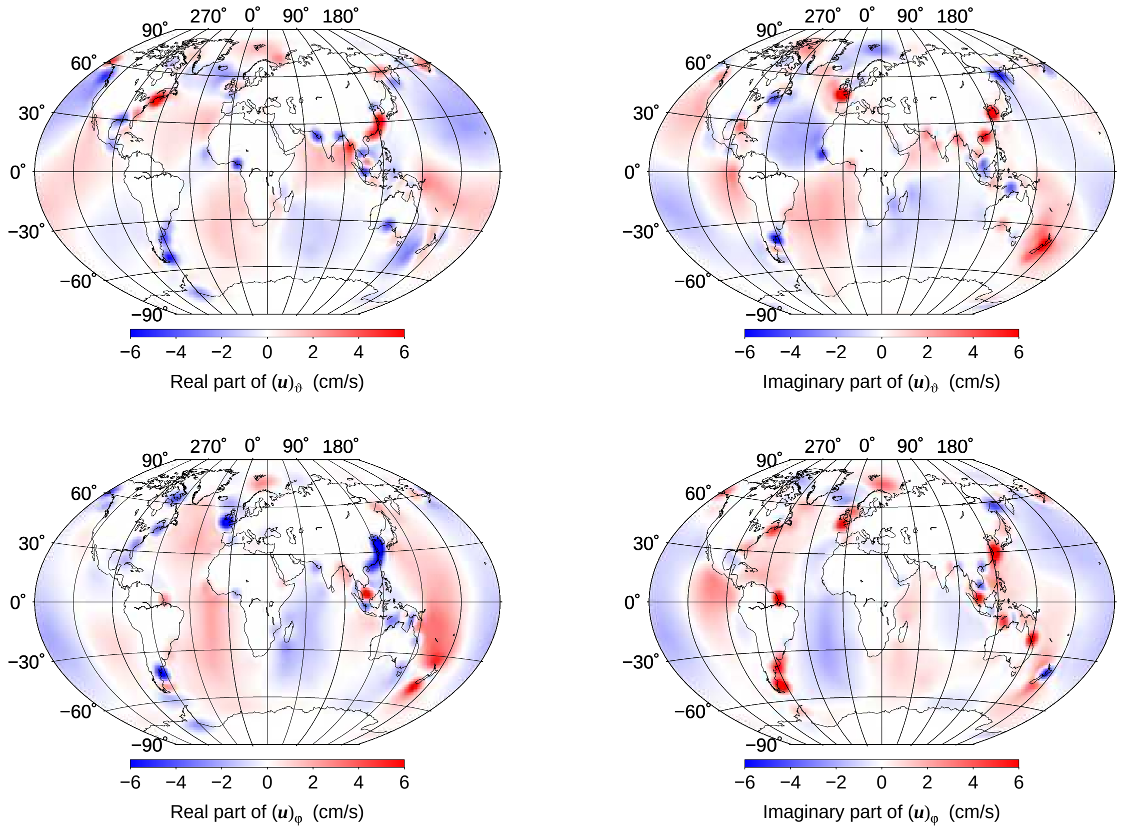

Figure 2.1: Real (left) and imaginary (right) parts of ϑ (top) and φ (bottom) components of the ocean velocities forced by M_2 tide synthesized from the spherical harmonics coefficients $\hat{u}^{\ell}_{jm}$.

3.2 Sm^{-1} at the ocean bottom due to varying water temperature and salinity. The electrical conductivity model is taken accordingly to Apel (1987),

$$\sigma_\mathrm{o}(T,s) = \sigma(25,s)\, e^{-\beta\Delta_\mathrm{T}} \,, \tag{2.49}$$

where

$$\Delta_\mathrm{T} = 25\,^\circ\mathrm{C} - T \,, \tag{2.50}$$

$$\begin{aligned} \beta &= \beta(\Delta, s) \\ &= 2,033 \cdot 10^{-2} + 1,266 \cdot 10^{-4}\,\Delta + 2,464 \cdot 10^{-6}\,\Delta^2 \\ &\quad - s(1,849 \cdot 10^{-5} - 2,551 \cdot 10^{-7}\,\Delta + 2,551 \cdot 10^{-8}\,\Delta^2) \end{aligned} \tag{2.51}$$

and

$$\sigma(25,s) = s(0,182521 - 1,46192 \cdot 10^{-3}\, s + 2,09324 \cdot 10^{-5}\, s^2 - 1,28205 \cdot 10^{-7}\, s^3) \tag{2.52}$$

with T for temperature in °C, Δ_T for temperature difference and s for salinity, which is set constantly by $s = 34.25$ psu. A uniform electrical conductivity of ocean, $\sigma_\mathrm{o} = 3.5$ S/m, is modelled by a constant temperature to $T = 8.0\,^\circ\mathrm{C}$. For studying the influence of the conductivity gradient through the ocean layer and for modelling the poloidal magnetic field, we use also a constant conductivity profile set by $\sigma_o = 3.5\ \mathrm{Sm}^{-1}$. In dependence on the numerical experiment, the ocean layer takes two different thicknesses. For the average tidal velocity field, the ocean layer depth is

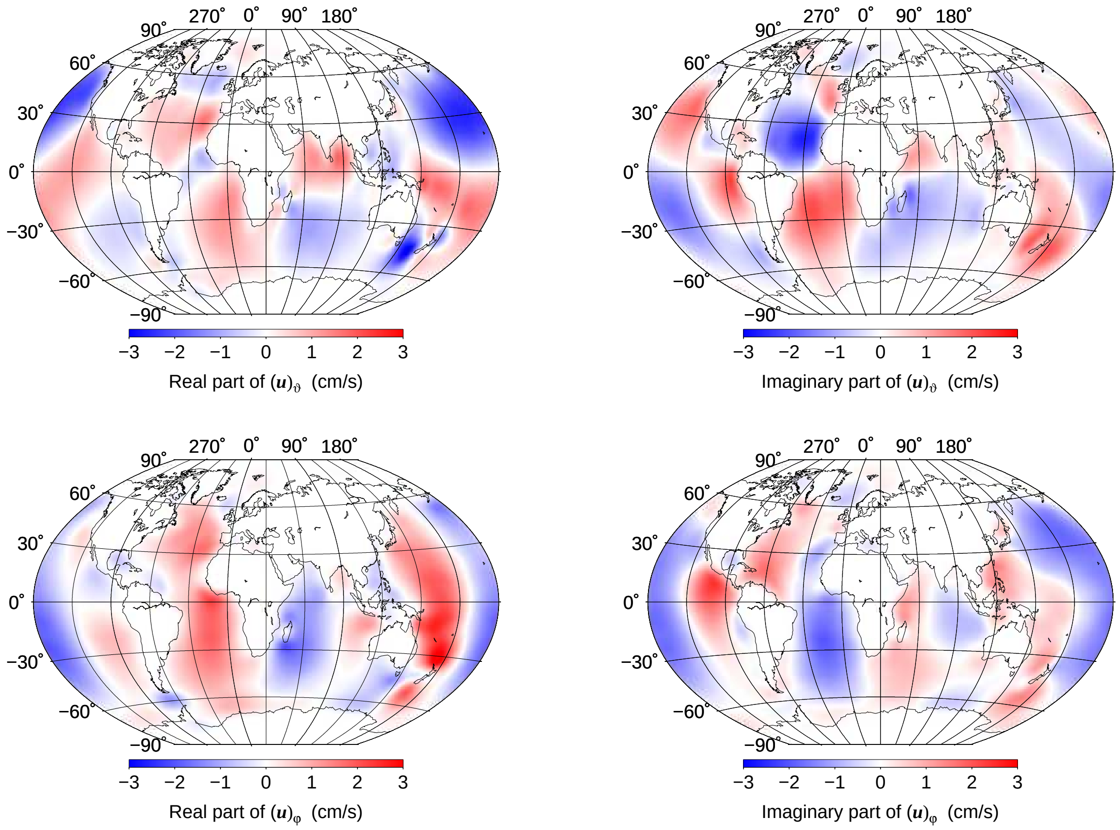

Figure 2.2: Real (left) and imaginary (right) parts of ϑ (top) and φ (bottom) components of the ocean velocities weighted by ocean depth thicknesses for M_2 tide, synthesized from the spherical harmonics coefficients $\hat{u}^{\ell}_{jm}$.

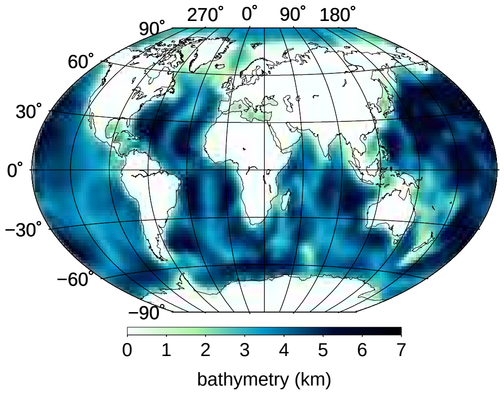

Figure 2.3: The bathymetry (in km) used to average M_2 tide velocity field in Figure 2.1.

considered to be $h = 1$ km. For radially integrated velocity field where the whole oceanic transport is considered, we use average ocean depth of $h = 4$ km. The conductivity of the underlying sediments, lithosphere and mantle is divided into 17 layers with different thicknesses (Figure 2.5 and Table 2.1 (on left)) and follows, up to a large extent, the model proposed by Lizarralde et al. (1995) and Baba et al. (2010) for the Northeastern Pacific mantle conductivity profile. The conductivity of the top, 4 km thick sedimentary layer is set equal to 0.3 Sm^{-1}. Underneath this layer, the conductivity gradually decreases to 0.001 Sm^{-1} at a depth of 50 km. Then, the conductivity

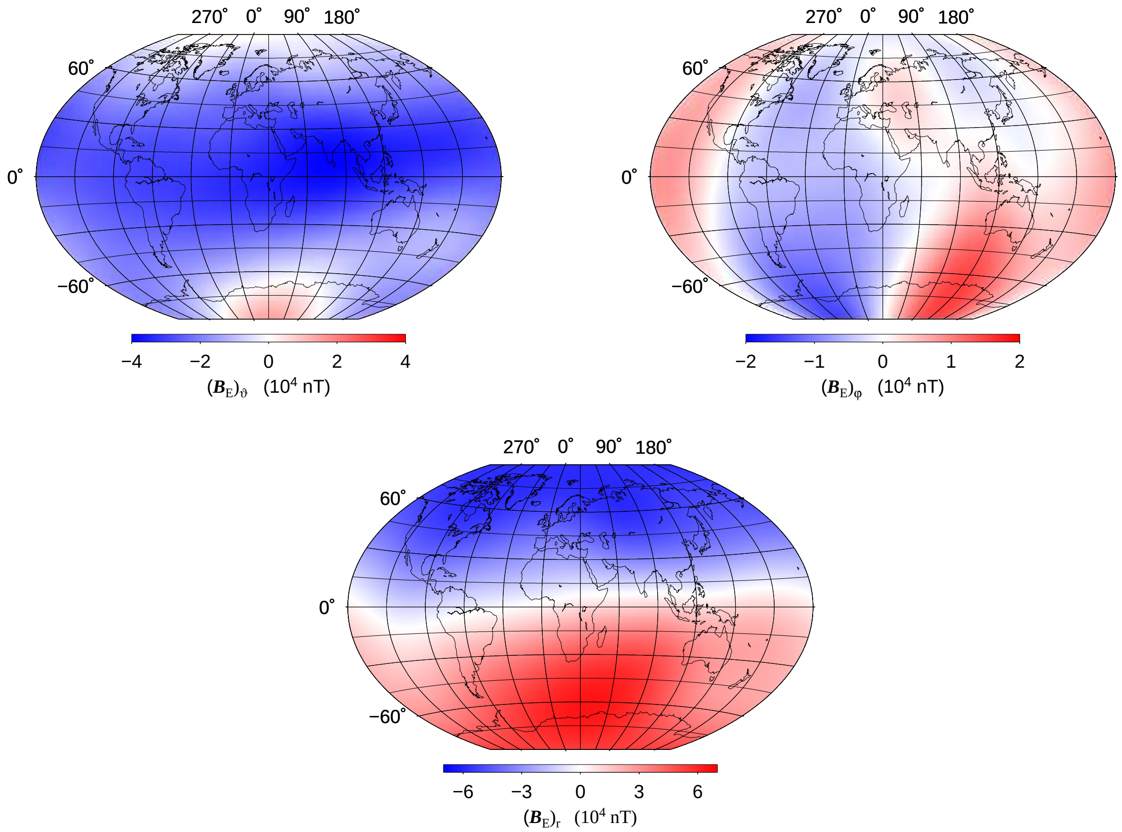

Figure 2.4: ϑ (left top), φ (right top) and r (bottom) components of the background magnetic field (in 10^4 nT) by spherical harmonics cut-off degree $j_{\max} = 6$ from Maus et al. (2010).

increases to 0.05 Sm^{-1} until a depth of 250 km. Below this maximum, the conductivity slightly decreases to 0.03 Sm^{-1} at 380 km. Finally, the conductivity at the top of the lower mantle is equal to 1 Sm^{-1} and is fixed at this rate downward, since its effect on the induced magnetic field is negligible. That affirms the numerical results in following chapters. The conductivity profile for layers beneath the seafloor is attached to the bottom of the ocean layer. Therefore, the exact radius of the layers in the profile depends on the thickness of the ocean layer ($h = 1$ or 4 km). We also use different uniform conductivity profiles for studying the sensitivity of the induced magnetic field in respect to a conductivity parameter. The discretization of the conductivity profiles differ for the individual numerical experiments. The numerical limitations given by analytical solutions with a high resistive (realistic) conductivity profile, such as shown in Table 2.1, do not allow a smoother discretization in this case. Such difficulties can be overcome using profile with higher conductivity such as in the case of the secondary poloidal magnetic field (Table 2.1 on right), or using the finite elements approach.

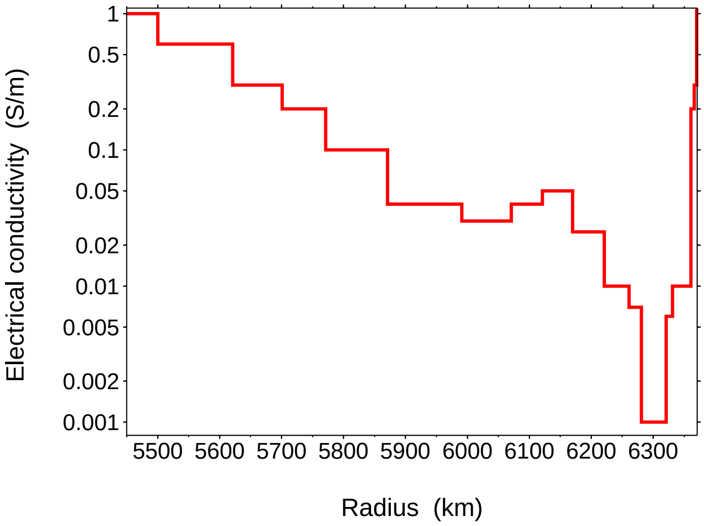

Figure 2.5: Radial profile of electrical conductivity σ_{m} (in Sm^{-1}) beneath the ocean layer corresponding to the conductivity profile in Table 2.1 on the left.

Toroidal and primary poloidal mag. field		
Radius	el. conductivity (S/m)	
(km)	toroidal	prim. poloidal
6371.00	4.7	3.5
6370.90	4.5	
6370.70	3.9	
6370.50	3.5	
6370.40	3.4	
6370.20	3.2	
6370	0.3	
6366	0.2	
6361	0.01	
6351	0.01	
6331	0.006	
6321	0.001	
6281	0.007	
6261	0.01	
6221	0.025	
6170	0.05	
6121	0.04	
6071	0.03	
5991	0.04	
5871	0.1	
5771	0.2	
5701	0.3	
5621	0.6	
5500	1.0	

Secondary poloidal magnetic field	
Radius (km)	el. conductivity (S/m)
6371	3.5
6370	0.3
6366	0.3
6362	0.25
6357	0.2
6352	0.15
6347	0.1
6342	0.08
6333	0.03
6317	0.01
6300	0.02
6280	0.05
6260	0.1
6240	0.08
6210	0.06
6190	0.04
6170	0.02
5768	0.1
5701	1.0
5600	1.0
5500	1.0

Table 2.1: On the left is shown the realistic radial profile of electrical conductivity with ocean layer depth $h = 1$ km. The profile for toroidal magnetic field divides the ocean in 6 layers with different conductivities, whereas the ocean conductivity for the poloidal magnetic field is considered uniform. The space beneath the sea floor is for toroidal and primary poloidal magnetic field divided in 17 layers with different conductivities. The first layer of the profile is 5500 km thick and starts in the centre of the sphere. The whole mantle is here discretized in 18 layers as has been used for the analytical solution. The discretization of the 17 different conductivity layers differ by the finite elements approach. In the table on the right is the adapted electrical conductivity profile used for the secondary poloidal magnetic field.

Chapter 3

Solution by the matrix propagator method

In this chapter we solve the magnetic induction equation (1.11) with a layer propagator method for both the toroidal and poloidal magnetic field generated by horizontal ocean flow for a given tidal frequency. Our approach is based on Pěč et al. (1985) who developed the matrix propagator method for computing magnetic field in a sphere that is induced by an external magnetospheric or ionospheric currents. We rebuild and extend this approach by including a source term acting inside a sphere. We assume that an internal source generates also the toroidal magnetic field and additionally develop a matrix propagator for the toroidal part of the magnetic field (Dostal et al., 2012). Recalling the assumptions made in section 1.2, we are searching the analytical solution of the the Helmholtz equation (1.14) in Fourier frequency domain,

$$\nabla^2 \boldsymbol{B} + k^2 \boldsymbol{B} = -\mu_0 \sigma \mathrm{curl}(\boldsymbol{u} \times \boldsymbol{B}_{\mathrm{E}}) \ , \tag{3.1}$$

with k as a wave number, $k^2 = -i\omega\mu_0\sigma$. The fundamental solution of a homogeneous Helmholtz equation is given by

$$\boldsymbol{B}_{\mathrm{hom}}(r,\Omega) = \sum_{jm\ell} \alpha^{\ell}_{jm} w_{\ell}(z) \boldsymbol{Y}^{\ell}_{jm}(\Omega) \ , \tag{3.2}$$

where $z = kr$, $\boldsymbol{Y}^{\ell}_{jm}(\Omega)$ are the vector spherical harmonics and $\alpha^{\ell}_{jm} w_{\ell}(z)$ stands for a linear combination of the spherical Bessel functions of the 1st and 2nd kind (Abramowitz and Stegun, 1970). The basic relations for the spherical Bessel functions and vector spherical harmonics are given in Appendix C and D, respectively. The summation in eq. (3.2) runs over $j = 1, 2, \ldots, \infty$, $m = -j, -j+1, \ldots, j$, and $\ell = j-1, j, j+1$. The linear combination of the spherical Bessel functions can be expressed by

$$\alpha^{\ell}_{jm} w_{\ell}(z) = a^{\ell}_{jm}\, j_{\ell}(z) + b^{\ell}_{jm}\, n_{\ell}(z) \ , \tag{3.3}$$

where j_ℓ and n_ℓ stand for the spherical Bessel functions of 1st and 2nd kind respectively and a^{ℓ}_{jm} and b^{ℓ}_{jm} are spherical harmonic coefficients to be determined. The complete solution of the inhomogeneous Helmholtz equation (3.1) is given by the sum of a homogeneous solution $\boldsymbol{B}_{\mathrm{hom}}$, expressed by eq. (3.2), and the particular solution $\boldsymbol{B}_{\mathrm{part}}$, that is $\boldsymbol{B} = \boldsymbol{B}_{\mathrm{hom}} + \boldsymbol{B}_{\mathrm{part}}$. The particular solution corresponding with the right hand side of the induction equation has been solved for the toroidal and poloidal case separately in sections 2.1 and 2.2. To complete the general specifications for the layer propagator, boundary conditions for magnetic field $\boldsymbol{B}$ and electric field $\boldsymbol{E}$ are prescribed at spherical interfaces across which the electrical conductivity σ changes discontinuously. As they are different for the toroidal and poloidal case they will be specified later in this chapter. The electric intensity $\boldsymbol{E}$, is expressed in terms of $\boldsymbol{B}$ by Ampère's current law in the quasi-static approximation,

$$\boldsymbol{E} = \frac{1}{\mu_0 \sigma} \operatorname{curl} \boldsymbol{B}. \tag{3.4}$$

3.1 Matrix propagator for the toroidal magnetic field

The aim of this section is to solve the induction equation for the toroidal magnetic field induced by ocean tidal flow in Fourier frequency domain for a particular frequency. We thus confine ourselves to a toroidal magnetic source term expressed by $\boldsymbol{F}$ in eq. (2.3),

$$\boldsymbol{F}_{\mathrm{T}}(r,\Omega) = \sum_{jm} \left[{}^{(1)}F^j_{jm} \left(\frac{r}{a}\right)^j + {}^{(2)}F^j_{jm} \left(\frac{a}{r}\right)^{j+1} \right] \boldsymbol{Y}^j_{jm}(\Omega), \tag{3.5}$$

where the label T stands for 'toroidal'. Since the assumed conductivity structure of the Earth is spherically symmetric and only a toroidal magnetic source is applied, the induced magnetic field is toroidal and can be expressed by the toroidal part of eqs (2.4), (2.5) and (3.2),

$$\boldsymbol{B}_{\mathrm{T}}(r,\Omega) = \sum_{jm} \left[\alpha^j_{jm} w_j(z) - \frac{i}{\omega} {}^{(1)}F^j_{jm} \left(\frac{r}{a}\right)^j - \frac{i}{\omega} {}^{(2)}F^j_{jm} \left(\frac{a}{r}\right)^{j+1} \right] \boldsymbol{Y}^j_{jm}(\Omega). \tag{3.6}$$

Here, the first, second and the third terms correspond to a homogeneous and two particular solutions of the Helmholtz equation (3.1), respectively. The associated electric intensity, expressed by Ampère's current law (3.4), is a spheroidal vector field,

$$\begin{aligned} \boldsymbol{E}_{\mathrm{S}}(r,\Omega) =& \frac{ik}{\mu_0 \sigma} \sum_{jm} \alpha^j_{jm} \left[\sqrt{\frac{j+1}{2j+1}}\, w_{j-1}(z) \boldsymbol{Y}^{j-1}_{jm}(\Omega) - \sqrt{\frac{j}{2j+1}}\, w_{j+1}(z) \boldsymbol{Y}^{j+1}_{jm}(\Omega) \right] \\ &+ \frac{1}{\omega \mu_0 \sigma\, a} \sum_{jm} \left[\sqrt{(j+1)(2j+1)}\, {}^{(1)}F^j_{jm} \left(\frac{r}{a}\right)^{j-1} \boldsymbol{Y}^{j-1}_{jm}(\Omega) \right. \\ &\left. \sqrt{j(2j+1)}\, {}^{(2)}F^j_{jm} \left(\frac{a}{r}\right)^{j+2} \boldsymbol{Y}^{j+1}_{jm}(\Omega) \right]. \end{aligned} \tag{3.7}$$

To guarantee the continuity on the interfaces between spherical layers with different electrical conductivity σ the tangential components of magnetic and electric intensity are required (Stratton, 1941):

$$\begin{aligned} \boldsymbol{e}_r \times \left[\boldsymbol{B}\right]^+_- &= 0\,, \\ \boldsymbol{e}_r \times \left[\boldsymbol{E}\right]^+_- &= 0\,, \end{aligned} \tag{3.8}$$

where $\boldsymbol{e}_r$ is the unit vector in radial direction, the symbol $[f]^+_-$ indicates the jump of the quantity f at a discontinuity. The tangential components of magnetic induction and electric intensity, required for expressing boundary conditions (eq. 3.8), are then

$$\boldsymbol{e}_r \times \boldsymbol{B}_{\mathrm{T}}(r,\Omega) = \sum_{jm} \left[\alpha^j_{jm} w_j(z) - \frac{i}{\omega} {}^{(1)}F^j_{jm} \left(\frac{r}{a}\right)^j - \frac{i}{\omega} {}^{(2)}F^j_{jm} \left(\frac{a}{r}\right)^{j+1} \right] \Big(\boldsymbol{e}_r \times \boldsymbol{Y}^j_{jm}(\Omega) \Big), \tag{3.9}$$

$$\begin{aligned} \boldsymbol{e}_r \times \boldsymbol{E}_{\mathrm{S}}(r,\Omega) =& i\omega r \sum_{jm} \alpha^j_{jm} \frac{1}{z^2} \frac{d}{dz} \Big(z w_j(z) \Big) \boldsymbol{Y}^j_{jm}(\Omega) \\ &+ \frac{1}{k^2 a} \sum_{jm} \left[(j+1)\, {}^{(1)}F^j_{jm} \left(\frac{r}{a}\right)^{j-1} - j\, {}^{(2)}F^j_{jm} \left(\frac{a}{r}\right)^{j+2} \right] \boldsymbol{Y}^j_{jm}(\Omega). \end{aligned} \tag{3.10}$$

3.1.1 Toroidal matrix propagator for a source-free layer

After describing the general specifications for the layer propagator we present the homogeneous solution of the matrix propagator for the toroidal magnetic field. We divide this spherical conductor into n homogeneous layers bounded by spheres of radii $r_1 < r_2 < \ldots < r_n = a$, where r_1 is the radius of the innermost sphere. Let the first m layers ($m < n$) approximate the solid mantle without an electric or magnetic source, while the $n-m$ upper layers approximate an ocean layer with the source electric current $\boldsymbol{j} = \sigma(\boldsymbol{u} \times \boldsymbol{B}_{\mathrm{E}})$. Equations (3.9) and (3.10) in a source-free layer, where ${}^{(\alpha)}F^j_{jm} = 0$, reduce to

$$\begin{aligned} \boldsymbol{e}_r \times \boldsymbol{B}_{\mathrm{T}}(r,\Omega) &= \sum_{jm} y_1(z)\Big(\boldsymbol{e}_r \times \boldsymbol{Y}^j_{jm}(\Omega)\Big), \\ \boldsymbol{e}_r \times \boldsymbol{E}_{\mathrm{S}}(r,\Omega) &= i\omega r \sum_{jm} y_2(z) \boldsymbol{Y}^j_{jm}(\Omega), \end{aligned} \tag{3.11}$$

where $y_1(z)$ and $y_2(z)$ are components of the 2×1 column vector $\boldsymbol{y}(z)$, which is defined as

$$\boldsymbol{y}(z) := \begin{pmatrix} \alpha^j_{jm} w_j(z) \\ \alpha^j_{jm} \dfrac{1}{z^2} \dfrac{d}{dz}\Big(z w_j(z)\Big) \end{pmatrix}. \tag{3.12}$$

Note that the dependency of $\boldsymbol{y}(z)$ on indexes j and m is not explicitly denoted to abbreviate notations. The continuity conditions (3.8) then require the continuity of $\boldsymbol{y}(z)$ at spherical interfaces between homogeneous, source-free layers,

$$\big[\boldsymbol{y}(z)\big]^+_- = 0. \tag{3.13}$$

Recalling that $\alpha^j_{jm} w_j(z)$ stands for a linear combination of the spherical Bessel functions of the 1st and 2nd kind, $j_j(z)$ and $n_j(z)$, eq. (3.12) can be written in matrix form as

$$\boldsymbol{y}(z) = \boldsymbol{K}(z)\, \boldsymbol{c}\,, \tag{3.14}$$

where $\boldsymbol{c}$ is a 2×1 column vector of arbitrary constants and $\boldsymbol{K}(z)$ is the 2×2 matrix with the two fundamental solutions of the homogeneous Helmholtz equation,

$$\boldsymbol{K}(z) := \begin{pmatrix} j_j(z) & n_j(z) \\ \dfrac{1}{z^2}\Big(z j_j(z)\Big)' & \dfrac{1}{z^2}\Big(z n_j(z)\Big)' \end{pmatrix}. \tag{3.15}$$

Here, the prime indicates differentiation with respect to the variable z. Furthermore, the inverse matrix to $\boldsymbol{K}(z)$, needed in the following step, has the form

$$\boldsymbol{K}^{-1}(z) = z^3 \begin{pmatrix} \dfrac{1}{z^2}\Big(z n_j(z)\Big)' & -n_j(z) \\ -\dfrac{1}{z^2}\Big(z j_j(z)\Big)' & j_j(z) \end{pmatrix}. \tag{3.16}$$

In the sth source-free layer ($s = 2, \ldots m$) with an electrical conductivity σ_s and wave number k_s, and bounded by radii r_{s-1} and r_s, the constants $\boldsymbol{c}$ can be eliminated by the relationship between the magnetic induction and the electric intensity at the upper and lower boundaries of the layer:

$$\boldsymbol{y}(z_1) = \boldsymbol{M}(z_1, z_2)\boldsymbol{y}(z_2), \tag{3.17}$$

where $z_1 := k_s r_s$, $z_2 := k_s r_{s-1}$, and the layer propagator matrix $\boldsymbol{M}(z_1, z_2)$ can be expressed in terms of the matrix $\boldsymbol{K}$ and its inversion $\boldsymbol{K}^{-1}$ as

$$\boldsymbol{M}(z_1, z_2) := \boldsymbol{K}(z_1)\boldsymbol{K}^{-1}(z_2). \tag{3.18}$$

Substituting for $\boldsymbol{K}$ and $\boldsymbol{K}^{-1}$ from eqs (3.15) and (3.16), we obtain

$$\boldsymbol{M}(z_1, z_2) = z_2 \begin{pmatrix} p_j + z_2 q_j & -z_2^2 p_j \\ \dfrac{1}{z_1^2}(p_j + z_1 r_j + z_2 q_j + z_1 z_2\, s_j) & \dfrac{z_2^2}{z_1^2}(-p_j - z_1 r_j) \end{pmatrix}, \tag{3.19}$$

where p_j, q_j, r_j and s_j are the cross-products of the spherical Bessel functions and their derivatives published by Pěč et al. (1985) and are shown including the recurrence relations by eqs (C.7 - C.10) in Appendix C. The inversion of matrix $\boldsymbol{K}$ and additional mathematical derivations for the $\boldsymbol{M}$ propagator are shown in Appendix B.1.2. The solution of eq. (3.14) in the innermost sphere ($s = 1$) must be finite at the origin, which implies that the constant in the spherical Bessel functions of the 2nd kind must be identically equal to zero, that is, $\boldsymbol{c} = (c_1, 0)^{\mathrm{T}}$. The solution for $0 \leq r \leq r_1$ thus takes a particular form, namely

$$\boldsymbol{y}(k_1 r) = c_1 \boldsymbol{k}(k_1 r), \tag{3.20}$$

where $\boldsymbol{k}(k_1 r)$ is the 2×1 column vector created from the first column of matrix $\boldsymbol{K}(z)$ and divided by $j_j(k_1 r_1)$ for numerical convenience. The solution in the sth spherical layer then follows from the upward continuation of the solution from the innermost sphere and the continuity condition of $\boldsymbol{y}(z)$ at the interfaces at $r_1 \ldots r_m$ (eq. 3.13). This corresponds to the multiplication of the product of the layer propagator matrices with the inner sphere solution taken at $r = r_1$. In the sth layer, ($r_{s-1} \leq r \leq r_s$, $s = 2, \ldots, m$), we obtain

$$\boldsymbol{y}(k_s r) = \boldsymbol{L}(k_s r, k_1 r_1) \boldsymbol{y}(k_1 r_1), \tag{3.21}$$

where

$$\boldsymbol{L}(k_s r, k_1 r_1) = \boldsymbol{M}(k_s r, k_s r_{s-1}) \boldsymbol{M}(k_{s-1} r_{s-1}, k_{s-1} r_{s-2}) \ldots \boldsymbol{M}(k_2 r_2, k_2 r_1). \tag{3.22}$$

Substituting for $\boldsymbol{y}(k_1 r_1)$ from eq. (3.20), we have

$$\boldsymbol{y}(k_s r) = c_1 \boldsymbol{L}(k_s r, k_1 r_1) \boldsymbol{k}(k_1 r_1), \tag{3.23}$$

where

$$\boldsymbol{k}(k_1 r_1) = \begin{pmatrix} 1 \\ \dfrac{1}{k_1^2 r_1^2} \Big[j + 1 - \chi_j(k_1 r_1) \Big] \end{pmatrix}, \tag{3.24}$$

and

$$\chi_j(z) := z j_{j+1}(z) / j_j(z) \ . \tag{3.25}$$

The function $\chi_j(z)$ and the corresponding recurrence relation for the function $\chi_j(z)$ are given in Pěč et al. (1985) and are summarized in the Appendix C.

3.1.2 Toroidal matrix propagator for the ocean layer

We divide the ocean, the spherical layer between $b \leq r \leq a$, where a, b stands for the top and bottom radius, respectively, in several spherical layers with different electrical conductivity in each layer. This allows us to estimate the influence of radially-varying electrical conductivity of ocean water on the generated magnetic field. The uppermost ocean layers, labeled by $m+1, m+2, \ldots, n$, and bounded by spheres of radii $r_{m+1}, r_{m+2}, \ldots, r_n$, with electrical conductivities $\sigma_{m+1}, \sigma_{m+2}, \ldots, \sigma_n$, and with the source electric current $\boldsymbol{j}_s = \sigma_s(\boldsymbol{u} \times \boldsymbol{B}_{\mathrm{E}})$, $s = m+1, m+2, \ldots, n$ describe the ocean-layer properties. Note that ocean velocity $\boldsymbol{u}$ and the main magnetic field $\boldsymbol{B}_{\mathrm{E}}$ are not labeled by the layer index s since both are assumed to be continuous functions of a position in the entire ocean layer (section 2.5). The tangential components of magnetic induction and the electric intensity within the sth ocean layer are given by eqs (3.9) and (3.10). To express them in a shorter form, we introduce the 2×1 column source-term vector

$$\boldsymbol{s}_s(r) := -\frac{i}{\omega} \begin{pmatrix} {}^{(1)}F^j_{jm}\left(\frac{r}{a}\right)^j + {}^{(2)}F^j_{jm}\left(\frac{a}{r}\right)^{j+1} \\ \frac{1}{k_s^2 a^2}\left[(j+1)\,{}^{(1)}F^j_{jm}\left(\frac{r}{a}\right)^{j-2} - j\,{}^{(2)}F^j_{jm}\left(\frac{a}{r}\right)^{j+3}\right] \end{pmatrix}, \tag{3.26}$$

where $r_{s-1} \leq r \leq r_s$, $s = m+1, m+2, \ldots, n$, and the dependency of $\boldsymbol{s}_s(r)$ on indexes j and m is not explicitly denoted. Then, eqs (3.9) and (3.10) in the sth source layer can be written in an analogous form as eq. (3.11) for a source-free layer,

$$\begin{aligned} \boldsymbol{e}_r \times \boldsymbol{B}_{\mathrm{T}}(r,\Omega) &= \sum_{jm} v_1(r)\Big(\boldsymbol{e}_r \times \boldsymbol{Y}^j_{jm}(\Omega)\Big), \\ \boldsymbol{e}_r \times \boldsymbol{E}_{\mathrm{S}}(r,\Omega) &= i\omega r \sum_{jm} v_2(r)\, \boldsymbol{Y}^j_{jm}(\Omega), \end{aligned} \tag{3.27}$$

where $v_1(r)$ and $v_2(r)$ are components of the 2×1 column vector $\boldsymbol{v}(r)$ expressed as

$$\boldsymbol{v}(r) = \boldsymbol{K}(k_s r)\boldsymbol{c}_s + \boldsymbol{s}_s(r). \tag{3.28}$$

Here, the matrix $\boldsymbol{K}(z)$ is given by eq. (3.15), k_s is the wave number for the sth ocean-layer parameters and $\boldsymbol{c}_s$ is a 2×1 column vector with arbitrary constants. These unknown constants can be eliminated by the values of magnetic induction and the electric intensity taken at the bottom ($r = r_{s-1}$) of the sth layer:

$$\boldsymbol{v}(r_{s-1}) = \boldsymbol{K}(k_s r_{s-1})\boldsymbol{c}_s + \boldsymbol{s}_s(r_{s-1}), \tag{3.29}$$

which yields

$$\boldsymbol{c}_s = \boldsymbol{K}^{-1}(k_s r_{s-1})[\boldsymbol{v}(r_{s-1}) - \boldsymbol{s}_s(r_{s-1})]. \tag{3.30}$$

The solution in the sth ocean layer for $r_{s-1} \leq r \leq r_s$ is then

$$\boldsymbol{v}(r) = \boldsymbol{M}(k_s r, k_s r_{s-1})[\boldsymbol{v}(r_{s-1}) - \boldsymbol{s}_s(r_{s-1})] + \boldsymbol{s}_s(r), \tag{3.31}$$

where the matrix $\boldsymbol{M}$ is provided by eq. (3.19). The continuity conditions (eqs 3.8) require the continuity of $\boldsymbol{v}(r)$ at spherical interfaces between homogeneous ocean source layers,

$$\big[\boldsymbol{v}(r)\big]_-^+ = 0. \tag{3.32}$$

To make use of this condition, let us consider the solution in the two innermost ocean layers, labeled by indexes $s = m+1$ and $s = m+2$, taken at radii r_{m+1} and $r_{m+1} \leq r \leq r_{m+2}$, respectively,

$$\begin{aligned} \boldsymbol{v}(r_{m+1}) &= \boldsymbol{M}(k_{m+1}r_{m+1}, k_{m+1}r_m)[\boldsymbol{v}(r_m) - \boldsymbol{s}_{m+1}(r_m)] + \boldsymbol{s}_{m+1}(r_{m+1}), \\ \boldsymbol{v}(r) &= \boldsymbol{M}(k_{m+2}r, k_{m+2}r_{m+1})[\boldsymbol{v}(r_{m+1}) - \boldsymbol{s}_{m+2}(r_{m+1})] + \boldsymbol{s}_{m+2}(r). \end{aligned} \tag{3.33}$$

By the continuity condition (eq. 3.32) considered at the interface $r = r_{m+1}$, the last two equations can be combined such that $\boldsymbol{v}(r_{m+1})$ is eliminated,

$$\begin{aligned} \boldsymbol{v}(r) = {} & \boldsymbol{L}(k_{m+2}r, k_{m+1}r_m)[\boldsymbol{v}(r_m) - \boldsymbol{s}_{m+1}(r_m)] \\ & + \boldsymbol{L}(k_{m+2}r, k_{m+2}r_{m+1})[\boldsymbol{s}_{m+1}(r_{m+1}) - \boldsymbol{s}_{m+2}(r_{m+1})] + \boldsymbol{s}_{m+2}(r), \end{aligned} \tag{3.34}$$

where matrix $\boldsymbol{L}(k_{m+2}r, k_{m+1}r_m)$ is given by eq. (3.22) and $\boldsymbol{L}(k_{m+2}r, k_{m+2}r_{m+1}) \equiv \boldsymbol{M}(k_{m+2}r, k_{m+2}r_{m+1})$. The procedure continues successively. The solution in the sth ocean layer,

$s = m+3, \ldots, n$, then follows from the upward continuation of the solution (eq. 3.34) in the $(m+2)$th ocean layer and the continuity condition (eq. 3.32) at the interface $r = r_{m+2}, \ldots, r_n$. In the sth layer, that is for $r_{s-1} \le r \le r_s$, we obtain

$$\begin{aligned} \boldsymbol{v}(r) = {} & \boldsymbol{L}(k_s r, k_{m+1} r_m)[\boldsymbol{v}(r_m) - \boldsymbol{s}_{m+1}(r_m)] \\ & + \boldsymbol{L}(k_s r, k_{m+2} r_{m+1})[\boldsymbol{s}_{m+1}(r_{m+1}) - \boldsymbol{s}_{m+2}(r_{m+1})] \\ & + \ldots \\ & + \boldsymbol{L}(k_s r, k_s r_{s-1})[\boldsymbol{s}_{s-1}(r_{s-1}) - \boldsymbol{s}_s(r_{s-1})] + \boldsymbol{s}_s(r). \end{aligned} \tag{3.35}$$

The continuity conditions (3.8) require the continuity of the tangential components of the magnetic induction and the electrical intensity at the ocean-bottom–solid mantle interface,

$$\boldsymbol{y}(k_m r_m) = \boldsymbol{v}(r_m). \tag{3.36}$$

Substituting for $\boldsymbol{y}(k_m r_m)$ from eq. (3.23) and then entering this result into eq. (3.35), we obtain

$$\begin{aligned} \boldsymbol{v}(r) = {} & \boldsymbol{L}(k_s r, k_{m+1} r_m)[c_1 \boldsymbol{L}(k_m r_m, k_1 r_1)\boldsymbol{a}(k_1 r_1) - \boldsymbol{s}_{m+1}(r_m)] \\ & + \boldsymbol{L}(k_s r, k_{m+2} r_{m+1})[\boldsymbol{s}_{m+1}(r_{m+1}) - \boldsymbol{s}_{m+2}(r_{m+1})] \\ & + \ldots \\ & + \boldsymbol{L}(k_s r, k_s r_{s-1})[\boldsymbol{s}_{s-1}(r_{s-1}) - \boldsymbol{s}_s(r_{s-1})] + \boldsymbol{s}_s(r)\ . \end{aligned} \tag{3.37}$$

Finally, the toroidal magnetic field at the Earth's surface must vanish, that is $v_1(r_n) = 0$, which gives the equation for unknown constant c_1,

$$\begin{aligned} c_1 = {} & \frac{1}{\big[\boldsymbol{L}(k_n r_n, k_1 r_1)\boldsymbol{z}(k_1 r_1)\big]_1} \Big[\boldsymbol{L}(k_n r_n, k_{m+1} r_m)\boldsymbol{s}_{m+1}(r_m) \\ & - \boldsymbol{L}(k_n r_n, k_{m+2} r_{m+1})[\boldsymbol{s}_{m+1}(r_{m+1}) - \boldsymbol{s}_{m+2}(r_{m+1})] \\ & - \ldots \\ & - \boldsymbol{L}(k_n r_n, k_n r_{n-1})[\boldsymbol{s}_{n-1}(r_{n-1}) - \boldsymbol{s}_n(r_{n-1})] - \boldsymbol{s}_n(r_n)\Big]_1, \end{aligned} \tag{3.38}$$

where $\big[\boldsymbol{k}\big]_1$ denotes the first component of vector $\boldsymbol{k}$. In summary, the solution $\boldsymbol{y}(k_s r)$ in the sth source-free layer, $r_{s-1} \le r \le r_s$, $s = 2, \ldots, m$, is expressed by eq. (3.23) with the constant c_1 given by eq. (3.38). The solution $\boldsymbol{v}(r)$ in the sth ocean layer, $r_{s-1} \le r \le r_s$, $s = m+1, \ldots, n$, is given by eq. (3.35) with $\boldsymbol{v}(r_m)$ given by eq. (3.36).

3.2 Matrix propagator for the poloidal magnetic field

3.2.1 Poloidal matrix propagator for a source-free layer

To satisfy the divergence-free condition for the poloidal magnetic field, $\boldsymbol{B}_\mathrm{P} = 0$, the substitution $\boldsymbol{B}_\mathrm{P} = \operatorname{curl} \boldsymbol{A}_\mathrm{T}$ is used and the derivation for the poloidal magnetic field is carried out in toroidal magnetic potential $\boldsymbol{A}_\mathrm{T}$. The derivation for the poloidal propagator method is analogous to that of magnetic field presented in section 3.1. First, we recall the induction equation (1.24),

$$\operatorname{curl}\operatorname{curl} \boldsymbol{A}_\mathrm{T} + \mu_0 \sigma \frac{\partial}{\partial t} \boldsymbol{A}_\mathrm{T} = \mu_0 \sigma \left[\boldsymbol{u} \times \boldsymbol{B}_0\right]_\mathrm{T}\ . \tag{3.39}$$

Next, we recall the relations for the source term (eq. 2.8) and the particular solution (eq. 2.9) for the toroidal magnetic potential,

$$\boldsymbol{G}_{\mathrm{T}}(r,\Omega) = \sum_{jm} G^{j}_{jm}(a)\,\left(\frac{r}{a}\right)^{j}\,\boldsymbol{Y}^{j}_{jm}(\Omega)\;, \tag{3.40}$$

$$\boldsymbol{A}_{\mathrm{T}}(r,\Omega) = \sum_{jm}\left[\alpha^{j}_{jm}\,w_j(z) - \frac{i}{\omega}\,G^{j}_{jm}(a)\,\left(\frac{r}{a}\right)^{j}\right]\boldsymbol{Y}^{j}_{jm}(\Omega)\;. \tag{3.41}$$

The boundary conditions between the spherical layers with different electrical conductivity require the continuity of the radial and tangential components of the magnetic field (Stratton, 1941):

$$\begin{aligned} \boldsymbol{e}_r \cdot \left[\boldsymbol{B}\right]^{+}_{-} &= 0\;, \\ \boldsymbol{e}_r \times \left[\boldsymbol{B}\right]^{+}_{-} &= 0\;, \end{aligned} \tag{3.42}$$

where $\boldsymbol{e}_r$ is the unit vector in radial direction and the symbol $[f]^{+}_{-}$ indicates the jump of the quantity f at a discontinuity. To express eq. (3.42) explicitly, the poloidal magnetic intensity $\boldsymbol{B}_{\mathrm{P}}$ is represented by (D.33), the homogeneous solution of the induction equation is then

$$\begin{aligned} \boldsymbol{B}^{\mathrm{hmg}}_{\mathrm{P}} &= \operatorname{curl}\boldsymbol{A}^{\mathrm{hmg}}_{\mathrm{T}} \\ &= i\sum_{jm}\alpha^{j}_{jm}\left[\sqrt{\frac{j}{2j+1}}\left(\frac{d}{dr}-\frac{j}{r}\right)w_j(r)\;\boldsymbol{Y}^{j+1}_{jm}(\Omega)\right. \\ &\quad\left.+\sqrt{\frac{j+1}{2j+1}}\left(\frac{d}{dr}+\frac{j+1}{r}\right)w_j(r)\;\boldsymbol{Y}^{j-1}_{jm}(\Omega)\right]\;. \end{aligned} \tag{3.43}$$

The radial and tangential components of $\boldsymbol{B}_{\mathrm{P}}$ in a source-free layer, where $G^{j}_{jm}=0$, reads as (see Appendix B by eqs (B.18) and (B.19))

$$\boldsymbol{e}_r \cdot \boldsymbol{B}_{\mathrm{P}}(r,\Omega) = \frac{i}{r}\sum_{jm}\alpha^{j}_{jm}\,\sqrt{j(j+1)}\;w_j(kr)\;Y_{jm}(\Omega)\;, \tag{3.44}$$

$$\boldsymbol{e}_r \times \boldsymbol{B}_{\mathrm{P}}(r,\Omega) = -\frac{1}{r}\sum_{jm}\alpha^{j}_{jm}\frac{d}{dr}[rw_j(kr)]\;\boldsymbol{Y}^{j}_{jm}(\Omega)\;. \tag{3.45}$$

Introducing a 2×1 column vector $\boldsymbol{y}(z)$

$$\boldsymbol{y}(z) := \begin{pmatrix} \alpha^{j}_{jm}\,w_j(z) \\ \alpha^{j}_{jm}\,\dfrac{d}{dz}\Big(z\,w_j(z)\Big) \end{pmatrix}\;, \tag{3.46}$$

we can describe equations (3.44) and (3.45) in a source-free layer in the form

$$\begin{aligned} \boldsymbol{e}_r \cdot \boldsymbol{B}_{\mathrm{P}}(r,\Omega) &= \sum_{jm} y_1(z)\;Y_{jm}\Omega)\;, \\ \boldsymbol{e}_r \times \boldsymbol{B}_{\mathrm{P}}(r,\Omega) &= \sum_{jm} y_2(z)\;\boldsymbol{Y}^{j}_{jm}(\Omega)\;, \end{aligned} \tag{3.47}$$

where $y_1(z)$ and $y_2(z)$ are components of vector $\boldsymbol{y}(z)$. Recalling that $\alpha^{j}_{jm}w_j(z)$ stands for a linear combination of the spherical Bessel functions of the 1st and 2nd kind, $j_j(z)$ and $n_j(z)$, eq. (3.46) can be written in matrix form as

$$\boldsymbol{y}(z) = \boldsymbol{K}(z)\,\boldsymbol{c}\;, \tag{3.48}$$

where $\boldsymbol{c}$ is a 2×1 column vector of arbitrary constants and $\boldsymbol{K}(z)$ is the 2×2 matrix whose columns are the two fundamental solutions of the homogeneous Helmholtz equation,

$$\boldsymbol{K}(z) := \begin{pmatrix} j_j(z) & n_j(z) \\ [z\, j_j(z)]' & [z\, n_j(z)]' \end{pmatrix} . \tag{3.49}$$

Here, the prime indicates differentiation with respect to the variable z. Furthermore, the inverse matrix to $\boldsymbol{K}(z)$, needed for building the matrix propagator, has the form

$$\boldsymbol{K}^{-1}(z) = z \begin{pmatrix} [z\, n_j'(z) + n_j(z)] & -n_j(z) \\ -[z\, j_j'(z) + j_j(z)] & j_j(z) \end{pmatrix} . \tag{3.50}$$

The derivation of the inverse matrix $\boldsymbol{K}^{-1}(z)$ is shown in Appendix B.1.2. In the sth source-free layer ($s = 2, \ldots m$) with an electrical conductivity σ_s and wave number k_s, and bounded by radii r_{s-1} and r_s, the constants $\boldsymbol{c}$ from eq. (3.48) can be eliminated by the relationship between the two components of the magnetic induct at the upper and lower boundaries of the layer:

$$\boldsymbol{y}(z_1) = \boldsymbol{M}(z_1, z_2)\boldsymbol{y}(z_2), \tag{3.51}$$

where $z_1 := k_s r_s$, $z_2 := k_s r_{s-1}$, and the layer propagator matrix $\boldsymbol{M}(z_1, z_2)$ can be expressed in terms of the matrix $\boldsymbol{K}$ and its inversion $\boldsymbol{K}^{-1}$ as

$$\boldsymbol{M}(z_1, z_2) := \boldsymbol{K}(z_1)\boldsymbol{K}^{-1}(z_2). \tag{3.52}$$

Substituting for $\boldsymbol{K}$ and $\boldsymbol{K}^{-1}$ from eqs (3.49) and (3.50), the propagator has the form

$$\boldsymbol{M}(z_1, z_2) = z_2 \begin{pmatrix} p_j + z_2 q_j & -p_j \\ p_j + z_1 r_j + z_2 q_j + z_1 z_2\, s_j & -p_j - z_1 r_j \end{pmatrix}, \tag{3.53}$$

where p_j, q_j, r_j and s_j are the cross-products of the spherical Bessel functions and their derivatives, see Appendix C. The derivation of relation (3.53) is shown in Appendix B.2.3. Magnetic field in the innermost sphere ($s = 1$) must be finite at the origin, which implies that the constant at the spherical Bessel functions of the 2nd kind must be identically equal to zero, that is, $\boldsymbol{c} = (c_1, 0)^{\mathrm{T}}$. The solution for $0 \le r \le r_1$ thus takes a particular form, namely

$$\boldsymbol{y}(k_1 r) = c_1 \boldsymbol{k}(k_1 r), \tag{3.54}$$

where $\boldsymbol{k}(k_1 r)$ is the 2×1 column vector created from the first column of matrix $\boldsymbol{K}(z)$ and divided by $j_j(k_1 r_1)$ for numerical convenience. The solution in the sth spherical layer then follows from the upward continuation of the solution from the innermost sphere and the continuity condition (3.13) of $\boldsymbol{y}(z)$ at the interfaces at $r_1 \ldots r_m$. This corresponds to the multiplication of the product of the layer propagator matrices with the inner sphere solution taken at $r = r_1$. In the sth layer, ($r_{s-1} \le r \le r_s$, $s = 2, \ldots, m$), we obtain

$$\boldsymbol{y}(k_s r) = \boldsymbol{L}(k_s r, k_1 r_1)\boldsymbol{y}(k_1 r_1), \tag{3.55}$$

where

$$\boldsymbol{L}(k_s r, k_1 r_1) = \boldsymbol{M}(k_s r, k_s r_{s-1})\boldsymbol{M}(k_{s-1} r_{s-1}, k_{s-1} r_{s-2}) \ldots \boldsymbol{M}(k_2 r_2, k_2 r_1). \tag{3.56}$$

Substituting for $\boldsymbol{y}(k_1 r_1)$ from eq. (3.54), we have

$$\boldsymbol{y}(k_s r) = c_1 \boldsymbol{L}(k_s r, k_1 r_1)\boldsymbol{k}(k_1 r_1), \tag{3.57}$$

where

$$\boldsymbol{k}(k_1 r_1) = \begin{pmatrix} 1 \\ j+1-\chi_j(k_1 r_1) \end{pmatrix} . \tag{3.58}$$

The function $\chi_j(z)$ is defined by eq. (3.25). The corresponding recurrence relation for the function $\chi_j(z)$ is included in the Appendix C.

3.2.2 Poloidal matrix propagator in the atmosphere

The ocean-generated poloidal magnetic field propagates to the atmosphere. For $r > a$, it is described by the internal Gauss coefficients ${}^bG^{(i)}_{jm}$ (likewise the background magnetic field) by equation (2.15)

$$\boldsymbol{B}_0(r,\Omega) = -\sum_{j=1}^{\infty} \sum_{m=-j}^{j} \sqrt{(j+1)(2j+1)} \left(\frac{a}{r}\right)^{j+2} {}^bG^{(i)}_{jm}\, \boldsymbol{Y}^{j+1}_{jm}(\Omega) . \tag{3.59}$$

The radial and tangential components of $\boldsymbol{B}_0$ are given by relations (D.37) and (D.40)

$$\boldsymbol{e}_r \cdot \boldsymbol{B}_0(r,\Omega) = \sum_{jm} (j+1) \left(\frac{a}{r}\right)^{j+2} {}^bG^{(i)}_{jm}\, Y_{jm}(\Omega) , \tag{3.60}$$

$$\boldsymbol{e}_r \times \boldsymbol{B}_0(r,\Omega) = -i \sum_{jm} \sqrt{j(j+1)} \left(\frac{a}{r}\right)^{j+2} {}^bG^{(i)}_{jm}\, \boldsymbol{Y}^{j}_{jm}(\Omega) . \tag{3.61}$$

Following, the solution for the radial and tangential components of the magnetic field in the atmosphere can be described by

$$\boldsymbol{y}(r) = \boldsymbol{C}^0_j \, {}^bG^{(i)}_{jm} \left(\frac{r}{a}\right)^{j+2} \tag{3.62}$$

with

$$\boldsymbol{C}^0_j = \begin{pmatrix} -\, i\, a \sqrt{\dfrac{(j+1)}{j}} \\ i\, a \sqrt{j(j+1)} \end{pmatrix} \tag{3.63}$$

that is derived in Appendix B in equation system (B.50).

3.2.3 Poloidal matrix propagator for the ocean layer

For poloidal magnetic field modelling, we assume that the whole ocean depth is represented by one spherical layer assigned by label 'm' with the vertical range $r_{\mathrm{m}-1} \le r \le r_{\mathrm{m}}$, where $r_{\mathrm{m}} = a$ and $r_{\mathrm{m}-1} = b$. We recall that the induced magnetic field in ocean layer, $\boldsymbol{B}^{\mathrm{m}}$, is the superposition of homogeneous, $\boldsymbol{B}^{\mathrm{m}}_{\mathrm{hmg}}$, and particular, $\boldsymbol{B}^{\mathrm{m}}_{\mathrm{part}}$, solutions,

$$\boldsymbol{B}^{\mathrm{m}} = \boldsymbol{B}^{\mathrm{m}}_{\mathrm{hmg}} + \boldsymbol{B}^{\mathrm{m}}_{\mathrm{part}} . \tag{3.64}$$

To express $\boldsymbol{B}^{\mathrm{m}}_{\mathrm{part}}$ in a shorter form, we use the 2 × 1 column source-term vector

$$\boldsymbol{s}(r) = \begin{pmatrix} 1 \\ j+1 \end{pmatrix} \frac{-i}{\omega}\, G^{j}_{jm}(a) \left(\frac{r}{a}\right)^{j} \tag{3.65}$$

that is derivated in Appendix B in equations system (B.50). Now, the solution for the magnetic field components in the ocean layer can be expressed by

$$\begin{aligned} \boldsymbol{e}_r \cdot \boldsymbol{B}_{\mathrm{P}}(r,\Omega) &= \sum_{jm} v_1(r)\; Y_{jm}(\Omega)\;, \\ \boldsymbol{e}_r \times \boldsymbol{B}_{\mathrm{P}}(r,\Omega) &= \sum_{jm} v_2(r)\; \boldsymbol{Y}^{j}_{jm}(\Omega)\;, \end{aligned} \tag{3.66}$$

where $v_1(r)$ and $v_2(r)$ are components of the 2×1 column vector $\boldsymbol{v}(r)$ in the form

$$\boldsymbol{v}(r) = \boldsymbol{K}(z)\boldsymbol{c} + \boldsymbol{s}(r). \tag{3.67}$$

Here, the matrix $\boldsymbol{K}(z)$, where $z = kr$, is given by eq. (3.49), k is the wave number for the ocean-layer parameters and $\boldsymbol{c}$ is a 2×1 column vector with arbitrary constants. The unknown constants $\boldsymbol{c}$ can be eliminated by the values of magnetic intensity – radial and tangential part respectively – taken at the bottom $(r = r_{\mathrm{m}-1})$ of the layer m. Equation (3.67) at the bottom of the ocean layer $(r = r_{m-1})$ has the form

$$\boldsymbol{v}(r_{\mathrm{m}-1}) = \boldsymbol{K}(k_{\mathrm{m}} r_{\mathrm{m}-1})\boldsymbol{c}^{\mathrm{m}} + \boldsymbol{s}(r_{\mathrm{m}-1})\;. \tag{3.68}$$

Assuming the solution at ocean bottom is known then for arbitrary radius r in the ocean layer we get

$$\boldsymbol{v}(r) = \boldsymbol{M}^{\mathrm{m}}(r, r_{\mathrm{m}-1})\, \boldsymbol{y}^{\mathrm{m}}(r_{\mathrm{m}-1}) + \boldsymbol{s}(r)\;, \tag{3.69}$$

where we substituted for $\boldsymbol{c}$ from equation (3.48), the matrix $\boldsymbol{M}^{\mathrm{m}}$ is provided by eq. (3.53) and the wave number for the ocean layers is k_{m}. The continuity condition at the ocean bottom can be written in the form

$$\boldsymbol{y}^{\mathrm{m}-1}(r_{\mathrm{m}-1}) = \boldsymbol{y}^{\mathrm{m}}(r_{\mathrm{m}-1}) + \boldsymbol{s}(r_{\mathrm{m}-1})\;. \tag{3.70}$$

Solving eq. (3.70) for $\boldsymbol{y}^{\mathrm{m}}(r_{\mathrm{m}-1})$ and substituting the result into the eq. (3.69), the solution inside the ocean layer $r_{\mathrm{m}-1} \le r \le r_{\mathrm{m}}$ is then

$$\boldsymbol{v}(r) = \boldsymbol{M}^{\mathrm{m}}(r, r_{\mathrm{m}-1})[\boldsymbol{y}^{\mathrm{m}-1}(r_{\mathrm{m}-1}) - \boldsymbol{s}(r_{\mathrm{m}-1})] + \boldsymbol{s}(r)\;. \tag{3.71}$$

To guarantee the continuity at the ocean-atmosphere interface $\boldsymbol{v}(r_{\mathrm{m}}) = \boldsymbol{y}^{\mathrm{m}+1}(r_{\mathrm{m}})$, we evaluate the solution (eq. 3.71) at the upper boundary of the ocean layer $r = r_{\mathrm{m}}$,

$$\boldsymbol{v}(r_{\mathrm{m}}) = \boldsymbol{M}^{\mathrm{m}}(r_{\mathrm{m}}, r_{\mathrm{m}-1})\left[\boldsymbol{y}^{\mathrm{m}-1}(r_{\mathrm{m}-1}) - \boldsymbol{s}(r_{\mathrm{m}-1})\right] + \boldsymbol{s}(r_{\mathrm{m}})\;. \tag{3.72}$$

In addition, the boundary condition at $r = r_{\mathrm{m}}$ from the atmosphere side is given by eq. (3.62). The whole system can be then described by

$$\boldsymbol{M}^{\mathrm{m}}(r_{\mathrm{m}}, r_{\mathrm{m}-1})\, \boldsymbol{L}(k_{\mathrm{m}-1} r_{\mathrm{m}-1}, k_1 r_1)\, \boldsymbol{k}(k_1 r_1)\; c_1 - \boldsymbol{C}^0_j\, {}^{b}G^{(i)}_{jm} = \boldsymbol{M}^{\mathrm{m}}(r_{\mathrm{m}}, r_{\mathrm{m}-1})\, \boldsymbol{s}(r_{\mathrm{m}-1}) - \boldsymbol{s}(r_{\mathrm{m}})\;, \tag{3.73}$$

where there are two unknowns, the coefficients c_1 and ${}^{b}G^{(i)}_{jm}$. Finally, we rewrite eq. (3.73) in matrix form with two equations

$$\begin{pmatrix} Q_1 & W_1 \\ Q_2 & W_2 \end{pmatrix} \begin{pmatrix} c_1 \\ {}^{b}G^{(i)}_{jm} \end{pmatrix} = \begin{pmatrix} P_1 \\ P_2 \end{pmatrix}\;. \tag{3.74}$$

The indexes $()_1$ and $()_2$ stand for the first and second components, respectively, and

$$\begin{aligned} \boldsymbol{Q} &= \boldsymbol{M}^{\mathrm{m}}(r_{\mathrm{m}}, r_{\mathrm{m}-1})\; \boldsymbol{L}(k_{\mathrm{m}-1} r_{\mathrm{m}-1}, k_1 r_1)\; \boldsymbol{k}(k_1 r_1)\;, \\ \boldsymbol{W} &= -\boldsymbol{C}^0_j\;, \\ \boldsymbol{P} &= \boldsymbol{M}^{\mathrm{m}}(r_{\mathrm{m}}, r_{\mathrm{m}-1})\, \boldsymbol{s}(r_{\mathrm{m}-1}) - \boldsymbol{s}(r_{\mathrm{m}})\;. \end{aligned} \tag{3.75}$$

3.3 Secondary poloidal magnetic field

For a model consisting of spherically symmetric layers with homogeneous conductivities used until now the computation of the generated magnetic field can be decomposed into separate calculations of toroidal and poloidal modes. By considering lateral variations of electric conductivity the two magnetic field components cannot be computed separately since they are coupled. A strong lateral electrical conductivity contrast at the ocean-continent boundary causes the so called coastal effect. The magnetic field generated due to this lateral conductivity contrast is referred as to the secondary poloidal component. As a matter of fact, the present method does not allow us a full exploitation of the mode conversion due to the coupling of the primary toroidal magnetic field with lateral heterogeneities in electrical conductivity. The following approach thus provides only a first estimate of the magnitude and spatial pattern of the secondary poloidal magnetic field. To make this estimate, we consider a one-layer ocean model and approximate the lateral distribution of electrical conductivity in the uppermost (ocean-continent) layer by a conductivity contrast between oceans ($\sigma_\mathrm{o} = 3.5$ S/m) and continents ($\sigma_\mathrm{c} = 10^{-3}$ S/m). Splitting the resistivity $1/\sigma$ into radially and laterally varying parts, $1/\sigma_0$ and $1/\sigma_1$, respectively,

$$\frac{1}{\sigma} = \frac{1}{\sigma_0(r)} + \frac{1}{\sigma_1(\Omega)}, \tag{3.76}$$

and considering the poloidal-toroidal decomposition of the magnetic induction, $\boldsymbol{B} = \boldsymbol{B}_\mathrm{P} + \boldsymbol{B}_\mathrm{T}$, the magnetic induction equation (1.11) reads as

$$\frac{1}{\mu_0}\mathrm{curl}\Big[\frac{1}{\sigma_0}\mathrm{curl}(\boldsymbol{B}_\mathrm{P} + \boldsymbol{B}_\mathrm{T})\Big] + \mathrm{curl}\Big[\frac{1}{\sigma_1}(\boldsymbol{j}_\mathrm{S} + \boldsymbol{j}_\mathrm{T})\Big] + \frac{\partial(\boldsymbol{B}_\mathrm{P} + \boldsymbol{B}_\mathrm{T})}{\partial t} = \mathrm{curl}(\boldsymbol{u} \times \boldsymbol{B}_\mathrm{E}), \tag{3.77}$$

where $\boldsymbol{j}_\mathrm{S,T} = \mathrm{curl}\,\boldsymbol{B}_\mathrm{T,P}/\mu_0$ are the spheroidal and toroidal components of electrical current density, respectively. Decomposing the product of electrical current density with the lateral conductivity variations as

$$\frac{1}{\sigma_1(\Omega)}(\boldsymbol{j}_\mathrm{S} + \boldsymbol{j}_\mathrm{T}) = \boldsymbol{\mathcal{E}}_\mathrm{S} + \boldsymbol{\mathcal{E}}_\mathrm{T}, \tag{3.78}$$

allows the induction equation to be written for the spheroidal and toroidal parts separately,

$$\frac{1}{\mu_0}\mathrm{curl}\Big(\frac{1}{\sigma_0}\mathrm{curl}\boldsymbol{B}_\mathrm{P}\Big) + \frac{\partial \boldsymbol{B}_\mathrm{P}}{\partial t} = \Big[\mathrm{curl}(\boldsymbol{u} \times \boldsymbol{B}_\mathrm{E})\Big]_\mathrm{T} - \mathrm{curl}\,\boldsymbol{\mathcal{E}}_\mathrm{T}. \tag{3.79}$$

$$\frac{1}{\mu_0}\mathrm{curl}\Big(\frac{1}{\sigma_0}\mathrm{curl}\boldsymbol{B}_\mathrm{T}\Big) + \frac{\partial \boldsymbol{B}_\mathrm{T}}{\partial t} = \Big[\mathrm{curl}(\boldsymbol{u} \times \boldsymbol{B}_\mathrm{E})\Big]_\mathrm{S} - \mathrm{curl}\,\boldsymbol{\mathcal{E}}_\mathrm{S}. \tag{3.80}$$

However, both equations are mutually coupled via terms $\boldsymbol{\mathcal{E}}_\mathrm{S,T}$ since each of them is generated by both the spheroidal and toroidal magnetic field components. F. Vivier (personal communication, 2011) has attempted to solve the coupled system of equations by an iterative method, but he encountered numerical instabilities in an iterative solution due to the coupling terms $\boldsymbol{\mathcal{E}}_\mathrm{S,T}$. Here, we will not attempt to find a stable iterative solution of the coupled system of equations (3.79) and (3.80), but will confine ourselves to computing the first iteration of the magnetic induction equation (3.79) for the secondary spheroidal magnetic field $\boldsymbol{B}_\mathrm{P}$. After solving eq. (3.80) with $\boldsymbol{\mathcal{E}}_\mathrm{S} = 0$ for the primary toroidal magnetic field $\boldsymbol{B}_\mathrm{T}$ by applying the matrix-propagator method developed in section 3.1, the term $\boldsymbol{\mathcal{E}}_\mathrm{T}$ is computed by the spherical harmonic analysis of the product of the electric current density $\boldsymbol{j}$ and the lateral conductivity variations $\sigma_1(\Omega)$, as indicated by eq. (3.78), and substituted into magnetic induction equation (3.79) for the secondary spheroidal magnetic field $\boldsymbol{B}_\mathrm{P}$. This equation, solved together with the free-divergence constraint on $\boldsymbol{B}_\mathrm{P}$ by the matrix-propagator method described in section 3.2, yields the secondary poloidal magnetic field.

3.4 Numerical results of the matrix-propagator method

With the presented analytical approach we estimate a possible range of magnitudes and global distribution of the induced toroidal, poloidal and the secondary poloidal magnetic field. We also study the sensitivity of the generated magnetic field with respect to variations of different parameters. We are interested in answering questions like the following. How deep does the ocean induced magnetic field penetrate for realistic values for ocean flow and an electrical conductivity profile inside and beneath the ocean layer? How does the conductivity profile influences the magnitude of the induced magnetic field? We study the influence of large velocities of the strong M_2 tidal flow in shallow-coastal regions on the generated magnetic field, but also the whole oceanic transport given by the M_2 tide. In addition, the classical approach enables an estimate of the secondary poloidal ocean-induced magnetic field generated by a conductivity contrast between the ocean and continent. In case of the toroidal magnetic field, the model also allows us to study the effect of the decay of oceanic flow with depth on the generated magnetic field. Furthermore, the analytical approach of the induction equation delivers an independent solution that can be used as a reference the for validation of numerical approaches presented in the following chapters. All calculations are carried out for spherical harmonic series with cut-off at degree $j_{\max} = 48$ with the exception of the secondary poloidal magnetic field where the cut-off degree is set by $j_{\max} = 43$. As we are constrained by a spherically symmetric model, we note that the model with the ocean layer of depth of $h = 1$ km and averaged ocean velocity field overestimates the magnitudes of generated magnetic signal in the regions with bathymetry smaller than $h = 1$ km and underestimates the generated magnetic signal in deeper ocean.

3.4.1 Toroidal magnetic field

We start the description with the behaviour of the toroidal magnetic field with depth. The profile of complex toroidal magnetic signals for three different uniform electrical conductivity profiles σ beneath the ocean layer ($\sigma_{\mathrm{m}} = 1\ \mathrm{Sm}^{-1}$, dashed lines; $\sigma_{\mathrm{m}} = 0.3\ \mathrm{Sm}^{-1}$, solid lines; $\sigma_{\mathrm{m}} = 0.1\ \mathrm{Sm}^{-1}$, dotted lines) is plotted in Figure 3.1. The propagation of the real (red) and imaginary (blue) part of the ϑ (top) and φ (bottom) components of the induced toroidal magnetic field by over the depth constant tidal flow between the radius $r = 5500$ km and sea surface is presented in the left-hands panels and the detail for the ocean layer in the right-hand panels. The average velocity field of M_2 tide (subsec. 2.6.1) is used for the thickness of the ocean layer of $h = 1$ km. The radial profile is taken at the location given by the yellow crosses in Figure 3.2.

The toroidal magnetic field vanishes at the atmosphere. Figure 3.1 clearly shows the decay of the magnetic signal towards the sea surface where it vanishes. The source term (eq. 2.1), acting constantly through the radial profile of the ocean layer generates the toroidal magnetic field that increases with the depth. The interface conditions (eqs 3.9 and 3.10) guarantee the continuity of the induced magnetic signal $\boldsymbol{B}_{\mathrm{T}}$ between the spherical layers. In the electrically conductive space beneath the ocean layer, the magnetic signal is decaying with the depth in dependency on the magnitude of electrical conductivity. A larger conductivity of the medium allows easier discharge of the induced electric currents and the magnetic field diminishes faster with depth. A more resistive medium in contrary hinder the discharge of electric currents and the generated magnetic field reaches deeper parts of the sphere. The uniform conductivity profiles cause a smooth decay of the toroidal magnetic field with depth that is beneath the radius $r = 5500$ km in all plotted examples of Fig. 3.1 already very tiny. The maximum of the magnetic signal is achieved at the bottom of the ocean layer and reaches the magnitude of 0.006 nT at the chosen location. This example provides us with a first estimate for the penetration depth of the induced magnetic signal that can be used as a starting radius for numerical calculation with matrix-propagator method. Beside the estimate of the magnetic signal depth, the behaviour of the magnetic field decay and its changes with respect to changes of the homogeneous conductivity profile provide us with a possibility for evaluation our numerical model. Model evaluation for the magnetic signal decay by non-homogeneous (realistic) conductivity profile is not possible. Additionally, as is shown in detail in the right-hand panel, changes in the conductivity profiles beneath the ocean layer influence also the behaviour of the magnetic signal in the ocean (marked by dark colour). But as the differences between the conductivity profiles in this numerical example are not large, the magnitudes of the magnetic fields in the ocean do not differ substantially.

The influence of the electrical conductivity parameter beneath the ocean on the magnitude of the toroidal magnetic field in the ocean reveals by comparing the presented numerical example above with the realistic mantle conductivity profile used in Figure 3.4. In this case we apply the same model setting with exception of the electrical conductivity profile beneath the ocean layer. The solid lines represent the toroidal magnetic field obtained by using realistic electrical conductivity profile (Fig. 2.5 and Table 2.1). A uniform conductivity profile beneath the ocean ($\sigma_\mathrm{m} = 1$ Sm^{-1}, dashed lines) will serve for the comparison of the magnetic signals for different electrical conductivities σ_m. In realistic case we separate the conductivity profile in 17 layers as shown in Fig. 2.5 with the minimum value for the conductivity of $\sigma = 10^{-3}$ Sm^{-1} at the radius $r = 6300$ km.

A highly resistive lithosphere and crust leads to a strong decay of the magnetic signal over solid Earth and reduce the magnitude over ocean layer to a half of that for an uniform conductivity profile beneath the ocean. Another observation we can make is that, for realistic conductivity profile, which is effectively more resistive beneath the sedimentary layer, the toroidal magnetic field has the largest amplitudes above the ocean bottom. A general tendency is that the more resistive the underlying mantle, the more the maximum of the toroidal magnetic field is shifted towards the centre of the ocean layer. In the limiting case where we would assume that the medium beneath the ocean layer is an insulator and that the conductivity of the ocean would be uniform, the toroidal magnetic field would reach the maximum in the middle of the ocean layer. Until now the conductivity profile of the ocean layer σ_o has been represented by realistic values given in table 2.1. To study the sensitivity of radially varying electrical conductivity of the ocean water on the generated toroidal magnetic field, we compare the above result with that for a uniform sea water conductivity, $\sigma_\mathrm{o} = 3.5$ Sm^{-1} (dotted lines on the right of Figure 3.4). The impact of uniform conductivity profile through the ocean layer column in comparison to the realistic one consists of a slight reduction in magnitudes of the magnetic signal, but no significant changes in the behaviour of the propagation of the magnetic field through the ocean layer are found. The uncertainties of the electrical conductivity of the solid Earth are in comparison to them of the ocean water larger. Therefore, the conductivity profile of the ocean is changed only slightly and results in comparison to the conductivity changes of the solid Earth only in a minor differences of the generated magnetic field.

The spatial distribution of the ϑ and φ components of the induced toroidal magnetic field is shown in Figure 3.2 where the yellow crosses mark the location of the radial profile in Figure 3.4. The magnetic field in Figure 3.2 is plotted at the bottom of the ocean layer. The spatial patterns of the induced magnetic field are dominated by small-scale features (high spectral frequencies) associated with the spatial distribution of high ocean velocities in shallow regions along the coasts, see Figure 2.1. The large-scale features (low spectral frequencies) generated over large deep oceanic basins with relatively slow ocean velocities are three times smaller in magnitude than small-scale features in shallow waters. In this first numerical experiment, we consider the averaged tidal flow velocity field in a layer with a constant depth of $h = 1$ km. The magnetic field in shallower regions than 1 km is overestimated while over deeper regions is underestimated. The highest amplitudes of the toroidal magnetic field in some coastal regions reach values up to 4×10^{-3} nT, as example, in East China sea, South China sea and Philippine sea (Figure 3.3).

In our second numerical experiment, we consider that the ocean flow is not contant over the depth, but decays in magnitude (not the direction) of the ocean velocities with ocean depth. The model in equation (2.13) of ocean velocities is intentionally designed to enable a linear change of ocean velocities with depth. We will consider the maximum linear decrease of ocean flow such that the velocities are set to equal to the input OMCT velocities at the top of the ocean layer and vanish at the ocean bottom. Figure 3.5 shows the ϑ and φ components of the induced toroidal magnetic field at the ocean bottom generated by this ocean flow. A comparison with the case of the constant oceanic flow over the depth (Figure 3.3) shows that the toroidal magnetic field induced by the horizontal flow with linear depth decay is three orders of magnitude larger than the field generated by the radially constant flow and reaches amplitudes at the ocean bottom up to 2 nT (Figure 3.6). A large difference in generated magnetic field between the constant and decaying ocean flows with the depth shows on the importance of this parameter on the induced toroidal magnetic field. This effect will be important for studying the toroidal magnetic field induced by a general (thermohaline and wind-driven) circulation. Including the linear flow decay with depth changes also the spatial distribution of the generated toroidal magnetic field. While by the constant average horizontal velocities over the ocean depth the toroidal magnetic field reflects the small-scale patterns of high ocean velocities along the coast, in the case with depth decaying flow, where the derivative term has dominant effect over the whole ocean, the toroidal magnetic signal over the large basins has larger amplitudes in comparison to the regions with high flow velocities. The spatial patterns become large-scaled, whereas the small-scale features in coastal regions are less dominant, as for instance, in areas along the coasts of Africa and India the induced magnetic field vanishes at all. Also, the magnetic field has now significant maxima in southern Atlantic basin, south of Madagascar and around New Zealand which are missing by the toroidal magnetic field generated by constant horizontal flow over the depth.

To estimate the sensitivity of the induced magnetic field to the conductivity profile beneath the ocean layer for the depth decaying horizontal flow, we set $\sigma_{\mathrm{m}} = 1\ \mathrm{Sm}^{-1}$ and obtain amplitudes up to 3 nT (Figures 3.7 and 3.8). This model setup generates the highest values of the toroidal magnetic field when the average ocean velocities are scaled by ocean layer of thickness of $h = 1$ km. Figure 3.9 shows the radial profile of the toroidal magnetic field induced by lineary decaying horizontal ocean flow taken at the location marked by yellow crosses in Figures 3.5 and 3.7. The behaviour and decay of the toroidal magnetic field for the uniform conductivity profile beneath the ocean layer, $\sigma_{\mathrm{m}} = 1\ \mathrm{Sm}^{-1}$, (dashed lines) is comparable with the case of constant flow over the depth. Notable is the decrease of the magnetic signal given by the realistic conductivity profile (highly resistive lithosphere and crust). The decay of the toroidal magnetic field caused by highly resistive layers (relatively to $\sigma_{\mathrm{m}} = 1\ \mathrm{Sm}^{-1}$) is stronger for case with constant flow over the depth, whereas for depth decaying flow the magnetic signal penetrates deeper into the sphere. That can be explained by large-scale magnetic field patterns for depth decaying flow as the long spatial wavelengths reaches deeper parts of the Earth. Finally, the dotted lines in the right-hand panel show the differences between the signal for a uniform ocean layer conductivity profile $\sigma_{\mathrm{o}} = 3.5\ \mathrm{Sm}^{-1}$ and the realistic one (full lines). The behaviour of the magnetic field in respect to this parameter is comparable with the case of constant horizontal flow over the depth.

In the third numerical experiment we study the influence of the whole oceanic transport on the generated magnetic field. We use ocean tidal flow integrated over the ocean depth and apply it inside an ocean layer with the average depth of $h = 4$ km. Figure 3.10 shows the real (left) and imaginary (right) parts of the ϑ (top) and φ (bottom) components of the induced toroidal magnetic field at the ocean bottom for realistic electrical conductivity profile. The strong magnetic signal reflects the areas with a large water transport. The large oceanic basins with a deep bathymetry dominate in the generated toroidal magnetic field, even if the flow velocities are smaller than those in coastal areas. The strong small-scale signals, like in the real part of the ϑ component along the coast of India, that can not be distinguished in the velocity fields (Fig. 2.2), are probably caused by the Indian subcontinent that divides the area in two separate basins: Arabian Sea and Bay of Bengal, where each of them generate a separate dipole field for the ϑ component. The amplitudes of the toroidal magnetic field generated by the whole transport of tidal flow reach values up to 7-8 10^{-3} nT (Figure 3.11). Noticeable are the strong amplitudes of the φ component in the equatorial area, where the dominant radial component of the background magnetic field $\boldsymbol{B}_\mathrm{E}$ is weak (Figure 2.4). This phenomenon can be explained by the influence of ϑ component of the background magnetic field which has its maximum in equatorial areas. The radial profile in Figure 3.12 shows the decay of the signal with depth for the realistic conductivity profile (solid lines) and the uniform conductivity profile beneath the ocean layer $\sigma_\mathrm{m} = 1$ Sm^{-1} (dashed lines). As the magnetic field generated by oceanic transport is dominated by long spatial wavelengths over deep ocean basins, the magnetic signal penetrate deeper into the Earth as is the case for the numerical experiment with average over the depth constant velocity field shown in Figure 3.4 and have similar behaviour to the case with depth decaying flow from Figure 3.9. It should be mentioned that by the model for ocean layer of the depth of $h = 4$ km, the conductivity profile presented in Table 2.1 has been shifted by 3 km into the depth.

3.4.2 Primary poloidal magnetic field

Now we turn our attention to the primary poloidal magnetic field generated by the magnetic source given by the equation (2.6). By the matrix-propagator method we face numerical limitations for the poloidal case given by numerical instabilities that do not allow for a numerical solution by the same parametrization as for the toroidal magnetic field shown above. The numerical difficulties of the matrix propagator are due to a high lateral resolution (spherical harmonic parametrization), low electrical conductivity and by discretization of the radial profile in thin layers. Such parametrization leads to large numerical values by tiny numerical differences between the bottom and top of the layer during the propagation which causes numerical instabilities.

Therefore, to be able to maintain the calculus for the decided cut-off degree of spherical harmonics $j_\mathrm{max} = 48$ in this chapter, we limit our solution only to two numerical examples with a uniform conductivity profile beneath the ocean layer with $\sigma_\mathrm{m} = 1$ Sm^{-1} and for the ocean layer $\sigma_\mathrm{o} = 3.5$ Sm^{-1}. These results will be used for the numerical comparison and validation with the results of the spectral finite-element approach in chapter 4. The chosen parametrization allows an easier comparison of the two applied mathematical methods, classical and spectral finite-element approach (chapter 4), for both components of the magnetic fields, the toroidal and poloidal part. Namely, as the matrix-propagator method requires sufficiently thick layers to get numerically stable solution, the spectral finite-element approach requires preferably thin finite-element layers because of the linear approximation between the nodes. Therefore, the requirements on the parametrization of the radial profile are different for both techniques. Using a uniform conductivity profile provides us a simple possibility of the comparison between the two mathematical approaches, independently of the radial profile discretization. As the poloidal magnetic field does not vanish at sea surface as the toroidal magnetic field it is convenient to plot its spatial distribution at the sea surface or above the sea surface where it can be measured.

The spatial distribution for two numerical examples obtained by the matrix propagator method are shown. Figure 3.14 represent the real (left) and imaginary (right) parts of the r (top), ϑ (middle) and φ (bottom) components of the induced poloidal magnetic field for the ocean layer of the depth of $h = 1$ km with average velocities and in Figure 3.13 for the ocean layer of the depth of $h = 4$ km with the whole oceanic transport. In both cases we use over the depth constant horizontal ocean flow and use the dipole background magnetic field ($\boldsymbol{B}_\mathrm{E}$) only. The corresponding radial profiles are included in chapter 4 in Figures 4.19 and 4.13 where the primary poloidal magnetic field will be discussed in more detail.

3.4.3 Secondary poloidal magnetic field

The analytical approach allows additionally making an estimate of the magnitude and the global distribution of the secondary ocean-induced poloidal magnetic field generated by the toroidal magnetic field by the strong conductivity contrast between the ocean and continent described in section 3.3. As the input for modelling the secondary poloidal magnetic field, we apply the electric field calculated in the first and third numerical examples for generating the toroidal magnetic field. Therefore, the input is the toroidal magnetic field induced by the average ocean velocities with the ocean layer of the depth of $h = 1$ km (Figure 3.2) and in second case the whole oceanic transport with the ocean layer of the depth of $h = 4$ km (Figure 3.10) and, therefore, originated by over the depth constant horizontal ocean flow of the M_2 tide presented in Figures 2.1 and 2.2, respectively.

The conductivity of the continents is set by $\sigma_\mathrm{c} = 10^{-3}$ Sm^{-1}. Similarly as for the primary poloidal magnetic field, we use the dipole background magnetic field only. To overcome the numerical difficulties of the analytical solution for the poloidal magnetic field described above and estimate the secondary poloidal magnetic field realistically, we reduce the cut-off degree of spherical harmonic series to $j_\mathrm{max} = 43$ and apply an adapted conductivity profile (see Table 2.1), where the resistive part of the conductivity profile decreases to value of $\sigma = 10^{-2}$ Sm^{-1} instead of $\sigma = 10^{-3}$ Sm^{-1}.

In the first case, for the average velocities and $h = 1$ km, we can see in Figure 3.15 that the magnetic signal has small-scale features and is concentrated along the ocean shorelines. It reflects the small-scale global patterns of the toroidal magnetic field in Figure 3.2 that are caused by high ocean velocities in shallow regions along the coast. This is the case, for example, along the east coast of North America, Argentine Sea, along the Indian subcontinent and the South China Sea. The high velocities along the coast together with the strong conductivity contrast at the same location essentially benefit to the secondary poloidal magnetic field. By this model setup, the amplitudes (Figure 3.16) reach values up to 4 nT for ϑ and φ component and 5 nT for the r component. The strong jump in conductivity along the coast causes the Gibbs phenomenon in spherical harmonic parametrization, which has been mitigated by weighing the spherical harmonic series by the Lanczos coefficients, similar as for the input velocity field in subsection 2.6.1. Still, as the magnetic signal is small-scaled, a remaining noise is apparent.

In our second example of the oceanic transport by ocean layer with the depth of $h = 4$ km (Figure 3.17), the induced secondary poloidal magnetic field has different spatial patterns. The magnetic signal does not only reflect the locations of high ocean velocities in coastal regions, but it appears along the coastlines more generally. The radial component especially distinguishes the shorelines, for example, the African continent. Comparing the secondary magnetic field with its source – the toroidal magnetic field in Figure 3.10, we find the explanation: The toroidal magnetic field generated predominantly by ocean transport in deep ocean areas consists of large-scale patterns, i.e., a low frequency signal that also reaches the coastlines. The amplitudes (Figure 3.18) achieve approximately the same values (4-5 nT) as the secondary poloidal magnetic field induced by high velocities along the coast. In this case, the input toroidal magnetic field is large-scale and the Gibbs phenomenon can be more efficiently reduced. This can be deduced by the comparison

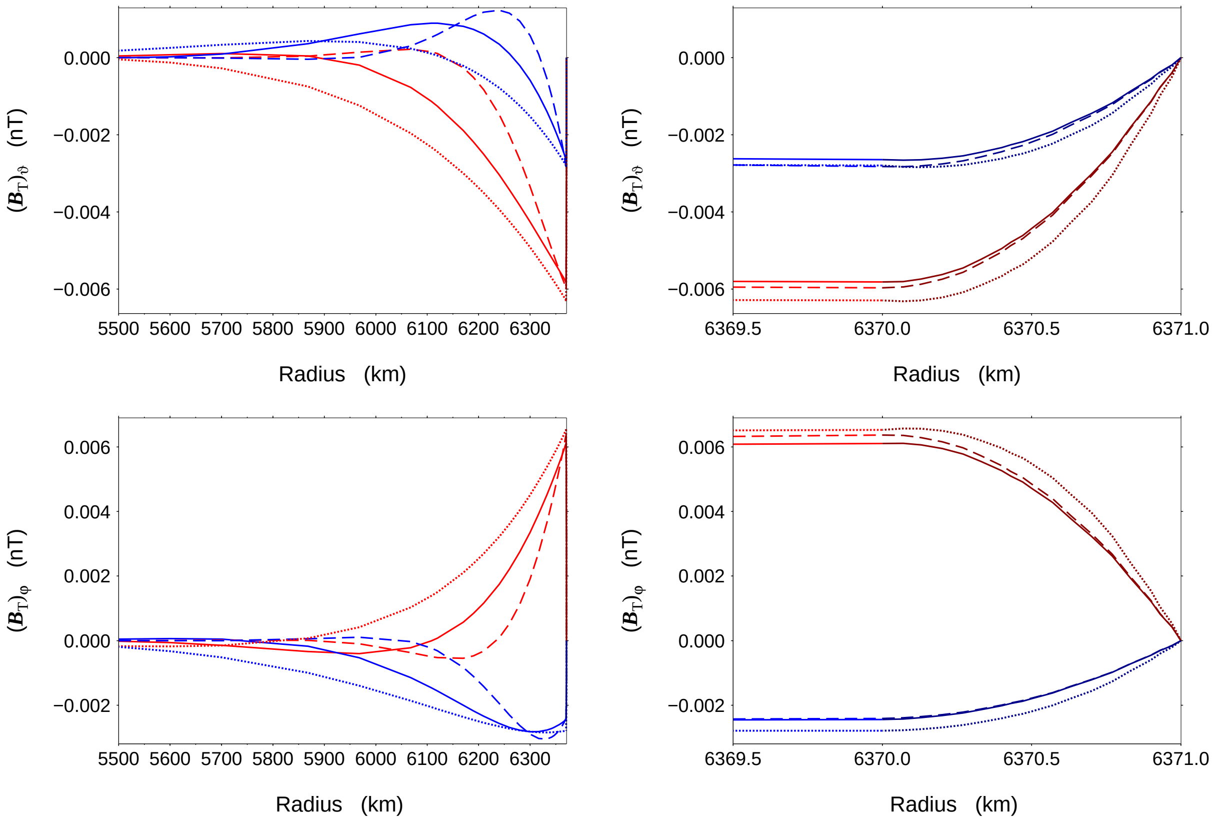

Figure 3.1: Real (red) and imaginary (blue) parts of the ϑ (top) and φ (bottom) components of the toroidal magnetic field (in nT) induced by over the depth constant tidal flow as functions of radius, beneath (left) and, in detail, inside the ocean layer (right), for three different uniform conductivity profiles beneath the ocean ($\sigma = 1$ Sm^{-1} - dashed lines; $\sigma = 0.3$ Sm^{-1} - solid lines; $\sigma = 0.1$ Sm^{-1} - dotted lines). The conductivity in ocean layer is $\sigma_{\mathrm{o}} = 3.5$ Sm^{-1}. The radial profiles are taken at the location given by the yellow crosses in Figure 3.2.

between the Figures 3.16 and 3.18. The comparison between the two numerical experiments for the secondary poloidal magnetic field shows the contribution to the induced magnetic signal of both, the high velocities near the coast and the whole oceanic transport. In addition, our estimates show that the secondary poloidal magnetic field reaches approximately the same magnitudes as the primary poloidal magnetic field, but with different spatial distribution. This will be elaborated further in the next chapter where the primary poloidal magnetic field is studied in more detail.

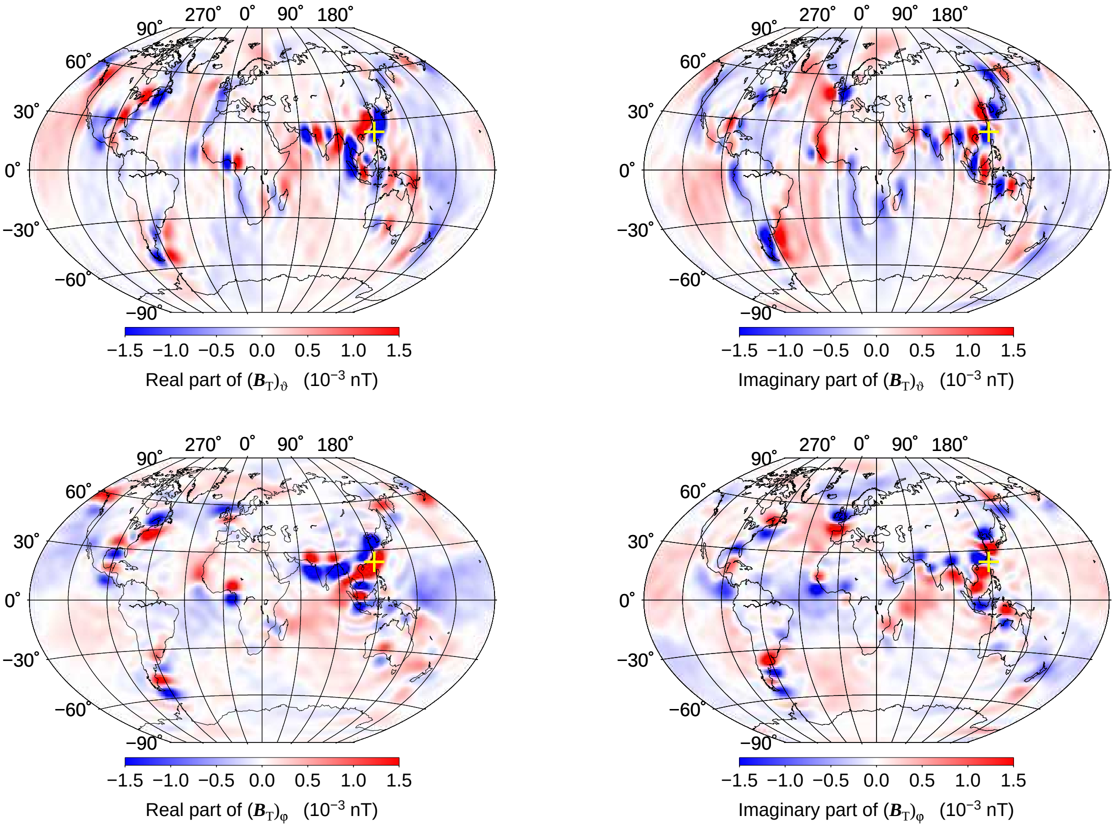

Figure 3.2: Real (left) and imaginary (right) parts of the ϑ (top) and φ (bottom) components of the toroidal magnetic field (in 10^{-3} nT) at the ocean bottom induced by over the depth constant tidal flow with the ocean layer of the depth of $h = 1$ km and the realistic electrical conductivity profile beneath and inside the ocean layer. The yellow crosses at 23° N, 120° E mark the location where the radial profiles of the toroidal magnetic field are plotted (see Fig. 3.4).

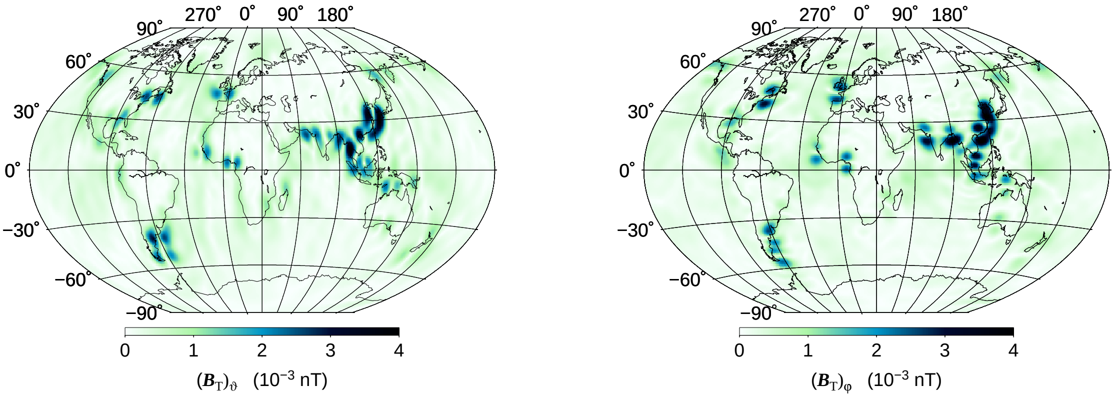

Figure 3.3: Amplitude of the ϑ (left) and φ (right) components of the toroidal magnetic field (in 10^{-3} nT) at the ocean bottom according to the magnetic field induced by condition in Fig. 3.2.

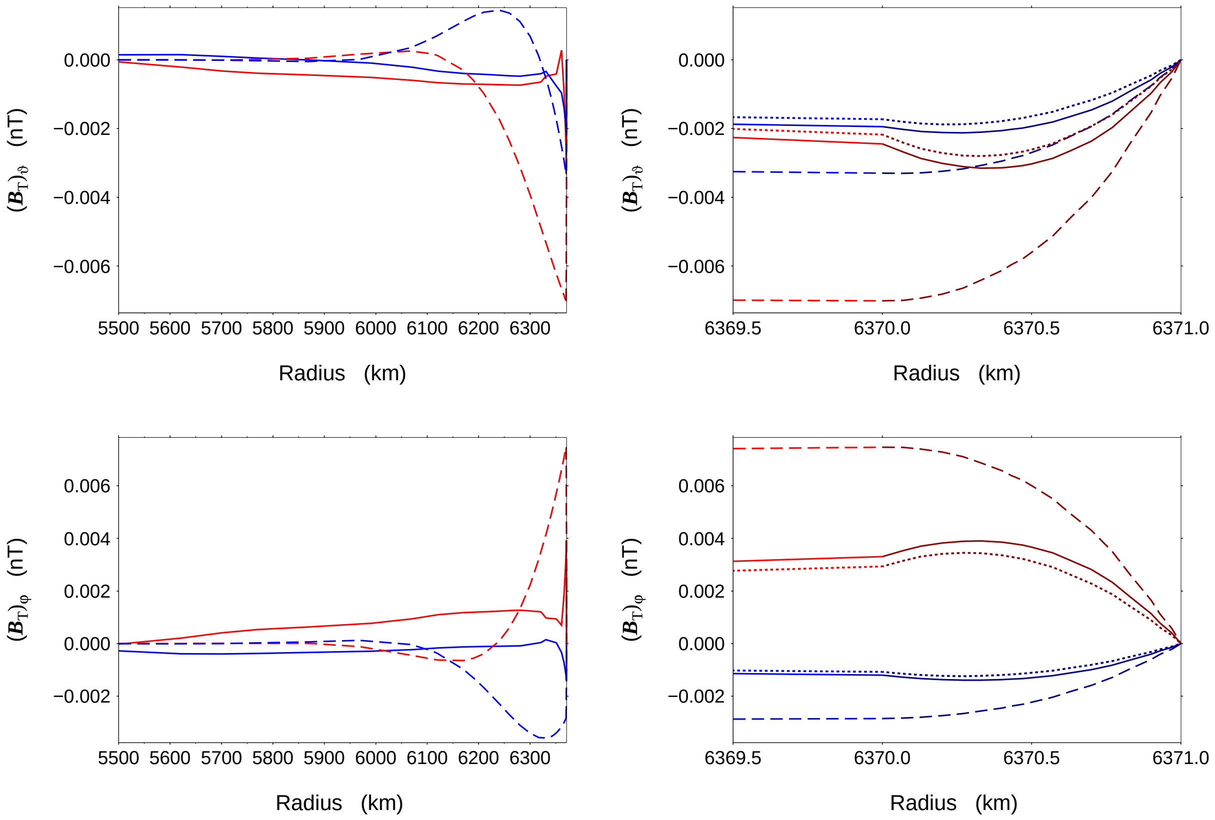

Figure 3.4: Real (red) and imaginary (blue) parts of the ϑ (top) and φ (bottom) components of the toroidal magnetic field (in nT) induced by over the depth constant tidal flow as functions of radius, beneath the ocean layer (left) and inside the ocean layer (right) for electrical conductivity profile with realistic (solid lines) and uniform profile beneath the ocean ($\sigma_\mathrm{m} = 1\ \mathrm{Sm}^{-1}$, dashed lines) and realistic conductivity profile inside the ocean. The dotted lines in the detail for ocean layer represent the case for realistic solid Earth and uniform ocean conductivity ($\sigma_\mathrm{o} = 3.5\ \mathrm{Sm}^{-1}$). The radial profiles are taken at the location given by the yellow crosses in Figure 3.2.

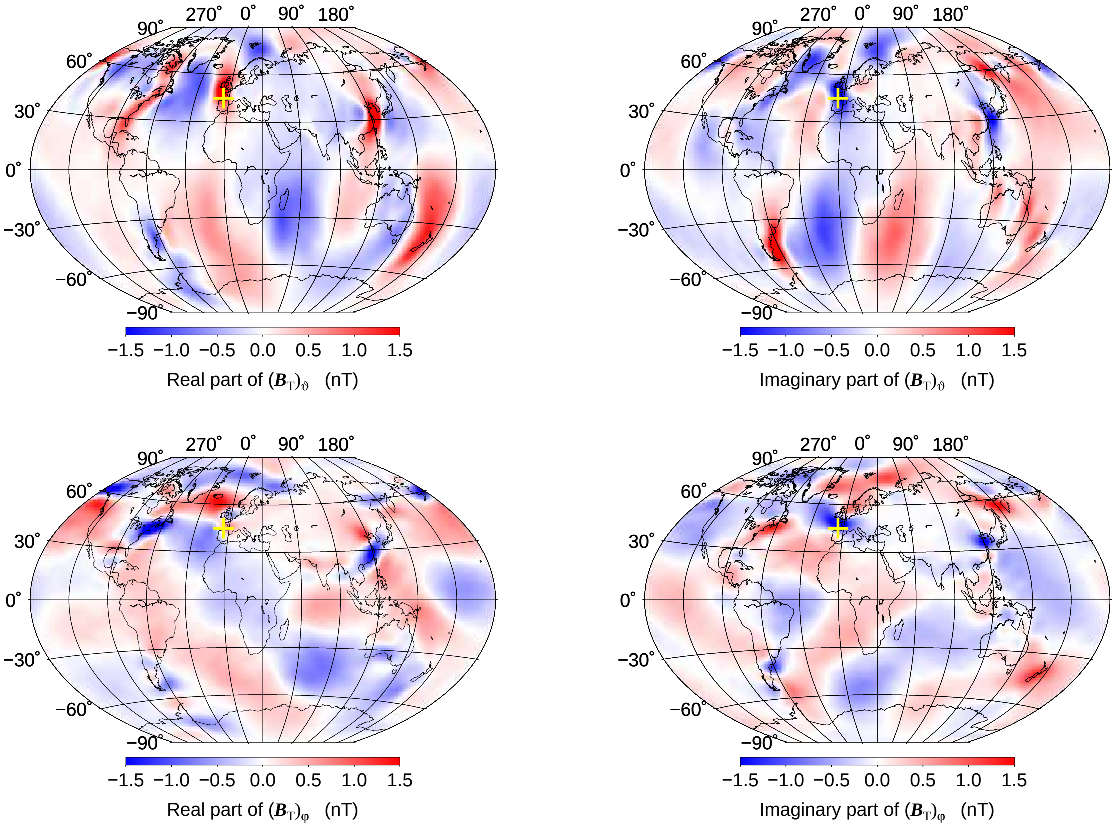

Figure 3.5: Real (left) and imaginary (right) parts of the ϑ (top) and φ (bottom) components of the toroidal magnetic field (in nT) at the ocean bottom induced by depth decaying horizontal ocean flow with the ocean layer of the depth of $h = 1$ km and realistic electrical conductivity profile beneath and inside the ocean. The yellow crosses at 45° N, 5° W mark the location where the radial profiles of the toroidal magnetic field are plotted (see Fig. 3.9).

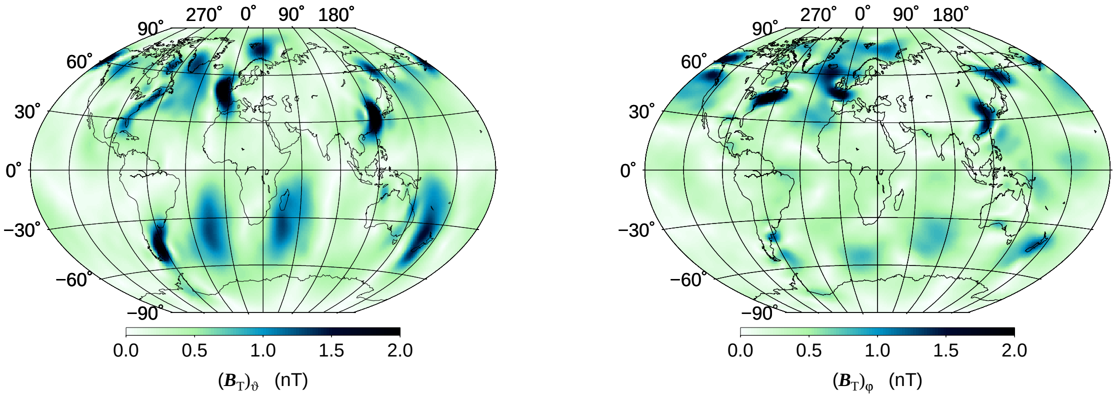

Figure 3.6: Amplitude of the ϑ (left) and φ (right) components of the toroidal magnetic field (in nT) at the ocean bottom according to the magnetic field induced by condition in Fig. 3.5.

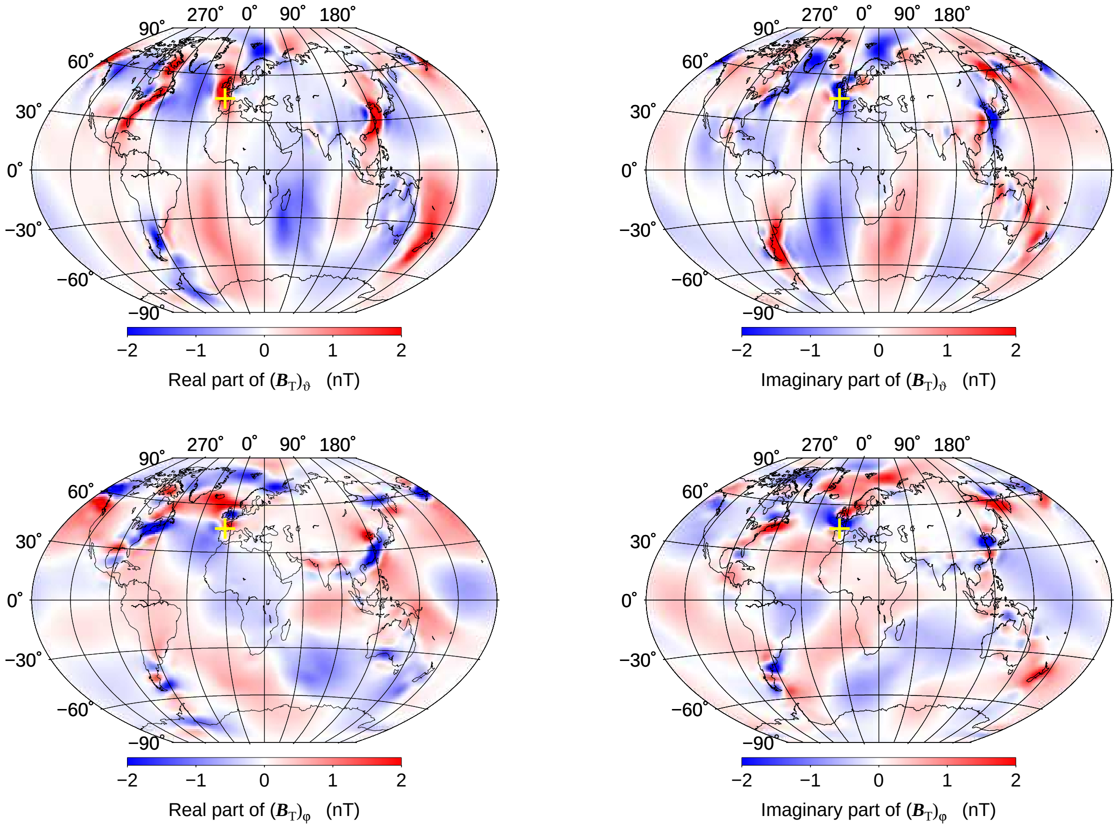

Figure 3.7: Real (left) and imaginary (right) parts of the ϑ (top) and φ (bottom) components of the toroidal magnetic field (in nT) at the ocean bottom induced by depth decaying horizontal ocean flow with the ocean layer of the depth of $h = 1$ km, electrical conductivity profile for the solid Earth $\sigma_\mathrm{m} = 1$ Sm^{-1} and realistic ocean conductivity profile. The yellow crosses at 45° N, 5° W mark the location where the radial profile of the toroidal magnetic field is plotted (see Figs. 3.9).

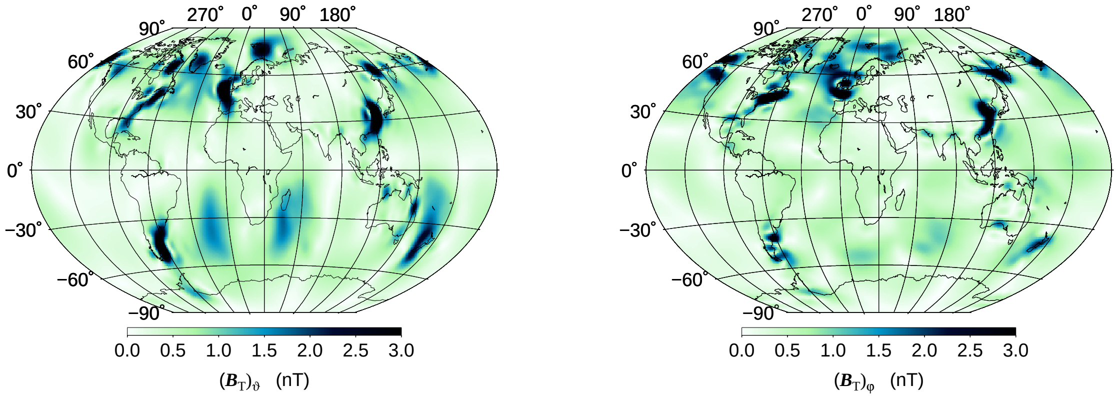

Figure 3.8: Amplitude of the ϑ (left) and φ (right) components of the toroidal magnetic field (in nT) at the ocean bottom according to the magnetic field induced by condition in Fig. 3.7.

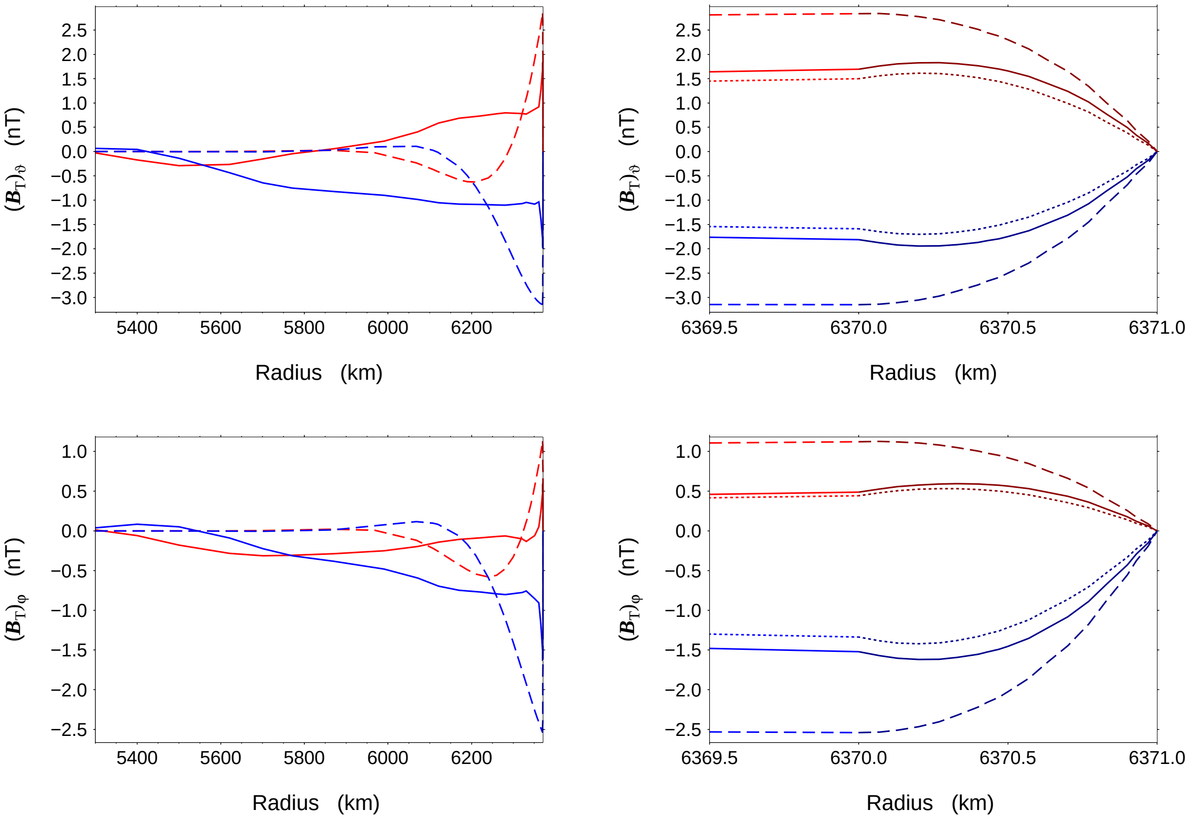

Figure 3.9: Real (red) and imaginary (blue) parts of the ϑ (top) and φ (bottom) components of the toroidal magnetic field (in nT) induced by depth decaying horizontal flow as functions of radius, beneath the ocean layer (left) and inside the ocean layer (right) for realistic (solid lines) and uniform ($\sigma_\mathrm{m} = 1$ Sm^{-1}, dashed lines) conductivity profile beneath the ocean and the realistic conductivity profile inside the ocean. The dotted lines in the detail for ocean layer represent the case for realistic solid Earth and uniform ocean conductivity ($\sigma_\mathrm{o} = 3.5$ Sm^{-1}). The radial profiles are taken at the location given by the yellow crosses in Figures 3.5 and 3.7.

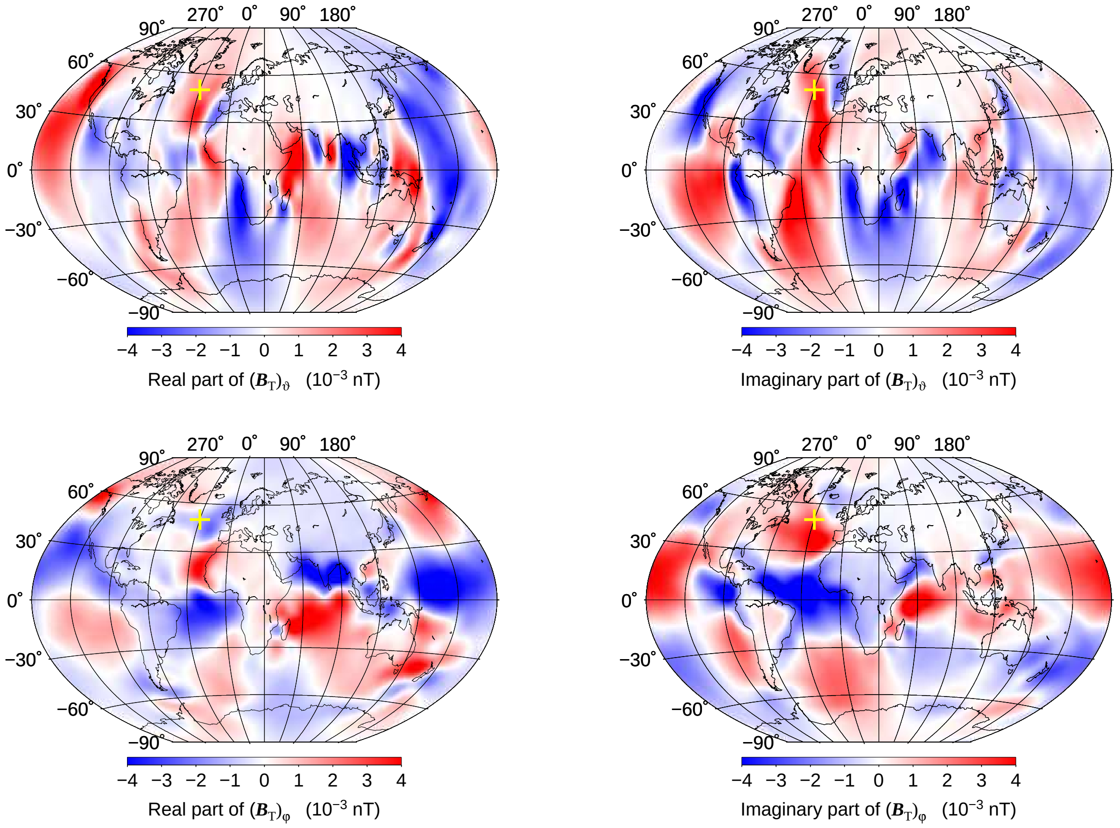

Figure 3.10: Real (left) and imaginary (right) parts of the ϑ (top) and φ (bottom) components of the toroidal magnetic field (in 10^{-3} nT) at the ocean bottom induced by over the depth constant tidal flow with the ocean layer of the depth of $h = 4$ km and the realistic electrical conductivity profile. The yellow crosses mark at 50° N, 30° W the location where the radial profiles of the toroidal magnetic field are plotted (see Figures 3.12).

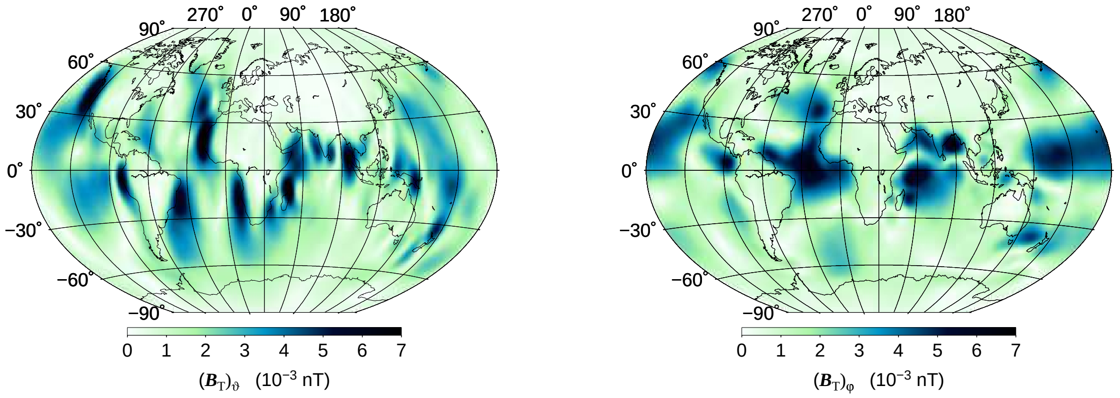

Figure 3.11: Amplitude of the ϑ (left) and φ (right) components of the toroidal magnetic field (in 10^{-3} nT) at the ocean bottom according to the magnetic field generated by condition in Figure 3.10.

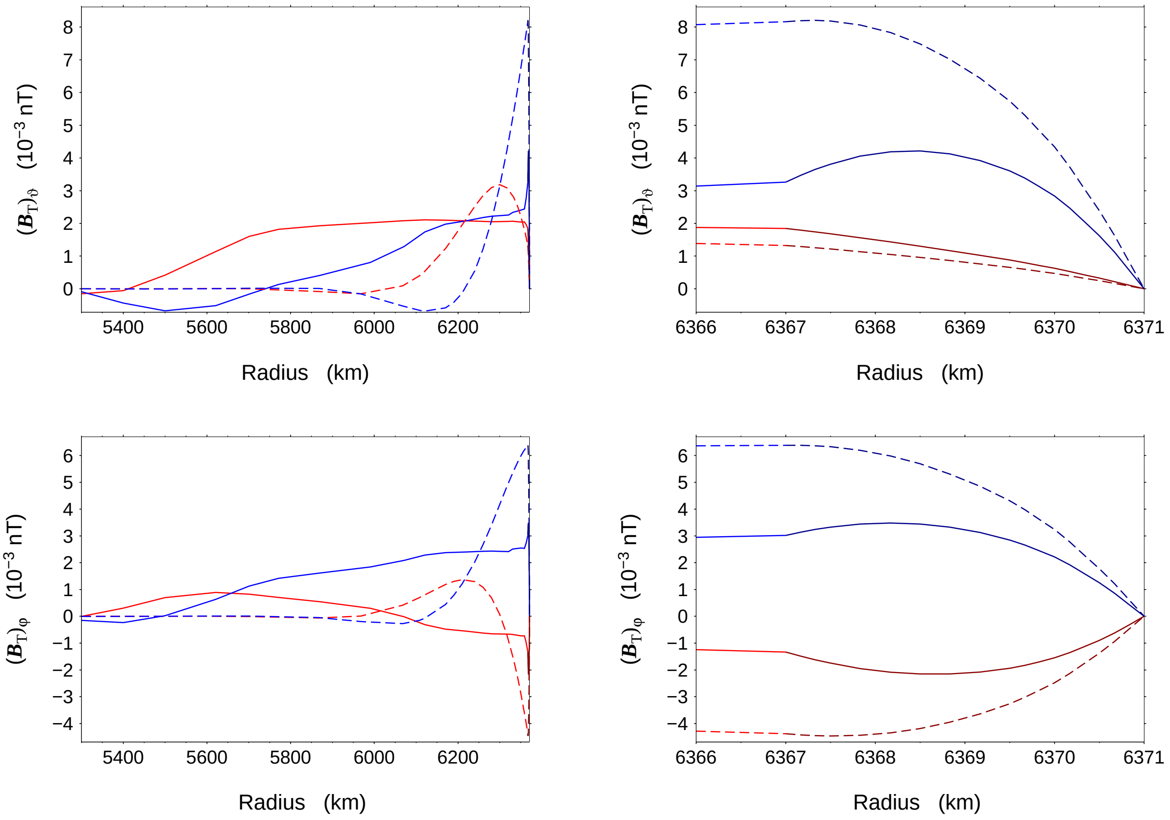

Figure 3.12: Real (red) and imaginary (blue) parts of the ϑ (top) and φ (bottom) components of the toroidal magnetic field (in 10^{-3} nT) induced by over the depth constant ocean flow as functions of radius, beneath (left) and inside (right) the ocean layer for realistic (solid lines) and uniform ($\sigma_\mathrm{m} = 1$ Sm^{-1}, dashed lines) conductivity profile beneath the ocean and realistic conductivity inside the ocean. The dotted lines in the detail for ocean layer represent the case for realistic solid Earth and uniform ocean conductivity ($\sigma_\mathrm{o} = 3.5$ Sm^{-1}). The radial profiles are taken at the location given by the yellow crosses in Figure 3.10.

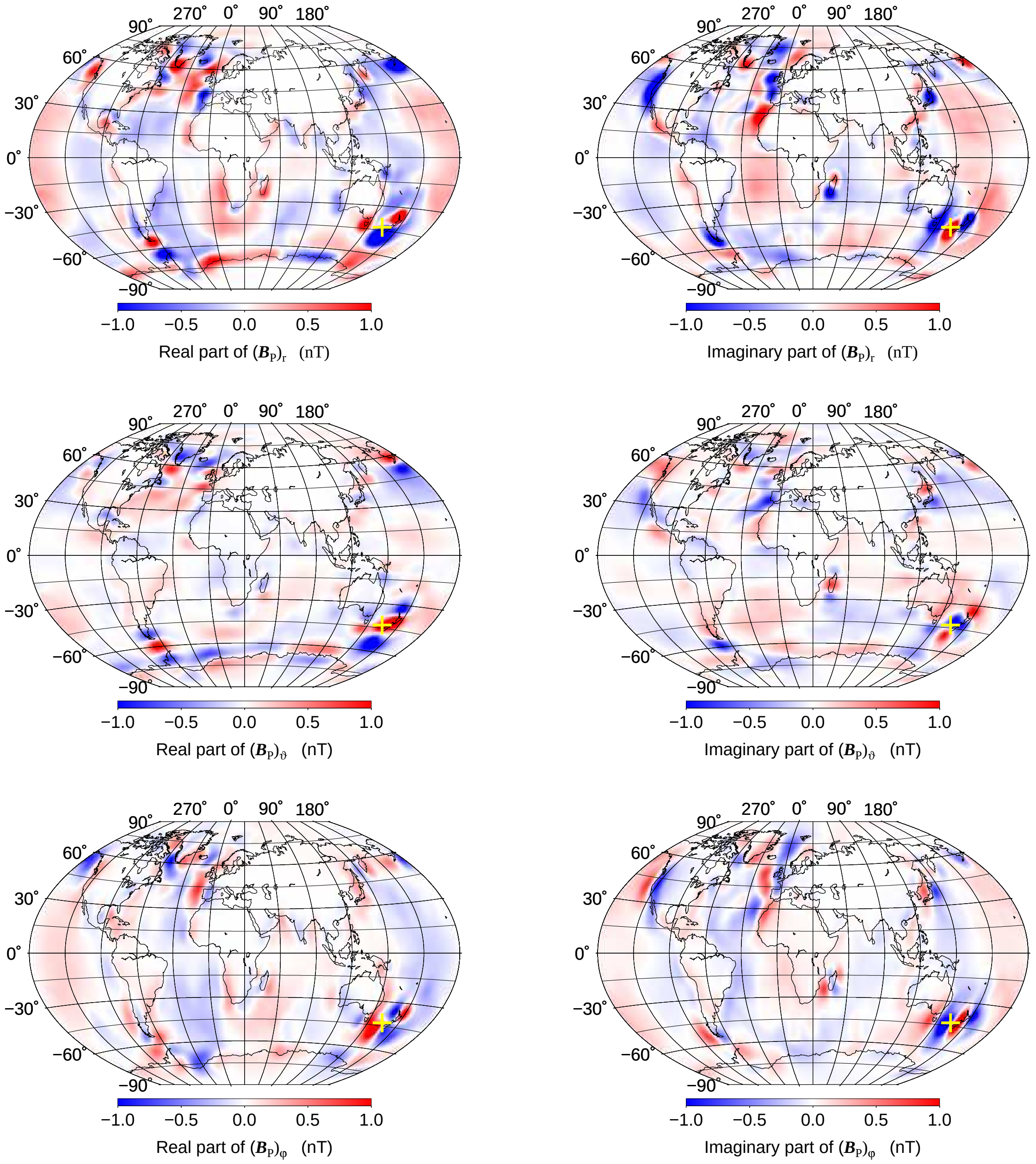

Figure 3.13: Real (left) and imaginary (right) parts of the r (top), ϑ (middle) and φ (bottom) components of the poloidal magnetic field (in nT) at top of the ocean induced by over the depth constant tidal flow with the ocean layer of the depth of $h = 4$ km, uniform electrical conductivity profile beneath ($\sigma_\mathrm{m} = 1\ \mathrm{Sm}^{-1}$) and inside ($\sigma_\mathrm{o} = 3.5\ \mathrm{Sm}^{-1}$) the ocean layer. The yellow crosses at 43° S, 164° E mark the location where the radial profiles of the poloidal magnetic field are plotted (see Figs. 4.13). Comparable result with variational method is shown in Figure 4.11.

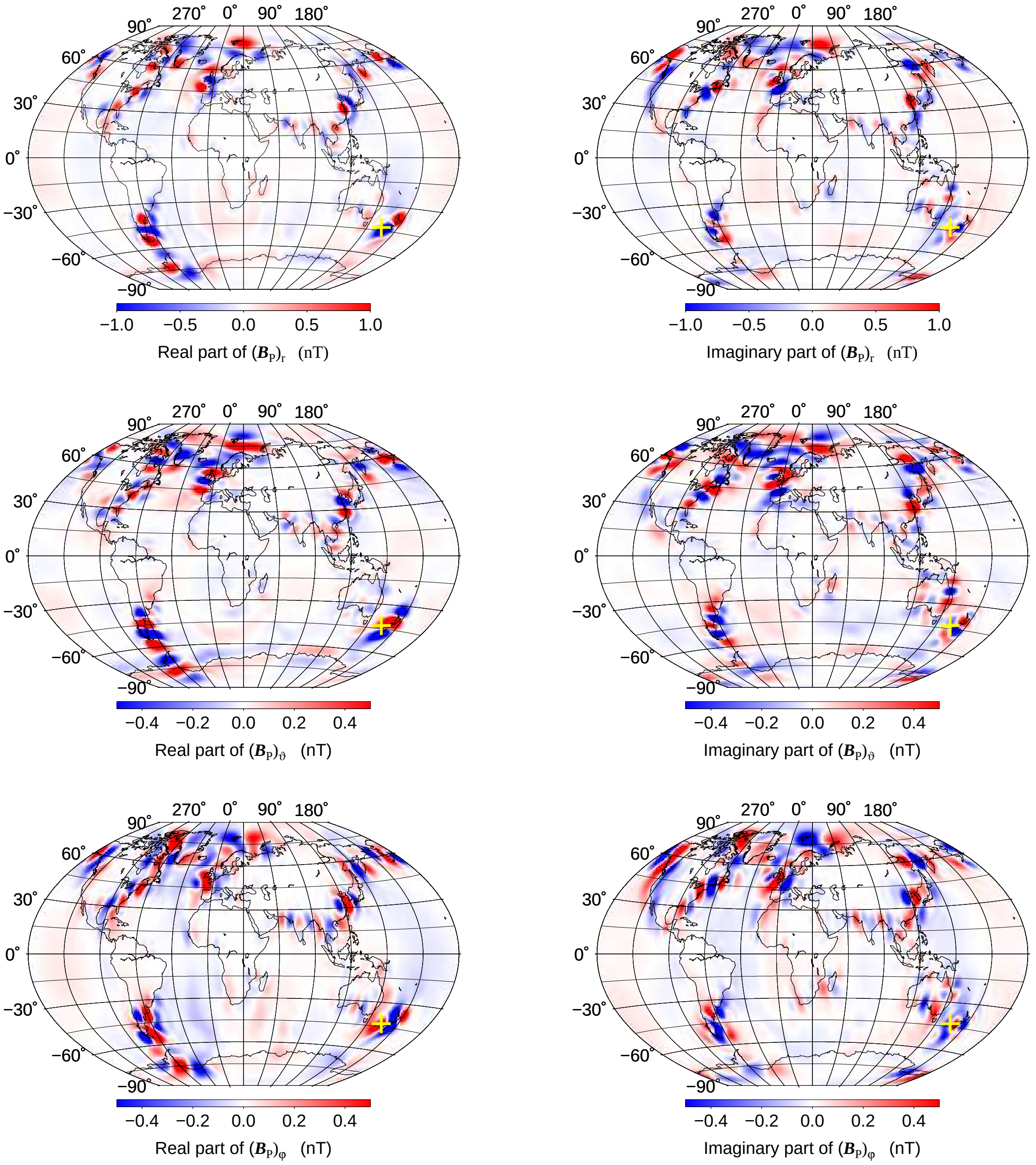

Figure 3.14: Real (left) and imaginary (right) parts of the r (top), ϑ (middle) and φ (bottom) components of the poloidal magnetic field (in nT) at top of the ocean induced by over the depth constant tidal flow with the ocean layer of the depth of $h = 1$ km, uniform electrical conductivity profile beneath ($\sigma_\mathrm{m} = 1$ Sm^{-1}) and inside ($\sigma_\mathrm{o} = 3.5$ Sm^{-1}) the ocean layer. The yellow crosses at 43° S, 164° E mark the location where the radial profiles of the poloidal magnetic field are plotted (see Figs. 4.19). Comparable result with variational method is shown in Figure 4.17.

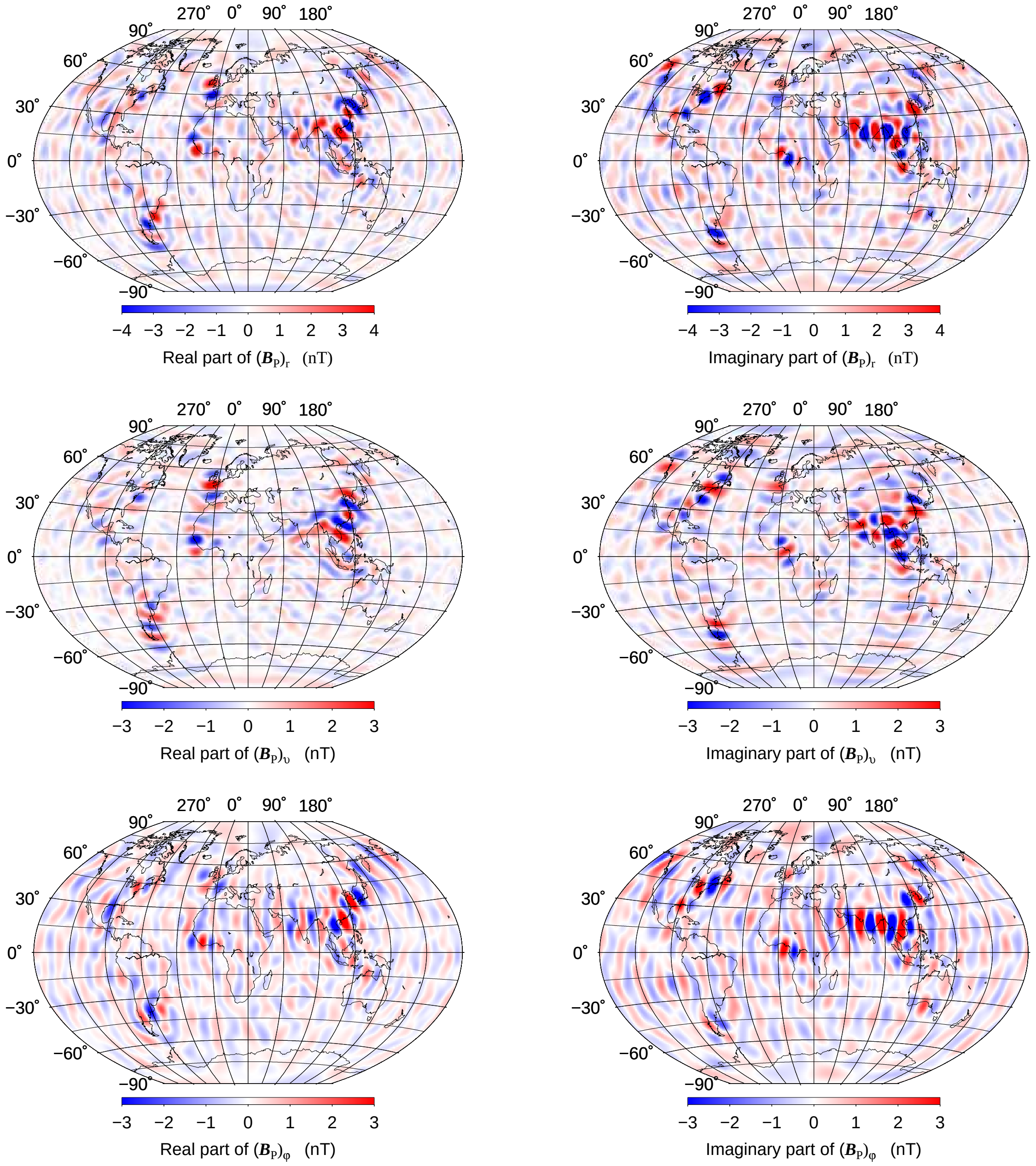

Figure 3.15: Real (left) and imaginary (right) parts of the r (top), ϑ (middle) and φ (bottom) components of the secondary poloidal magnetic field (in nT) at top of the ocean induced by over the depth constant tidal flow with the ocean layer of the depth of $h = 1$ km.

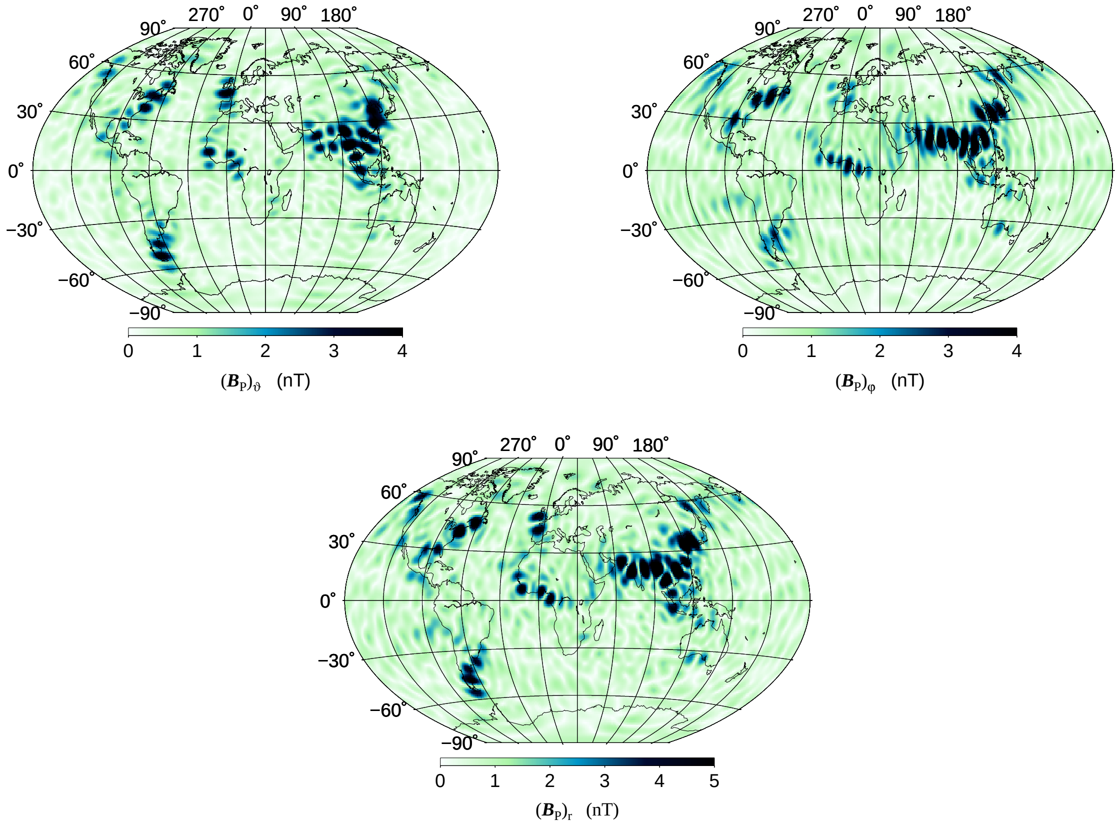

Figure 3.16: Amplitude of the ϑ (top left), φ (top right) and r (bottom) components of the secondary poloidal magnetic field (in nT) at top of the ocean according to the magnetic field induced by condition in Figure 3.15.

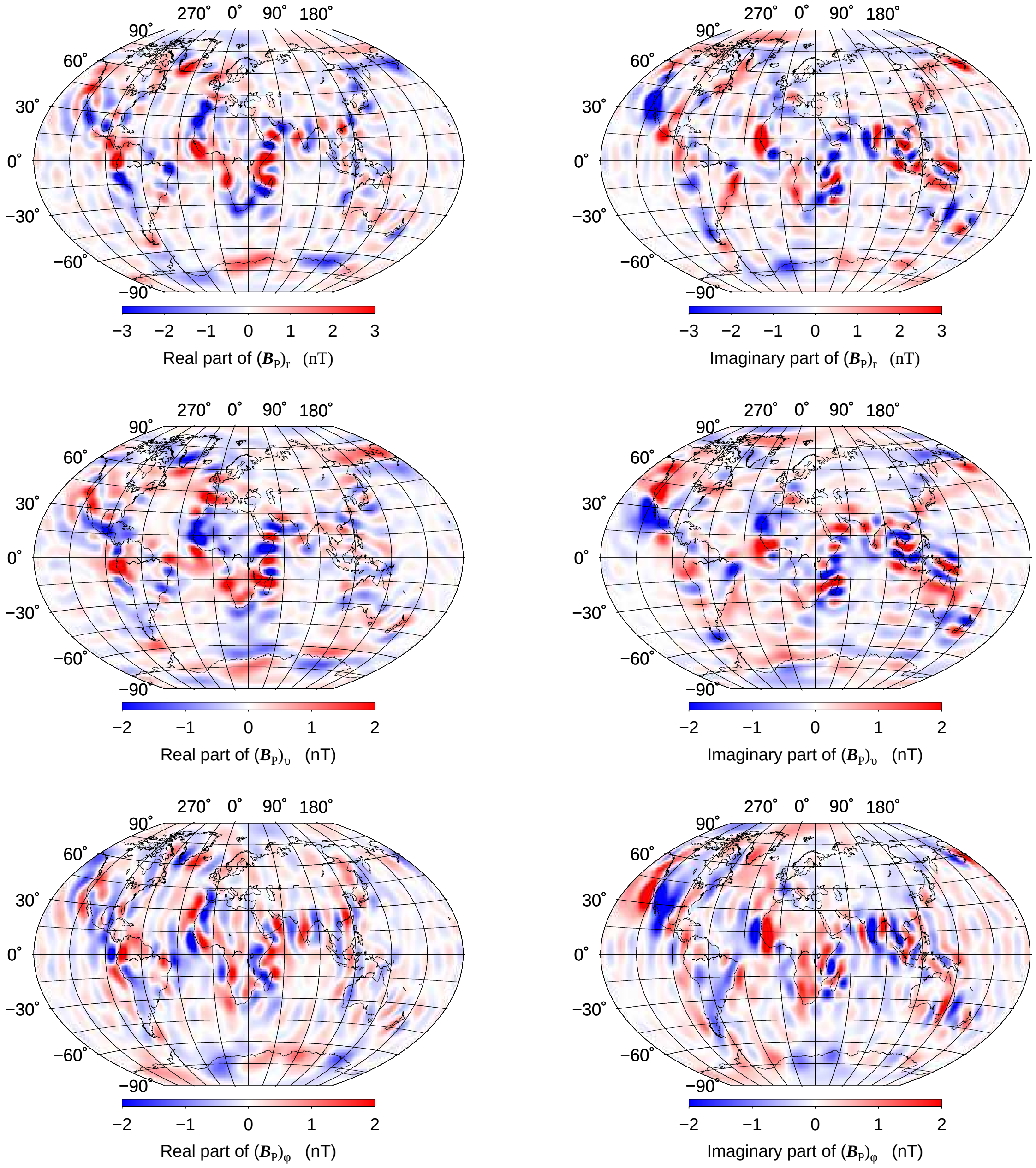

Figure 3.17: Real (left) and imaginary (right) parts of the r (top), ϑ (middle) and φ (bottom) components of the secondary poloidal magnetic field (in nT) at top of the ocean induced by over the depth constant tidal flow with the ocean layer of the depth of $h = 4$ km.

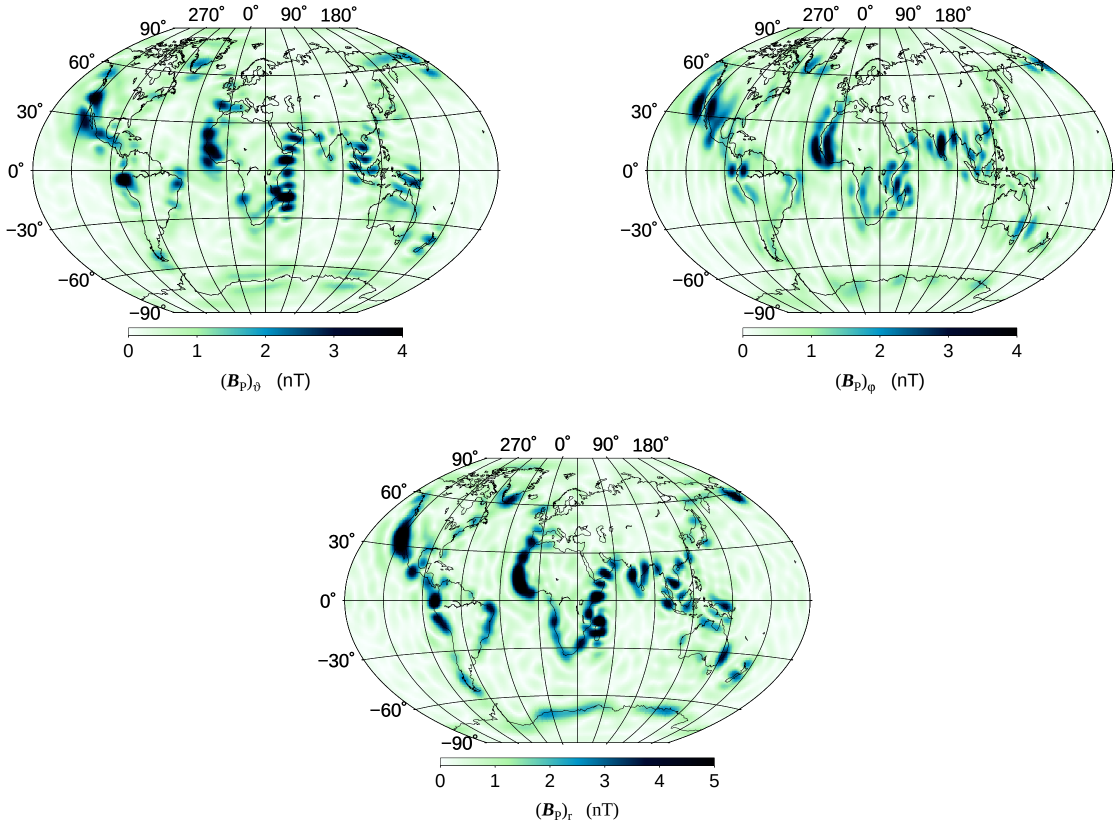

Figure 3.18: Amplitude of the ϑ (top left), φ (top right) and r (bottom) components of the secondary poloidal magnetic field (in nT) at top of the ocean according to the magnetic field induced by condition in Figure 3.17.

Chapter 4

Spectral finite-element approach for ocean-induced magnetic field in Fourier frequency domain

The numerical solution of the ocean-induced magnetic fields presented in this chapter is based on the spectral-finite element approach introduced by to Martinec (1997) and Martinec (1999). For the spherically symmetric model of electrical conductivity (subsection 2.6.3), the electromagnetic induction is formulated in variational (weak) sense. The induction equation is solved for both, the toroidal and poloidal modes of the magnetic field. The poloidal mode is, as in the previous chapter, solved in terms of toroidal magnetic potential $\boldsymbol{A}_\mathrm{T}$.

4.1 Weak formulation for toroidal magnetic field

Starting with the Earth's model approximated by an electric conductive sphere $\mathcal{G}$, the electromagnetic induction is governed by the magnetic diffusion (induction) equation (1.13). In the Fourier frequency domain, this equation is derived in section 1.2,

$$\frac{1}{\mu_0}\operatorname{curl}\left(\frac{1}{\sigma(r)}\operatorname{curl}\boldsymbol{B}_\mathrm{T}\right)+i\omega\boldsymbol{B}_\mathrm{T}=[\operatorname{curl}(\boldsymbol{u}\times\boldsymbol{B}_0)]_\mathrm{T}\,. \tag{4.1}$$

For the toroidal mode, the magnetic field is confined to sphere $\mathcal{G}$ and, therefore, it vanishes on the Earth surface $\partial\mathcal{G}$,

$$\boldsymbol{B}_\mathrm{T}=\boldsymbol{0}\qquad\qquad\text{on }\partial\mathcal{G}\,. \tag{4.2}$$

Let us introduce the functional space

$$\mathcal{V}:=\{\boldsymbol{B}_\mathrm{T}|\boldsymbol{B}_\mathrm{T}\in\mathcal{L}_2(\mathcal{G}),\operatorname{curl}\boldsymbol{B}_\mathrm{T}\in\mathcal{L}_2(\mathcal{G})\}\,, \tag{4.3}$$

where the $\mathcal{L}_2(\mathcal{G})$ is the space of square integrable functions in $\mathcal{G}$. Additionally, we introduce so called test functions $\delta\boldsymbol{B}_\mathrm{T}$ that belongs to the same functional space as $\boldsymbol{B}_\mathrm{T}$, $\delta\boldsymbol{B}_\mathrm{T}\in\mathcal{V}$. For function from the space $\mathcal{V}$, we introduce the energy functionals of the forms

$$\mathscr{A}(\boldsymbol{B},\delta\boldsymbol{B}):=\frac{1}{\mu_0}\int_\mathcal{G}\frac{1}{\sigma}(\operatorname{curl}\boldsymbol{B}\cdot\operatorname{curl}\delta\boldsymbol{B})\,dV \tag{4.4}$$

$$\mathscr{B}(\boldsymbol{B},\delta\boldsymbol{B}):=\int_\mathcal{G}\left(\frac{\partial\boldsymbol{B}}{\partial t}\cdot\delta\boldsymbol{B}\right)dV \tag{4.5}$$

and the forcing functional

$$\mathscr{F}(\delta \boldsymbol{B}) := \int_{\mathcal{G}_{\mathrm{O}}} \operatorname{curl}(\boldsymbol{u} \times \boldsymbol{B}_E) \cdot \delta \boldsymbol{B} \, dV \; . \tag{4.6}$$

The forcing functional $\mathscr{F}$ is associated with the source term in the ocean layer $\mathcal{G}_{\mathrm{O}}$. The medium beneath the ocean layer is source free. The magnetic diffusion equation is homogeneous and

$$\mathscr{F}(\delta \boldsymbol{B}) := 0 \; . \tag{4.7}$$

The weak formulation consists of finding $\boldsymbol{B}_{\mathrm{T}} \in \mathcal{V}$ such that for any test-functions $\delta \boldsymbol{B}_{\mathrm{T}} \in \mathcal{V}$, the variational equality

$$\mathscr{A}(\boldsymbol{B}_{\mathrm{T}}, \delta \boldsymbol{B}_{\mathrm{T}}) + \mathscr{B}(\boldsymbol{B}_{\mathrm{T}}, \delta \boldsymbol{B}_{\mathrm{T}}) = \mathscr{F}(\delta \boldsymbol{B}_{\mathrm{T}}) \tag{4.8}$$

is satisfied.

To show the **equivalence** of the weak solution with the strong solution for sufficiently smooth functions, we use **Green's theorem**. According to this theorem (Křížek and Neittaanmäki (1990), Theorem 2.8), if Ω_0 is bounded domain with Lipschitz boundary $\partial\Omega_0$ and $v, w \in \mathcal{W}_2^1(\Omega)$ and $v, w \in \mathcal{L}_2(\partial\Omega)$, the following identity holds (Green's identity):

$$\int_{\Omega_0} \frac{\partial v}{\partial x_j} \, w \, dV + \int_{\Omega_0} v \, \frac{\partial w}{\partial x_j} \, dV = \int_{\partial\Omega_0} v \, w \, n_j \, dS \; . \tag{4.9}$$

In particular, for

$$v = (\operatorname{curl} \boldsymbol{U})_k \tag{4.10}$$

$$w = V_i \tag{4.11}$$

Green's theorem takes the form

$$\int_{\Omega_0} \frac{\partial (\operatorname{curl} \boldsymbol{U})_k}{\partial x_j} \, V_i \, dV - \int_{\Omega_0} (\operatorname{curl} \boldsymbol{U})_k \, \frac{\partial V_i}{\partial x_j} \, dV = \int_{\partial\Omega_0} (\operatorname{curl} \boldsymbol{U})_k \, V_i \, n_j \, dS \; . \tag{4.12}$$

Multiplying this equation by Levi-Civita symbol ε_{ijk} and summing up over all indices i, j, k, we obtain

$$\int_{\Omega_0} [\operatorname{curl}(\operatorname{curl} \boldsymbol{U})]_i \; V_i \, dV - \int_{\Omega_0} (\operatorname{curl} \boldsymbol{U})_k \; (\operatorname{curl} \boldsymbol{V})_k \, dV = \int_{\partial\Omega_0} (\boldsymbol{n} \times \operatorname{curl} \boldsymbol{U})_i \, V_i \, dS \; , \tag{4.13}$$

or,

$$\int_{\Omega_0} \operatorname{curl} \operatorname{curl} \boldsymbol{U} \; \boldsymbol{V} \, dV - \int_{\Omega_0} \operatorname{curl} \boldsymbol{U} \; \operatorname{curl} \boldsymbol{V} \, dV = \int_{\partial\Omega_0} (\boldsymbol{n} \times \operatorname{curl} \boldsymbol{U}) \, \boldsymbol{V} \, dS \; . \tag{4.14}$$

Using Green's theorem in equation (4.8), we have

$$\begin{aligned} &\frac{1}{\mu_0} \int_{\mathcal{G}} \operatorname{curl} \left(\frac{1}{\sigma} \operatorname{curl} \boldsymbol{B} \right) \cdot \delta \boldsymbol{B} \, dV + \frac{1}{\mu_0} \int_{\partial\mathcal{G}} \frac{1}{\sigma} \operatorname{curl} \boldsymbol{B} \cdot (\boldsymbol{n} \times \delta \boldsymbol{B}) \, dS + \int_{\mathcal{G}} \left(\frac{\partial \boldsymbol{B}}{\partial t} \cdot \delta \boldsymbol{B} \right) dV \\ &= \int_{\mathcal{G}} \operatorname{curl}(\boldsymbol{u} \times \boldsymbol{B}) \cdot \delta \boldsymbol{B} \, dV \; . \end{aligned} \tag{4.15}$$

Then the volume integrals yield

$$\frac{1}{\mu_0} \operatorname{curl} \left(\frac{1}{\sigma} \operatorname{curl} \boldsymbol{B} \right) + \frac{\partial \boldsymbol{B}}{\partial t} = \operatorname{curl}(\boldsymbol{u} \times \boldsymbol{B}_0) \qquad \text{in } \mathcal{G} \; . \tag{4.16}$$

Moreover, we consider the relation

$$\boldsymbol{a} \cdot (\boldsymbol{b} \times \boldsymbol{c}) = \boldsymbol{b} \cdot (\boldsymbol{c} \times \boldsymbol{a}) = \boldsymbol{c} \cdot (\boldsymbol{a} \times \boldsymbol{b}) \tag{4.17}$$

and equation (3.4)

$$\boldsymbol{E}_{\mathrm{S}} = \frac{1}{\mu_0 \sigma} \operatorname{curl} \boldsymbol{B}_{\mathrm{T}} \ . \tag{4.18}$$

The integrand of the surface integral in eq. (4.15) takes the form

$$\frac{1}{\mu_0 \sigma} \operatorname{curl} \boldsymbol{B}_{\mathrm{T}} \cdot (\boldsymbol{e}_r \times \delta \boldsymbol{B}_{\mathrm{T}}) = \boldsymbol{E}_{\mathrm{S}} \cdot (\boldsymbol{e}_r \times \delta \boldsymbol{B}_{\mathrm{T}}) = \boldsymbol{\delta B_{\mathrm{T}}} \cdot (\boldsymbol{e}_r \times \boldsymbol{E}_{\mathrm{S}}) \ . \tag{4.19}$$

The definition of the solution space contains the condition $\boldsymbol{B}_{\mathrm{T}} = \boldsymbol{0}$ on $\partial \mathcal{G}$ (eq. 4.2). Hence, the surface integrand in eq. (4.15) is equal to zero, and the weak formulation is equivalent to the strong solution.

4.1.1 Spherical harmonics parametrization over angular coordinates

We parametrize $\boldsymbol{B}$ and $\delta \boldsymbol{B}$ in lateral direction $\Omega = (\vartheta, \varphi)$ by vector spherical harmonics. The spherical harmonic representation (D.10) of the toroidal magnetic field takes the form

$$\left\{ \begin{array}{c} \boldsymbol{B}_{\mathrm{T}}(r, \Omega) \\ \delta \boldsymbol{B}_{\mathrm{T}}(r, \Omega) \end{array} \right\} = \sum_{j=1}^{\infty} \sum_{m=-j}^{j} \left\{ \begin{array}{c} B^j_{jm}(r) \\ \delta B^j_{jm}(r) \end{array} \right\} \boldsymbol{Y}^j_{jm}(\Omega) \ . \tag{4.20}$$

We introduce

$$R^{j+1}_{jm}(r) = i \sqrt{\frac{j}{2j+1}} \left(\frac{d}{dr} - \frac{j}{r} \right) B^j_{jm}(r) \ , \tag{4.21}$$

$$R^{j-1}_{jm}(r) = i \sqrt{\frac{j+1}{2j+1}} \left(\frac{d}{dr} + \frac{j+1}{r} \right) B^j_{jm}(r) \ , \tag{4.22}$$

then for toroidal field B^j_{jm}

$$\operatorname{curl} B^j_{jm}(r) \, \boldsymbol{Y}^j_{jm}(\Omega) = R^{j+1}_{jm}(r) \, \boldsymbol{Y}^{j+1}_{jm}(\Omega) + R^{j-1}_{jm}(r) \, \boldsymbol{Y}^{j-1}_{jm}(\Omega) \tag{4.23}$$

which results in the expression

$$\begin{aligned} \operatorname{curl} \boldsymbol{B}_{\mathrm{T}}(r) \cdot \operatorname{curl} \delta \boldsymbol{B}_{\mathrm{T}}(r) = & \sum_{j_1=1}^{\infty} \sum_{m_1=-j_1}^{j_1} \sum_{\ell=j_1-1}^{j_1+1,2} R^{\ell_1}_{j_1 m_1}(r) \, \boldsymbol{Y}^{\ell_1}_{j_1 m_1}(\Omega) \\ & \times \sum_{j_2=1}^{\infty} \sum_{m_2=-j_2}^{j_2} \sum_{\ell_2=j_1-1}^{j_2+1,2} \delta R^{\ell_2}_{j_2 m_2}(r) \, \boldsymbol{Y}^{\ell_2}_{j_2 m_2}(\Omega) \ . \end{aligned} \tag{4.24}$$

The relation for complex conjugate of spheroidal vector spherical harmonics (eq. D.21) is

$$\boldsymbol{Y}^{j \pm 1 \, *}_{jm}(\Omega) = (-1)^m \, \boldsymbol{Y}^{j \pm 1}_{j-m}(\Omega) \ . \tag{4.25}$$

Furthermore, we make use of the orthonormality property (eq. D.20) and write for $\ell = j - 1$ and $\ell = j + 1$

$$\int_{\Omega_0} \boldsymbol{Y}^{\ell_1 \, *}_{j_1 m_1}(\Omega) \, \boldsymbol{Y}^{\ell_2}_{j_2 m_2}(\Omega) \, d\Omega = \int_{\Omega_0} (-1)^{m_1} \, \boldsymbol{Y}^{\ell_1}_{j_1 -m_1}(\Omega) \, \boldsymbol{Y}^{\ell_2}_{j_2 m_2}(\Omega) \, d\Omega = \delta_{j_1 j_2} \delta_{m_1 m_2} \delta_{\ell_1 \ell_2} \ . \tag{4.26}$$

Then the $\mathscr{A}$ functional (eq. 4.4) takes the form

$$\mathscr{A}(\boldsymbol{B}_\mathrm{T}, \delta\boldsymbol{B}_\mathrm{T}) = \frac{1}{\mu_0} \int_{r=0}^{a} \frac{1}{\sigma(r)} \int_{\Omega_0} \sum_{j_1=1}^{\infty} \sum_{m_1=-j_1}^{j_1} \sum_{\ell_1=j_1-1}^{j_1+1,2} R^{\ell_1}_{j_1 m_1}(r)\, \boldsymbol{Y}^{\ell_1}_{j_1 m_1}(\Omega)$$
$$\times \sum_{j_2=1}^{\infty} \sum_{m_2=-j_2}^{j_2} \sum_{\ell_2=j_2-1}^{j_2+1,2} \delta R^{\ell_2}_{j_2 m_2}(r)\, \boldsymbol{Y}^{\ell_2}_{j_2 m_2}(\Omega)\, d\Omega\, r^2\, dr \tag{4.27}$$

and after applying the orthonormality properties of vector spherical harmonics, the last equation leads to the final form

$$\boxed{\mathscr{A}(\boldsymbol{B}_\mathrm{T}, \delta\boldsymbol{B}_\mathrm{T}) = \frac{1}{\mu_0} \sum_{j=1}^{\infty} \sum_{m=-j}^{j} (-1)^m \sum_{\ell=j-1}^{j+1,2} \int_{r=0}^{a} \frac{1}{\sigma(r)} R^{\ell}_{j-m}(\boldsymbol{B}_\mathrm{T}, r) R^{\ell}_{jm}(\delta\boldsymbol{B}_\mathrm{T}, r)\, r^2\, dr} \; . \tag{4.28}$$

The complex conjugate of the toroidal vector spherical harmonics (eq. D.21) is

$$\boldsymbol{Y}^{j\,*}_{jm}(\Omega) = (-1)^{m+1}\, \boldsymbol{Y}^{j}_{j-m}(\Omega) \tag{4.29}$$

and with the use of the orthonormality property of the vector spherical harmonics (eq. D.20) for the toroidal case

$$\int_{\Omega_0} \boldsymbol{Y}^{j_1\,*}_{j_1 m_1}(\Omega)\, \boldsymbol{Y}^{j_2}_{j_2 m_2}(\Omega)\, d\Omega = \int_{\Omega_0} (-1)^{m_1+1}\, \boldsymbol{Y}^{j_1}_{j_1 -m_1}(\Omega)\, \boldsymbol{Y}^{j_2}_{j_2 m_2}(\Omega)\, d\Omega = \delta_{j_1 j_2} \delta_{m_1 m_2} \; . \tag{4.30}$$

Hence, equation (4.5) reads as

$$\boxed{\mathscr{B}(\boldsymbol{B}_\mathrm{T}, \delta\boldsymbol{B}_\mathrm{T}) = -i\omega \sum_{j=1}^{\infty} \sum_{m=-j}^{j} (-1)^{m+1} \int_{r=0}^{a} B^{j}_{j-m}(r)\, \delta B^{j}_{jm}(r)\, r^2\, dr} \; . \tag{4.31}$$

Analogous for $\boldsymbol{F} = \mathrm{curl}(\boldsymbol{u} \times \boldsymbol{B}_\mathrm{E})$ from equation (2.1) represented in form of eq. (3.5) we write for the right hand side (eq. 4.6)

$$\mathscr{F}(\delta\boldsymbol{B}_\mathrm{T}) = \int_{\mathcal{G}_\mathrm{O}} \boldsymbol{F} \cdot \delta\boldsymbol{B}_\mathrm{T}\, dV \; . \tag{4.32}$$

Setting b for the radius at bottom of the ocean layer, we have

$$\boxed{\mathscr{F}(\delta\boldsymbol{B}_\mathrm{T}) = -\sum_{j=1}^{\infty} \sum_{m=-j}^{j} (-1)^{m+1} \int_{r=b}^{a} F^{j}_{j-m}(r)\, \delta B^{j}_{jm}(r)\, r^2\, dr} \; . \tag{4.33}$$

4.1.2 Finite-element approximation in radial coordinate

In radial direction, the sphere is divided in arbitrary spaced sub-intervals by nodes $0 = r_1 < r_2 < \ldots < r_{P+1} < r_P < r_{P+1} = a$. The piecewise linear basis functions (finite elements) $\psi_k(r_i) = \delta_{k,i}$ can be used as the basis functions of the Sobolev functional space $\mathcal{W}^1_2(0,a)$ (Křížek and Neittaanmäki, 1990). Thus, on a given interval between two nodes $r_k \le r \le r_{k+1}$, only two basis functions are non-zero,

$$\psi_k(r) = \frac{r_{k+1} - r}{h_k} \; , \qquad \psi_{k+1}(r) = \frac{r - r_k}{h_k} \; , \tag{4.34}$$

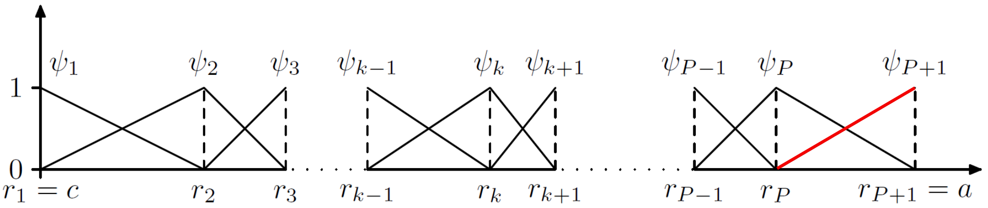

Figure 4.1: Piecewise linear finite elements that span the interval $[0, a]$. On each sub-interval $[r_k, r_{k+1}]$ only the two base functions ψ_k and ψ_{k+1} are non-zero. In the case of the toroidal magnetic field the basis function ψ_{P+1} is zero due to condition given by eq. (4.2) . Therefore, the basis function ψ_{P+1} (marked by red) is non-zero only by poloidal magnetic field. Figure courteously taken from Tosi (2007).

where $h_k := r_{k+1} - r_k$. A scheme of the piecewise-linear finite elements are shown in Figure 4.1. The solution for $\boldsymbol{B}^j_{jm}(r)$ and the test function $\delta\boldsymbol{B}^j_{jm}(r)$ are elements of the Sobolev space $\mathcal{W}^1_2(0, a)$. Therefore, they will be approximated by a linear combination of the basis functions $\psi_k(r)$,

$$\left\{ \begin{array}{c} B^j_{jm}(r) \\ \delta B^j_{jm}(r) \end{array} \right\} = \sum_{k=1}^{P} \left\{ \begin{array}{c} B^{j,k}_{jm} \\ \delta B^{j,k}_{jm} \end{array} \right\} \psi_k(r) \; . \tag{4.35}$$

Considering the Dirichlet boundary condition given by eq. (4.2) in toroidal case the function $\psi_{P+1}(a)$ is omitted from the functional space $\mathcal{W}^1_2(0, a)$. Therefore, the upper limit of the summation in equation (4.36) is set by P. We now use the finite elements parametrization to approximate the weak formulation in the radial direction. First we express the functional $\mathscr{B}$, see eq. (4.32), in the finite-element parametrization

$$\begin{aligned} &\int_{r=0}^{a} B^j_{j-m}(r)\, \delta B^j_{jm}(r)\, r^2\, dr \\ &\quad = \sum_{k=1}^{P} \int_{r_k}^{r_{k+1}} \Big(B^{\ell,k}_{j-m}\, \psi_k(r) + B^{\ell,k+1}_{j-m}\, \psi_{k+1}(r) \Big) \Big(\delta B^{\ell,k}_{jm}\, \psi_k(r) + \delta B^{\ell,k+1}_{jm}\, \psi_{k+1}(r) \Big)\, r^2\, dr \\ &\quad = \sum_{k=1}^{P} \Big(I^{(1)}_k B^{\ell,k}_{j-m}\, \delta B^{\ell,k}_{jm} + I^{(2)}_k B^{\ell,k}_{j-m}\, \delta B^{\ell,k+1}_{jm} + I^{(2)}_k\, B^{\ell,k+1}_{j-m}\, \delta B^{\ell,k}_{jm} + I^{(3)}_k B^{\ell,k+1}_{j-m}\, \delta B^{\ell,k+1}_{jm} \Big) \; , \end{aligned} \tag{4.36}$$

with $B^{\ell,P+1}_{jm} = 0$ and $\delta B^{\ell,P+1}_{jm} = 0$, and where we introduced the following integrals

$$\begin{aligned} I^{(1)}_k &:= \int_{r_k}^{r_{k+1}} \psi_k\,(r)\psi_k(r)\, r^2\, dr = \frac{h_k}{30}\,(r^2_{k+1} + 3r_k r_{k+1} + 6r^2_k) \; , \\ I^{(2)}_k &:= \int_{r_k}^{r_{k+1}} \psi_k\,(r)\psi_{k+1}(r)\, r^2\, dr = \frac{h_k}{60}\,(3r^2_{k+1} + 4r_k r_{k+1} + 3r^2_k) \; , \\ I^{(3)}_k &:= \int_{r_k}^{r_{k+1}} \psi_{k+1}\,(r)\psi_{k+1}(r)\, r^2\, dr = \frac{h_k}{30}\,(6r^2_{k+1} + 3r_k r_{k+1} + r^2_k) \; . \end{aligned} \tag{4.37}$$

Then the functional $\mathscr{B}$ takes the form

$$\begin{aligned} \mathscr{B}(\boldsymbol{B}_{\mathrm{T}}, \delta\boldsymbol{B}_{\mathrm{T}}) = -i\omega \sum_{j=1}^{\infty} \sum_{m=-j}^{j} (-1)^{m+1} \sum_{k=1}^{P} \Big(& I^{(1)}_k B^{\ell,k}_{j-m}\, \delta B^{\ell,k}_{jm} + I^{(2)}_k B^{\ell,k}_{j-m}\, \delta B^{\ell,k+1}_{jm} \\ & + I^{(2)}_k\, B^{\ell,k+1}_{j-m}\, \delta B^{\ell,k}_{jm} + I^{(3)}_k B^{\ell,k+1}_{j-m}\, \delta B^{\ell,k+1}_{jm} \Big) \; . \end{aligned} \tag{4.38}$$

Second, we express the functional $\mathscr{A}$, see eq. (4.29), in finite-element parametrization. For the interval $r_k \leq r \leq r_{k+1}$, we have

$$\frac{d}{dr}\psi_k(r) = \frac{d}{dr}\left(\frac{r_{k+1}-r}{h_k}\right) = -\frac{1}{h_k} \ , \tag{4.39}$$

$$\frac{d}{dr}\psi_{k+1}(r) = \frac{d}{dr}\left(\frac{r-r_k}{h_k}\right) = \frac{1}{h_k} \ . \tag{4.40}$$

The rotation of toroidal field is defined by equation (D.33). In the finite-element parametrization we can write

$$\mathcal{R}^{j-1}_{jm}(\boldsymbol{B}_{\mathrm{T}}, r) = i\sqrt{\frac{j+1}{2j+1}}\left[\left(-\frac{1}{h_k} + \frac{j+1}{r}\psi_k(r)\right) B^{j,k}_{jm} + \left(\frac{1}{h_k} + \frac{j+1}{r}\psi_{k+1}(r)\right) B^{j,k+1}_{jm}\right] \ , \tag{4.41}$$

$$\mathcal{R}^{j+1}_{jm}(\boldsymbol{B}_{\mathrm{T}}, r) = i\sqrt{\frac{j}{2j+1}}\left[\left(-\frac{1}{h_k} - \frac{j}{r}\psi_k(r)\right) B^{j,k}_{jm} + \left(\frac{1}{h_k} - \frac{j}{r}\psi_{k+1}(r)\right) B^{j,k+1}_{jm}\right] \ . \tag{4.42}$$

Finally,

$$\mathscr{A}(\boldsymbol{B}_{\mathrm{T}}, \delta\boldsymbol{B}_{\mathrm{T}}) = \frac{1}{\mu_0}\sum_{j=1}^{\infty}\sum_{m=-j}^{j}(-1)^m \sum_{\ell=j-1}^{j+1,2}\sum_{k=1}^{P}\frac{1}{\sigma_k}\int_{r_k}^{r_{k+1}} \mathcal{R}^{\ell}_{j-m}(\boldsymbol{B}_{\mathrm{T}}, r)\, \mathcal{R}^{\ell}_{jm}(\delta\boldsymbol{B}_{\mathrm{T}}, r)\, r^2\, dr \ . \tag{4.43}$$

Since electrical conductivity $\sigma(r) \in \mathcal{L}_2(\mathcal{G})$, the radial dependence of σ can be approximated by piecewise constant functions $\sigma(r) = \sigma_k$ with $r_k < r < r_{k+1}$. As $\sigma(r)$ does not vary with respect to r on each sub-interval $r_k < r < r_{k+1}$, the integration reduces to the computation of the type

$$\int_{r_k}^{r_{k+1}} \psi_i\,(r)\psi_j(r)\, r^2\, dr \ , \tag{4.44}$$

where i and j are equal to k and/or $k+1$. This integral can be evaluated analytically or numerically, for example, by means of the Gauss-Legendre numerical quadrature with the weights equal to 1 and the nodes $x_{1,2} = \pm 1/\sqrt{3}$ (Press et al., 1993),

$$\int_{r_k}^{r_{k+1}} \mathcal{R}^{\ell}_{jm}(\boldsymbol{B}, r)\, r^2\, dr = \sum_{\alpha=1}^{2}\mathcal{R}^{\ell}_{jm}(\boldsymbol{B}, r_\alpha)\,\frac{r_\alpha^2\, h_k}{2} \ , \tag{4.45}$$

where

$$r_\alpha = \frac{1}{2}(h_k x_\alpha + r_k + r_{k+1}) \ , \qquad \alpha = 1, 2 \ . \tag{4.46}$$

4.2 Finite-element, spherical harmonic parametrization of the toroidal source term

In this section we parametrize the toroidal source term $\boldsymbol{F}$ in terms of finite elements and spherical harmonics. The source term $\boldsymbol{F} = \mathrm{curl}(\boldsymbol{u} \times \boldsymbol{B}_{\mathrm{E}})$ is used in the weak formulation in equation (4.6)

$$\mathscr{F}(\delta\boldsymbol{B}) := \int_{\mathcal{G}_{\mathrm{O}}} \boldsymbol{F}\cdot\delta\boldsymbol{B}\, dV \ . \tag{4.47}$$

We recall the toroidal part of the source term by equation 2.3,

$$\boldsymbol{F}_{\mathrm{T}}(r, \Omega) = \sum_{jm} F^{j}_{jm}(r)\, \boldsymbol{Y}^{j}_{jm}(\Omega), \tag{4.48}$$

where

$$F^j_{jm}(r) = {}^{(1)}F^j_{jm}\left(\frac{r}{a}\right)^j + {}^{(2)}F^j_{jm}\left(\frac{a}{r}\right)^{j+1} . \tag{4.49}$$

We separate the integral over the ocean layer ($\mathcal{G}_\mathrm{O}$) in lateral (Ω) and radial ($b \le r \le a$) directions, where b stand for the ocean bottom, and write for the toroidal part of $\mathscr{F}(\delta\boldsymbol{B}_\mathrm{T})$,

$$\mathscr{F}(\delta\boldsymbol{B}_\mathrm{T}) = \int_{r=b}^{a}\int_{\Omega_0} \boldsymbol{F}_\mathrm{T}(r,\Omega)\cdot\delta\boldsymbol{B}_\mathrm{T}\; d\Omega\; r^2\; dr\; . \tag{4.50}$$

The test function $\delta\boldsymbol{B}_\mathrm{T}$ is parametrized according equation (4.20) and we write

$$\mathscr{F}(\delta\boldsymbol{B}_\mathrm{T}) = \int_{r=b}^{a}\int_{\Omega_0} \sum_{\substack{j_1\, m_1\\ j_2\, m_2}} F^{j_1}_{j_1,m_1}(r)\; \boldsymbol{Y}^{j_1}_{j_1,m_1}(\Omega)\cdot\delta B^{j_2}_{j_2,m_2}(r)\; \boldsymbol{Y}^{j_2}_{j_2,m_2}(\Omega)\; d\Omega\; r^2\; dr\; . \tag{4.51}$$

By the relation for complex conjugation of $\boldsymbol{Y}^j_{jm}(\Omega)$ (eq. 4.30) and the orthonormality property of $\boldsymbol{Y}^j_{jm}(\Omega)$ (eq. 4.31), we obtain

$$\mathscr{F}(\delta\boldsymbol{B}_\mathrm{T}) = \sum_{jm}(-1)^{m+1}\int_{r=b}^{a} F^j_{j-m}(r)\,\delta B^j_{jm}(r)\, r^2\, dr\; . \tag{4.52}$$

Dividing the interval $\langle b, a\rangle$ for $\delta\boldsymbol{B}_\mathrm{T}(r)$ into sub-intervals according to equation (4.36), we have

$$\begin{aligned}\mathscr{F}(\delta\boldsymbol{B}_\mathrm{T}) = &\sum_{j=1}^{\infty}\sum_{m=-j}^{j}(-1)^{m+1}\sum_{k=M}^{P}\int_{r_k}^{r_{k+1}}\left[{}^{(1)}F^j_{j-m}\left(\frac{r}{a}\right)^j + {}^{(2)}F^j_{j-m}\left(\frac{a}{r}\right)^{j+1}\right]\\ &\times\left[\delta B^{j,k}_{jm}\;\psi_k(r) + \delta B^{j,k+1}_{jm}\;\psi_{k+1}(r)\right] r^2 dr\; .\end{aligned} \tag{4.53}$$

The integral over r yields,

$$\begin{aligned}\mathscr{F}(\delta\boldsymbol{B}_\mathrm{T}) = &\sum_{j=1}^{\infty}\sum_{m=-j}^{j}(-1)^{m+1}\sum_{k=M}^{P}\left[\left(\frac{1}{a}\right)^j\left({}^{(1)}F^j_{j-m}\delta B^{j,k}_{jm}\;Q^{(1)}_k + {}^{(1)}F^j_{j-m}\delta B^{j,k+1}_{jm}\;Q^{(2)}_k\right)\right.\\ &\left.+\; a^{j+1}\left({}^{(2)}F^j_{j-m}\delta B^{j,k}_{jm}\;Q^{(3)}_k + {}^{(2)}F^j_{j-m}\delta B^{j,k+1}_{jm}\;Q^{(4)}_k\right)\right]\; ,\end{aligned} \tag{4.54}$$

where M labels the finite-element node at the ocean bottom, so that $r_M = b$ and $Q^{(i)}_k$ stands for the following integrals:

$$Q^{(1)}_k = \int_{r_k}^{r_{k+1}} r^{j+2}\;\psi_k(r)\; dr\; , \tag{4.55}$$

$$Q^{(2)}_k = \int_{r_k}^{r_{k+1}} r^{j+2}\;\psi_{k+1}(r)\; dr\; , \tag{4.56}$$

$$Q^{(3)}_k = \int_{r_k}^{r_{k+1}} r^{-j+1}\;\psi_k(r)\; dr\; , \tag{4.57}$$

$$Q^{(4)}_k = \int_{r_k}^{r_{k+1}} r^{-j+1}\;\psi_{k+1}(r)\; dr\; . \tag{4.58}$$

They can be evaluated analytically as

$$Q^{(1)}_k = \frac{1}{h_k}\left[\frac{r_{k+1}}{j+3}\left(r^{j+3}_{k+1} - r^{j+3}_k\right) - \frac{1}{j+4}\left(r^{j+4}_{k+1} - r^{j+4}_k\right)\right]\; , \tag{4.59}$$

$$Q^{(2)}_k = \frac{1}{h_k}\left[\frac{1}{j+4}\left(r^{j+4}_{k+1} - r^{j+4}_k\right) - \frac{r_k}{j+3}\left(r^{j+3}_{k+1} - r^{j+3}_k\right)\right]\; , \tag{4.60}$$

$$Q^{(3)}_k = \frac{1}{h_k}\left(\int_{r_k}^{r_{k+1}} r_{k+1}\; r^{-j+1}\; dr - \int_{r_k}^{r_{k+1}} r^{-j+2}\; dr\right)\; , \tag{4.61}$$

$$Q^{(4)}_k = \frac{1}{h_k}\left(\int_{r_k}^{r_{k+1}} r^{-j+2}\; dr - \int_{r_k}^{r_{k+1}} r_k\; r^{-j+1}\; dr\right) \tag{4.62}$$

with the solutions for $Q_k^{(3)}$ and $Q_k^{(4)}$ given by:
for $j=1$ and $j>3$

$$Q_k^{(3)} = \frac{1}{h_k}\left[\frac{r_{k+1}}{-j+2}\left(r_{k+1}^{-j+2} - r_k^{-j+2}\right) - \frac{1}{-j+3}\left(r_{k+1}^{-j+3} - r_k^{-j+3}\right)\right] , \tag{4.63}$$

$$Q_k^{(4)} = \frac{1}{h_k}\left[\frac{1}{-j+3}\left(r_{k+1}^{-j+3} - r_k^{-j+3}\right) - \frac{r_k}{-j+2}\left(r_{k+1}^{-j+2} - r_k^{-j+2}\right)\right] , \tag{4.64}$$

for $j=2$

$$Q_k^{(3)} = \frac{1}{h_k}\left[r_{k+1}\ \ln\left(\frac{r_{k+1}}{r_k}\right) - \frac{1}{-j+3}\left(r_{k+1}^{-j+3} - r_k^{-j+3}\right)\right] , \tag{4.65}$$

$$Q_k^{(4)} = \frac{1}{h_k}\left[\frac{1}{-j+3}\left(r_{k+1}^{-j+3} - r_k^{-j+3}\right) - r_k\ \ln\left(\frac{r_{k+1}}{r_k}\right)\right] , \tag{4.66}$$

and for $j=3$

$$Q_k^{(3)} = \frac{1}{h_k}\left[\frac{r_{k+1}}{-j+2}\left(r_{k+1}^{-j+2} - r_k^{-j+2}\right) - \ln\left(\frac{r_{k+1}}{r_k}\right)\right] , \tag{4.67}$$

$$Q_k^{(4)} = \frac{1}{h_k}\left[\ln\left(\frac{r_{k+1}}{r_k}\right) - \frac{r_k}{-j+2}\left(r_{k+1}^{-j+2} - r_k^{-j+2}\right)\right] . \tag{4.68}$$

4.2.1 The spectral-finite element approach for toroidal magnetic field

We now formulate the spectral-finite element solution to the boundary-value problem given by equation (4.8). We introduce the solution space for the toroidal magnetic field

$$\mathcal{V}_\mathrm{h} = \left\{ \boldsymbol{B}_\mathrm{h} | \boldsymbol{B}_\mathrm{h} = \sum_{j=1}^{j_\mathrm{max}} \sum_{m=-j}^{j} \sum_{k=1}^{P} B_{jm}^{j,k}\ \psi_k(r)\ \boldsymbol{Y}_{jm}^{j}(\Omega) \right\} , \tag{4.69}$$

where j_max and P are finite cut-off degrees in lateral and radial direction, respectively. $\mathcal{V}_\mathrm{h}$ is a finite-dimensional subspace of the solution space $\mathcal{V}$. The Galerkin method for approximating the solution to the problem (4.8) consists of finding $\boldsymbol{B}_\mathrm{h} \in \mathcal{V}_\mathrm{h}$ such that

$$\mathscr{A}(\boldsymbol{B}_\mathrm{h}, \delta\boldsymbol{B}_\mathrm{h}) + \mathscr{B}(\boldsymbol{B}_\mathrm{h}, \delta\boldsymbol{B}_\mathrm{h}) = \mathscr{F}(\delta\boldsymbol{B}_\mathrm{h}) \qquad \forall \delta\boldsymbol{B}_\mathrm{h} \in \mathcal{V}_\mathrm{h} . \tag{4.70}$$

Through eq. (4.71) the solution of the induction equation is reduced to a system of linear algebraic equations, the so-called Galerkin system. The discrete solution $\boldsymbol{B}_\mathrm{h}$ of the Galerkin system of linear algebraic equations is called the spectral-finite element solution. The Galerkin system of equations (4.71) is completely decoupled and degenerated. Its matrix diagonal-block form and the spectral property of each block-diagonal is associated with a specific angular degree j. Moreover, each block is band-diagonal with a finite bandwidth because of the finite support of the finite elements ψ_k and ψ_{k+1}. We solve the system of equations (4.71) by the LU decomposition modified for a linear algebraic system with a band-diagonal matrix. An example of the block-diagonal matrix of the Galerkin system is shown in Figure 4.2.

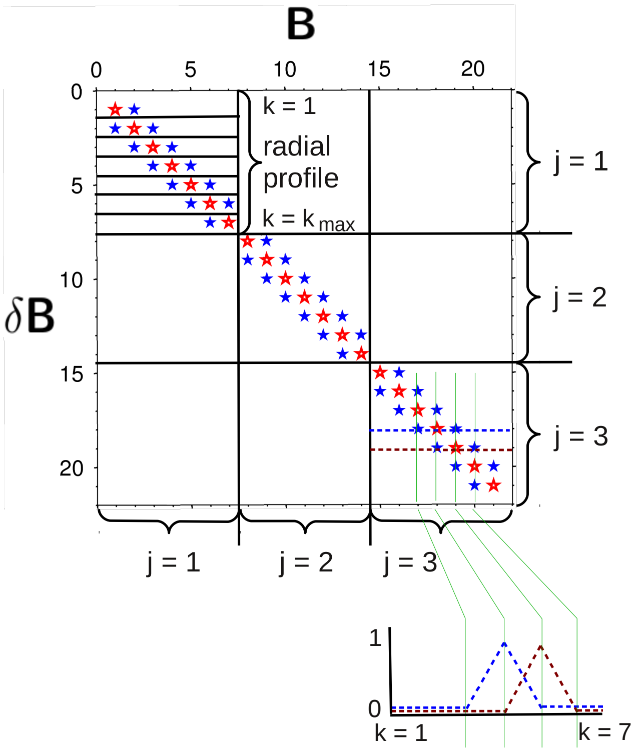

Figure 4.2: Example of the block-diagonal matrix of the Galerkin system for $j_{\max} = 3, k_{\max} = 7$. The dashed red and blue lines at the right bottom show the behaviour of the linear finite-element functions $\psi_k(r)$ for the particular test functions $\delta\boldsymbol{B}$ used to parametrize $\boldsymbol{B}$ and $\delta\boldsymbol{B}$ in radial direction.

4.3 Weak formulation for the poloidal magnetic field in terms of toroidal vector potential

In this section we turn our attention to the poloidal part of the magnetic signal expressed in terms of the toroidal magnetic potential $\boldsymbol{A}$. We start with the induction equation (1.24),

$$\operatorname{curl}\operatorname{curl}\boldsymbol{A}_{\mathrm{T}} + \mu_0\sigma\frac{\partial}{\partial t}\boldsymbol{A}_{\mathrm{T}} = \mu_0\sigma\left(\boldsymbol{u}\times\boldsymbol{B}_{\mathrm{E}}\right) \qquad \text{in } \mathcal{G}\ . \tag{4.71}$$

As the poloidal magnetic field is not confined only to the Earth's interior, we also consider the atmosphere $\mathcal{A}$ ($r \geq a, \sigma = 0$) where the induction equation (1.24) reduces to

$$\operatorname{curl}\operatorname{curl}\boldsymbol{A}_0 = 0 \qquad \text{in } \mathcal{A}\ , \tag{4.72}$$

where $\boldsymbol{A}_0$ is the toroidal magnetic potential in atmosphere. The continuity condition at the boundary between the ocean and atmosphere is

$$\boldsymbol{A}_{\mathrm{T}} = \boldsymbol{A}_0 \qquad \text{on } \partial\mathcal{G}\ . \tag{4.73}$$

We define the functionals

$$\mathscr{A}(\boldsymbol{A},\delta\boldsymbol{A}) := \int_{\mathcal{G}}(\operatorname{curl}\boldsymbol{A}\cdot\operatorname{curl}\delta\boldsymbol{A})\,dV\ , \tag{4.74}$$

$$\mathscr{B}(\boldsymbol{A},\delta\boldsymbol{A}) := \mu_0\int_{\mathcal{G}}\sigma(r)\left(\frac{\partial\boldsymbol{A}}{\partial t}\cdot\delta\boldsymbol{A}\right)dV\ , \tag{4.75}$$

$$\mathscr{A}_0(\boldsymbol{A}_0,\delta\boldsymbol{A}_0) := \int_{\mathcal{A}}(\operatorname{curl}\boldsymbol{A}_0\cdot\operatorname{curl}\delta\boldsymbol{A}_0)\,dV\ , \tag{4.76}$$

$$\mathscr{F}(\delta\boldsymbol{A}) := \mu_0\int_{\mathcal{G}}\sigma(r)\,(\boldsymbol{u}\times\boldsymbol{B}_{\mathrm{E}})\cdot\delta\boldsymbol{A}\,dV\ . \tag{4.77}$$

We introduce functional spaces for the Earth $\mathcal{V}$ and atmosphere $\mathcal{V}_0$

$$\mathcal{V} := \{\boldsymbol{A}_{\mathrm{T}} | \boldsymbol{A}_{\mathrm{T}} \in L_2(\mathcal{G}), \operatorname{curl} \boldsymbol{A}_{\mathrm{T}} \in L_2(\mathcal{G}), \operatorname{div} \boldsymbol{A}_{\mathrm{T}} = 0 \text{ in } \mathcal{G}\} \ , \tag{4.78}$$

$$\mathcal{V}_0 := \{\boldsymbol{A}_0 | \boldsymbol{A}_0 \in C_2(\mathcal{A}), \operatorname{div} \boldsymbol{A}_0 = 0 \text{ in } \mathcal{A}, \boldsymbol{A}_{\mathrm{T}} = \boldsymbol{A}_0 \text{ on } \partial\mathcal{G}, \boldsymbol{A}_0 \mid_{r\to\infty} = 0\} \ . \tag{4.79}$$

The weak formulation of the problem, eqs (4.72)-(4.74), consists of finding $\boldsymbol{A}_{\mathrm{T}} \in \mathcal{V}$ and $\boldsymbol{A}_0 \in \mathcal{V}_0$ such that, at fixed time, the following variational equation is satisfied

$$\mathscr{A}(\boldsymbol{A}_{\mathrm{T}}, \delta\boldsymbol{A}_{\mathrm{T}}) + \mathscr{B}(\boldsymbol{A}_{\mathrm{T}}, \delta\boldsymbol{A}_{\mathrm{T}}) + \mathscr{A}_0(\boldsymbol{A}_0, \delta\boldsymbol{A}_0) = \mathscr{F}(\delta\boldsymbol{A}_{\mathrm{T}}) \qquad \begin{matrix} \forall \delta\boldsymbol{A}_{\mathrm{T}} \in \mathcal{V} \\ \forall \delta\boldsymbol{A}_0 \in \mathcal{V}_0 \end{matrix} \ . \tag{4.80}$$

The equivalence of the weak solution with the strong solution for sufficiently smooth functions can be shown by using Green's theorem (eq. 4.9) in the variational equation (4.81),

$$\begin{aligned} &\int_{\mathcal{G}} \operatorname{curl}\operatorname{curl} \boldsymbol{A}_{\mathrm{T}} \cdot \delta\boldsymbol{A}_{\mathrm{T}}\, dV + \int_{\partial\mathcal{G}} \operatorname{curl} \boldsymbol{A}_{\mathrm{T}} \cdot (\boldsymbol{n} \times \delta\boldsymbol{A}_{\mathrm{T}})\, dS + \mu_0 \int_{\mathcal{G}} \sigma(r,\vartheta) \left(\frac{\partial \boldsymbol{A}_{\mathrm{T}}}{\partial t} \cdot \delta\boldsymbol{A}_{\mathrm{T}} \right) dV + \\ &\int_{\mathcal{A}} \operatorname{curl}\operatorname{curl} \boldsymbol{A}_0 \cdot \delta\boldsymbol{A}_0\, dV + \int_{\partial\mathcal{A}} \operatorname{curl} \boldsymbol{A}_0 \cdot (\boldsymbol{n} \times \delta\boldsymbol{A}_0)\, dS = \mathscr{F}(\delta\boldsymbol{A}_{\mathrm{T}}) \ . \end{aligned} \tag{4.81}$$

Since this equation must hold for all $\delta\boldsymbol{A}_{\mathrm{T}} \in \mathcal{V}$ and $\delta\boldsymbol{A}_0 \in \mathcal{V}_0$, we have

$$\operatorname{curl}\operatorname{curl} \boldsymbol{A}_{\mathrm{T}} + \mu_0 \sigma \frac{\partial \boldsymbol{A}_{\mathrm{T}}}{\partial t} = \mu_0 \sigma (\boldsymbol{u} \times \boldsymbol{B}_{\mathrm{E}}) \qquad \text{in } \mathcal{G} \ , \tag{4.82}$$

$$\operatorname{curl}\operatorname{curl} \boldsymbol{A}_0 = 0 \qquad \text{in } \mathcal{A} \ . \tag{4.83}$$

By this, eq. (4.82) is reduced to

$$\int_{\partial\mathcal{G}} \operatorname{curl} \boldsymbol{A}_{\mathrm{T}} \cdot (\boldsymbol{n} \times \delta\boldsymbol{A}_{\mathrm{T}})\, dS + \int_{\partial\mathcal{A}} \operatorname{curl} \boldsymbol{A}_0 \cdot (\boldsymbol{n} \times \delta\boldsymbol{A}_0)\, dS = 0 \ . \tag{4.84}$$

The surface of the spherical atmosphere layer can be defined as the surface of the Earth on the inner side by $\partial\mathcal{A}_{\mathrm{in}}$ at $r = a$ and a sphere $\partial\mathcal{A}_{\mathrm{out}}$ at $r \to \infty$ on the outer side. Then the surface of the atmosphere $\partial\mathcal{A} = \partial\mathcal{A}_{\mathrm{in}} \cup \partial\mathcal{A}_{\mathrm{out}}$. Taking into account the opposite orientation of the normal vectors $\boldsymbol{n}$ at Earth surface between $\partial\mathcal{G}$ and $\partial\mathcal{A}_{\mathrm{in}}$

$$\boldsymbol{n} \mid_{\partial\mathcal{A}_{\mathrm{in}}} = -\boldsymbol{e}_r \tag{4.85}$$

and the condition

$$\boldsymbol{A}_0 \mid_{r\to\infty} = 0 \tag{4.86}$$

the second integral in eq. (4.85) reduces to

$$\int_{\partial\mathcal{G}} \operatorname{curl} \boldsymbol{A}_{\mathrm{T}} \cdot (\boldsymbol{e}_r \times \delta\boldsymbol{A}_{\mathrm{T}})\, dS - \int_{\partial\mathcal{A}_{\mathrm{in}}} \operatorname{curl} \boldsymbol{A}_0 \cdot (\boldsymbol{e}_r \times \delta\boldsymbol{A}_0)\, dS = 0 \ . \tag{4.87}$$

Since $\boldsymbol{B}_{\mathrm{P}} = \operatorname{curl} \boldsymbol{A}_{\mathrm{T}}$ and $\boldsymbol{B}_0 = \operatorname{curl} \boldsymbol{A}_0$, we have

$$\int_{\partial\mathcal{G}} \boldsymbol{B}_{\mathrm{P}} \cdot (\boldsymbol{e}_r \times \delta\boldsymbol{A}_{\mathrm{T}})\, dS - \int_{\partial\mathcal{A}_{\mathrm{in}}} \boldsymbol{B}_0 \cdot (\boldsymbol{e}_r \times \delta\boldsymbol{A}_0)\, dS = 0 \ . \tag{4.88}$$

Since $\partial\mathcal{G} = \partial\mathcal{A}_{\mathrm{in}}$ and $\boldsymbol{A}_{\mathrm{T}}(a) = \boldsymbol{A}_0(a)$, it follows that $\boldsymbol{B}_{\mathrm{P}}(a) = \boldsymbol{B}_0(a)$ which guarantees a continuity of magnetic induction vector on the Earth's surface. In the solid Earth and ocean (domain $\mathcal{G}$), the toroidal magnetic potentials are parametrized as

$$\left\{ \begin{matrix} \boldsymbol{A}_{\mathrm{T}} \\ \delta\boldsymbol{A}_{\mathrm{T}} \end{matrix} \right\} = \sum_{j=1}^{\infty} \sum_{m=-j}^{j} \left\{ \begin{matrix} A_{jm}^{j}(r) \\ \partial A_{jm}^{j}(r) \end{matrix} \right\} \boldsymbol{Y}_{jm}^{j}(\Omega) \ . \tag{4.89}$$

Substituting eq. (4.90) into (4.76) yields

$$
\begin{aligned}
\mathscr{B}(\boldsymbol{A}_\mathrm{T}, \delta\boldsymbol{A}_\mathrm{T}) &= \mu_0 \int_\mathcal{G} \sigma(r) \left(\frac{\partial \boldsymbol{A}_\mathrm{T}}{\partial t} \cdot \delta\boldsymbol{A}_\mathrm{T} \right) dV \\
&= \mu_0 (i\,\omega) \int_\mathcal{G} \sigma(r)\, (\boldsymbol{A}_\mathrm{T} \cdot \delta\boldsymbol{A}_\mathrm{T})\, dV \\
&= i\,\omega\,\mu_0 \int_{r=0}^{a} \int_{\Omega_0} \sigma(r) \sum_{j_1=1}^{\infty} \sum_{m_1=-j_1}^{j_1} A^{j_1}_{j_1 m_1}(r)\, \boldsymbol{Y}^{j_1}_{j_1 m_1}(\Omega) \\
&\quad \times \sum_{j_2=1}^{\infty} \sum_{m_2 - j_2}^{j_2} \delta A^{j_2}_{j_2 m_2}(r)\, \boldsymbol{Y}^{j_2}_{j_2 m_2}(\Omega)\, d\Omega\, r^2\, dr\ .
\end{aligned} \tag{4.90}
$$

We use now the orthonormality property of toroidal vector spherical harmonics (eq. D.20) and complex conjugation of $\boldsymbol{Y}^{j}_{jm}(\Omega)$ (eq. 4.30) and obtain

$$
\mathscr{B}(\boldsymbol{A}_\mathrm{T}, \delta\boldsymbol{A}_\mathrm{T}) = i\,\omega\,\mu_0 \sum_{j=1}^{\infty} \sum_{m=-j}^{j} (-1)^{m+1} \int_{r=0}^{a} \sigma(r)\, A^{j}_{j-m}(r)\, \delta A^{j}_{jm}(r)\, r^2\, dr\ . \tag{4.91}
$$

Using eq. (D.33), we have

$$
\operatorname{curl} \boldsymbol{A}_\mathrm{T}(r,\Omega) = \sum_{j=1}^{\infty} \sum_{m=-j}^{j} \sum_{\ell=j-1}^{j+1,2} \mathcal{R}^{\ell}_{jm}(\boldsymbol{A}_\mathrm{T}, r)\, \boldsymbol{Y}^{\ell}_{jm}(\Omega)\ , \tag{4.92}
$$

where

$$
\mathcal{R}^{j-1}_{jm}(\boldsymbol{A}_\mathrm{T}, r) = i \sqrt{\frac{j+1}{2j+1}} \left(\frac{d}{dr} + \frac{j+1}{r} \right) A^{j}_{jm}(r)\ , \tag{4.93}
$$

$$
\mathcal{R}^{j+1}_{jm}(\boldsymbol{A}_\mathrm{T}, r) = i \sqrt{\frac{j}{2j+1}} \left(\frac{d}{dr} - \frac{j}{r} \right) A^{j}_{jm}(r)\ . \tag{4.94}
$$

Substituting eq. (4.93) into eq. (4.75), we obtain

$$
\begin{aligned}
\mathscr{A}(\boldsymbol{A}_\mathrm{T}, \delta\boldsymbol{A}_\mathrm{T}) &= \int_\mathcal{G} (\operatorname{curl} \boldsymbol{A}_\mathrm{T} \cdot \operatorname{curl} \delta\boldsymbol{A}_\mathrm{T})\; dV \\
&= \sum_{j=1}^{\infty} \sum_{m=-j}^{j} (-1)^m \sum_{\ell=j-1}^{j+1,2} \int_{r=0}^{a} \mathcal{R}^{\ell}_{j-m}(\boldsymbol{A}_\mathrm{T}, r) \mathcal{R}^{\ell}_{jm}(\delta\boldsymbol{A}_\mathrm{T}, r)\, r^2\; dr\ .
\end{aligned} \tag{4.95}
$$

4.3.1 Toroidal magnetic potential in the atmosphere

Let us parametrize the toroidal magnetic potential in the atmosphere in the form

$$
\boldsymbol{A}_0 = -i\,a \sum_{j=1}^{\infty} \sqrt{\frac{j+1}{j}} \left(\frac{a}{r} \right)^{j+1} \sum_{m=-j}^{j} {}^{b}G^{(i)}_{jm}\, \boldsymbol{Y}^{j}_{jm}(\Omega)\ . \tag{4.96}
$$

Keeping in mind $\boldsymbol{B}_0 = \operatorname{curl} \boldsymbol{A}_0$ we show the equivalence of representation of $\boldsymbol{A}_0$, eq. (4.97), with the representation of the poloidal magnetic field $\boldsymbol{B}_0$ in the atmosphere by eq. (3.59). By eq. (4.93), we have

$$\begin{aligned}
\boldsymbol{B}_0 &= \operatorname{curl}\boldsymbol{A}_0 \\
&= -i\,a\sum_{j=1}^{\infty} i\sqrt{\frac{j}{2j+1}}\left(\frac{d}{dr}-\frac{j}{r}\right)\sqrt{\frac{j+1}{j}}\left(\frac{a}{r}\right)^{j+1}\sum_{m=-j}^{j} {}^{b}G^{(i)}_{jm}\,\boldsymbol{Y}^{j+1}_{jm}(\Omega) \\
&= -\sum_{j=1}^{\infty}\sqrt{(j+1)(2j+1)}\left(\frac{a}{r}\right)^{j+2}\sum_{m=-j}^{j} {}^{b}G^{(i)}_{jm}\,\boldsymbol{Y}^{j+1}_{jm}(\Omega)
\end{aligned} \tag{4.97}$$

which is equivalent to representation of $\boldsymbol{B}_0$ by eq. (3.59). Furthermore,

$$\begin{aligned}
\mathscr{A}_0(\boldsymbol{A}_0,\delta\boldsymbol{A}_0) &= \int_{\mathcal{A}}(\operatorname{curl}\boldsymbol{A}_0\cdot\operatorname{curl}\delta\boldsymbol{A}_0)\,dV \\
&= \int_{r=a}^{\infty}\int_{\Omega_0}(\operatorname{curl}\boldsymbol{A}_0\cdot\operatorname{curl}\delta\boldsymbol{A}_0)\,dV \\
&= \int_{r=a}^{\infty}\int_{\Omega_0}\sum_{j_1=1}^{\infty}\sum_{m_1=-j}^{j}\sqrt{(j_1+1)(2j_1+1)}\left(\frac{a}{r}\right)^{j_1+2} {}^{b}G^{(i)}_{j_1m_1}\,\boldsymbol{Y}^{j_1+1}_{j_1m_1}(\Omega) \\
&\quad\times\sum_{j_2=1}^{\infty}\sum_{m_2=-j}^{j}\sqrt{(j_2+1)(2j_2+1)}\left(\frac{a}{r}\right)^{j_2+2}\delta G^{(i)}_{j_2m_2}\,\boldsymbol{Y}^{j_2+1}_{j_2m_2}(\Omega)\,d\Omega\,r^2\,dr \\
&= \sum_{j=1}^{\infty}\sum_{m=-j}^{j}(-1)^m\,(j+1)(2j+1)\,{}^{b}G^{(i)}_{j-m}\,\delta G^{(i)}_{jm}\int_{r=a}^{\infty}\left(\frac{a}{r}\right)^{2j+4} r^2\,dr\;.
\end{aligned} \tag{4.98}$$

Evaluating the integral analytically,

$$\int_{r=a}^{\infty}\left(\frac{a}{r}\right)^{2j+4} r^2\,dr = a^{2j+4}\int_{r=a}^{\infty} r^{-2j-2}\,dr = \frac{a^{2j+4}}{-2j-1}\frac{1}{r^{2j+1}}\bigg|_{r=a}^{\infty} = \frac{a^3}{2j+1} \tag{4.99}$$

we obtain

$$\mathscr{A}_0(\boldsymbol{A}_0,\delta\boldsymbol{A}_0) = a^3\sum_{j=1}^{\infty}\sum_{m=-j}^{j}(-1)^m\,(j+1)\,{}^{b}G^{(i)}_{j-m}\,\delta G^{(i)}_{jm}\;. \tag{4.100}$$

4.3.2 The continuity condition

We now consider the continuity condition eq. (4.74) at the interface between the ocean and atmosphere $\partial\mathcal{G}$. By the choice of the functional space $\mathcal{V}_0$, see eq. (4.80), the magnetic potential is continuous on $\partial\mathcal{G}$,

$$\boldsymbol{A}_{\mathrm{T}} = \boldsymbol{A}_0 \qquad\qquad \text{on } \partial\mathcal{G}\;. \tag{4.101}$$

Substituting for $\boldsymbol{A}_{\mathrm{T}}$ from eq. (4.90) and for $\boldsymbol{A}_0$ from eq. (4.97),we have

$$A^{j}_{jm}(a) = -i\,a\sqrt{\frac{j+1}{j}}\,{}^{b}G^{(i)}_{jm} \tag{4.102}$$

or, equivalently

$${}^{b}G^{(i)}_{jm} = \frac{i}{a}\sqrt{\frac{j}{j+1}}\,A^{j}_{jm}(a)\;. \tag{4.103}$$

The same relation is valid for a test function from the space $\mathcal{V}_0$,

$$\delta G^{(i)}_{jm} = \frac{i}{a}\sqrt{\frac{j}{j+1}}\,\delta A^j_{jm}(a)\ . \tag{4.104}$$

The substitution of ${}^bG^{(i)}_{jm}$ and $\delta G^{(i)}_{jm}$ into eq. (4.101) yields the sesquilinear form $\mathscr{A}_0(\boldsymbol{A}_0, \delta\boldsymbol{A}_0)$ expressed in terms of $A^j_{jm}(a)$ and $\delta A^j_{jm}(a)$,

$$\begin{aligned}\mathscr{A}_0(\boldsymbol{A}_0, \delta\boldsymbol{A}_0) &= a^3 \sum_{j=1}^{\infty}\sum_{m=-j}^{j} (-1)^m\ (j+1)\left(\frac{i}{a}\right)\left(\frac{i}{a}\right)\frac{j}{j+1}\,A^j_{j-m}(a)\,\delta A^j_{jm}(a)\\ &= -a\sum_{j=1}^{\infty}\sum_{m=-j}^{j} (-1)^m j\,A^j_{j-m}(a)\,\delta A^j_{jm}(a)\ .\end{aligned} \tag{4.105}$$

Finally, we summarize for the left hand side of equation (4.81)

$$\mathscr{A}(\boldsymbol{A}_\mathrm{T}, \delta\boldsymbol{A}_\mathrm{T}) = \sum_{j=1}^{\infty}\sum_{m=-j}^{j} (-1)^m \sum_{\ell=j-1}^{j+1,2} \int_{r=0}^{a} \mathcal{R}^{\ell}_{j-m}(\boldsymbol{A}_\mathrm{T}, r)\ \mathcal{R}^{\ell}_{jm}(\delta\boldsymbol{A}_\mathrm{T}, r)\ r^2\ dr\ , \tag{4.106}$$

$$\mathscr{B}(\boldsymbol{A}_\mathrm{T}, \delta\boldsymbol{A}_\mathrm{T}) = i\,\omega\,\mu_0 \sum_{j=1}^{\infty}\sum_{m=-j}^{j} (-1)^{m+1} \int_{r=0}^{a} \sigma(r)\,A^j_{j-m}(r)\,\delta A^j_{jm}(r)\,r^2\,dr\ , \tag{4.107}$$

$$\mathscr{A}_0(\boldsymbol{A}_0, \delta\boldsymbol{A}_0) = -a\sum_{j=1}^{\infty}\sum_{m=-j}^{j} (-1)^m\ j\,A^j_{j-m}(a)\,\delta A^j_{jm}(a)\ . \tag{4.108}$$

4.3.3 Finite-element approximation of toroidal magnetic potential in radial direction

In analogy to subsection 4.1.2, the parametrization in radial direction of the toroidal magnetic potential is given by the radially-dependent finite element $\psi_k(r)$,

$$\left\{\begin{array}{c} A^j_{jm}(r) \\ \delta A^j_{jm}(r) \end{array}\right\} = \sum_{k=1}^{P+1} \left\{\begin{array}{c} A^{j,k}_{jm} \\ \delta A^{j,k}_{jm} \end{array}\right\} \psi_k(r) \qquad\qquad \text{in } \mathcal{G}\ . \tag{4.109}$$

Note that the function ψ_{P+1} is considered since the toroidal magnetic potential continues from $\mathcal{G}$ to the atmosphere $\mathcal{A}$. The integral over r in eq. (4.108) for a constant conductivity is

$$\begin{aligned}&\int_{r=0}^{a} A^j_{j-m}(r)\ \delta A^j_{jm}(r)\ r^2\ dr\\ &\quad= \sum_{k=1}^{P}\left(I^{(1)}_k A^{\ell,k}_{j-m}\ \delta A^{\ell,k}_{jm} + I^{(2)}_k A^{\ell,k}_{j-m}\ \delta A^{\ell,k+1}_{jm} + I^{(2)}_k\ A^{\ell,k+1}_{j-m}\ \delta A^{\ell,k}_{jm} + I^{(3)}_k A^{\ell,k+1}_{j-m}\ \delta A^{\ell,k+1}_{jm}\right)\ ,\end{aligned} \tag{4.110}$$

where $I^{(i)}_k$ are given by equations in eq. (4.38). Hence, the functional $\mathscr{B}$ is then

$$\begin{aligned}\mathscr{B}(\boldsymbol{A}_\mathrm{T}, \delta\boldsymbol{A}_\mathrm{T}) = i\,\omega\,\mu_0 \sum_{j=1}^{\infty}\sum_{m=-j}^{j} (-1)^{m+1} \sum_{k=1}^{P} \sigma_k &\left(I^{(1)}_k A^{\ell,k}_{j-m}\ \delta A^{\ell,k}_{jm}\right.\\ &\left.+ I^{(2)}_k A^{\ell,k}_{j-m}\ \delta A^{\ell,k+1}_{jm} + I^{(2)}_k\ A^{\ell,k+1}_{j-m}\ \delta A^{\ell,k}_{jm} + I^{(3)}_k A^{\ell,k+1}_{j-m}\ \delta A^{\ell,k+1}_{jm}\right)\ .\end{aligned} \tag{4.111}$$

Moreover,

$$\mathcal{R}^{j-1}_{jm}(\boldsymbol{A}_\mathrm{T},r) = i\sqrt{\frac{j+1}{2j+1}}\left[\left(-\frac{1}{h_k}+\frac{j+1}{r}\psi_k(r)\right)A^{j,k}_{jm}+\left(\frac{1}{h_k}+\frac{j+1}{r}\psi_{k+1}(r)\right)A^{j,k+1}_{jm}\right] \ , \tag{4.112}$$

$$\mathcal{R}^{j+1}_{jm}(\boldsymbol{A}_\mathrm{T},r) = i\sqrt{\frac{j}{2j+1}}\left[\left(-\frac{1}{h_k}-\frac{j}{r}\psi_k(r)\right)A^{j,k}_{jm}+\left(\frac{1}{h_k}-\frac{j}{r}\psi_{k+1}(r)\right)A^{j,k+1}_{jm}\right] \ , \tag{4.113}$$

and then

$$\mathscr{A}(\boldsymbol{A}_\mathrm{T},\delta\boldsymbol{A}_\mathrm{T}) = \sum_{j=1}^{\infty}\sum_{m=-j}^{j}(-1)^m\sum_{\ell=j-1}^{j+1,2}\sum_{k=1}^{P}\int_{r_k}^{r_{k+1}}\mathcal{R}^{\ell}_{j-m}(\boldsymbol{A}_\mathrm{T},r)\,\mathcal{R}^{\ell}_{jm}(\delta\boldsymbol{A}_\mathrm{T},r)\,r^2\,dr\ . \tag{4.114}$$

4.3.4 Finite-element, spherical harmonic parametrization of the poloidal source term

We now express the source term on the right hand side of equation (4.81)

$$\mathscr{F}(\delta\boldsymbol{A}_\mathrm{T}) = \mu_0\int_{\mathcal{G}}\sigma(r)\,\boldsymbol{G}\cdot\delta\boldsymbol{A}_\mathrm{T}\,dV \ , \tag{4.115}$$

where the conductivity of the ocean layer for the poloidal case is set constant $\sigma(r)=\sigma_\mathrm{o}$ and $\boldsymbol{G}$ is defined by eq. (2.6)

$$\boldsymbol{G} = \boldsymbol{u}\times\boldsymbol{B}_\mathrm{E}\ . \tag{4.116}$$

To compare the results against the matrix propagator, we search for the source term $\boldsymbol{G}_\mathrm{T}$ in the form of equation (2.8)

$$\boldsymbol{G}_\mathrm{T}(r,\Omega) = \sum_{jm}G^j_{jm}(a)\left(\frac{r}{a}\right)^j\boldsymbol{Y}^j_{jm}(\Omega)\ , \tag{4.117}$$

where G^j_{jm} are defined by equation (2.26). Using the spherical harmonics expansion of the toroidal part of the test function given by equation (4.90), the source term can be expressed analogous to equation (4.92) in the form

$$\mathscr{F}(\delta\boldsymbol{A}_\mathrm{T}) = \mu_0\sum_{j=1}^{\infty}\sum_{m=-j}^{j}(-1)^{m+1}\int_b^a\sigma(r)\,G^j_{jm}\,\delta A^j_{jm}(r)\,r^2dr \tag{4.118}$$

for the ocean layer ($b\le r\le a$) and

$$\mathscr{F}(\delta\boldsymbol{A}_\mathrm{T}) = 0 \tag{4.119}$$

beneath the ocean layer ($r\le b$). Hence,

$$\mathscr{F}(\delta\boldsymbol{A}_\mathrm{T}) = \mu_0\,\sigma_\mathrm{o}\sum_{j=1}^{\infty}\frac{1}{a^j}\sum_{m=-j}^{j}(-1)^{m+1}\sum_{k=M}^{P+1}G^j_{jm}\left(Q^{(1)}_k\,\delta A^{j,k}_{jm}+Q^{(2)}_k\,\delta A^{j,k+1}_{jm}\right)\ , \tag{4.120}$$

where M labels the finite-element node at the ocean bottom. Radial integrals over the finite-element functions $\psi_k(r)$ are given by $Q^{(1)}_k$ and $Q^{(2)}_k$, see eqs (4.56) and (4.57).

4.3.5 The spectral-finite element approach for toroidal magnetic potential

In analogy to subsection 4.2.1, we now formulate the spectral-finite element solution to the problem given by equation (4.81). We introduce the solution spaces for the toroidal magnetic field

$$\mathcal{V}_\mathrm{h} = \left\{ \boldsymbol{A}_\mathrm{h} | \boldsymbol{A}_\mathrm{h} = \sum_{j=1}^{j_\mathrm{max}} \sum_{m=-j}^{j} \sum_{k=1}^{P+1} A_{jm}^{j,k} \, \psi_k(r) \, \boldsymbol{Y}_{jm}^{j}(\Omega) \right\} \tag{4.121}$$

and

$$\mathcal{V}_{0,\mathrm{h}} = \left\{ \boldsymbol{A}_{0,\mathrm{h}} | \boldsymbol{A}_{0,\mathrm{h}} = \sum_{j=1}^{j_\mathrm{max}} \sum_{m=-j}^{j} A_{0,jm}^{j}(a) \, \boldsymbol{Y}_{jm}^{j}(\Omega) \right\} , \tag{4.122}$$

where j_max and P are finite cut-off degrees in lateral and radial direction, respectively. $\mathcal{V}_\mathrm{h}$ and $\mathcal{V}_{0,\mathrm{h}}$ are finite-dimensional subspaces of the solution spaces $\mathcal{V}$ and $\mathcal{V}_0$ (eqs 4.79 and 4.80), respectively. The Galerkin method for approximating the solution to the problem (eq. 4.81) consists of finding $\boldsymbol{A}_\mathrm{h} \in \mathcal{V}_\mathrm{h}$ such that

$$\mathscr{A}(\boldsymbol{A}_\mathrm{h}, \delta\boldsymbol{A}_\mathrm{h}) + \mathscr{B}(\boldsymbol{A}_\mathrm{h}, \delta\boldsymbol{A}_\mathrm{h}) + \mathscr{A}_0(\boldsymbol{A}_{0,\mathrm{h}}, \delta\boldsymbol{A}_{0,\mathrm{h}}) = \mathscr{F}(\delta\boldsymbol{A}_\mathrm{h}) \qquad \begin{array}{c} \forall \delta\boldsymbol{A}_\mathrm{h} \in \mathcal{V}_\mathrm{h} \\ \forall \delta\boldsymbol{A}_{0,\mathrm{h}} \in \mathcal{V}_{0,\mathrm{h}} \end{array} . \tag{4.123}$$

By equation (4.124), the induction equation is reduced to solve a system of linear algebraic equations (Galerkin system). The discrete solution $\boldsymbol{A}_\mathrm{h}$ of the Galerkin system of linear algebraic equations is called the spectral-finite element solution. The solution of the Galerkin system is analogous to sec. 4.2.1.

4.3.6 Derivation of the poloidal magnetic field from toroidal magnetic potential

The poloidal magnetic field is now derived from the toroidal magnetic potential by eq. (1.20) $\boldsymbol{B}_\mathrm{P} = \mathrm{curl}\, \boldsymbol{A}_\mathrm{T}$. We recall the basic functions $\psi_k(r)$ and $\psi_{k+1}(r)$ for the radial direction (eq. 4.35) and their derivations (eq. 4.40 and 4.41) and consider that r belongs to the interval $r_k \le r \le r_{k+1}$. Applying the relation (D.33) for rotation the linear combination of the basic function yields then for $r_k \le r \le r_{k+1}$

$$B_{jm}^{j-1}(r) = i\sqrt{\frac{j+1}{2j+1}} \left[\left(-\frac{1}{h_k} + \frac{j+1}{r}\psi_k(r) \right) A_{jm}^{j,k} + \left(\frac{1}{h_k} + \frac{j+1}{r}\psi_{k+1}(r) \right) A_{jm}^{j,k+1} \right] , \tag{4.124}$$

$$B_{jm}^{j+1}(r) = i\sqrt{\frac{j}{2j+1}} \left[\left(-\frac{1}{h_k} - \frac{j}{r}\psi_k(r) \right) A_{jm}^{j,k} + \left(\frac{1}{h_k} - \frac{j}{r}\psi_{k+1}(r) \right) A_{jm}^{j,k+1} \right] \tag{4.125}$$

and

$$\boldsymbol{B}_\mathrm{P}(r,\Omega) = \sum_{j=1}^{j_\mathrm{max}} \sum_{m=-j}^{j} \sum_{\ell=j-1}^{j+1,2} B_{jm}^{\ell}(r) \, \boldsymbol{Y}_{jm}^{\ell}(\Omega) . \tag{4.126}$$

4.3.7 Poloidal magnetic field in the atmosphere

The poloidal field in atmosphere is described by eq. (2.15)

$$\boldsymbol{B}_0(r,\Omega) = -\sum_{j=1}^{\infty} \sqrt{(j+1)(2j+1)} \left(\frac{a}{r}\right)^{j+2} \sum_{m=-j}^{j} {}^{b}G_{jm}^{(i)} \, \boldsymbol{Y}_{jm}^{j+1}(\Omega) . \tag{4.127}$$

Using relations (D.37) and (D.36), the radial and tangential parts of $\boldsymbol{B}_0$ are

$$\boldsymbol{e}_r \cdot \boldsymbol{B}_0(r,\Omega) = \sum_{j=1}^{\infty} (j+1) \left(\frac{a}{r}\right)^{j+2} \sum_{m=-j}^{j} {}^{b}G_{jm}^{(i)} \, Y_{jm}(\Omega) \; , \tag{4.128}$$

$$\boldsymbol{e}_r \times \boldsymbol{B}_0(r,\Omega) = -i \sum_{j=1}^{\infty} \sqrt{j(j+1)} \left(\frac{a}{r}\right)^{j+2} \sum_{m=-j}^{j} {}^{b}G_{jm}^{(i)} \, \boldsymbol{Y}_{jm}^{j}(\Omega) \; . \tag{4.129}$$

4.4 Results of the spectral-finite element approach

The independent numerical method presented in this chapter enables the reproduction and extension of modelling the toroidal and poloidal magnetic field presented in the previous chapter 3. The numerical solutions of the induction equation (1.13) and (1.24) will be carried out with the source terms derived in chapter 2. As the source is identical for both, the classical and the weak formulation methods, the results are comparable if the identical parametrization of the electrical conductivity profile is used. This allows an internal validation of the methods. In addition, the weak-formulation solution allows us to overcome numerical limitations of the analytical solution. Therefore, in this chapter, the focus is devoted to compare the solutions by the matrix-propagator method with the solutions by the spectral-finite element approach and study the primary poloidal magnetic field in more detail which was not possible by the classical method in the previous chapter.

4.4.1 Toroidal magnetic field

We first return to the toroidal magnetic field that has been already discussed in detail in chapter 3. Here, we recall the numerical examples calculated by the matrix-propagator method and compare them with spectral-finite element solution to validate the correctness of the later method. In Figure 4.3, we compare the radial profiles of the toroidal magnetic field generated by over the depth constant horizontal ocean flow with ocean of the depth of $h = 1$ km, a uniform electrical conductivity profile beneath the ocean layer, $\sigma_{\mathrm{m}} = 1 \ \mathrm{Sm}^{-1}$, and the realistic conductivity profile of the ocean. With the given parametrization, the radial profiles show good agreement without significant differences. By this comparison we focus only on the studying the behaviour of the two models. As mentioned in subsection 2.6.3, the two mathematical approaches require different numerical discretization in radial direction. A uniform and numerically unpretentious conductivity profile simplifies the validation by allowing an arbitrarily fine profile discretization suited for each method. In this way the eventual differences caused by different numeric for each method can be avoided.

Further, we also reproduce the three numerical experiments shown in Figures 3.2, 3.5 and 3.10 from chapter 3 and present the equivalent results calculated with spectral finite-elements approach in Figures 4.4, 4.5 and 4.6, respectively. A very good agreement can be found in the case for large-scale patterns, namely the toroidal magnetic field generated by oceanic transport (Fig. 4.6) and the depth decaying ocean flow (Fig. 4.5). But there are small differences in the case where small-scale signals dominate, such as for the toroidal magnetic field generated by over the depth constant horizontal tidal flow with average velocities, see Figure 4.4. The matrix-propagator method shows oscillating behaviour of the toroidal magnetic signal over large areas where the signal has small magnitudes due to high resistive layer beneath the ocean. This shows numerical limitations of the analytical solution that can be circumvented by using the weak formulation. Using a less resistive uniform conductivity profile or a lower cut-off degree for spherical harmonic expansion, the result of the analytical approach stabilizes and the differences between the two methods vanish.

4.4.2 Poloidal magnetic field

Now we turn our attention to the primary poloidal magnetic field. The poloidal magnetic field is generally modeled only for over the depth constant tidal flow and for the background magnetic field $\boldsymbol{B}_{\mathrm{E}}$ with dipole term only. In addition, the electrical conductivity profile for the ocean layer is constant, set equal to $\sigma_{\mathrm{o}} = 3.5\ \mathrm{Sm}^{-1}$. As already mentioned, a good numerical performance of the weak formulation enable us to study the behaviour of the poloidal magnetic field in detail. The advantage of this approach is that numerical stability is independent of the electrical conductivity distribution beneath the ocean layer such that the mantle can even be considered as an insulator ($\sigma_{\mathrm{m}} = 0\ \mathrm{Sm}^{-1}$). We use this advantage in our first numerical experiment for the ocean layer of the depth of $h = 4$ km, using as input flow the whole M_2 tide transport and the space beneath the ocean layer is considered to be an insulator. This model setup is comparable to the thin sheet approximation applied in the studies by (Tyler et al., 2003) and (Kuvshinov and Olsen, 2005). The r, ϑ and φ components of the poloidal magnetic field are shown in Figure 4.7. The spatial patterns are generally large-scale but show also small-scale features like, for example, around New Zealand. The amplitudes (Figure 4.8) of the small-scale spatial features achieve values of 3 nT for the horizontal and 4-5 nT for the radial components, respectively. The large-scale patterns reach amplitudes of 2 nT.

Until now, we validated our results only by comparing two independent methods, the analytical and numerical approaches, used in this thesis. That only allows an internal validation of our calculus. However, an external validation against published results are also essential for our studies. The present day modelling of a global ocean-induced magnetic field is limited to a thin sheet approximation. In addition, the published results on global scale modelling show only the radial component of primary induced poloidal magnetic field. One of the intention behind the model setup in this numerical experiment is to create comparable model conditions for external validations.

In Figure 4.9 we compare the amplitude of the radial component of the M_2 tide against the result by Dostal (2009). A positive result is that the amplitudes reach nearly the same size. The amplitude of the finite-layer approximation reaches 4 nT while 6 nT for the thin sheet layer when using the same OMCT velocity field. Also, the regions where large amplitudes appear are partly coincident, like the region around New Zealand, the Atlantic Ocean west of Europa and the Pacific Ocean south of Alaska. But there are also differences. A striking difference is the missing strong magnetic signal in the Indian Ocean in the left panel of Figure 4.9 and the missing signal close the west coast of Africa in the right panel. The amplitudes around New Zealand and in the Atlantic Ocean between Greenland and Europe are also not at the same places. Whereas the magnetic signal in the solution by the thin layer approximation is concentrated in the centers of ocean basins, the signal in the finite-layer solution is concentrated more to coastal border. The reason for these differences is due to the spherical symmetry of our conductivity model. The continent areas in the thin sheet approximation are not a part of the solution domain for solving electromagnetic induction problem. The continents are considered as insulators. The generated spherical electric field is discharged only over the ocean areas. In the spherically symmetric model, the continents are assumed to have the same electrical conductivity as the ocean. Therefore, the electric currents discharging the induced magnetic field are not experienced of any barrier over continent areas. This crucially influences the flow of electric currents and the resulting magnetic field. In the bottom panel of Figure 4.9 we additionally show the result by Maus and Kuvshinov (2004) for the M2 tide with the input velocity field from TPXO 6.1 model. This comparison allows us to make an external verification of our finite-layer model with the accepted results from thin sheet modeling. Additionally, as we use the same input data for all calculations in this thesis, the results on the toroidal, primary and secondary poloidal magnetic fields are consistently related.

The radial profile of this numerical experiment (Figure 4.10) allows us to make an additional internal validation. The assumption of a insulating space beneath the ocean layer together with a constant conductivity of the ocean layer create a conductivity model symmetry with respect to the middle of the ocean layer. Since the different field parametrizations beneath and above the ocean a radial symmetry of the solution with respect to the middle of ocean layer allows a check for the variational method. A slight deviation from this symmetry that can especially be seen in the real (red) part of the radial component can be explained by geometrical space asymmetry in radial direction of a sphere. Whereas the geometrical space beneath the ocean shrinks with depth, the space above the ocean extends out with height. As the signal of the r-component penetrates deeper into the Earth, its asymmetry is more visible. It is also noticeable along the profile that horizontal components revise the polarity, whereas the polarity of the radial component does not change through the ocean layer. As the poloidal magnetic field penetrates into the source-free electric conductive layers, it generates additional electric currents that accelerate the energy discharge of the magnetic field. If the space is considered as an insulator, the magnetic field penetrates deeper into the sphere. Therefore, for the resistive underground we plot the radial profile starting in the centre of the Earth to see how deep the magnetic signal penetrates and whether the magnetic signal vanishes in the centre of the Earth.

In next two numerical experiments we keep the ocean depth $h = 4$ km but will change the conductivity profile. First, we use the uniform conductivity beneath the ocean layer by setting $\sigma_\mathrm{m} = 1\ \mathrm{Sm}^{-1}$. This setup allows us to make a validation with the solution by the matrix-propagator method. In Figure 4.13 we compare the radial profiles computed by the two methods; solid lines (red and blue) represent the solution by the matrix-propagator method and dashed lines (black) shows the spectral-finite element approach. The profiles show a good agreement for all three components. In this case, there is also a polarity reversal of the lateral components. Because of uniform conductivity, the magnetic field decays smoothly with depth but it shows a different behaviour as for the case of resistive mantle. The poloidal magnetic signal vanishes already beneath the radius of $r = 5800$ km. The lateral component of the magnetic field at bottom of the ocean layer has noticeable larger magnitude than at sea surface. The amplitudes at sea surface (Figure 4.12) reach values of 2 nT for radial component and are only about a half of the amplitudes by resistive mantle in Figure 4.8. Due to resistive mantle, the discharge processes of electromagnetic energy are confined to the ocean layer, while a part of the energy can also be discharged below the ocean layer when the mantle is conductive. Hence, the induced electromagnetic energy is redistributed and the magnitude of the magnetic field at the top of the ocean is reduced. Comparing the global distribution for the resistive and conductive mantle in Figures 4.7 and 4.11, we find that the magnitude of the poloidal magnetic field changes from one to the other case, but the spatial patterns remain essentially the same.

In the last numerical experiment for the tidal flow transport and the ocean layer depth of $h = 4$ km, we use the realistic conductivity profile. The poloidal magnetic field at the top of the ocean layer is shown in Figure 4.14. The spatial distribution does not change with respect to the two examples above, but the change of the conductivity profile influences the magnitude of magnetic field. The amplitudes (Figure 4.15) at the sea surface are two times larger than for the case with a high conductive profile and slightly smaller than for the resistive profile. To get a closer look into the differences between the magnetic signals we compare the radial profile of the poloidal magnetic field for the realistic case (solid lines) with the profile of the poloidal magnetic field generated for the case of resistant mantle (dashed lines) (Figure 4.16). The behaviour of the magnetic signals with depth are similar to radius of $r = 5700$ km. This can be explained by a high resistivity of the lithosphere, crust and upper mantle. Beneath this radius the conductivity increases and the form of the magnetic signal is similar to the case with the conductive profile in Figure 4.13, the signal decreases fast and vanishes beneath the radius of $r = 5200$ km.

In the last two numerical experiments we again use the average velocity field of the M_2 tidal flow for the ocean layer of the depth of $h = 1$ km. In one case we apply the uniform conductivity profile $\sigma = 1$ Sm^{-1}, which allows us one additional internal validation by the comparison of the results with the matrix-propagator method (Figure 3.14). Also here, as for the toroidal case, the signal is dominated by small-scale features caused by large ocean velocities. The spatial distribution shows a good agreement between the two methods. In addition, Figure 4.19 shows the radial profile where the solution of the matrix-propagator method is plotted in solid lines (red and blue) and compared to the spectral-finite element approach in dashed lines (black), and we can again see a good agreement. The amplitudes reach of about 1 nT and 2 nT for the lateral and radial components, respectively (Figure 4.18).

In a second and last numerical experiment, we use the realistic conductivity profile. Similar to the above example, a higher resistivity beneath the ocean layer causes an increase in the magnetic signal at the sea surface but no change in the spatial distribution (Figure 4.20). The amplitudes reach values of about 2 nT and 3 nT for the lateral and radial components, respectively (Figure 4.21). The amplitudes are smaller than for the whole oceanic transport of the M_2 tide and the magnetic signals are concentrated to coastal regions with high ocean velocities. In the radial profile (Figure 4.19), we compare the realistic case (solid lines) with the magnetic field for a resistant mantle (dashed lines). Also here, the propagation of the poloidal magnetic fields show a similar behaviour up to the depth, where the electrical conductivity of realistic case starts to increase, which allows a discharge of the energy and the poloidal magnetic field vanishes.

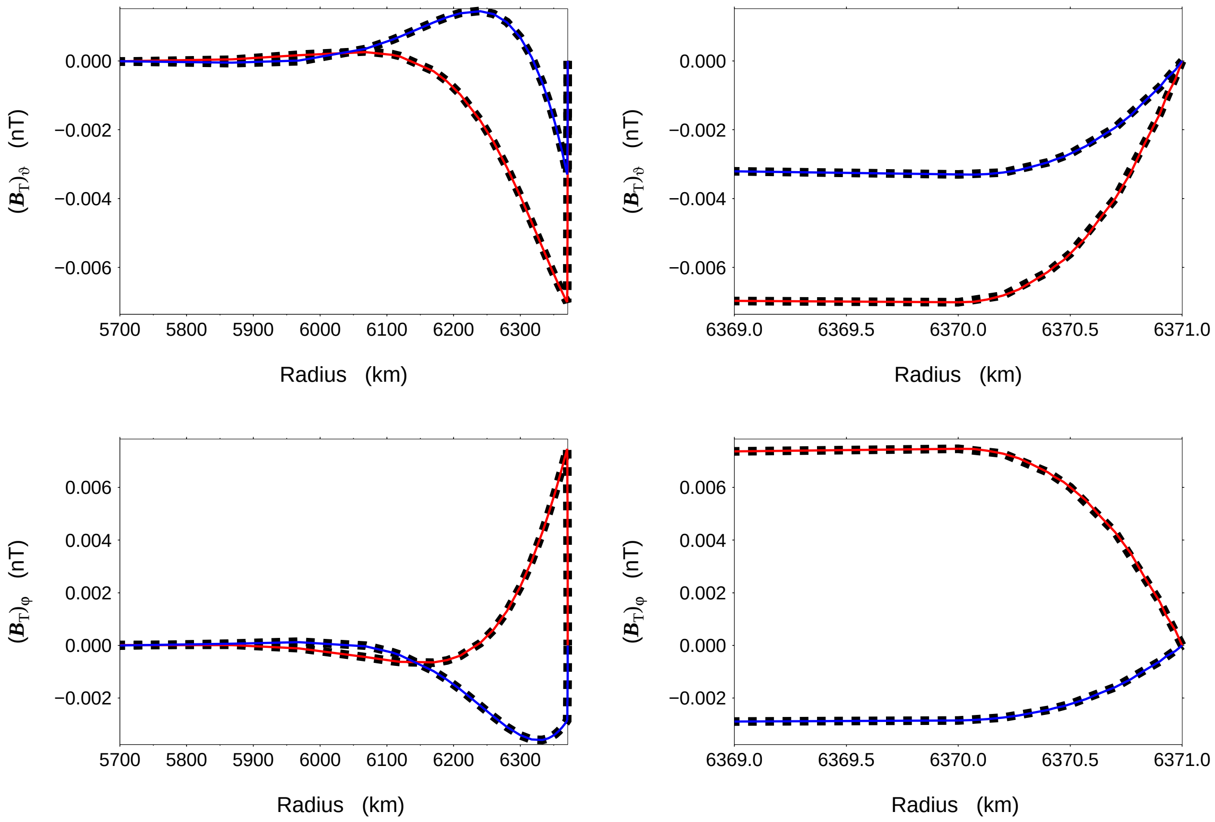

Figure 4.3: Real (red) and imaginary (blue) parts of the ϑ (top) and φ (bottom) components of the toroidal magnetic field (in nT) induced by over the depth constant tidal flow as functions of radius, beneath the ocean (left) and, in detail, inside the ocean layer (right), for uniform electrical conductivity profile beneath ($\sigma_\mathrm{m} = 1$ Sm^{-1}) and realistic inside the ocean layer for the matrix-propagator method (solid lines) and the variational method (black rectangles lines). The radial profiles are taken at the location given by the yellow crosses in Figures 3.2 and 4.4.

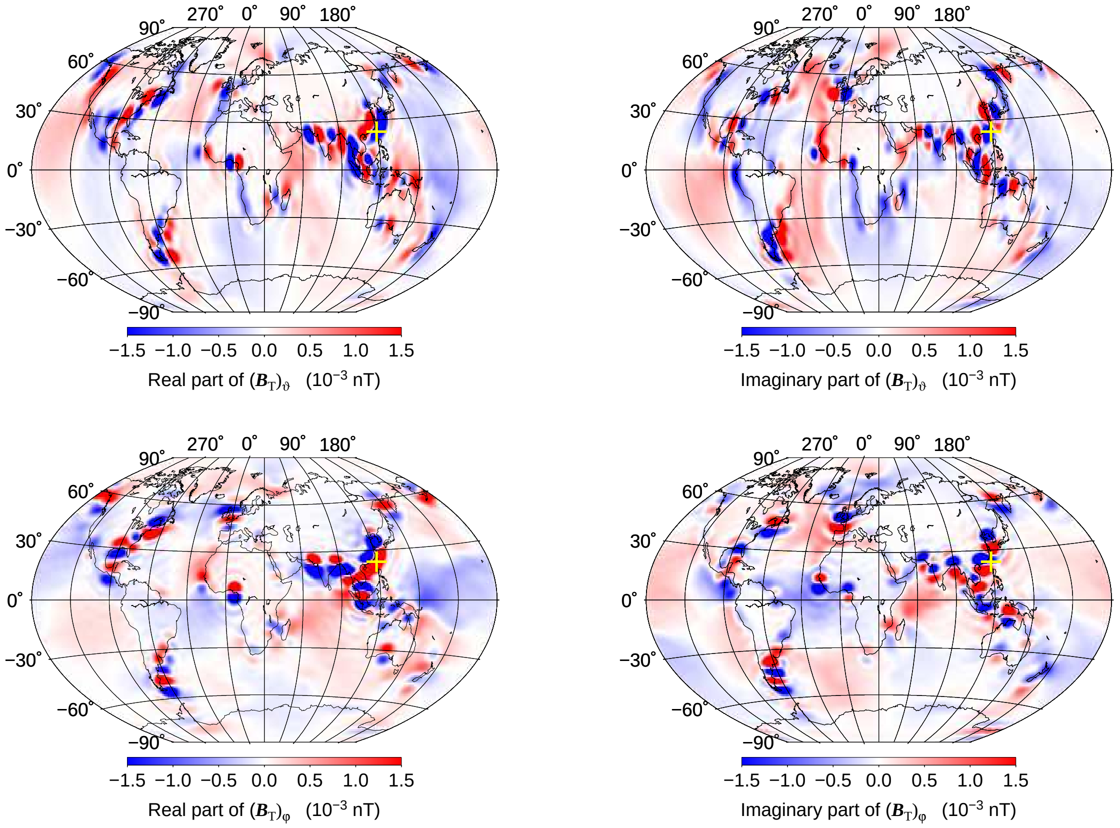

Figure 4.4: Real (left) and imaginary (right) parts of the ϑ (top) and φ (bottom) components of the toroidal magnetic field (in 10^{-3} nT) at the ocean bottom induced by over the depth constant tidal flow by ocean layer depth $h = 1$ km and realistic electrical conductivity profile beneath and inside the ocean layer. The yellow crosses at 23° N, 130° E mark the location where the radial profiles of the toroidal magnetic field with uniform electrical conductivity are plotted (see Figs. 4.3). A comparable result obtained with matrix-propagator method is shown in Figure 3.2.

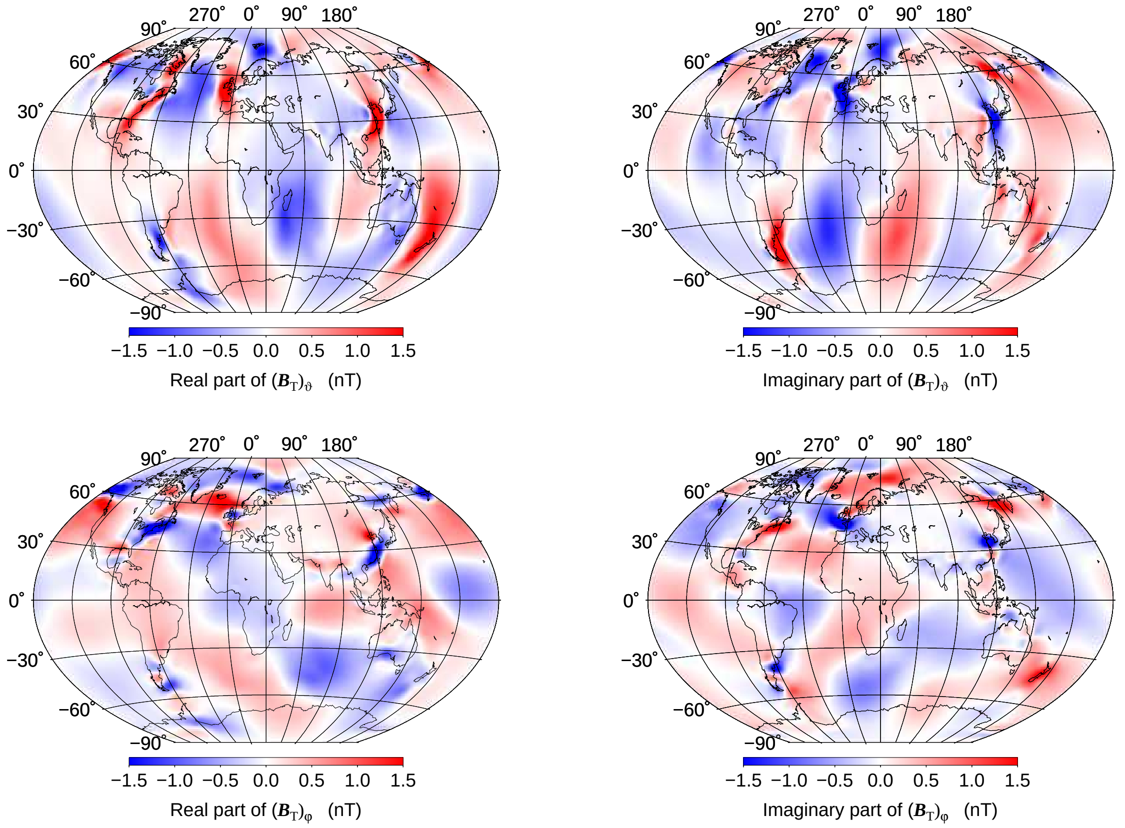

Figure 4.5: Real (left) and imaginary (right) parts of the ϑ (top) and φ (bottom) components of the toroidal magnetic field (in nT) at the ocean bottom induced by depth decaying horizontal flow with the ocean layer of the depth of $h = 1$ km and realistic electrical conductivity profile beneath and inside the ocean layer. A comparable result obtained with matrix-propagator method is shown in Figure 3.5.

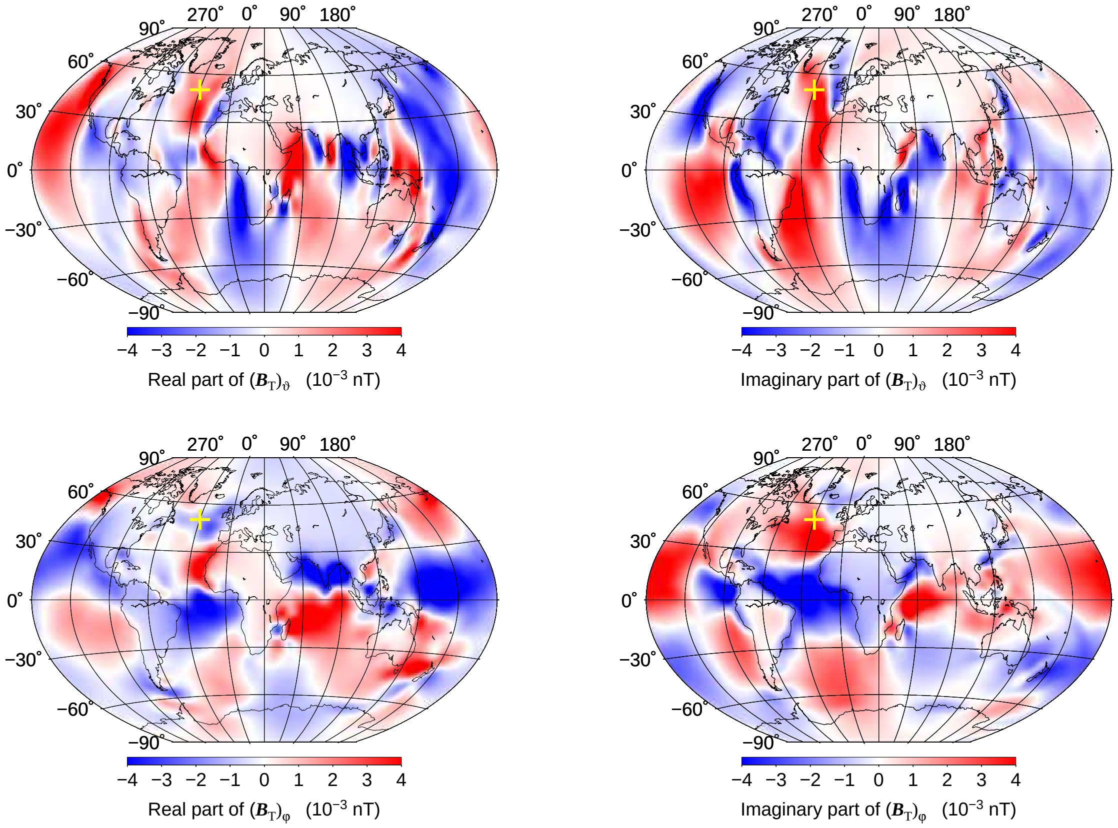

Figure 4.6: Real (left) and imaginary (right) parts of the ϑ (top) and φ (bottom) components of the toroidal magnetic field (in 10^{-3} nT) at the ocean bottom induced by over the depth constant tidal flow with ocean layer of the depth of $h = 4$ km and realistic electrical conductivity profile beneath and inside the ocean layer. A Comparable result obtained with matrix-propagator method is shown in Figure 3.10. The yellow crosses at 50° N, 30° W mark the location where the corresponding radial profiles calculated by matrix-propagator method are plotted (see Figs. 3.12).

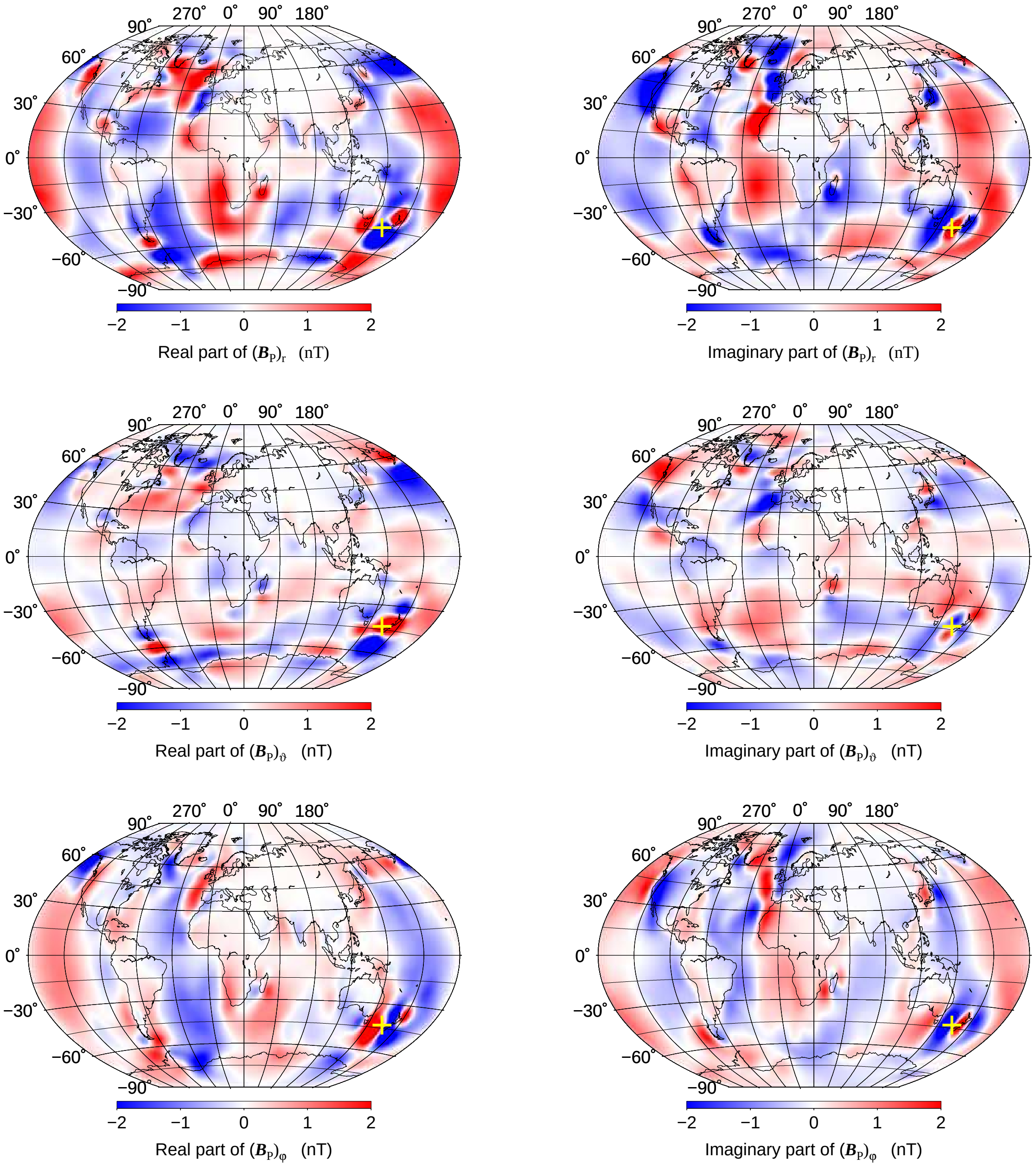

Figure 4.7: Real (left) and imaginary (right) parts of the r (top), ϑ (middle) and φ (bottom) components of the poloidal magnetic field (in nT) at top of the ocean induced by over the depth constant tidal flow with ocean layer of the depth of $h = 4$ km, with insulating underground ($\sigma_\mathrm{m} = 0$ Sm^{-1}) and ocean layer conductivity $\sigma_\mathrm{o} = 3.5$ Sm^{-1}. The yellow crosses at 43° S, 164° E mark the location where the radial profiles of the poloidal magnetic field are plotted (see Figs. 4.10).

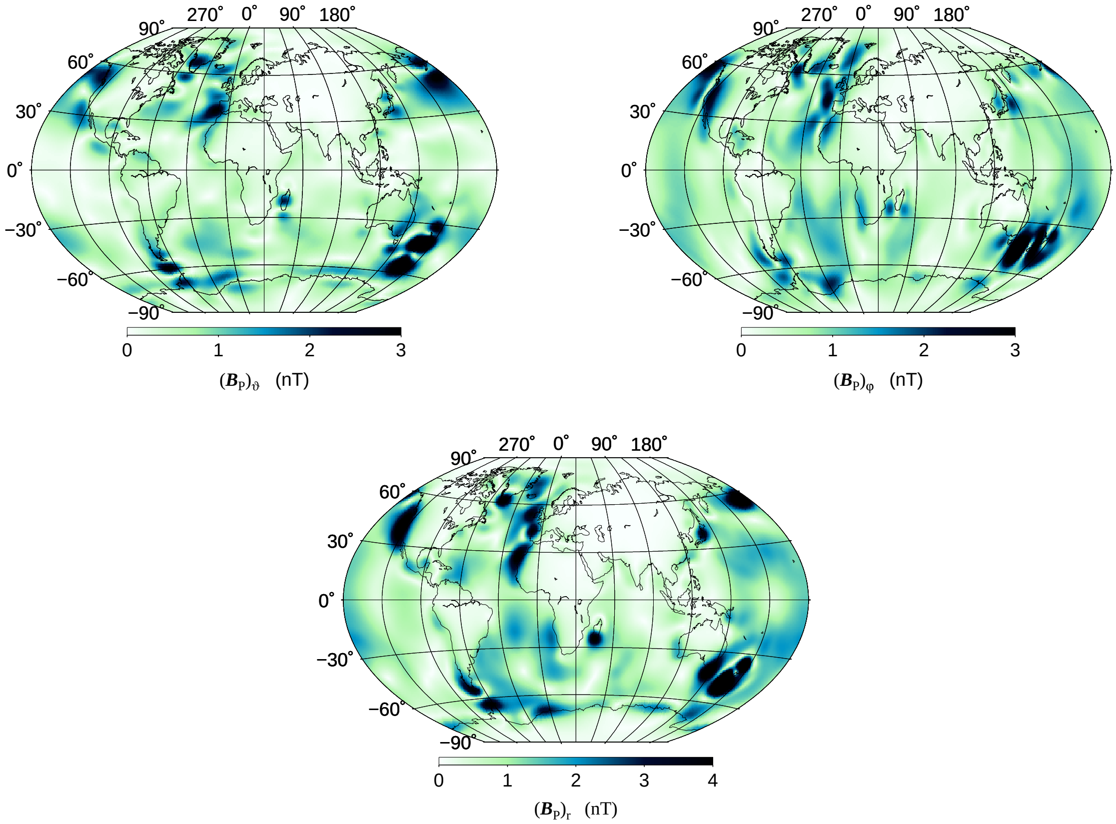

Figure 4.8: Amplitude of the ϑ (top left), φ (top right) and r (bottom) components of the induced poloidal magnetic field (in nT) at top of the ocean according to the magnetic field generated by condition in Figure 4.7.

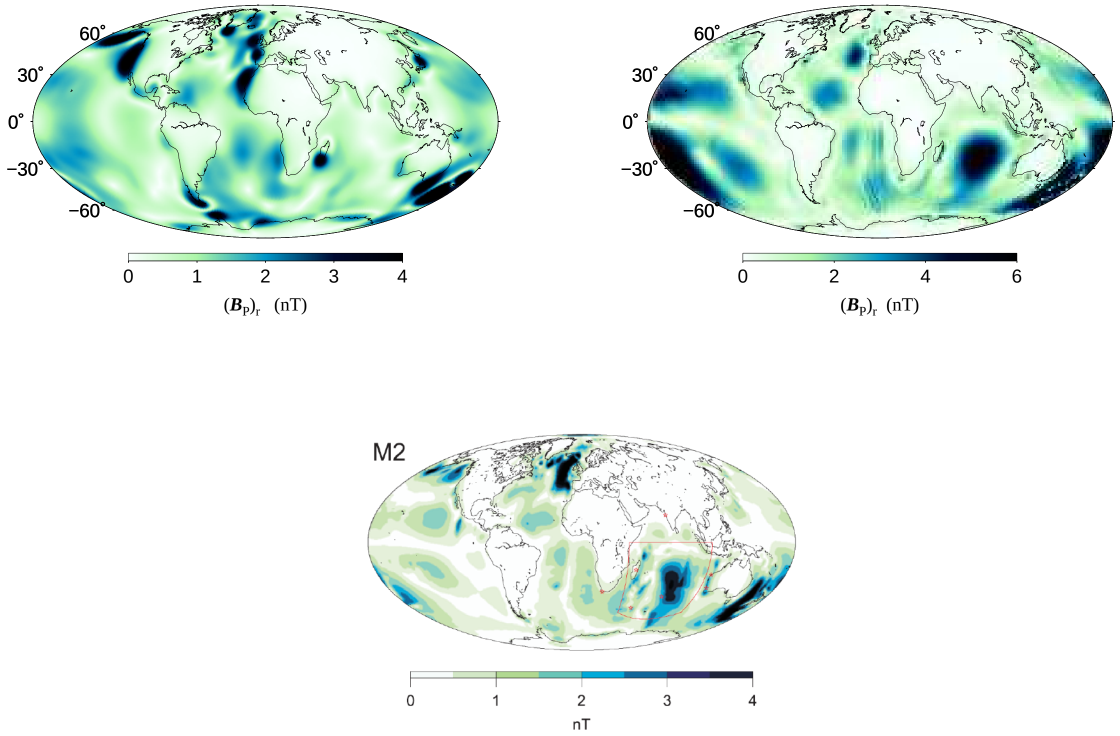

Figure 4.9: Comparison of the r component of the induced poloidal magnetic field (in nT) at the top of the ocean. On the top left panel the amplitude of the magnetic field generated in Figure 4.7 and on the top right panel the result from thin sheet approximation from Dostal (2009). The OMCT input ocean velocity field is for both calculations identical. At the bottom panel the amplitudes calculated with thin sheet approximation by Maus and Kuvshinov (2004) using the ocean velocity data set from TPXO 6.1. (Mind that the scale bars are not identical.)

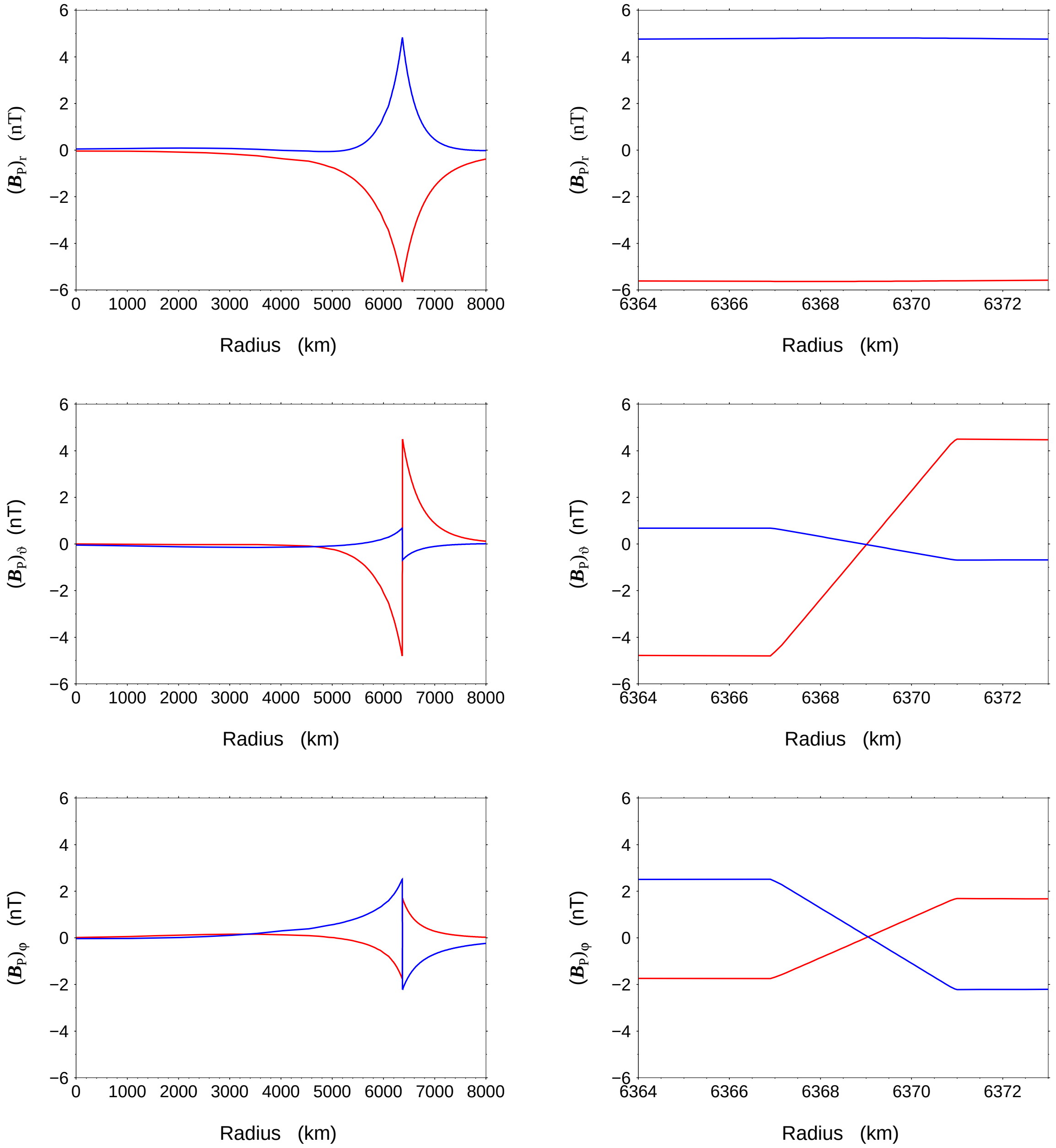

Figure 4.10: Real (red) and imaginary (blue) parts of the r (top), ϑ (middle) and φ (bottom) components of the poloidal magnetic field (in nT) induced by over the depth constant tidal flow as functions of radius, beneath the ocean (left) and, in detail, inside the ocean layer (right) with uniform electrical conductivity profile beneath the ocean $\sigma_\mathrm{m} = 0\ \mathrm{Sm}^{-1}$ and inside the ocean layer $\sigma_\mathrm{o} = 3.5\ \mathrm{Sm}^{-1}$. The radial profiles are taken at the location given by the yellow crosses in Figure 4.7.

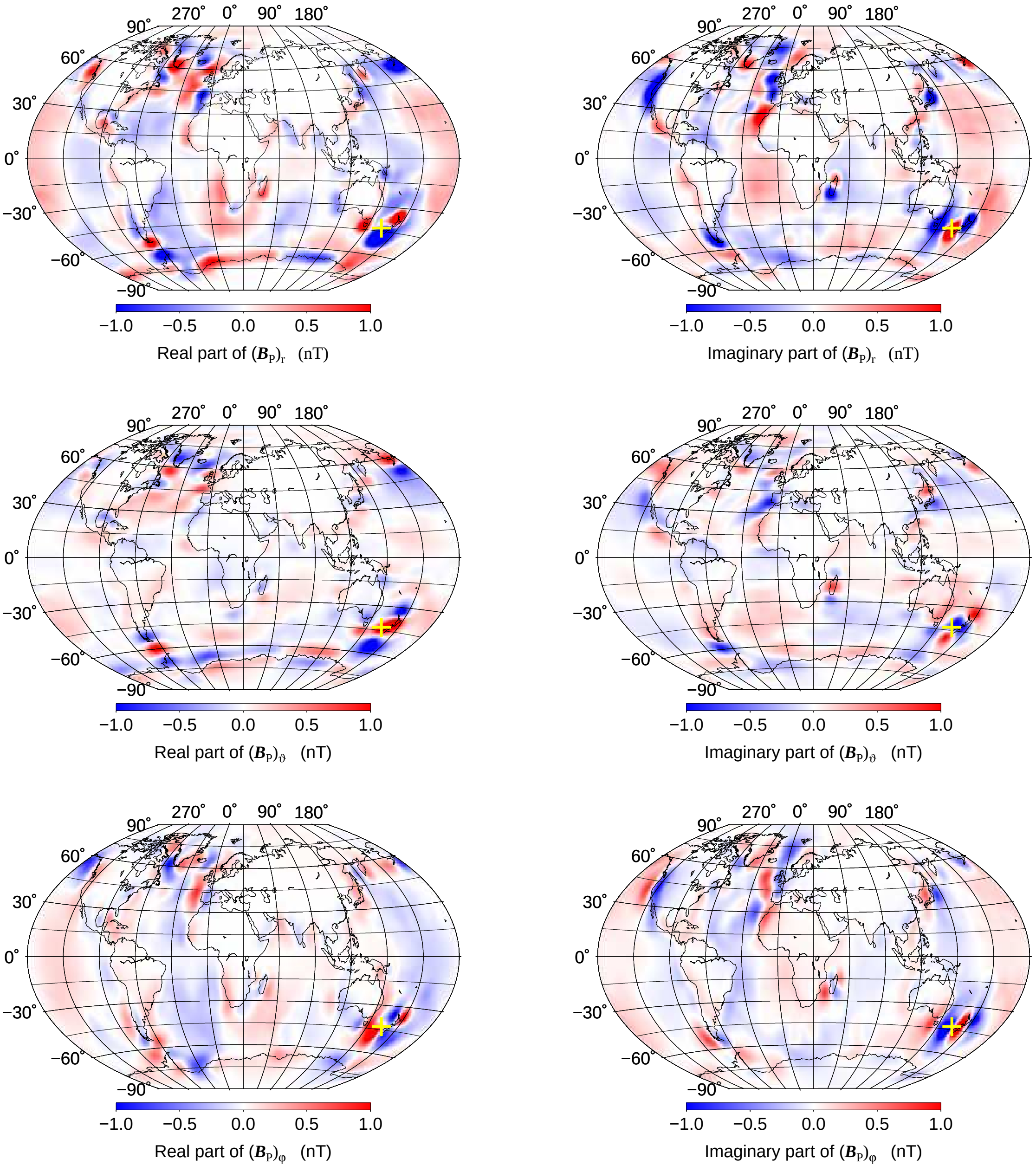

Figure 4.11: Real (left) and imaginary (right) parts of the r (top), ϑ (middle) and φ (bottom) components of the poloidal magnetic field (in nT) at top of the ocean induced by over the depth constant tidal flow with ocean layer of the depth of $h = 4$ km, uniform electrical conductivity profile beneath ($\sigma_\mathrm{m} = 1\ \mathrm{Sm}^{-1}$) and inside the ocean ($\sigma_\mathrm{o} = 3.5\ \mathrm{Sm}^{-1}$). The yellow crosses at 43° S, 164° E mark the location where the radial profiles of the poloidal magnetic field are plotted (see Figs. 4.13). Comparable result with matrix-propagator method is shown in Figure 3.13.

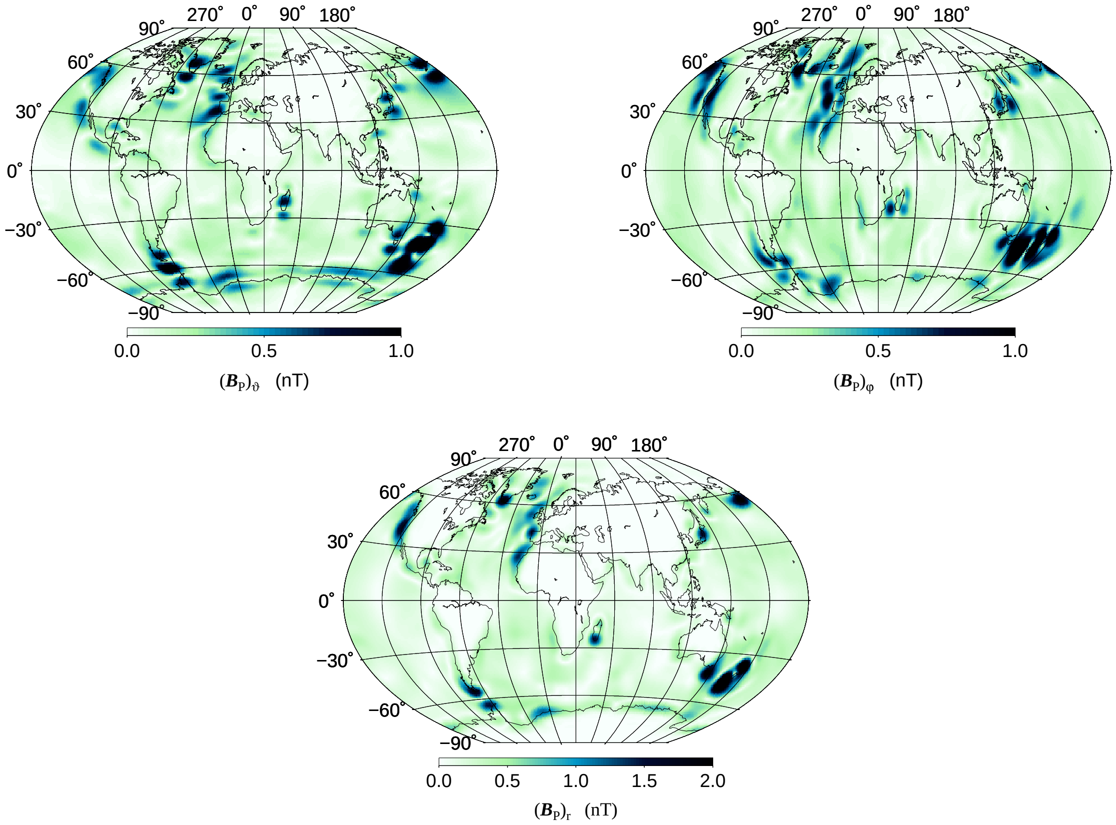

Figure 4.12: Amplitude of the ϑ (top left), φ (top right) and r (bottom) components of the induced poloidal magnetic field (in nT) at top of the ocean according to the magnetic field generated by condition in Figure 4.11.

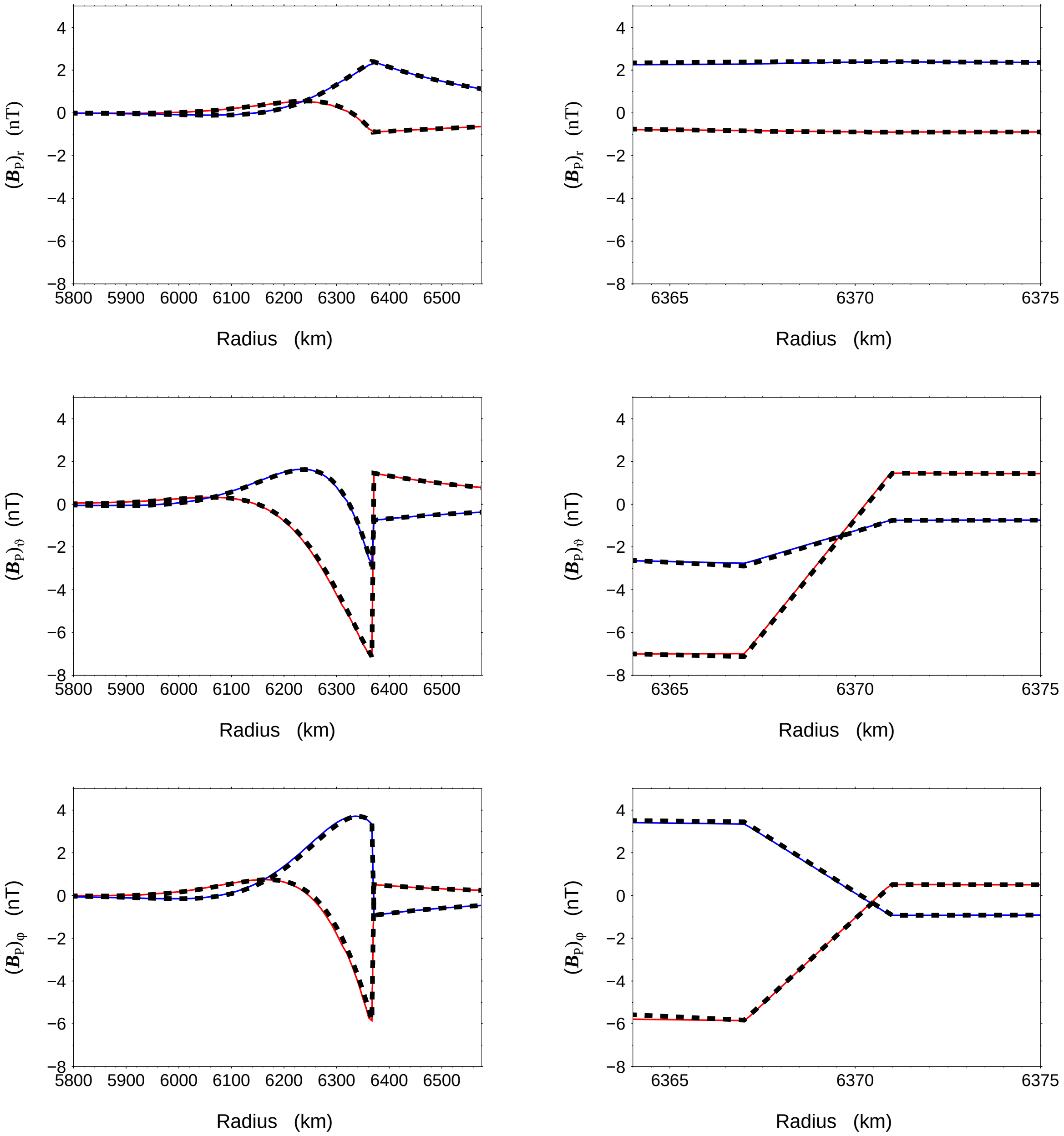

Figure 4.13: Real (red) and imaginary (blue) parts of the r (top), ϑ (middle) and φ (bottom) components of the poloidal magnetic field induced by over the depth constant tidal flow as functions of radius, beneath (left) and, in detail, inside the ocean layer (right), with ocean layer of the depth of $h = 4$ km, uniform electrical conductivity profile beneath ($\sigma_\mathrm{m} = 1\ \mathrm{Sm}^{-1}$) and inside ($\sigma_\mathrm{o} = 3.5\ \mathrm{Sm}^{-1}$) the ocean layer. The black rectangles lines represent the solution of the variational method compared with the solution of the matrix-propagator method in solid colored lines. The radial profiles are taken at the location given by the yellow crosses in Figures 4.11 and 3.13.

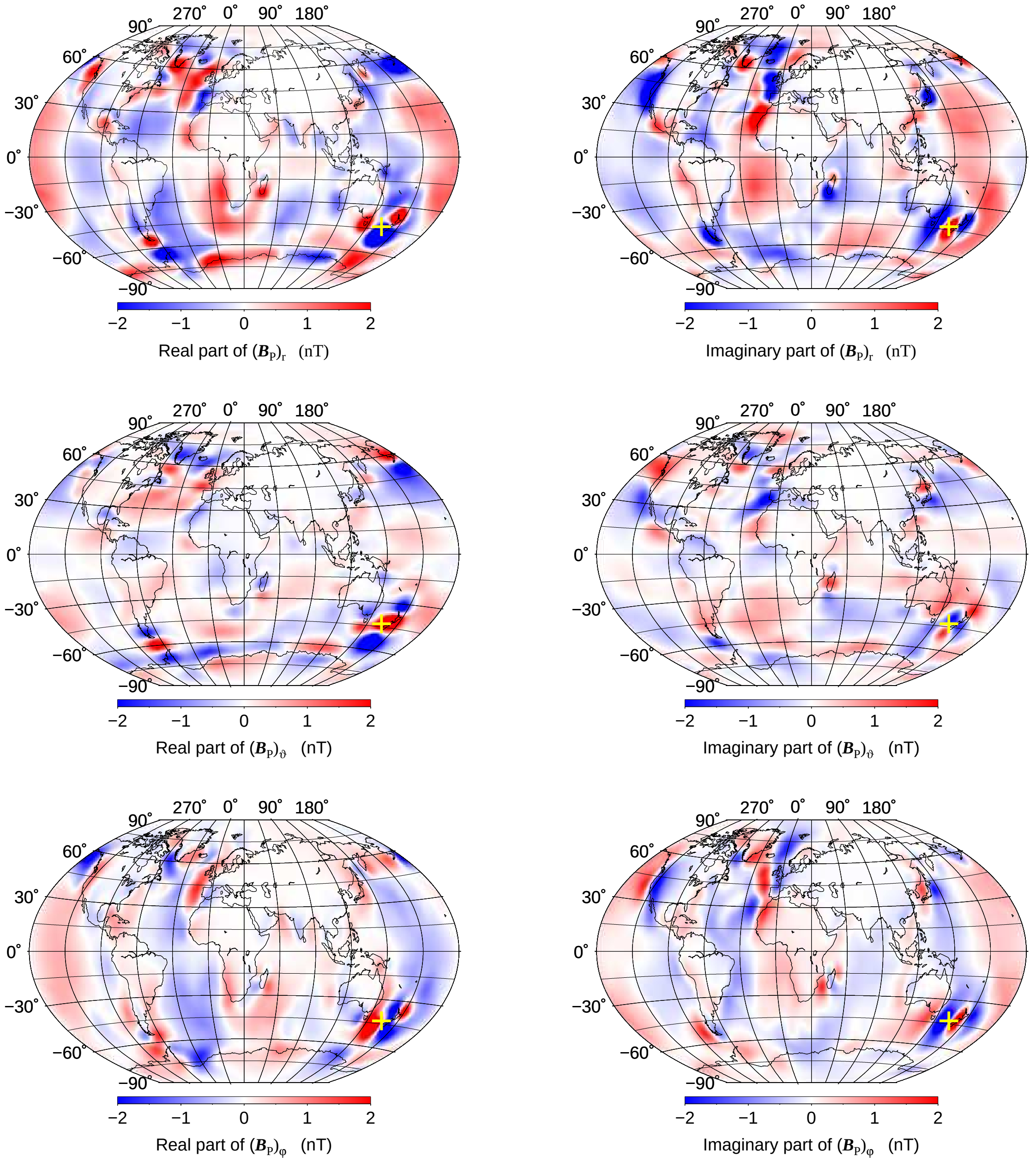

Figure 4.14: Real (left) and imaginary (right) parts of the r (top), ϑ (middle) and φ (bottom) components of the poloidal magnetic field (in nT) at top of the ocean induced by over the depth constant tidal flow with ocean layer of the depth of $h = 4$ km, realistic electrical conductivity profile beneath the ocean and uniform conductivity inside the ocean layer ($\sigma_{\mathrm{o}} = 3.5\ \mathrm{Sm}^{-1}$). The yellow crosses at 43° S, 164° E mark the location where the radial profiles of the poloidal magnetic field are plotted (see Figs. 4.16).

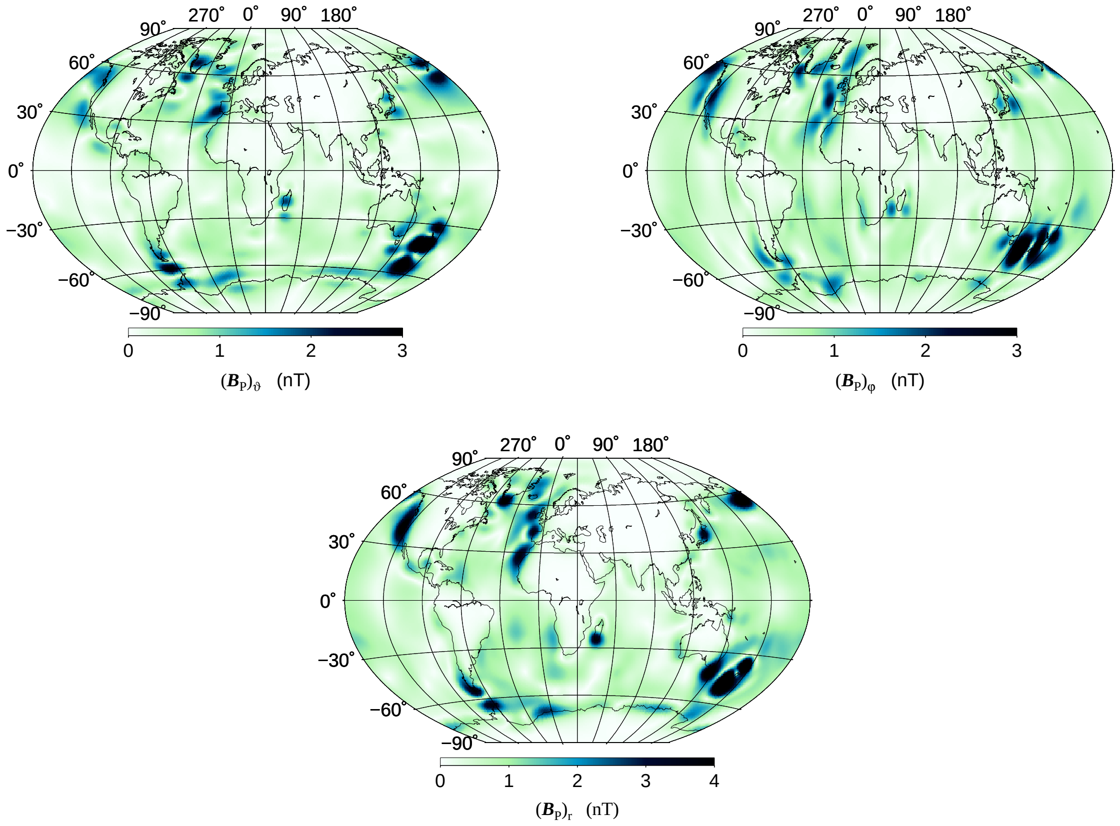

Figure 4.15: Amplitude of the ϑ (top left), φ (top right) and r (bottom) components of the poloidal magnetic field (in nT) at top of the ocean according to the magnetic field induced by condition in Figure 4.14.

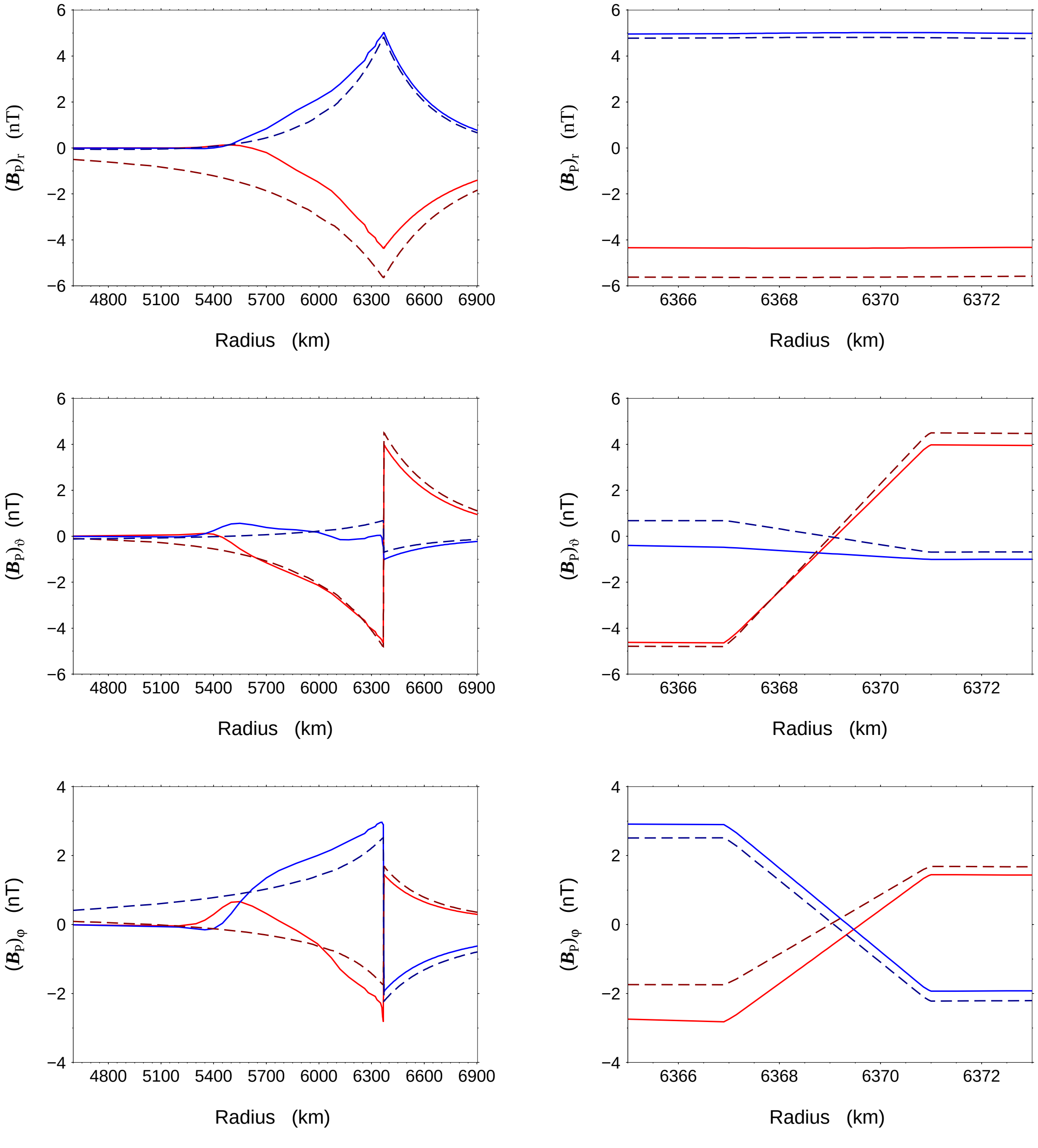

Figure 4.16: Real (red) and imaginary (blue) parts of the r (top), ϑ (middle) and φ (bottom) components of the poloidal magnetic field induced by over the depth constant tidal flow as functions of radius, beneath (left) and, in detail, inside the ocean layer (right) with realistic electrical conductivity profile beneath the ocean and uniform conductivity inside the ocean layer (solid lines). The dashed lines represent the solution with insulating underground ($\sigma_\mathrm{m} = 0$ Sm^{-1}). The radial profiles are taken at the location given by the yellow crosses in Figure 4.14.

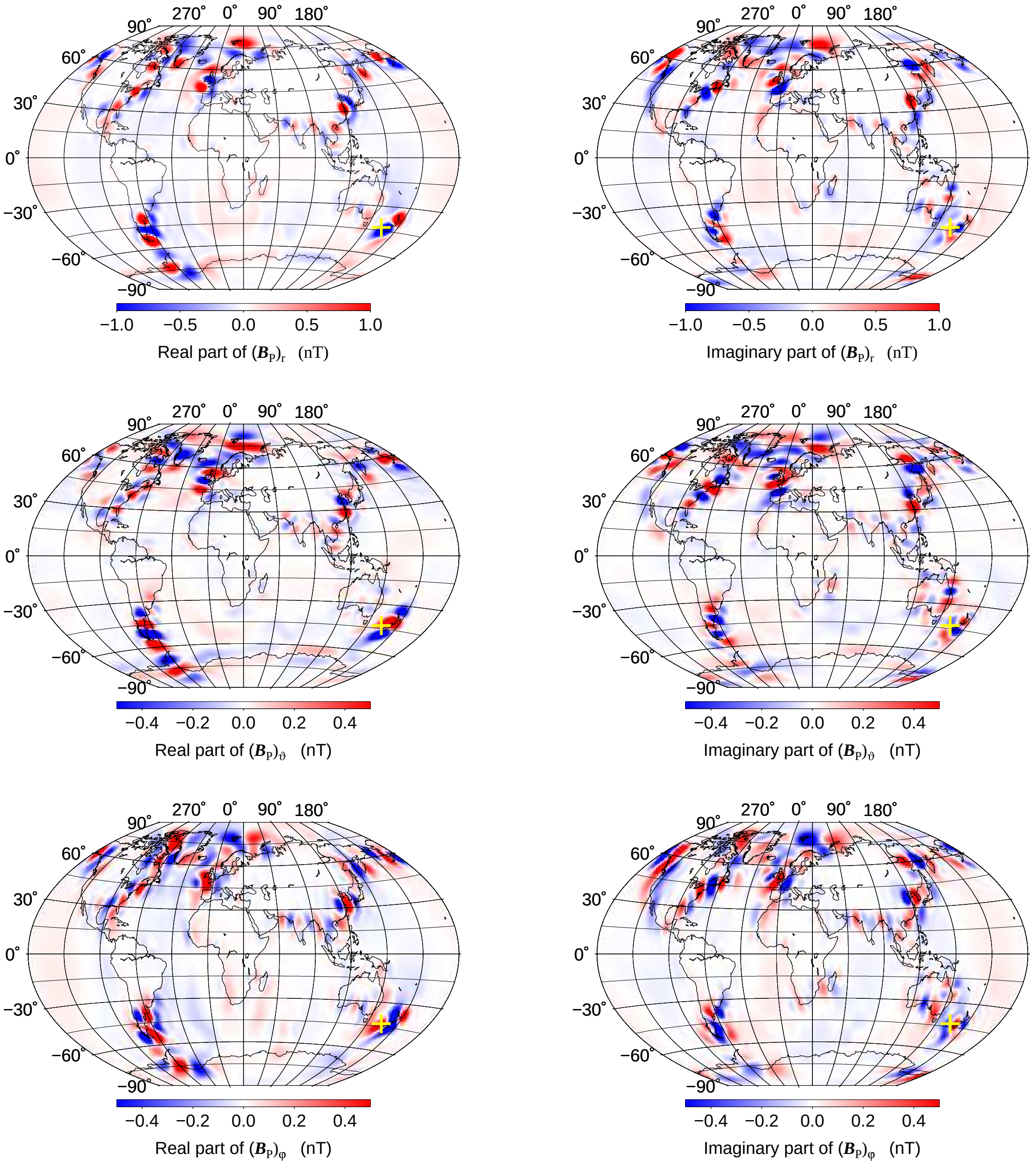

Figure 4.17: Real (left) and imaginary (right) parts of the r (top), ϑ (middle) and φ (bottom) components of the poloidal magnetic field (in nT) at top of the ocean induced by over the depth constant tidal flow with the ocean layer of the depth of $h = 1$ km, uniform electrical conductivity profile beneath ($\sigma_{\mathrm{m}} = 1$ Sm^{-1}) and inside ($\sigma_{\mathrm{o}} = 3.5$ Sm^{-1}) the ocean layer. The yellow crosses at 43° S, 164° E mark the location where the radial profiles of the poloidal magnetic field are plotted (see Figs. 4.19). Comparable result with matrix-propagator method is shown in Figure 3.14.

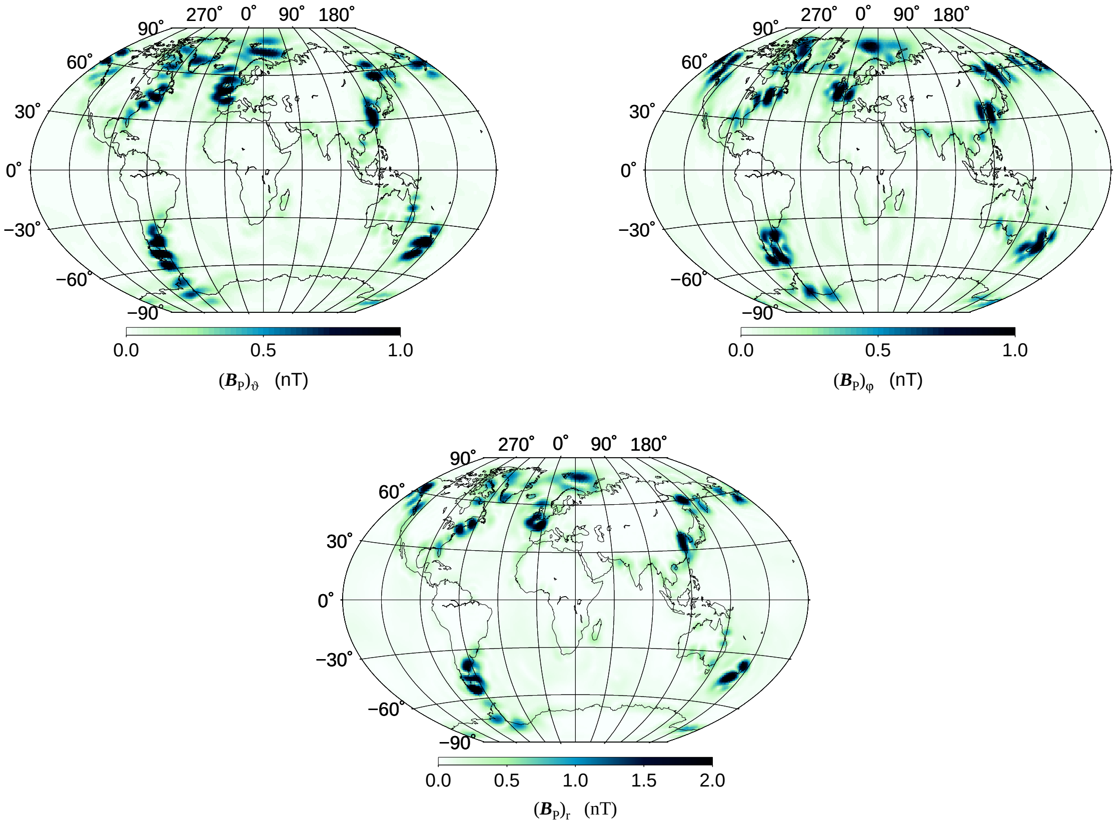

Figure 4.18: Amplitude of the ϑ (top left), φ (top right) and r (bottom) components of the poloidal magnetic field (in nT) at top of the ocean according to the magnetic field induced by condition in Figure 4.17.

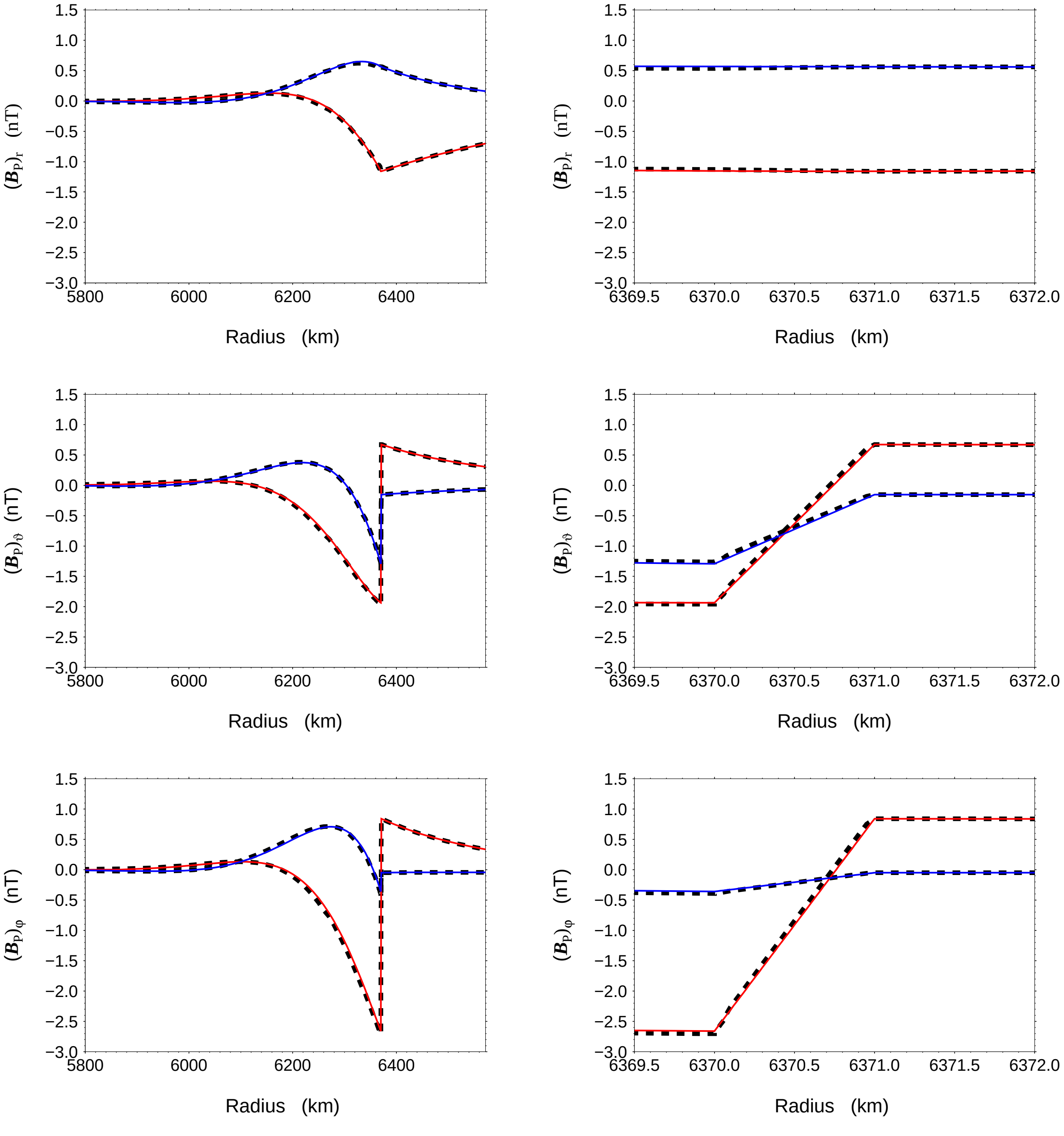

Figure 4.19: Real (red) and imaginary (blue) parts of the r (top), ϑ (middle) and φ (bottom) components of the poloidal magnetic field induced by over the depth constant tidal flow as functions of radius, beneath (left) and, in detail, inside the ocean layer (right) with uniform electrical conductivity profile beneath ($\sigma_\mathrm{m} = 1$ Sm^{-1}) and inside ($\sigma_\mathrm{o} = 3.5$ Sm^{-1}) the ocean layer. The black rectangles lines represent the solution of the variational method compared with the solution of the matrix-propagator method in solid colored lines. The radial profiles are taken at the location given by the yellow crosses in Figures 4.17 and 3.14.

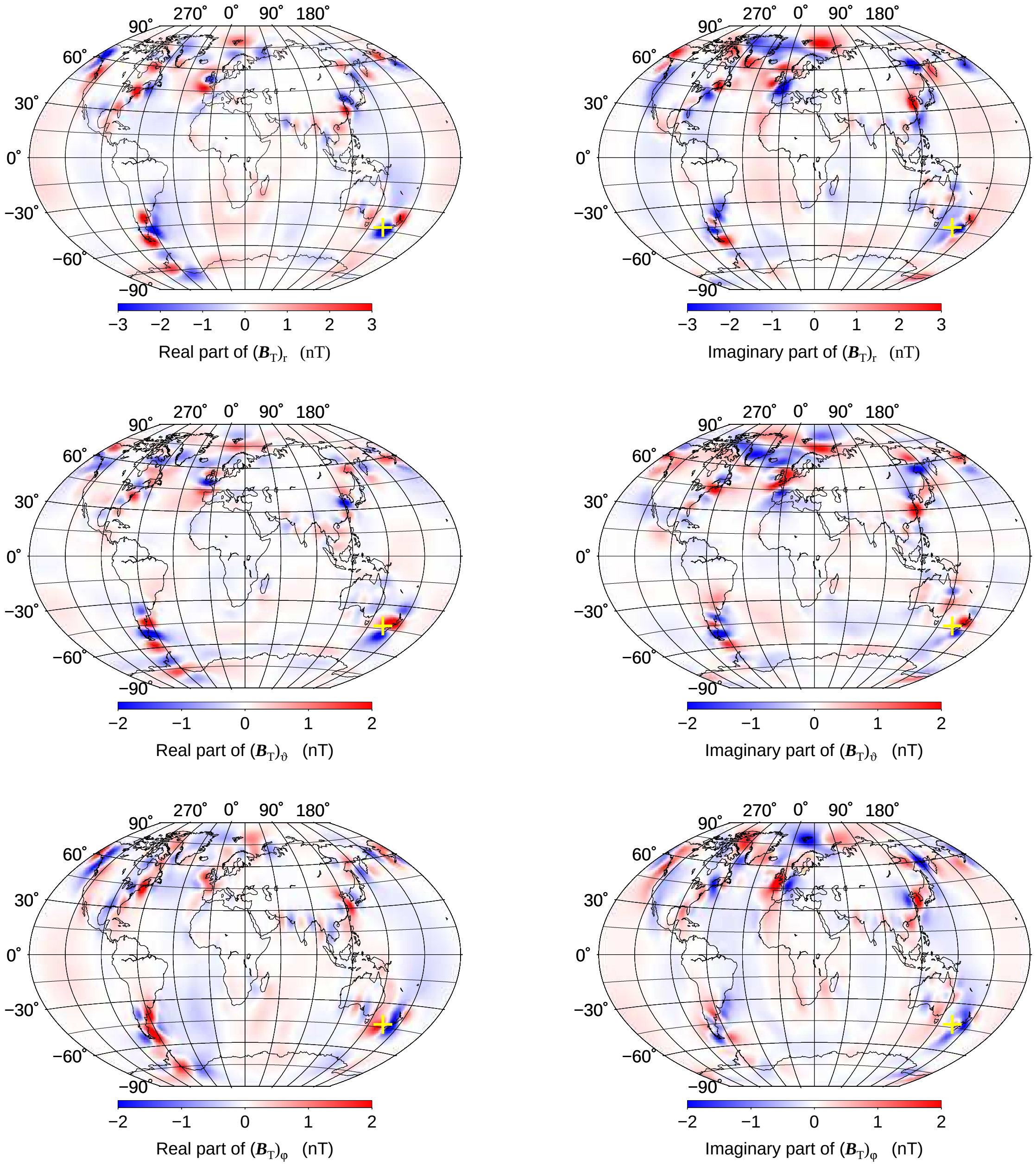

Figure 4.20: Real (left) and imaginary (right) parts of the r (top), ϑ (middle) and φ (bottom) components of the poloidal magnetic field (in nT) at top of the ocean induced by over the depth constant tidal flow with the ocean layer of the depth of $h = 1$ km, realistic electrical conductivity profile beneath the ocean and uniform conductivity inside the ocean layer ($\sigma_\mathrm{o} = 3.5\ \mathrm{Sm}^{-1}$). The yellow crosses at 43° S, 164° E mark the location where the radial profiles of the poloidal magnetic field are plotted (see Figs. 4.22).

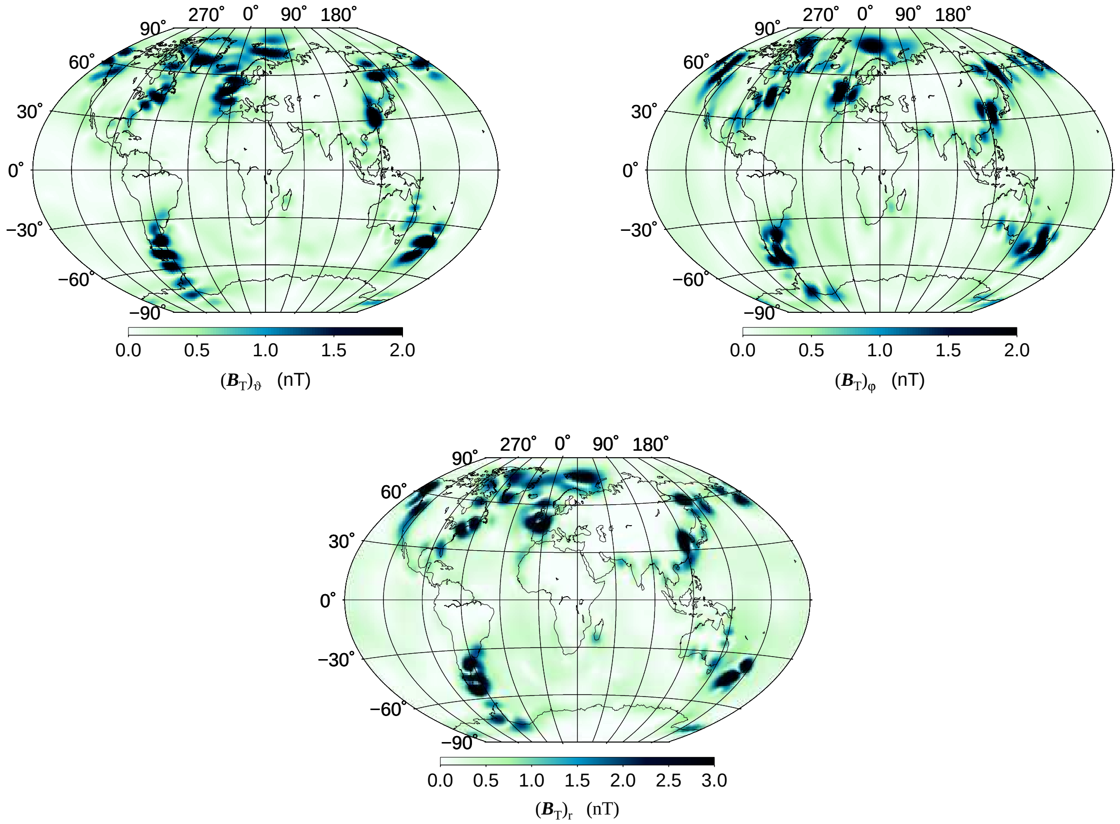

Figure 4.21: Amplitude of the ϑ (top left), φ (top right) and r (bottom) components of the poloidal magnetic field (in nT) at top of the ocean according to the magnetic field induced by condition in Figure 4.20.

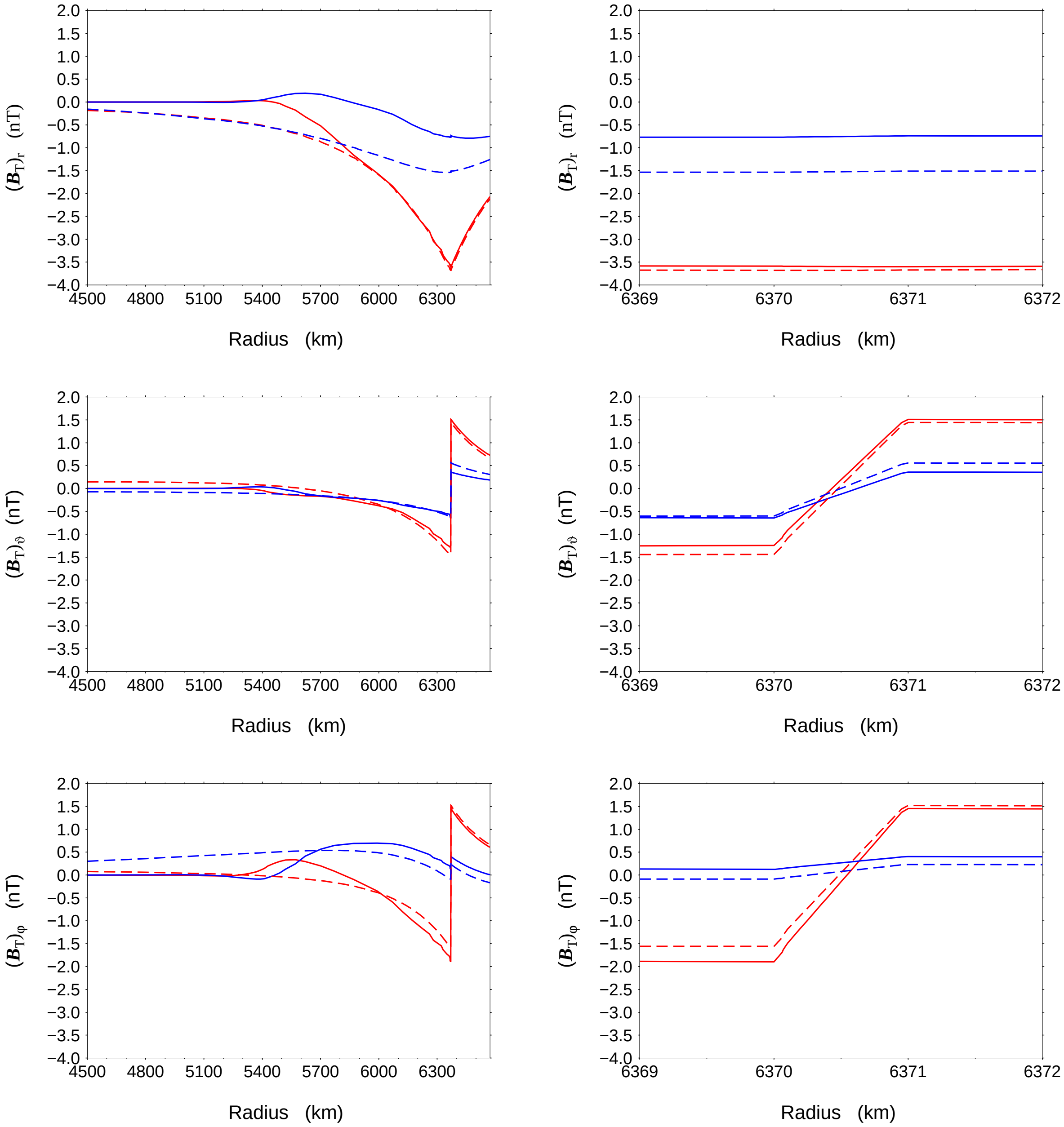

Figure 4.22: Real (red) and imaginary (blue) parts of the r (top), ϑ (middle) and φ (bottom) components of the poloidal magnetic field induced by over the depth constant tidal flow as functions of radius, beneath (left) and, in detail, inside the ocean layer (right) with realistic electrical conductivity profile (solid lines) and insulating underground (dashed lines) beneath the ocean layer. The radial profiles are take at the location given by the yellow crosses in Figure 4.20.

Chapter 5

Spectral finite-element approach for ocean-induced magnetic field in time domain

In this chapter we present the solution for the toroidal ocean-induced magnetic field in the time domain. The approach is based on the numerical method derived in chapter 4 combined with the time domain solution presented by Martinec et al. (2003).

5.1 Time domain solution for the toroidal magnetic field

The induction equation in the time domain has been derived in chapter 1, see eq. (1.16),

$$\frac{1}{\mu_0}\,\mathrm{curl}\left(\frac{1}{\sigma}\;\mathrm{curl}\,\boldsymbol{B}^{i+1}\right)+\frac{\boldsymbol{B}^{i+1}-\boldsymbol{B}^{i}}{\Delta t}=\mathrm{curl}(\boldsymbol{u}_{i+1}\times\boldsymbol{B}_0)\;. \tag{5.1}$$

It can be rewritten in the form

$$\frac{1}{\mu_0}\,\mathrm{curl}\left(\frac{1}{\sigma}\;\mathrm{curl}\,\boldsymbol{B}^{i+1}\right)+\frac{1}{\Delta t}\boldsymbol{B}^{i+1}=\frac{1}{\Delta t}\boldsymbol{B}^{i}+\mathrm{curl}(\boldsymbol{u}_{i+1}\times\boldsymbol{B}_0)\;. \tag{5.2}$$

Then the weak formulation consists of finding $\boldsymbol{B}\in\mathcal{V}$ such that, at fixed time, the following variational equation is satisfied

$$\mathscr{A}(\boldsymbol{B}^{i+1},\delta\boldsymbol{B})+\frac{1}{\Delta t}\,\mathscr{B}(\boldsymbol{B}^{i+1},\delta\boldsymbol{B})=\frac{1}{\Delta t}\,\mathscr{B}(\boldsymbol{B}^{i},\delta\boldsymbol{B})+\mathscr{F}(\delta\boldsymbol{B})\qquad\forall\delta\boldsymbol{B}\in\mathcal{V}\;. \tag{5.3}$$

The functional space $\mathcal{V}$ is defined by equation (4.3). The energy functionals have analogous forms to those for the toroidal magnetic field in Fourier frequency domain (section 4.1)

$$\mathscr{A}(\boldsymbol{B}^{i},\delta\boldsymbol{B}):=\frac{1}{\mu_0}\int_{\mathcal{G}}\frac{1}{\sigma}(\mathrm{curl}\,\boldsymbol{B}^{i}\cdot\mathrm{curl}\,\delta\boldsymbol{B})\,dV\;, \tag{5.4}$$

$$\mathscr{B}(\boldsymbol{B}^{i},\delta\boldsymbol{B}):=\int_{\mathcal{G}}\left(\boldsymbol{B}^{i}\cdot\delta\boldsymbol{B}\right)dV \tag{5.5}$$

and the forcing functional has the form

$$\mathscr{F}(\delta\boldsymbol{B}):=\int_{\mathcal{G}_{\mathrm{O}}}\mathrm{curl}(\boldsymbol{u}_{i+1}\times\boldsymbol{B}_0)\cdot\delta\boldsymbol{B}\,dV\;. \tag{5.6}$$

In analogy to the Fourier frequency domain, the parametrized functionals $\mathscr{A}$, $\mathscr{F}$ are given by equations (4.44) and (4.55), respectively. The functional $\mathscr{B}$ is defined by equation (4.39), where the angular frequency ω is omitted. With this parametrization, the numerical solution of eq. (5.3) is given by a solution of the Galerkin system, which is analogous to that in subsection 4.2.1,

$$\mathscr{A}(\boldsymbol{B}_{\mathrm{h}}^{i+1}, \delta\boldsymbol{B}_{\mathrm{h}}) + \frac{1}{\Delta t}\,\mathscr{B}(\boldsymbol{B}_{\mathrm{h}}^{i+1}, \delta\boldsymbol{B}_{\mathrm{h}}) = \frac{1}{\Delta t}\,\mathscr{B}(\boldsymbol{B}_{\mathrm{h}}^{i}, \delta\boldsymbol{B}_{\mathrm{h}}) + \mathscr{F}(\delta\boldsymbol{B}_{\mathrm{h}}) \qquad \forall\delta\boldsymbol{B}_{\mathrm{h}} \in \mathcal{V}_{\mathrm{h}}\ , \quad (5.7)$$

where $\mathcal{V}_{\mathrm{h}}$ is the solution space defined by eq. (4.70).

5.2 Numerical results of the time domain

Calculations in the time domain are carried out for the same ocean velocities $\boldsymbol{u}$ as in the previous chapters for modelling in the Fourier frequency domain. We discretize the M_2 tide period in 20 time steps ($\Delta t = \frac{1}{20}\,T_{M_2}$) according to relation (2.47), calculate the source term separately for every time instant and create a source-term time series. As is already indicated by label i, $\boldsymbol{B}^i$ in the functional $\mathscr{B}$ on the right hand side of eq. (5.7) is given by the solution in the previous time step.

Since the initial value of $\boldsymbol{B}$ is not known, an arbitrary $\boldsymbol{B}$ is used for its initialization (for example zero), and the so called spin-up process is necessary to perform. During the spin-up process, the model is loaded by a source term until an equilibrium between the input of the energy and the energy dissipation is achieved. Therefore calculations are started by repeating successively the periodical tidal wave several times until the time evolution of a new solution is identical with the previous one. Due to periodical signal variations with magnetic field polarity change, the spin-up process necessities repetitions of the tidal period only several times.

In this section, we present a solution only for one numerical experiment described by the ocean layer of the depth of $h = 1$ km, average over the depth constant horizontal ocean velocity field and realistic conductivity profile for the ocean and the mantle. The analytical solution of this numerical experiment has already been discussed from the point of physics in chapter 3. Here, we focus on the validation of the time domain solution by comparing it with the analytical solution in Fourier frequency domain.

Figure 5.1 compares the real and imaginary parts of the ϑ and φ components of the analytical solution in Fourier frequency domain against the 1. and 15. time-instant snapshot of the time domain solution. The results agree well in magnitude and spatial patterns, but small differences are apparent. They are given by numerical limitation of the analytical solution due to the realistic parametrization of the model, which was already discussed in previous chapters. The real and imaginary part of the solution in the Fourier frequency domain are orthogonal to each other. This property of a periodical signal corresponds to 90° angular shift, which can also be found in the time-domain solution. By discretization of the tidal signal period into 20 time steps, we find that the time span between the 15. and 1. time instant again corresponds with the 90° angular shift of the signal period.

Figure 5.2 presents the time evolution of the φ component of the toroidal magnetic field at the ocean bottom over one period of M_2 tide. The time instants are numbered for every image, but not all time instants are shown. Beside the time evolution of spatial patterns, the polarity reverse of the magnetic field after a half of the period is apparent. The images labeled by x and $10 + x$ show the pair with the same spatial distribution but the opposite polarity. As the magnetic field repeats after every period, the last image, is continued again by the image labeled with number 1.

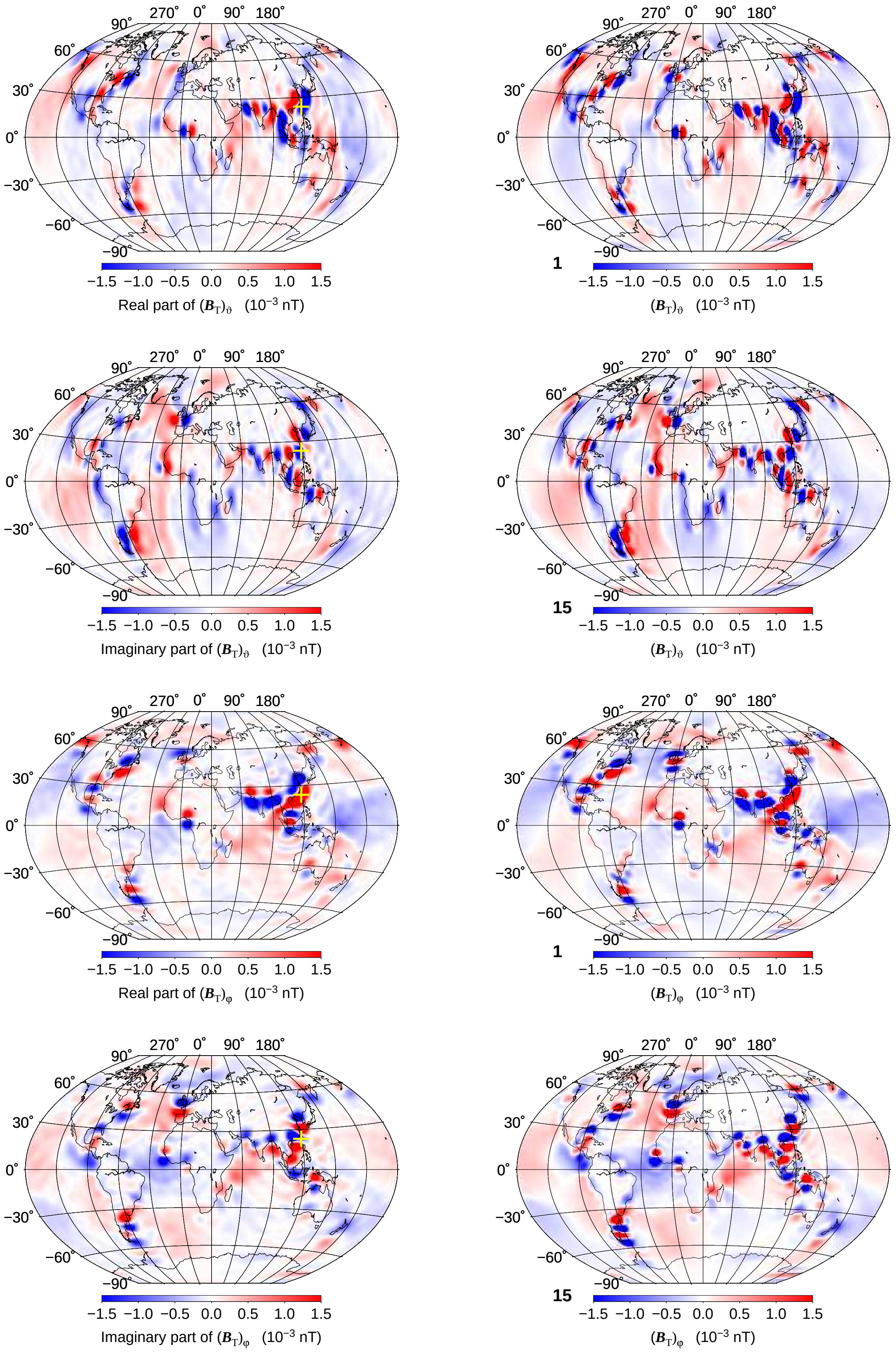

Figure 5.1: Comparison of the analytical solution in Fourier frequency domain from Fig. 3.2 (left-hands panels) against the time domain solution (right-hands panels) for the toroidal magnetic field (in 10^{-3} nT) at the ocean bottom induced by over the depth constant tidal flow for the ocean layer of the depth of $h = 1$ km and the realistic electrical conductivity profile beneath and inside the ocean layer. The top two rows show the ϑ component, the bottom two the φ component. The real (cos) part of the magnetic field (shown in first and third row) correspond with the 1. and the imaginary (sin) part with the 15. time instant of the numerical solution, respectively.

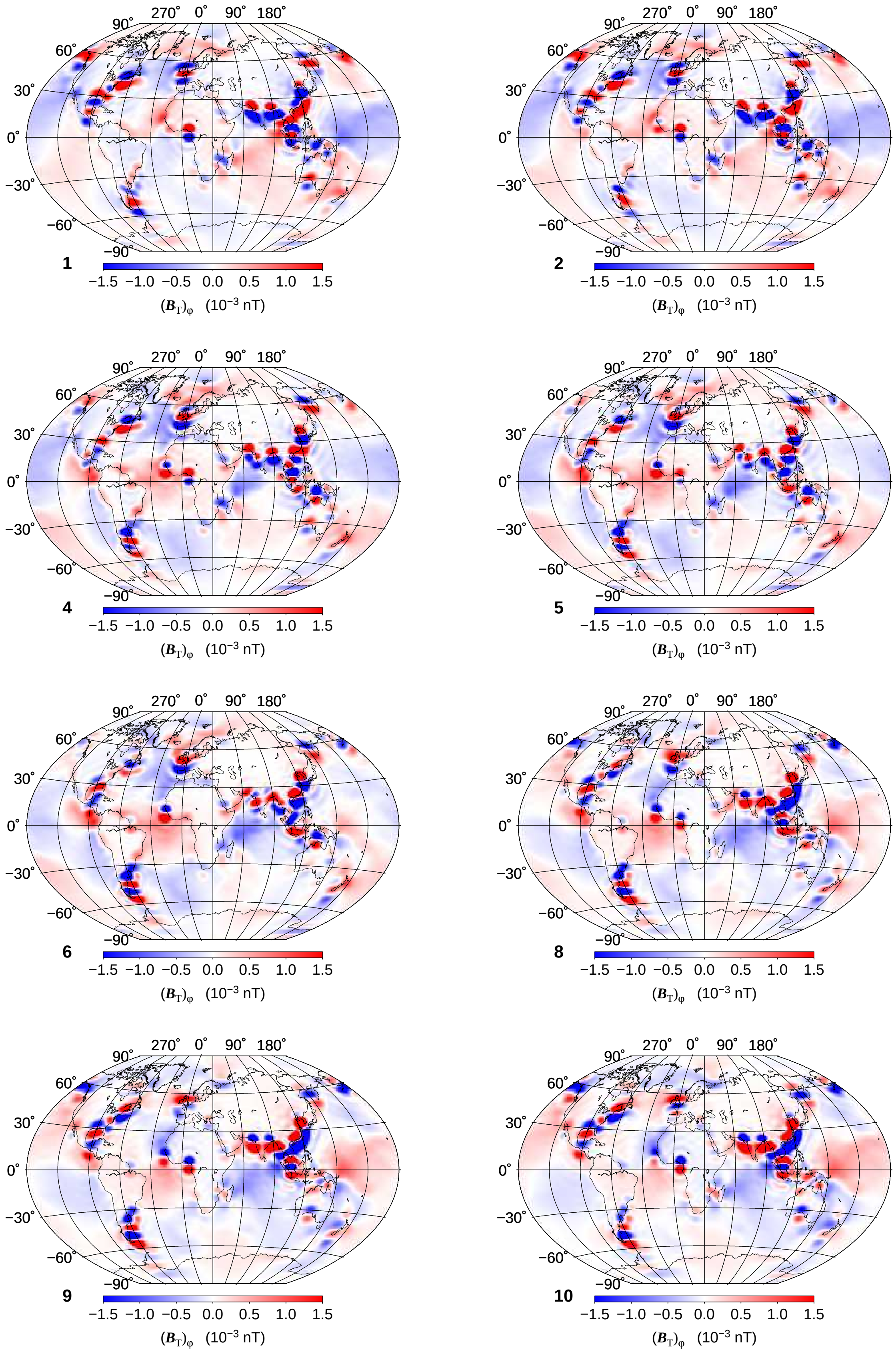

Figure 5.2: The time evolution of the φ component for toroidal magnetic field (in 10^{-3} nT) at the ocean bottom induced by over the depth constant tidal flow with the ocean layer of the depth of $h = 1$ km and realistic electrical conductivity profile beneath and inside the ocean layer. The M_2 tide period is discretized in 20 time instants, $\Delta t = \dfrac{1}{20}\,T_{M_2}$. (Not all time instants shown.)

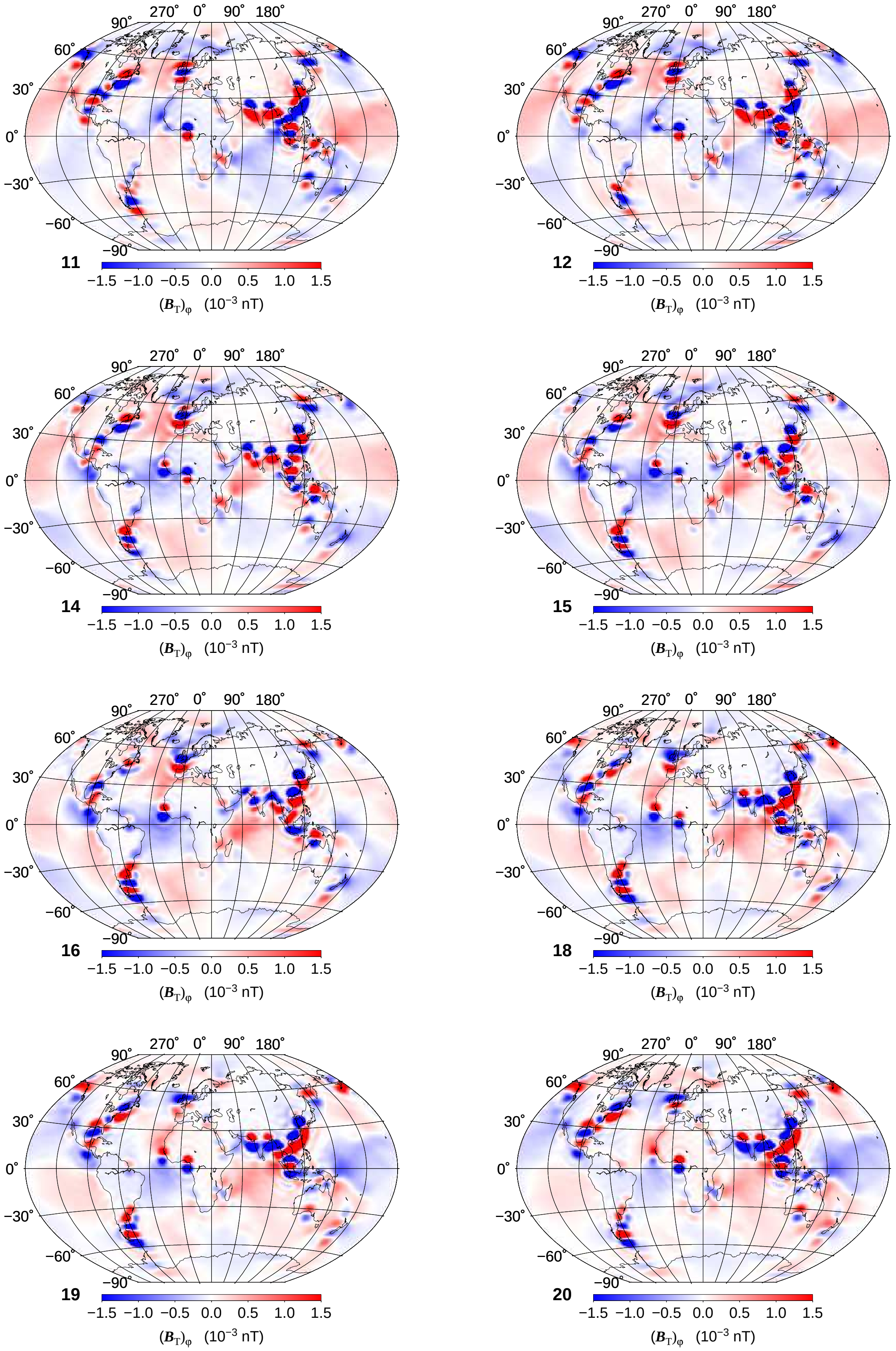

Figure 5.2: (Continued)

Summary and Outlook

Increasing accuracy of space-borne magnetometers, especially by the recently launched mission Swarm, renew the question about the identification of global magnetic features induced by oceans and their use as an indicator for oceanic dynamic. For understanding the dynamic of ocean-induced magnetic fields, their structures, magnitudes and behaviours with respect to different parameters necessitate a numerical modelling. The present day thin-sheet models for computing global ocean-induced magnetic field are not sufficient for examining the magnetic signal in detail. Therefore, in this thesis we developed a new finite-layer model where the Earth is approximated by a sphere with a spherically symmetric distribution of electrical conductivity. Using realistic input oceanic flow of M_2 tide, simulated by Oceanic Model for Circulation and Tides (OMCT), main magnetic field and a radial profile of electric conductivity, our model allows separated calculations of the toroidal and poloidal modes of the ocean-induced magnetic field. As the calculation of both magnetic modes are based on the same input data and parametrization, the comparison between the toroidal and poloidal parts can be carried out with respect to magnitude, structure and behaviour.

Our numerical simulations show that the induced toroidal magnetic field is extremely sensitive to the vertical gradient of horizontal ocean flow. Depending on the size of this gradient, the magnitudes of induced toroidal magnetic field at ocean bottom vary from 10^{-3} nT for over the depth constant flow up to several nT if a linear decay of the horizontal ocean flow is imposed. Therefore, the common opinion in the geophysical community dealing with the CHAMP magnetic data that the toroidal component of the magnetic field induced by ocean circulation is larger by an order of magnitude than the induced poloidal part can not be confirmed. This idea originated from Sanford (1971) who estimated that the toroidal magnetic field induced by ocean circulation may be as large as 100 nT. However, neither recent model simulations, nor observations of the toroidal magnetic field can not confirm it since the toroidal magnetic field is not directly observable by coastal magnetic observatories or satellite missions.

We should emphasize that our results on the amplitudes of the toroidal magnetic field are valid for a tidally-forced ocean circulation, while the estimate of 100 nT (Sanford, 1971) has been done for a magnetic field induced by a general ocean circulation model. This may differ in spatial pattern, amplitude and frequency contents in comparison to tidal ocean circulation. Moreover, the limited spatial resolution may also cause the reduction of amplitudes of the induced toroidal magnetic field. Being explicit, we have not found a model setup for the M_2 tidal ocean flow that induces the toroidal magnetic field reaching amplitudes of 100 nT.

The primary poloidal ocean-induced magnetic field reach amplitudes of several nT at the sea surface and it corresponds to the radial component of magnetic field modelled by the thin-sheet approximation. The amplitudes of the primary poloidal magnetic field has already been published by Kuvshinov and Olsen (2005) and Maus and Kuvshinov (2004) and are, in general, accepted by the geomagnetic community. Nevertheless, the spatial patterns show the differences between the thin-sheet model and finite-layer model calculations. These can be explained by considering a different parametrization of continental conductivity. Whereas the thin-sheet approach excludes the continent areas from the solution domain and, therefore, the continents have electrical conductivity zero, the continents in a spherically symmetric model have the conductivity of oceans. However, the differences in spatial distribution of electrical conductivity do not essentially influence the study of the magnetic diffusion in radial direction of the primary poloidal magnetic field inside and beneath the ocean layer.

Additionally, as the finite-layer model enables simulations of the toroidal magnetic field, the secondary poloidal ocean-induced magnetic field, the so called coastal effect, can be estimated. We show that, due to the conductivity contrast between the ocean and continent of the order of $\Delta\sigma = 10^{-3}$ Sm^{-1}, a poloidal magnetic field is generated with magnitudes of the primary poloidal magnetic field. However, the spatial distribution between the two poloidal magnetic fields differ considerable. Whereas the primary part has rather large-scale features over ocean areas, the secondary part is small-scaled and concentrated along coasts.

To examine the correctness of the forward modelling, the validation of obtained results has been carried out. For external verification of our results, we compare them with the thin-sheet approximation. Due to a limited number of published studies on a global scale, internal validations create an essential part of this thesis. For this purpose, the diffusion of the induced magnetic field is solved by two independent methods, the classical (strong) solution and the modern (weak) solution. The agreement between the two methods is confirmed by our calculations. Additional examinations have been carried out by varying input parameters for the individual numerical experiments to test the numerical solutions. For example, considering a symmetric model set up with respect to the ocean layer for the primary poloidal magnetic field and compare the symmetry of the simulated magnetic field beneath and above the ocean layer, we tested different mathematical parametrization of a solution in the atmosphere and mantle.

Using only one particular tidal wave with a well known frequency of input ocean velocities, the solution of the two methods has been carried out in the Fourier frequency domain. As one of the applied approach offers a possibility for a solution in time domain, the input velocity data has been discretized and the toroidal magnetic field for the M_2 tide in time domain has been calculated. A mutual comparison with the solutions in the Fourier frequency domain confirms the results of the time-domain approach.

We should emphasize that different factors limit the accuracy of calculations. For example, a rather sparse lateral resolution of the input ocean velocities, a spherically symmetric conductivity model or a simple conductivity contrast at the ocean-continent boundary mainly influences the resulting magnetic field. These are effects that may reduce or amplify the simulated fields. Moreover, our results are valid for a tidally-forced ocean circulation only. As the structure of a general ocean circulation differ in comparison to the tidal circulation, the resulting magnetic field is expected to differ in amplitudes and spatial patterns.

Nevertheless, the variations of the model input parameters allow not only carrying out an internal validation and testing the numerical behaviour of the model, but also offer an insight into the behaviour of the magnetic field in respect to variations of the ocean flow, electric conductivity structure or the background magnetic field. This sensitivity analysis contributes essentially for understanding the key parameters influencing the generated magnetic fields. In particular, we show a strong sensitivity of the induced magnetic field in respect to the variation of radial conductivity profile beneath the ocean and, in case of the toroidal mode, also thorough the ocean. The results of our study additionally show a different sensitivity of two magnetic modes with respect to a radial conductivity profile. While a high resistivity of crust and lithosphere hinders the penetration of the vertical electrical currents into the mantle and therefore also the penetration of the toroidal magnetic signal, the penetration of the poloidal magnetic signal is hindered by a high conductivity of the medium beneath the ocean where electrical currents discharge the poloidal magnetic field.

Further, we show the influence of the vertical gradient of the flow on the toroidal magnetic field. For instance, a strong linear decay of the horizontal ocean flow between the top and bottom of the ocean layer generates toroidal magnetic signal that is by far larger than that generated by over the depth constant flow. This is an important aspect for modelling the ocean-induced magnetic field driven by a general ocean circulation. We also alternated the input ocean velocity fields to examine the difference between using the whole oceanic transport on one hand and the average tidal flow dominated by large velocities in shallow coastal region on the other hand. Three calculated magnetic field constituents, the toroidal, primary poloidal and secondary poloidal parts show different spatial distributions for the two scenarios but are comparable in the magnitude.

The presented work examined the ocean-induced magnetic field variations on a global scale by considering the ocean as a volume source of the magnetic signal. The used mathematical approach allows a new insight into the magnetic field driven by ocean circulation. Especially, the volume source opens the possibility to consider the toroidal mode of the magnetic field and therefore also the secondary effects of the ocean induced magnetic signal can be estimated. The results show the possibility of the ocean-induced magnetic field to be measured outside of the ocean, and, in particular, in view of the given specifications of the new satellite mission Swarm also at the satellite attitudes. The identification of such signals would help, on one hand, a better understanding of the geomagnetic field and, on the other hand, to use the observed magnetic signal as an additional sensor understanding processes of the global oceanic circulation.

Outlook

The focus of this thesis was creating a finite-layer model for solving the induction problem in ocean and its independent validation. We obtained many new scientific findings about the ocean-induced magnetic field such as the magnitudes, spatial distribution, the behaviour of the magnetic field with respect to different parameters or the penetration depth of the magnetic signal in the Earth mantle. Still, open questions remain, where some of them have arised when writing this thesis. It is challenging to solve them by continuing to develop the model.

The presented solution in the time domain is done for the toroidal mode of the magnetic field only. An extension for the poloidal mode is still to be done and should be complemented in future. The solution in the time domain opens the possibility to study the ocean-induced magnetic field originated by a general ocean circulation which is of different origin than the tidal flow. Whereas over the depth constant tidal flow consists of periodical short time signal variations, short time variations of a general ocean circulation are rather small, but they contain permanent flow constituents with a strong vertical gradient. The importance of the vertical gradient of the flow for the toroidal magnetic field has been demonstrated in one of the numerical experiments in this thesis. Due to the coastal effect it is expected that the magnetometer records at coast sites contain a signal of the secondary poloidal magnetic field originated by a general ocean circulation.

One of the most important steps for further development is to extend the finite-layer model to a 3D induction model, which allows modelling a laterally heterogeneous electrical conductivity such as a conductivity jump at the ocean-continent boundary, or at the ocean bottom.

The results delivered by the forward modelling are intended, in the first step, to be used for the identification of the ocean-induced magnetic constituents in the space born and coastal site magnetometers. Strong tidally induced signal variations with known frequencies should facilitate this process. Once the ocean originated signal is identified in magnetic records, the measured signal can be assimilated into ocean modelling, and the ocean modelling can be improved. From the geomagnetic point of view, the model-predicted data can also be used for dealiasing the magnetic records from space-borne magnetometers for the oceanic part. The ability to remove the ocean-induced signal, in particular, the permanent contribution given by a general circulation, should help to identify other geomagnetic constituents, especially, the lithospheric magnetic part. Further on, the oceanic electromagnetic field could be used as a source for the estimation of conductivity structures close to ocean areas.

List of symbols

The list contains symbols used generally through the whole thesis. Locally defined and used symbols for mathematical description are not listed.

$\boldsymbol{A}$	magnetic vector potential $[\boldsymbol{A}] = \frac{\mathrm{Vs}}{\mathrm{m}}$
$\boldsymbol{A}_\mathrm{T}$	toroidal magnetic potential
$\boldsymbol{A}_0$	toroidal magnetic potential in atmosphere
$\mathcal{A}$	atmosphere $(r \geq a, \sigma = 0)$
a	radius of the Earth - top of the ocean $(a = 6371\mathrm{km})$
$\boldsymbol{B}$	magnetic flux density $[\boldsymbol{B}] = \mathrm{T} = \frac{\mathrm{Vs}}{\mathrm{m}^2}$
$\boldsymbol{B}_\mathrm{E}$	background (main) magnetic flux density of the Earth
$\boldsymbol{B}_\mathrm{P}$	poloidal magnetic flux density
$\boldsymbol{B}_\mathrm{T}$	toroidal magnetic flux density
$\boldsymbol{B}_0$	poloidal magnetic flux density in atmosphere
b	radius of ocean layer bottom $[b] = \mathrm{km}$
$\boldsymbol{D}$	dielectric displacement
$\boldsymbol{E}$	electric field intensity $[\boldsymbol{E}] = \frac{\mathrm{V}}{\mathrm{m}}$
$\boldsymbol{E}_\mathrm{S}$	spheroidal electric field intensity
$\boldsymbol{e}_r, \boldsymbol{e}_\vartheta, \boldsymbol{e}_\varphi$	unit base vectors for radial direction, co-latitude and longitude
$\boldsymbol{F}$	source term for the toroidal magnetic field
$\boldsymbol{G}$	source term for the poloidal magnetic field in term of toroidal magnetic potential
G_{jm}	orthonormal normalized Gauss coefficients of the magnetic field
$G_{jm}^{(i)}$	Gauss coefficients for the internal sources
$G_{jm}^{(e)}$	Gauss coefficients for the external sources
${}^{b}G_{jm}^{(i)}$	orthonormal fully-normalized Gauss coefficients of the induced magnetic field
$\mathcal{G}$	space of the solid Earth + ocean (sphere with $r = a$)

$\mathcal{G}_\mathrm{O}$	space containing the ocean layer
$\partial\mathcal{G}$	surface of the solid Earth + ocean (sphere with $r = a$)
g_{jm}	Schmidt semi-normalized coefficients of the magnetic field
$\boldsymbol{H}$	magnetic field intensity $[\boldsymbol{H}] = \frac{\mathrm{A}}{\mathrm{m}}$
j_ℓ,	Bessel functions of the first kind
j'_ℓ	derivation of the Bessel functions of first kind
i	$i = \sqrt{-1}$
i	label for time instant
$\boldsymbol{j}$	electric current density $[\boldsymbol{j}] = \frac{\mathrm{A}}{\mathrm{m}^2}$
$\boldsymbol{K}$	2×2 matrix with fundamental solutions of the homogeneous Helmholtz equation
k	wave number, $k^2 = -i\omega\mu_0\sigma$
$\boldsymbol{L}$	matrix propagator over several layers
$\boldsymbol{M}$	layer propagator matrix $\boldsymbol{M}(\mathrm{top}, \mathrm{bottom})$
$\boldsymbol{n}$	outward directed normal vector
n_ℓ	Bessel functions of the second kind
n'_ℓ	derivation of the Bessel functions of second kind
$P_{jm}(\cos\vartheta)$	associated Legendre functions
$P_j^m(\cos\vartheta)$	orthonormal normalized associated Legendre functions
$\hat{P}_j^m(\cos\vartheta)$	Schmidt semi-normalized associated Legendre functions
r	radius $[r] = \mathrm{m}$
$\boldsymbol{r}$	radius vector $\boldsymbol{r} = (r, \Omega)$
$\boldsymbol{s}$	source term
s	salinity $[s] = 34.25$ psu (in sec. 2.6.3)
T	time period $[T] = \mathrm{s}$
T	temperature $[T] =$ °C (in sec. 2.6.3)
t_i	time instant
$\boldsymbol{u}$	horizontal velocities of the ocean flow $[\boldsymbol{u}] = \frac{\mathrm{m}}{\mathrm{s}}$ $\boldsymbol{u} = u_\vartheta\,\boldsymbol{e}_\vartheta + u_\varphi\,\boldsymbol{e}_\varphi$
$\boldsymbol{y}$	homogeneous solution of the Helmholtz equation
$\boldsymbol{v}$	solution of the Helmholtz equation in ocean layer $\boldsymbol{v} = \boldsymbol{y} + \boldsymbol{s}$

Y_{jm}	scalar spherical harmonics of degree j and order m
$\boldsymbol{Y}^{\ell}_{jm}$	vector spherical harmonics of degree j and order m
z	$z = kr$
Δt	time step
Δ_{T}	temperature difference (in sec. 2.6.3)
δ_{ij}	Kronecker delta symbol
ϵ_0	permittivity for vacuum $\epsilon_0 = 8.854187817 \cdot 10^{-12} \frac{\mathrm{F}}{\mathrm{m}}$
ϵ_r	permittivity coefficient
η	Lanczos coefficients (for weighing the spherical harmonic series)
ϑ	geographical latitude
μ_0	permeability of vacuum $\mu_0 = 4\pi \cdot 10^{-7} \frac{\mathrm{V\ s}}{\mathrm{A\ m}}$
μ_r	permeability coefficient
π	ratio of a circle's circumference $\pi = 3.14\ldots$
ρ	charge density $[\rho] = \frac{\mathrm{C}}{\mathrm{m}^3}$
σ	electrical conductivity $[\sigma] = \frac{\mathrm{S}}{\mathrm{m}}$
σ_{c}	electrical conductivity of the continent $\sigma_{\mathrm{c}} = 10^{-3}\ \frac{\mathrm{S}}{\mathrm{m}}$
σ_{o}	electrical conductivity of the ocean layer (if constant ocean conductivity $\sigma_{\mathrm{o}} = 3.5\ \frac{\mathrm{S}}{\mathrm{m}}$)
σ_{m}	electrical conductivity beneath the ocean layer (mantle, lithosphere and crust)
ψ_k, ψ_{k+1}	set of basis functions for finite elements in radial direction
φ	geographical longitude
Ω	$\Omega = (\varphi, \vartheta)$
ω	angular frequency $\omega = \frac{2\pi}{T}$

Bibliography

Abramowitz, M., Stegun, I. A., 1970. Handbook of Mathematical Functions. Dover, New York, NY.

Apel, J. R., 1987. Principles of ocean physics. Vol. 38 of Inte. Academic Press.

Baba, K., Utada, H., Goto, T.-n., Kasaya, T., Shimizu, H., Tada, N., Nov. 2010. Electrical conductivity imaging of the Philippine Sea upper mantle using seafloor magnetotelluric data. Physics of the Earth and Planetary Interiors 183 (1-2), 44–62.

Bronstein, I. N., Semendjaev, K. A., Musiol, G., Mhlig, H., 1997. Taschenbuch der Matematik. Verlag Harri Deutsch.

Chapman, S., 1919. Phylosophical Transactions; I. The Solar and Lunar Diurnal Variations of Terrestrial Magnetism.

Chapman, S., Bartels, J., 1962. Geomagnetism, 1962nd Edition. Vol. I. and II. Oxford ; Clarendon Press.

Chave, A., Luther, D. S., 1990a. Low-Frequency , Motionally Induced Electromagnetic Fields in the Ocean 1 . Theory 95, 7185–7200.

Chave, A. D., 1983. On the theory of electromagnetic induction in the Earth by ocean currents. Journal of Geophysical Research 88 (B4), 3531.
URL `http://doi.wiley.com/10.1029/JB088iB04p03531`

Chave, A. D., Luther, D. S., 1990b. Low-frequency, motionally induced electromagnetic fields in the ocean: 1. Theory. Journal of Geophysical Research 95 (C5), 7185.

Dobslaw, H., 2007. Modellierung der allgemeinen ozeanischen Dynamik zur Korrektur und Interpretation von Satellitendaten. Ph.D. thesis, Technische Universitaet Dresden.

Dostal, J., 2009. Prädiktion ozeanischer Tidensignale in Satellitenbeobachtungen des Erdmagnetfeldes. Tech. rep., GFZ Potsdam.

Dostal, J., Martinec, Z., Thomas, M., May 2012. The modelling of the toroidal magnetic field induced by tidal ocean circulation. Geophysical Journal International 189 (2), 782–798.
URL `http://doi.wiley.com/10.1111/j.1365-246X.2012.05407.x`

Drijfhout, S., Heinze, C., Latif, M., Maier-Reimer, E., 1996. Mean circulation and internal variability in an ocean primitive equation model. J. Phys. Oceanogr., 26, 559–580.

Duchon, C. E., Aug. 1979. Lanczos Filtering in One and Two Dimensions. Journal of Applied Meteorology 18 (8), 1016–1022.
URL `http://journals.ametsoc.org/doi/abs/10.1175/1520-0450(1979)018<1016:LFIOAT>2.0.CO;2`

ESA_SP-1279-6, 2004. Swarm - The Earth's Magnetic Field and Environment Explorers. Tech. rep., ESA Publications Division ESTEC, Noordwijk The Netherlands.

Faraday, M., 1832. Experimental Researches in Electricity. URL `http://archive.org/details/philtrans01461252`

Friis-Christensen, E., Luehr, H., Hulot, G., 2006. Swarm: A constellation to study the Earth's magnetic field. Earth Planets Space 58 (4), 351–358.

Golubev, Y., Jul. 2011. Ocean-generated magnetic field study based on satellite geomagnetic measurements: 1. An error reduction technique for gridded data. Journal of Geophysical Research 116 (C7), C07028.

Golubev, Y., Sep. 2012. Ocean-generated magnetic field study based on satellite geomagnetic measurements: 2. Signal inference. Journal of Geophysical Research 117 (C9), C09006.

Kuvshinov, A., Avdeev, D. B., Pankratov, O. V., Golyshev, S. A., Olsen, N., 2002. Modelling electromagnetic fields in a 3D spherical earth using a fast integral equation approach. In: Zhdanov, M. S., Wannamaker, P. E. (Eds.), Three-dimensional electromagnetics, Proceedings of the second international symposium. Elsevier, New York, Ch. 3.

Kuvshinov, A., Olsen, N., 2005. 3-D Modelling of the Magnetic Fields Due to Ocean Tidal Flow. In: Reigberg, C., Luehr, H., Schwintzer, P., Wickert, J. (Eds.), Earth Observation with CHAMP, Results from Three Years in Orbit. Springer, Heidelberg, Ch. 2, pp. 359 – 365.

Kuvshinov, A. V., Oct. 2008. 3-D Global Induction in the Oceans and Solid Earth: Recent Progress in Modeling Magnetic and Electric Fields from Sources of Magnetospheric, Ionospheric and Oceanic Origin. Surveys in Geophysics 29 (2), 139–186.

Křížek, M., Neittaanmäki, P., 1990. Finite Element Approximation of Variational Problems and Applications. Longman Scientific and Technical, New York.

Larsen, J. C., Nov. 1968. Electric and Magnetic Fields Induced by Deep Sea Tides. Geophysical Journal International 16 (1), 47–70. URL `http://gji.oxfordjournals.org/cgi/doi/10.1111/j.1365-246X.1968.tb07135.x`

Lilley, F., White, A., Heinson, G. S., 2001. Earth's magnetic field: ocean current contributions to vertical profiles in deep oceans. Geophysical Journal International 147 (1), 163–175.

Lilley, F. E. M., Hitchman, A. P., Milligan, P. R., Pedersen, T., Nov. 2004. Sea-surface observations of the magnetic signals of ocean swells. Geophysical Journal International 159 (2), 565–572.

Lizarralde, D., Chave, A., Hirth, G., Schultz, A., 1995. Northeastern Pacific mantle conductivity profile from long-period magnetotelluric sounding using Hawaii-to-California submarine cable data. Journal of Geophysical Research 100 (B9), 17837.

Longuet-Higgins, M., 1949. The electrical and magnetic effects of tidal streams. Mon. Notic. Roy. Astron. Soc., Geophys. Suppl. 58, 295.

Longuet-Higgins, M., Stern, M. E., Stommel, H., 1954. The electrical fields induced by ocean currents and waves, with applications to the method of towed electrodes. Papers in Physical Oceanography and Meteorology 13, 1–37.

Luther, D. S., Filloux, J. H., Chave, A. D., 1991. Low-frequency, motionally induced electromagnetic fields in the ocean: 2. Electric field and Eulerian current comparison. Journal of Geophysical Research 96 (C7), 12797.

Mandea, M., Thebault, E., 2007. The changing faces of the Earth's Magnetic Field. Commision for the geological map of the world, France, Paris.

Manoj, C., Kuvshinov, A., Maus, S., Luehr, H., 2006. Ocean circulation generated magnetic signals. Earth, Planets and Space 58, 429–437.

Manoj, C., Kuvshinov, A., Neetu, S., Harinarayana, T., Mar. 2010. Can undersea voltage measurements detect tsunamis? Earth, Planets and Space 62 (3), 353–358.

Manoj, C., Maus, S., Chulliat, A., Jan. 2011. Observation of Magnetic Fields Generated by Tsunamis. Eos, Transactions American Geophysical Union 92 (2), 13.
URL `http://doi.wiley.com/10.1029/2011EO020002`

Martinec, Z., Sep. 1997. Spectral-finite-element approach to two-dimensional electromagnetic induction in a spherical earth. Geophysical Journal International 130 (3), 583–594.
URL `http://gji.oxfordjournals.org/cgi/doi/10.1111/j.1365-246X.1997.tb01854.x`

Martinec, Z., Jan. 1999. Spectral-finite element approach to three-dimensional electromagnetic induction in a spherical earth. Geophysical Journal International 136 (1), 229–250.
URL `http://doi.wiley.com/10.1046/j.1365-246X.1999.00713.x`

Martinec, Z., Feb. 2002. Geomagnetic induction in multiple eccentrically nested spheres. Geophysical Journal International 132 (1), 96–110.
URL `http://doi.wiley.com/10.1046/j.1365-246x.1998.00392.x`

Martinec, Z., Everett, M. E., Velímský, J., Oct. 2003. Time-domain, spectral finite-element approach to transient 2-D geomagnetic induction in a spherical heterogeneous Earth. Geophysical Journal International 155 (1), 33–43.

Maus, S., Kuvshinov, A., 2004. Ocean tidal signals in observatory and satellite magnetic measurements. Geophysical Research Letters 31 (15), L15313.

Maus, S., Manoj, C., Rauberg, J., Michaelis, I., Luehr, H., Dec. 2010. NOAA/NGDC candidate models for the 11th generation International Geomagnetic Reference Field and the concurrent release of the 6th generation Pomme magnetic model. Earth, Planets and Space 62 (10), 729–735.

Maus, S., Rother, M., Hemant, K., Stolle, C., Lühr, H., Kuvshinov, A., Olsen, N., Feb. 2006. Earth's lithospheric magnetic field determined to spherical harmonic degree 90 from CHAMP satellite measurements. Geophysical Journal International 164 (2), 319–330.
URL `http://gji.oxfordjournals.org/cgi/doi/10.1111/j.1365-246X.2005.02833.x`

Press, W. H., Teukolsky, S. A., Vetterling, W. T., Flannery, B. P., Feb. 1993. Numerical Recipes in FORTRAN; The Art of Scientific Computing. Cambridge University Press.
URL `http://dl.acm.org/citation.cfm?id=563041`

Pěč, K., Martinec, Z., Pěčová, J., Hvoždara, M., Jun. 1985. Matrix approach to the solution of electromagnetic induction in a spherically layered earth. Studia Geophysica et Geodaetica 29 (2), 139–162.
URL `http://link.springer.com/10.1007/BF01585717`

Sanford, T. B., May 1971. Motionally induced electric and magnetic fields in the sea. Journal of Geophysical Research 76 (15), 3476–3492.
URL `http://doi.wiley.com/10.1029/JC076i015p03476`

Souček, O., Martinec, Z., Velímský, J., May 2011. Vector potential formulation of a quasi-static EM induction problem: existence, uniqueness and stability of the weak solution. GEM - International Journal on Geomathematics 2 (2), 265–279.
URL `http://link.springer.com/10.1007/s13137-011-0019-9`

Stommel, H., 1948. The theory of the electric Field induced in deep ocean currents. J. Mar. Res. 7 (3), 386 – 392.

Stratton, J. A., 1941. Electromagnetic Theory. Mcgraw Hill Book Company, New York.

Szuts, B. Z., 2008. The Interpretation of Motionally Induced Electric Fileds in Ocean of Complex Geometry. Phd thesis, University of Washington.

Szuts, Z. B., Jun. 2010a. Relationship between ocean velocity and motionally induced electrical signals: 1. In the presence of horizontal velocity gradients. Journal of Geophysical Research 115 (C6), C06003.

Szuts, Z. B., Jun. 2010b. Relationship between ocean velocity and motionally induced electrical signals: 2. In the presence of sloping topography. Journal of Geophysical Research 115 (C6), C06004.

Szuts, Z. B., Apr. 2012. Using motionally-induced electric signals to indirectly measure ocean velocity: Instrumental and theoretical developments. Progress in Oceanography 96 (1), 108–127.

Thomas, M., 2002. Ozeanisch induzierte Erdrotationsschwankungen - Ergebnisse eines Simultanmodells für Zirkulation und ephemeridische Gezeiten im Weltozean. Phd thesis, Universitaet Hamburg.

Toh, H., Satake, K., Hamano, Y., Fujii, Y., Goto, T., Feb. 2011. Tsunami signals from the 2006 and 2007 Kuril earthquakes detected at a seafloor geomagnetic observatory. Journal of Geophysical Research 116 (B2), B02104.

Tosi, N., 2007. Numerical modeling of present-day mantle convection. Ph.D. thesis, Charles University in Prague.

Tyler, R. H., Maus, S., Lühr, H., Jan. 2003. Satellite observations of magnetic fields due to ocean tidal flow. Science (New York, N.Y.) 299 (5604), 239–241.

Tyler, R. H., Mysak, L. A., Oberhuber, J. M., 1997a. Electromagnetic fields generated by a three dimensional global ocean circulation. Journal of Geophysical Research 102 (C3), 5531.

Tyler, R. H., Sanford, T. B., Oberhuber, J. M., 1997b. Geophysical challenges in using large-scale ocean-generated em fields to determine the ocean flow. Journal of Geomagnetism and Geoelectricity 49, 1351–1372.

van Bemmelen, W., 1912. Der lunare Variation des Erdmagnetismus. Meteorologische Zeitschrift Mai, 218–231.

van Bemmelen, W., 1913. Berechtigung zu meiner Abhandlung ueber die lunare Variation des Erdmagnetismus. Meteorologische Zeitschrift Dezember, 589–594.

Varshalovich, D. A., Moskalev, A. N., Khersonskii, V. K., 1988. Quantum Theory of Angular Momentum. World Scientific Publications, Singapore.

Vennerstrom, S., Friis-Christensen, E., Luehr, H., Moretto, T., Olsen, N., Manoj, C., Ritter, P., Rastaetter, L., Kuvshinov, A., Maus, S., 2005a. DSRI Report Swarm The impact of combined magnetic and electric field analysis and of ocean circulation effects on Swarm mission performance. Tech. rep., Danish National space Centre (DNSC).
URL `http://esamultimedia.esa.int/docs/EarthObservation/Swarm/E2E_GPS_ACC_FR.pdf`

Vennerstrom, S., Friis-Christensen, E., Luehr, H., Moretto, T., Olsen, N., Manoj, C., Ritter, P., Rastaetter, L., Kuvshinov, A., Maus, S., 2005b. Earth observation with CHAMP, Results from three years in orbit. Springer, Ch. 3-D modell, pp. 359–361.

Vivier, F., Meier-Reimer, E., Tyler, R. H., 2004. Simulations of magnetic fields generated by the Antarctic Circumpolar Current at satellite altitude: Can geomagnetic measurements be used to monitor the flow? Geophysical Research Letters 31, L10306.

Winch, D. E., Ivers, D. J., Turner, J. P. R., Stening, R. J., Feb. 2005. Geomagnetism and Schmidt quasi-normalization. Geophysical Journal International 160 (2), 487–504.

Wolff, J. O., Maier-Reimer, E., Legutke, S., 1997. The Hamburg Ocean Primitive Equation Model HOPE. Tech. rep., Deutsches Klimarechenzentrum, Hamburg.

Appendix A

Spherical harmonic analysis of horizontal ocean velocities

Let a vector field $\boldsymbol{u}$ defined on the unit sphere $[0,\pi]\times[-\pi,\pi]$ be represented as a series of vector spherical harmonics $\boldsymbol{Y}^{\ell}_{jm}(\vartheta,\varphi)$ in the form of eq. (2.12). To perform the spherical harmonic analysis of its values prescribed on the unit sphere, it is convenient to represent $\boldsymbol{u}$ in terms of the vector spherical harmonics $\boldsymbol{Y}^{(\lambda)}_{jm}(\vartheta,\varphi)$, $\lambda=-1,0,1$. The reason is that, in contrast to the vectors $\boldsymbol{Y}^{\ell}_{jm}(\vartheta,\varphi)$, the vectors $\boldsymbol{Y}^{(\lambda)}_{jm}(\vartheta,\varphi)$ are separated in orientation with respect to the r and (ϑ,φ) directions. Specifically, the vector $\boldsymbol{Y}^{(-1)}_{jm}(\vartheta,\varphi)$ is normal to the sphere surface, whereas the vectors $\boldsymbol{Y}^{(0)}_{jm}(\vartheta,\varphi)$ and $\boldsymbol{Y}^{(1)}_{jm}(\vartheta,\varphi)$ are tangential Varshalovich et al. (1988),

$$\begin{aligned}
\boldsymbol{Y}^{(-1)}_{jm}(\vartheta,\varphi) &= Y_{jm}(\vartheta,\varphi)\boldsymbol{e}_r,\\
\boldsymbol{Y}^{(1)}_{jm}(\vartheta,\varphi) &= \frac{1}{\sqrt{j(j+1)}}\left[\frac{\partial Y_{jm}(\vartheta,\varphi)}{\partial\vartheta}\boldsymbol{e}_\vartheta+\frac{1}{\sin\vartheta}\frac{\partial Y_{jm}(\vartheta,\varphi)}{\partial\varphi}\boldsymbol{e}_\varphi\right],\\
\boldsymbol{Y}^{(0)}_{jm}(\vartheta,\varphi) &= \frac{i}{\sqrt{j(j+1)}}\left[\frac{1}{\sin\vartheta}\frac{\partial Y_{jm}(\vartheta,\varphi)}{\partial\varphi}\boldsymbol{e}_\vartheta-\frac{\partial Y_{jm}(\vartheta,\varphi)}{\partial\vartheta}\boldsymbol{e}_\varphi\right],
\end{aligned}\tag{A.1}$$

where $Y_{jm}(\vartheta,\varphi)$ are scalar spherical harmonics and i is the imaginary unit. In particular, a vector field $\boldsymbol{u}$ that has no radial component, such is the case for the horizontal ocean velocity field $\boldsymbol{u}$ introduced in section 2.1, where

$$\boldsymbol{u}(\vartheta,\varphi)=u_\vartheta(\vartheta,\varphi)\boldsymbol{e}_\vartheta+u_\varphi(\vartheta,\varphi)\boldsymbol{e}_\varphi,\tag{A.2}$$

and, in addition, assuming that $\boldsymbol{u}$ is a square integrable function on the unit sphere, then $\boldsymbol{u}$ can be represented in terms of $\boldsymbol{Y}^{(0)}_{jm}(\vartheta,\varphi)$ and $\boldsymbol{Y}^{(1)}_{jm}(\vartheta,\varphi)$ as

$$\boldsymbol{u}(\vartheta,\varphi)=\sum_{j=0}^{\infty}\sum_{m=-j}^{j}\sum_{\lambda=0,1}u^{(\lambda)}_{jm}\boldsymbol{Y}^{(\lambda)}_{jm}(\vartheta,\varphi).\tag{A.3}$$

In addition, when $\boldsymbol{u}$ is a real-valued function on the unit sphere, its coefficients satisfy

$$u^{(\lambda)}_{j-m}=(-1)^{m+\lambda+1}\left[u^{(\lambda)}_{jm}\right]^*,\tag{A.4}$$

where the asterisk stands for the complex conjugation. The purpose of spherical harmonics analysis is to estimate two sets of coefficients $u^{(\lambda)}_{jm}$, $\lambda=0,1$, from the measurements of the horizontal components $u_\vartheta(\vartheta,\varphi)$ and $u_\varphi(\vartheta,\varphi)$ of $\boldsymbol{u}$ on the unit sphere. The individual samples will be called $u_{k\ell}=u_\vartheta(\vartheta_k,\varphi_\ell)$ and $v_{k\ell}=u_\varphi(\vartheta_k,\varphi_\ell)$. Throughout this work, we assume that these measurements are performed over an equal angular grid where the separation between parallels, $\Delta\vartheta = \pi/N$, where N is an integer, is constant and is equal to the separation between meridians, $\Delta\varphi = \Delta\vartheta = \Delta$. For such a regular grid, data consist of values determined at the intersections of the grid and indexes k and ℓ take the values $0 \leq k \leq N-1$ and $0 \leq \ell \leq 2N-1$. Thus, there are $2N^2$ points in the equal angular grid for each component u_ϑ and u_φ, which implies that the number of fully recoverable coefficients $u_{jm}^{(0)}$ and $u_{jm}^{(1)}$ is finite. In analogy with 2-D Fourier series, Colombo (1981) has shown that the Nyquist frequency in the case of spherical harmonics is π/Δ. This implies that the maximum angular degree $j_{\max}$ up to which the coefficients $u_{jm}^{(\lambda)}$ are fully recoverable and are free of the alias effect, is given by the inequality $j_{\max} < \pi/\Delta$, or $j_{\max} < N$. As a consequence, the expansion (A.3) must be replaced by a truncated spherical harmonic series,

$$\boldsymbol{u}(\vartheta,\varphi) = \sum_{j=1}^{j_{\max}} \sum_{m=-j}^{j} \sum_{\lambda=0,1} u_{jm}^{(\lambda)} \boldsymbol{Y}_{jm}^{(\lambda)}(\vartheta,\varphi). \tag{A.5}$$

Note that the summation over j starts from $j=1$, since $\boldsymbol{Y}_{00}^{(0)}(\vartheta,\varphi) = \boldsymbol{Y}_{00}^{(1)}(\vartheta,\varphi) = 0$ for any (ϑ,φ). In other words, $4N^2$ data are disposable for determining $j_{\max}(j_{\max}+3)$ complex harmonic coefficients $u_{jm}^{(0)}$ and $u_{jm}^{(1)}$ because of the validity of eq. (A.4) for the negative-order coefficients. Estimates above the Nyquist frequency are usually regarded as meaningless. In the terminology of inverse problems, the determination of $u_{jm}^{(0)}$ and $u_{jm}^{(1)}$ is an overdetermined problem with no exact solution. In the following, the coefficients $u_{jm}^{(0)}$ and $u_{jm}^{(1)}$ will be estimated by the least-squares method.

We suppose that the data samples $u_{k\ell}$ and $v_{k\ell}$, measured over the equal angular grid,

$$\begin{aligned} \vartheta_k &= \Delta/2 + k\Delta, \quad k = 0,1,\ldots,N-1, \\ \varphi_\ell &= \ell\Delta, \qquad\qquad \ell = 0,1,\ldots,2N-1, \end{aligned} \tag{A.6}$$

with $\Delta = \pi/N$, satisfy the observation equation of the form

$$\boldsymbol{y} = \boldsymbol{X}\boldsymbol{\beta} + \boldsymbol{e}, \tag{A.7}$$

where $\boldsymbol{y}$ is the column vector of $4N^2$ data samples,

$$\boldsymbol{y} = \{(u_{k\ell}, v_{k\ell}), k = 0,1,\ldots,N-1, \ell = 0,1,\ldots,2N-1\}, \tag{A.8}$$

$\boldsymbol{\beta}$ is the column vector of $j_{\max}(j_{\max}+3)$ coefficients $u_{jm}^{(1)}$ and $u_{jm}^{(0)}$,

$$\boldsymbol{\beta} = \{(u_{jm}^{(1)}, u_{jm}^{(0)}), j = 1,\ldots,j_{\max}, m = 0,1,\ldots,j\}, \tag{A.9}$$

and $\boldsymbol{X}$ is the design matrix with the elements

$$X_{k\ell,jm} = \frac{1}{\sqrt{j(j+1)}} \begin{pmatrix} \dfrac{\partial Y_{jm}(\vartheta,\varphi)}{\partial\vartheta} & \dfrac{i}{\sin\vartheta}\dfrac{\partial Y_{jm}(\vartheta,\varphi)}{\partial\varphi} \\ \dfrac{1}{\sin\vartheta}\dfrac{\partial Y_{jm}(\vartheta,\varphi)}{\partial\varphi} & -i\dfrac{\partial Y_{jm}(\vartheta,\varphi)}{\partial\vartheta} \end{pmatrix}_{(\vartheta_k,\varphi_\ell)}. \tag{A.10}$$

Because of data errors $\boldsymbol{e}$, eq. (A.7) is mathematically inconsistent and an exact solution to this system does not exist. By assuming that errors $\boldsymbol{e}$ have zero means and are uncorrelated, the least-squares estimate $\hat{\boldsymbol{\beta}}$ of parameters $\boldsymbol{\beta}$ is given by the normal equations (e.g. Koch, 1999)

$$\boldsymbol{X}^\dagger \boldsymbol{X}\,\hat{\boldsymbol{\beta}} = \boldsymbol{X}^\dagger \boldsymbol{y}, \tag{A.11}$$

where the dagger stands for the conjugate transpose. The elements of the normal matrix $\boldsymbol{X}^\dagger \boldsymbol{X}$ are

$$(\boldsymbol{X}^\dagger \boldsymbol{X})_{j_1 m_1, j_2 m_2} = \begin{pmatrix} B^{11}_{j_1 m_1, j_2 m_2} & B^{12}_{j_1 m_1, j_2 m_2} \\ B^{21}_{j_1 m_1, j_2 m_2} & B^{22}_{j_1 m_1, j_2 m_2} \end{pmatrix} \frac{1}{\sqrt{j_1(j_1+1) j_2(j_2+1)}} \tag{A.12}$$

with the elements

$$\begin{aligned}
B^{11}_{j_1 m_1, j_2 m_2} &= \sum_{k\ell} \left(\frac{\partial Y^*_{j_1 m_1}(\vartheta,\varphi)}{\partial \vartheta} \frac{\partial Y_{j_2 m_2}(\vartheta,\varphi)}{\partial \vartheta} + \frac{1}{\sin^2\vartheta} \frac{\partial Y^*_{j_1 m_1}(\vartheta,\varphi)}{\partial \varphi} \frac{\partial Y_{j_2 m_2}(\vartheta,\varphi)}{\partial \varphi} \right)_{(\vartheta_k,\varphi_\ell)}, \\
B^{12}_{j_1 m_1, j_2 m_2} &= \sum_{k\ell} \frac{i}{\sin\vartheta} \left(\frac{\partial Y^*_{j_1 m_1}(\vartheta,\varphi)}{\partial \vartheta} \frac{\partial Y_{j_2 m_2}(\vartheta,\varphi)}{\partial \varphi} - \frac{\partial Y^*_{j_1 m_1}(\vartheta,\varphi)}{\partial \varphi} \frac{\partial Y_{j_2 m_2}(\vartheta,\varphi)}{\partial \vartheta} \right)_{(\vartheta_k,\varphi_\ell)}, \\
B^{21}_{j_1 m_1, j_2 m_2} &= B^{12}_{j_1 m_1, j_2 m_2}, \\
B^{22}_{j_1 m_1, j_2 m_2} &= B^{11}_{j_1 m_1, j_2 m_2}.
\end{aligned} \tag{A.13}$$

For the equal angular grid, $\varphi_\ell = 2\pi\ell/2N$, it holds that

$$\sum_{\ell=0}^{2N-1} e^{im\varphi_\ell} = \begin{cases} 2N, & m = 0, \\ 0, & \text{otherwise.} \end{cases} \tag{A.14}$$

This condition, applied to the elements of the normal matrix, eliminates the summation over longitudinal index ℓ and requires that $m_1 = m_2$,

$$\begin{aligned}
B^{11}_{j_1 m_1, j_2 m_2} &= 2N \sum_{k=0}^{N-1} \left(\frac{\partial P_{j_1 m_1}(\vartheta)}{\partial \vartheta} \frac{\partial P_{j_2 m_2}(\vartheta)}{\partial \vartheta} + \frac{m_1^2}{\sin^2\vartheta} P_{j_1 m_1}(\vartheta) P_{j_2 m_2}(\vartheta) \right)_{\vartheta=\vartheta_k} \delta_{m_1 m_2}, \\
B^{12}_{j_1 m_1, j_2 m_2} &= -2N m_1 \sum_{k=0}^{N-1} \frac{1}{\sin\vartheta} \left(\frac{\partial P_{j_1 m_1}(\vartheta)}{\partial \vartheta} P_{j_2 m_1}(\vartheta) + \frac{\partial P_{j_2 m_1}(\vartheta)}{\partial \vartheta} P_{j_1 m_1}(\vartheta) \right)_{\vartheta=\vartheta_k} \delta_{m_1 m_2},
\end{aligned} \tag{A.15}$$

where $\delta_{m_1 m_2}$ is the Kronecker delta symbol. The last equation shows that the matrix of normal equations for the equal angular grid is sparse. To make use of it for fast numerical solutions of the normal equations, the spherical harmonic coefficients $u^{(1)}_{jm}$ and $u^{(0)}_{jm}$ are arranged in such a way that all those of the same order m are grouped together. Then, the normal matrix has a block diagonal form. For each order $m_1 > 0$, the block is of dimension $2(j_{\max} - m_1 + 1)$. The largest block is for the order $m_1 = 0$ and is of the dimension $2j_{\max}$. The smallest block is for $m_1 = j_{\max}$ and is of dimension 2×2.

Transformation of SH coefficients of horizontal velocity field from $\boldsymbol{Y}^{(\lambda)}_{jm}(\vartheta,\varphi)$ to $\boldsymbol{Y}^{\ell}_{jm}(\vartheta,\varphi)$ representations

As has been stated above the least squares estimate is carried out for $\boldsymbol{u}$ represented in vector spherical harmonics $\boldsymbol{Y}^{(\lambda)}_{jm}(\Omega)$ due to their explicit orientation with respect to radial and horizontal directions. All other calculations in the thesis are carried out in $\boldsymbol{Y}^{\ell}_{jm}(\Omega)$ representation. The spherical harmonic series for $\boldsymbol{u}$ are defined as follow

$$\begin{aligned}
\boldsymbol{u}(\vartheta,\varphi) &= \sum_{jm\lambda} u^{(\lambda)}_{jm} \, \boldsymbol{Y}^{(\lambda)}_{jm}(\vartheta,\varphi) \\
&= \sum_{jm\ell} u^{\ell}_{jm} \, \boldsymbol{Y}^{\ell}_{jm}(\vartheta,\varphi) \, .
\end{aligned} \tag{A.16}$$

The spherical harmonics coefficients of the two representations can be related with the help of relations (D.14), (D.15), (D.16),

$$\begin{aligned} u_{jm}^{j-1} &= \sqrt{\frac{j+1}{2j+1}}\, u_{jm}^{(1)} + \sqrt{\frac{j}{2j+1}}\, u_{jm}^{(-1)} \,, \\ u_{jm}^{j+1} &= \sqrt{\frac{j}{2j+1}}\, u_{jm}^{(1)} - \sqrt{\frac{j+1}{2j+1}}\, u_{jm}^{(-1)} \,, \\ u_{jm}^{j} &= u_{jm}^{(0)} \,. \end{aligned} \tag{A.17}$$

In the case where the radial component of $\boldsymbol{u}$ is zero, $u_r = u_{jm}^{(-1)} = 0$, the transformation relations reduce to

$$\begin{aligned} u_{jm}^{j-1} &= \sqrt{\frac{j+1}{2j+1}}\, u_{jm}^{(1)} \,, \\ u_{jm}^{j+1} &= \sqrt{\frac{j}{2j+1}}\, u_{jm}^{(1)} \,, \\ u_{jm}^{j} &= u_{jm}^{(0)} \,. \end{aligned} \tag{A.18}$$

Appendix B

Matrix propagator

This appendix supplements some derivations for the matrix-propagator method presented in chapter 3. In particular, the sections B.1 and B.2 supplement the derivations for the toroidal and poloidal mode in sections 3.1 and 3.2, respectively.

B.1 Toroidal matrix propagator

B.1.1 Interface conditions for a homogeneous solution

We first derive the interface conditions for the toroidal matrix propagator given by a homogeneous part of the Helmholtz equation (1.14). To guarantee the continuity of a solution for the magnetic field $\boldsymbol{B}_{\mathrm{T}}$ on the spherical layer interface given by a discontinuity of electric conductivity $\sigma(r)$, the tangential component of magnetic and the tangential component of electric field are required to pass continuously through it (eq. Stratton (1941)),

$$\begin{aligned} \boldsymbol{e}_r \times \big[\boldsymbol{B}\big]_-^+ &= 0, \\ \boldsymbol{e}_r \times \big[\boldsymbol{E}\big]_-^+ &= 0. \end{aligned} \tag{B.1}$$

With the help of the relations (D.36) - (D.40), the interface condition for the toroidal magnetic field takes the form

$$\begin{aligned} \boldsymbol{e}_r \times \boldsymbol{B}_{\mathrm{T}}(r,\Omega,k) &= \sum_{jm} \alpha^j_{jm}\, w_j(kr)\, [\boldsymbol{e}_r \times \boldsymbol{Y}^j_{jm}(\Omega)] \\ &= i \sum_{jm} \alpha^j_{jm}\, w_j(kr)\, \left[\sqrt{\frac{j+1}{2j+1}}\boldsymbol{Y}^{j-1}_{jm}(\Omega) + \sqrt{\frac{j}{2j+1}}\boldsymbol{Y}^{j+1}_{jm}(\Omega)\right] . \end{aligned} \tag{B.2}$$

With relation (3.7), the interface condition for the spheroidal electric field is

$$\begin{aligned} \boldsymbol{e}_r \times \boldsymbol{E}_{\mathrm{S}}(r,\Omega,k) &= \frac{i}{\sigma\mu_0} \sum_{jm} \alpha^j_{jm} \left[\sqrt{\frac{j}{2j+1}} \left(\frac{d}{dr} - \frac{j}{r}\right) w_j(kr)\, (i) \sqrt{\frac{j}{2j+1}}\, \boldsymbol{Y}^j_{jm}(\Omega) \right. \\ &\quad \left. + \sqrt{\frac{j+1}{2j+1}} \left(\frac{d}{dr} + \frac{j+1}{r}\right) w_j(kr)\, (i) \sqrt{\frac{j+1}{2j+1}}\, \boldsymbol{Y}^j_{jm}(\Omega)\right] \\ &= \frac{i^2}{\sigma\mu_0} \sum_{jm} \alpha^j_{jm} \left[\left(\frac{d}{dr} + \frac{(-j^2) + (j+1)^2}{(2j+1)r}\right) w_j(kr)\, \boldsymbol{Y}^j_{jm}(\Omega)\right] \\ &= -\frac{1}{\sigma\mu_0} \sum_{jm} \alpha^j_{jm} \left(\frac{d}{dr} + \frac{1}{r}\right) w_j(kr)\, \boldsymbol{Y}^j_{jm}(\Omega) \\ &= -\frac{1}{r\sigma\mu_0} \sum_{jm} \alpha^j_{jm} \frac{d}{dr}[r w_j(kr)]\, \boldsymbol{Y}^j_{jm}(\Omega) . \end{aligned} \tag{B.3}$$

B.1.2 Derivation of the matrix propagator for the toroidal case

Starting by the matrix $\boldsymbol{K}$ for the toroidal mode (eq. 3.15) consisting of the fundamental solutions given by linear combination of the Bessel functions 1st and 2nd kind, we derive now the propagator $\boldsymbol{M}$ for a homogenous solution through a layer with a constant electrical conductivity σ (and therefore, a constant wave number k). The matrix $\boldsymbol{K}$ for an arbitrary layer indexed by s has the form

$$\begin{aligned}\boldsymbol{K}_j^s(r) &= \begin{pmatrix} j_j(z) & n_j(z) \\ \frac{1}{z^2}\frac{d}{dz}[z\, j_j(z)] & \frac{1}{z^2}\frac{d}{dz}[z\, n_j(z)] \end{pmatrix}_{z\,=\,z_s} \\ &= \begin{pmatrix} j_j(z) & n_j(z) \\ \frac{1}{z^2}[z\, j_j'(z) + j_j(z)] & \frac{1}{z^2}[z\, n_j'(z) + n_j(z)] \end{pmatrix}_{z\,=\,z_s} .\end{aligned} \tag{B.4}$$

First, the inversion of matrix $\boldsymbol{K}$ is required. A general form of 2×2 inverse matrix is following Bronstein et al. (1997). If

$$\boldsymbol{K} = \begin{pmatrix} k_{11} & k_{12} \\ k_{21} & k_{22} \end{pmatrix} , \tag{B.5}$$

then

$$\boldsymbol{K}^{-1} = \frac{1}{k_{11}k_{22} - k_{12}k_{21}} \begin{pmatrix} k_{22} & -k_{12} \\ -k_{21} & k_{11} \end{pmatrix} \tag{B.6}$$

provided that $k_{11}k_{22} - k_{12}k_{21} \neq 0$. The determinant of $\boldsymbol{K}$ given by (B.4) is

$$\begin{aligned} det\boldsymbol{K} &= \frac{1}{z^2}\{j_j(z)[z\, n_j'(z) + n_j(z)] - n_j(z)[z\, j_j'(z) + j_j(z)]\} \\ &= \frac{1}{z^2}\; z[j_j(z)n_j'(z) - j_j'(z)n_j(z)] \\ &= \frac{1}{z^3} , \end{aligned} \tag{B.7}$$

where we use the Wronskian determinant (Abramowitz and Stegun, 1970)

$$\frac{1}{z^2} = j_j(z)n_j'(z) - j_j'(z)n_j(z) . \tag{B.8}$$

The inverse matrix than takes the form

$$\begin{aligned}\boldsymbol{K}^{-1}(z) &= z\, z^2 \begin{pmatrix} \frac{1}{z^2}\, [z\, n_j'(z) + n_j(z)] & -n_j(z) \\ -\frac{1}{z^2}\, [z\, j_j'(z) + j_j(z)] & j_j(z) \end{pmatrix} \\ &= z \begin{pmatrix} z\, n_j'(z) + n_j(z) & -z^2\, n_j(z) \\ -[z\, j_j'(z) + j_j(z)] & z^2\, j_j(z) \end{pmatrix} .\end{aligned} \tag{B.9}$$

Let $z_1 = z_s = k_s r_s$ be the top and $z_2 = z_{s-1} = k_s r_{s-1}$ be the bottom of a spherical layer s. Then the transformation between the top-bottom interface values y_1^s and y_2^s is

$$\left(\boldsymbol{y}_{jm}^s\right)_{r_s} = \boldsymbol{M}^s(k_s r_s, k_s r_{s-1}) \left(\boldsymbol{y}_{jm}^s\right)_{r_{s-1}} , \tag{B.10}$$

where $\boldsymbol{M}^s$ stands for the transformation matrix through a spherical layer s

$$\begin{aligned}\boldsymbol{M}^s &= \boldsymbol{K}^s_j(k_s r_s)[\boldsymbol{K}^s_j(k_s r_{s-1})]^{-1} \\ &= \begin{pmatrix} j_j(z_1) & n_j(z_1) \\ \dfrac{1}{z_1^2}\,[z_1\, j_j'(z_1) + j_j(z_1)] & \dfrac{1}{z_1^2}\,[z_1\, n_j'(z_1) + n_j(z_1)] \end{pmatrix} \\ &\quad z_2 \begin{pmatrix} z_2\, n_j'(z_2) + n_j(z_2) & -z_2^2\, n_j(z_2) \\ -\,[z_2\, j_j'(z_2) + j_j(z_2)] & z_2^2\, j_j(z_2) \end{pmatrix} .\end{aligned} \tag{B.11}$$

Using the cross-products for the spherical Bessel functions in appendix C (eqs C.7 - C.10), the matrix elements can be arranged as

$$\begin{aligned} m_{11} &= z_2\{j_j(z_1)[z_2\, n_j'(z_2) + n_j(z_2)] - n_j(z_1)[z_2\, j_j'(z_2) + j_j(z_2)]\} \\ &= z_2(p_j + z_2\, g_j)\ , \end{aligned} \tag{B.12}$$

$$\begin{aligned} m_{12} &= z_2^2\, z_2[-j_j(z_1)n_j(z_2) + n_j(z_1)j_j(z_2)] \\ &= -z_2^2\, z_2\, p_j\ , \end{aligned} \tag{B.13}$$

$$\begin{aligned} m_{21} &= \frac{1}{z_1^2}\, z_2\{[z_1\, j_j'(z_1) + j_j(z_1)][z_2 n_j'(z_2) + n_j(z_2)] - [z_1\, n_j'(z_1) + n_j(z_1)][z_2\, j_j'(z_2) + j_j(z_2)]\} \\ &= \frac{1}{z_1^2}\, z_2(p_j + z_1 r_j + z_2 g_j + z_1 z_2 s_j)\ , \end{aligned} \tag{B.14}$$

$$\begin{aligned} m_{22} &= z_2\, z_2^2\, \frac{1}{z_1^2}\, \{-[z_1\, j_j'(z_1) + j_j(z_1)]\, n_j(z_2) + j_j(z_2)\, [z_1\, n_j'(z_1) + n_j(z_1)]\}\ , \\ &= z_2\, z_2^2\, \frac{1}{z_1^2}\, (-p_j - z_1 r_j)\ . \end{aligned} \tag{B.15}$$

Hence,

$$\boldsymbol{M}^s = z_2 \begin{pmatrix} p_j + z_2\, g_j & -z_2^2\, p_j \\ \dfrac{1}{z_1^2}\, (p_j + z_1\, r_j + z_2\, g_j + z_1\, z_2\, s_j) & \dfrac{1}{z_1^2}\, z_2^2\, (-p_j - z_1\, r_j) \end{pmatrix} . \tag{B.16}$$

B.2 Poloidal matrix propagator

In this section we derive the interface conditions for the poloidal matrix-propagator method given by a homogeneous part of the Helmholtz equation (1.24). To guarantee the continuity of a solution for the magnetic field $\boldsymbol{B}_{\mathrm{P}}$ on a spherical layer interface given by a discontinuity of electric conductivity $\sigma(r)$, the radial and tangential components of magnetic field (eqs 3.42) are required to pass continuously through it (eq. Stratton (1941)),

$$\begin{aligned} \boldsymbol{e}_r \cdot \big[\boldsymbol{B}\big]_-^+ &= 0, \\ \boldsymbol{e}_r \times \big[\boldsymbol{B}\big]_-^+ &= 0. \end{aligned} \tag{B.17}$$

B.2.1 A homogeneous solution

The induction equation for the poloidal magnetic field (eq. 1.24) is represented in magnetic potential $\boldsymbol{A}$. Therefore, we use the relation (D.33) to obtain the representation of magnetic field $\boldsymbol{B}$.

Additionally, with the relations (D.36) - (D.40), we express the normal and tangential components of the poloidal magnetic field in the following form,

$$\begin{aligned}
\boldsymbol{e}_r \cdot \boldsymbol{B}_{\mathrm{P}}(r,\Omega,k) &= i\sum_{jm}\alpha^j_{jm}\left[\sqrt{\frac{j}{2j+1}}\left(\frac{d}{dr}-\frac{j}{r}\right)w_j(kr)\ \boldsymbol{e}_r\ \boldsymbol{Y}^{j+1}_{jm}(\Omega)\right.\\
&\quad\left.+\sqrt{\frac{j+1}{2j+1}}\left(\frac{d}{dr}+\frac{j+1}{r}\right)w_j(kr)\ \boldsymbol{e}_r\ \boldsymbol{Y}^{j-1}_{jm}(\Omega)\right]\\
&= i\sum_{jm}\alpha^j_{jm}\left[\sqrt{\frac{j}{2j+1}}\left(\frac{d}{dr}-\frac{j}{r}\right)w_j(kr)\ \left(-\sqrt{\frac{j+1}{2j+1}}\right)\ Y_{jm}(\Omega)\right.\\
&\quad\left.+\sqrt{\frac{j+1}{2j+1}}\left(\frac{d}{dr}+\frac{j+1}{r}\right)w_j(kr)\ \sqrt{\frac{j}{2j+1}}\ Y_{jm}(\Omega)\right]\\
&= i\sum_{jm}\alpha^j_{jm}\left[\frac{\sqrt{j(j+1)}}{2j+1}\ \frac{j+j+1}{r}\right]w_j(kr)\ Y_{jm}(\Omega)\\
&= \frac{i}{r}\sum_{jm}\alpha^j_{jm}\ \sqrt{j(j+1)}\ w_j(kr)\ Y_{jm}(\Omega)
\end{aligned} \tag{B.18}$$

and

$$\begin{aligned}
\boldsymbol{e}_r \times \boldsymbol{B}_{\mathrm{P}}(r,\Omega,k) &= i\sum_{jm}\alpha^j_{jm}\left[\sqrt{\frac{j}{2j+1}}\left(\frac{d}{dr}-\frac{j}{r}\right)w_j(kr)\ (i)\sqrt{\frac{j}{2j+1}}\ \boldsymbol{Y}^{j}_{jm}(\Omega)\right.\\
&\quad\left.+\sqrt{\frac{j+1}{2j+1}}\left(\frac{d}{dr}+\frac{j+1}{r}\right)w_j(kr)\ (i)\sqrt{\frac{j+1}{2j+1}}\ \boldsymbol{Y}^{j}_{jm}(\Omega)\right]\\
&= i^2\sum_{jm}\alpha^j_{jm}\left[\left(\frac{d}{dr}+\frac{(-j^2)+(j+1)^2}{(2j+1)r}\right)w_j(kr)\ \boldsymbol{Y}^{j}_{jm}(\Omega)\right]\\
&= -\sum_{jm}\alpha^j_{jm}\left(\frac{d}{dr}+\frac{1}{r}\right)w_j(kr)\ \boldsymbol{Y}^{j}_{jm}(\Omega)\\
&= -\frac{1}{r}\sum_{jm}\alpha^j_{jm}\frac{d}{dr}[rw_j(kr)]\ \boldsymbol{Y}^{j}_{jm}(\Omega)\ .
\end{aligned} \tag{B.19}$$

B.2.2 The particular solution

The particular solution for the poloidal case is given by eqs (2.9) and (2.10),

$$\boldsymbol{A}^{\mathrm{part}}_{\mathrm{T}}(r,\Omega,\omega) = -\frac{i}{\omega}\sum_{jm}G^j_{jm}(a)\left(\frac{r}{a}\right)^j\boldsymbol{Y}^j_{jm}(\Omega). \tag{B.20}$$

Let be

$$A^j_{jm}(r) := -\frac{i}{\omega}\ G^j_{jm}(a)\ \left(\frac{r}{a}\right)^j\ , \tag{B.21}$$

then, considering the relation (D.33), we express eq. (B.20) in terms of the magnetic intensity

$$\begin{aligned}
\boldsymbol{B}^{\mathrm{part}}_{\mathrm{P}} &= \operatorname{curl}\boldsymbol{A}^{\mathrm{part}}_{\mathrm{T}}\\
&= i\sum_{jm}\left[\sqrt{\frac{j}{2j+1}}\left(\frac{d}{dr}-\frac{j}{r}\right)A^j_{jm}(r)\ \boldsymbol{Y}^{j+1}_{jm}(\Omega)\right.\\
&\quad\left.+\sqrt{\frac{j+1}{2j+1}}\left(\frac{d}{dr}+\frac{j+1}{r}\right)A^j_{jm}(r)\ \boldsymbol{Y}^{j-1}_{jm}(\Omega)\right]\ .
\end{aligned} \tag{B.22}$$

First, we consider the derivative term in eq. (B.22);

$$\frac{d}{dr}\,A^{j}_{jm}(r) = \frac{d}{dr}\left[\left(\frac{-i}{\omega}\right)\;G^{j}_{jm}(a)\;\left(\frac{r}{a}\right)^{j}\right] = \frac{j}{r}\left(\frac{-i}{\omega}\right)\;G^{j}_{jm}(a)\;\left(\frac{r}{a}\right)^{j} = \frac{j}{r}\,A^{j}_{jm}(r)\;. \tag{B.23}$$

We substitute the result from eq. (B.23) in eq. (B.22) and find that the first summand of eq. (B.22) is zero. For the second term, we get

$$\begin{aligned}\boldsymbol{B}^{\rm part}_{\rm P}(r,\Omega,\omega) &= i\sum_{jm}\sqrt{\frac{j+1}{2j+1}}\left(\frac{j}{r}+\frac{j+1}{r}\right)\left(\frac{-i}{\omega}\right)\;G^{j}_{jm}(a)\;\left(\frac{r}{a}\right)^{j}\;\boldsymbol{Y}^{j-1}_{jm}(\Omega)\\ &= \sum_{jm}\sqrt{(j+1)(2j+1)}\,\frac{1}{r\omega}\,G^{j}_{jm}(a)\;\left(\frac{r}{a}\right)^{j}\;\boldsymbol{Y}^{j-1}_{jm}(\Omega)\;.\end{aligned} \tag{B.24}$$

Finally, the boundary condition given by the normal and tangential parts of the magnetic field, respectively, can by expressed with the relations (D.36) and (D.38),

$$\begin{aligned}\boldsymbol{e}_r\cdot\boldsymbol{B}^{\rm part}_{\rm P}(r,\Omega,\omega) &= \sum_{jm}\sqrt{\frac{j}{2j+1}}\;\sqrt{(j+1)(2j+1)}\;\frac{1}{r\omega}\,G^{j}_{jm}(a)\;\left(\frac{r}{a}\right)^{j}\;\;Y_{jm}(\Omega)\\ &= \frac{1}{\omega a}\sum_{jm}\sqrt{j(j+1)}\;G^{j}_{jm}(a)\;\left(\frac{r}{a}\right)^{j-1}\;\;Y_{jm}(\Omega)\;,\end{aligned} \tag{B.25}$$

$$\begin{aligned}\boldsymbol{e}_r\times\boldsymbol{B}^{\rm part}_{\rm P}(r,\Omega,\omega) &= i\sum_{jm}\sqrt{\frac{j+1}{2j+1}}\;\sqrt{(j+1)(2j+1)}\;\frac{1}{r\omega}\,G^{j}_{jm}(a)\;\left(\frac{r}{a}\right)^{j}\;\boldsymbol{Y}^{j}_{jm}(\Omega)\\ &= \frac{i}{\omega a}\sum_{jm}(j+1)\;G^{j}_{jm}(a)\;\left(\frac{r}{a}\right)^{j-1}\;\;\boldsymbol{Y}^{j}_{jm}(\Omega)\;.\end{aligned} \tag{B.26}$$

B.2.3 Derivation of the matrix propagator for the poloidal case

Starting by the matrix $\boldsymbol{K}$ for poloidal mode (eq. 3.49) consisting of the fundamental solutions given by a linear combination of the Bessel functions 1st and 2nd kind, we derive now the propagator $\boldsymbol{M}$ for a homogenous solution through a layer with constant electrical conductivity σ (and therefore, constant wave number k). The matrix $\boldsymbol{K}$ for the s layer has the form

$$\boldsymbol{K}^{s}_{j}(r) = \left(\begin{array}{cc} j_j(z) & n_j(z)\\ [z\,j'_j(z)+j_j(z)] & [z\,n'_j(z)+n_j(z)]\end{array}\right)_{z\,=\,z_s}\;. \tag{B.27}$$

According to relations (B.5), and (B.6) we determine the inverse matrix. The needed determinant by considering the Wronskian relation (B.8) has the form

$$\begin{aligned} det\boldsymbol{K} &= j_j(z)[z\,n'_j(z)+n_j(z)] - n_j(z)[z\,j'_j(z)+j_j(z)]\\ &= z[j_j(z)n'_j(z) - j'_j(z)n_j(z)]\\ &= \frac{1}{z}\;.\end{aligned} \tag{B.28}$$

The inverse matrix is then

$$\boldsymbol{K}^{-1}(z) = z\left(\begin{array}{cc} [z\,n'_j(z)+n_j(z)] & -n_j(z)\\ -[z\,j'_j(z)+j_j(z)] & j_j(z)\end{array}\right)\;. \tag{B.29}$$

Let $z_1 = z_s = k_s r_s$ be the top and $z_2 = z_{s-1} = k_s r_{s-1}$ be a bottom of the s spherical layer. Then the transformation between the top-bottom interface values y_1^s and y_2^s is

$$\left(\boldsymbol{y}_{jm}^s\right)_{r_s} = \boldsymbol{M}^s(k_s r_s, k_s r_{s-1})\left(\boldsymbol{y}_{jm}^s\right)_{r_{s-1}} , \tag{B.30}$$

where $\boldsymbol{M}^s$ stands for the transformation matrix through a spherical layer s

$$\begin{aligned} \boldsymbol{M}^s &= \boldsymbol{K}_j^s(k_s r_s)[\boldsymbol{K}_j^s(k_s r_{s-1})]^{-1} \\ &= z_2 \begin{pmatrix} j_j(z_1) & n_j(z_1) \\ [z_1\, j_j'(z_1) + j_j(z_1)] & [z_1\, n_j'(z_1) + n_j(z_1)] \end{pmatrix} \begin{pmatrix} z_2\, n_j'(z_2) + n_j(z_2) & -n_j(z_2) \\ -\left[z_2\, j_j'(z_2) + j_j(z_2)\right] & j_j(z_2) \end{pmatrix} . \end{aligned} \tag{B.31}$$

Using the cross-products for the spherical Bessel functions in appendix C (eqs C.7 - C.10), the matrix elements are of the form,

$$\begin{aligned} m_{11} &= z_2\{j_j(z_1)[z_2\, n_j'(z_2) + n_j(z_2)] - n_j(z_1)[z_2\, j_j'(z_2) + j_j(z_2)]\} , \\ &= z_2(p_j + z_2\, g_j) \end{aligned} \tag{B.32}$$

$$\begin{aligned} m_{12} &= z_2[-j_j(z_1)n_j(z_2) + n_j(z_1)j_j(z_2)] , \\ &= -z_2\, p_j \end{aligned} \tag{B.33}$$

$$\begin{aligned} m_{21} &= z_2\{[z_1\, j_j'(z_1) + j_j(z_1)][z_2 n_j'(z_2) + n_j(z_2)] - [z_1\, n_j'(z_1) + n_j(z_1)][z_2\, j_j'(z_2) + j_j(z_2)]\} , \\ &= z_2(p_j + z_1 r_j + z_2 g_j + z_1 z_2 s_j) \end{aligned} \tag{B.34}$$

$$\begin{aligned} m_{22} &= z_2\{-[z_1\, j_j'(z_1) + j_j(z_1)]\, n_j(z_2) + j_j(z_2)[z_1\, n_j'(z_1) + n_j(z_1)]\} . \\ &= z_2\,(-p_j - z_1 r_j) \end{aligned} \tag{B.35}$$

Hence,

$$\boldsymbol{M}^s = z_2 \begin{pmatrix} p_j + z_2 g_j & -p_j \\ p_j + z_1 r_j + z_2 g_j + z_1 z_2 s_j & -p_j - z_1 r_j \end{pmatrix} . \tag{B.36}$$

B.2.4 Derivation of the solution in the source layer for poloidal case

To describe the generated poloidal magnetic field, let us divide the space into three different spherical domains connected by spherical interfaces. The first domain, the Earth's mantle and crust, is defined by an electric conductive sphere without a source term of electromagnetic induction. The solution for $\boldsymbol{B}$ in this domain is described by a homogeneous part of the Helmholtz equation. The second domain is the atmosphere which is considered as an insulator, and therefore, there are no electric currents passing through it. Nevertheless, as the poloidal magnetic field penetrates into the atmosphere, it is a part of the solution domain. The magnetic field in the atmosphere can be described by the Gauss coefficients ${}^bG_{jm}^{(i)}$. Between these two domain the ocean layer is placed. It is an electric conductive space with a source of the induced magnetic field. The solution for $\boldsymbol{B}$ in the domain is described by the Helmhotz equation with a source of the magnetic field which corresponds to the particular solution of this equation. Magnetic fields in particular domains are connected by appropriate boundary conditions at the interfaces. First, we recall some relations for the poloidal magnetic field from section 3.2. The ocean layer is assigned by label 'm' with the radial distances r, $r_{\mathrm{m}-1} \leq r \leq r_{\mathrm{m}}$, where $r_{\mathrm{m}} = a$ and $r_{\mathrm{m}-1} = b$. We recall equation (3.64) that expresses the magnetic field in ocean layer $\boldsymbol{B}^{\mathrm{m}}$ as the sum of homogeneous $\boldsymbol{B}^{\mathrm{m}}_{\mathrm{hmg}}$ and particular $\boldsymbol{B}^{\mathrm{m}}_{\mathrm{part}}$ solutions,

$$\boldsymbol{B}^{\mathrm{m}} = \boldsymbol{B}^{\mathrm{m}}_{\mathrm{hmg}} + \boldsymbol{B}^{\mathrm{m}}_{\mathrm{part}} \; . \tag{B.37}$$

We also recall that the interface conditions for a homogeneous solution are given by eqs (B.18) and (B.19),

$$\boldsymbol{e}_r \cdot \boldsymbol{B}_{\mathrm{hmg}}(r, \Omega, k) = \frac{i}{r} \sum_{jm} \alpha_{jm} \sqrt{j(j+1)}\; w_j(kr)\; Y_{jm}(\Omega) \; , \tag{B.38}$$

$$\boldsymbol{e}_r \times \boldsymbol{B}_{\mathrm{hmg}}(r, \Omega, k) = -\frac{1}{r} \sum_{jm} \alpha_{jm} \frac{d}{d(kr)} [k\, r\, w_j(kr)]\; \boldsymbol{Y}^{j}_{jm}(\Omega) \; , \tag{B.39}$$

and for the particular solution by eqs (B.25) and (B.26),

$$\boldsymbol{e}_r \cdot \boldsymbol{B}_{\mathrm{part}}(r, \Omega, \omega) = \frac{1}{\omega\, a} \sum_{jm} G^{j}_{jm}(a)\; \sqrt{j(j+1)}\; \left(\frac{r}{a}\right)^{(j-1)}\; Y_{jm}(\Omega) \; , \tag{B.40}$$

$$\boldsymbol{e}_r \times \boldsymbol{B}_{\mathrm{part}}(r, \Omega, \omega) = \frac{i}{\omega\, a} \sum_{jm} G^{j}_{jm}(a)\; (j+1)\; \left(\frac{r}{a}\right)^{(j-1)}\; \boldsymbol{Y}^{j}_{jm}(\Omega) \; . \tag{B.41}$$

Additionally, the interface conditions at the Earth's surface from the atmosphere side are given by eqs (3.60) and (3.61),

$$\boldsymbol{e}_r \cdot \boldsymbol{B}(r, \Omega) = \sum_{jm} (j+1)\; \left(\frac{a}{r}\right)^{j+2}\; {}^{b}G^{(i)}_{jm}\; Y_{jm}(\Omega) \; , \tag{B.42}$$

$$\boldsymbol{e}_r \times \boldsymbol{B}(r, \Omega) = -i \sum_{jm} \sqrt{j(j+1)}\; \left(\frac{a}{r}\right)^{j+2}\; {}^{b}G^{(i)}_{jm}\; \boldsymbol{Y}^{j}_{jm}(\Omega) \; . \tag{B.43}$$

Having recalled necessary relations, we can express the interface conditions at the boundaries of the ocean (label 'm' stands for the ocean). The label m − 1 assigns the neighbouring layer beneath the ocean with radii $r \leq r_{\mathrm{m}-1}$ and label m + 1 stands for the atmosphere with radii $r \geq r_{\mathrm{m}}$. The two interface conditions at the bottom of the ocean layer ($r = r_{\mathrm{m}-1}$) are

$$\boldsymbol{e}_r \cdot \boldsymbol{B}^{\mathrm{m}-1}_{\mathrm{hmg}}(r_{\mathrm{m}-1}) = \boldsymbol{e}_r \cdot \boldsymbol{B}^{\mathrm{m}}_{\mathrm{hmg}}(r_{\mathrm{m}-1}) + \boldsymbol{e}_r \cdot \boldsymbol{B}^{\mathrm{m}}_{\mathrm{part}}(r_{\mathrm{m}-1}) \; , \tag{B.44}$$

$$\boldsymbol{e}_r \times \boldsymbol{B}^{\mathrm{m}-1}_{\mathrm{hmg}}(r_{\mathrm{m}-1}) = \boldsymbol{e}_r \times \boldsymbol{B}^{\mathrm{m}}_{\mathrm{hmg}}(r_{\mathrm{m}-1}) + \boldsymbol{e}_r \times \boldsymbol{B}^{\mathrm{m}}_{\mathrm{part}}(r_{\mathrm{m}-1}) \; . \tag{B.45}$$

The two interface conditions at the surface of the ocean layer ($r = r_{\mathrm{m}}$) are

$$\boldsymbol{e}_r \cdot \boldsymbol{B}^{\mathrm{m}}_{\mathrm{hmg}}(r_{\mathrm{m}}) + \boldsymbol{e}_r \cdot \boldsymbol{B}^{\mathrm{m}}_{\mathrm{part}}(r_{\mathrm{m}}) = \boldsymbol{e}_r \cdot \boldsymbol{B}^{\mathrm{m}+1}(r_{\mathrm{m}}) \; , \tag{B.46}$$

$$\boldsymbol{e}_r \times \boldsymbol{B}^{\mathrm{m}}_{\mathrm{hmg}}(r_{\mathrm{m}}) + \boldsymbol{e}_r \times \boldsymbol{B}^{\mathrm{m}}_{\mathrm{part}}(r_{\mathrm{m}}) = \boldsymbol{e}_r \times \boldsymbol{B}^{\mathrm{m}+1}(r_{\mathrm{m}}) \; . \tag{B.47}$$

For $\boldsymbol{B}^{\mathrm{m}-1}_{\mathrm{hmg}}(r_{\mathrm{m}-1})$ in eq. (B.44) we use equation (3.23),

$$\boldsymbol{y}^{\mathrm{m}-1}(r_{\mathrm{m}-1}) = c_1 \boldsymbol{L}(k_{\mathrm{m}-1}\, r_{\mathrm{m}-1}, k_1 r_1)\, \boldsymbol{k}(k_1 r_1) \; . \tag{B.48}$$

Connecting the three solution domains together, the problem is fully described. The particular solution $\boldsymbol{B}^{\mathrm{m}}_{\mathrm{part}}$ in the ocean is given by the source term. To evaluate the magnetic field in the ocean, we additionally have to find a homogeneous solution in the ocean, $\boldsymbol{B}^{\mathrm{m}}_{\mathrm{hmg}}$, denoted also as $\boldsymbol{y}^{\mathrm{m}}(r)$, which is unknown variable to be determined. The solution in the ocean layer depends also on the properties and behaviour of the magnetic field in neighbouring solution domains - the atmosphere and the layers beneath the ocean. To evaluate the solution at the ocean bottom, we use equation (B.48), where coefficient c_1 is unknown. The forth and last unknown in our system is the Gauss coefficients ${}^bG^{(i)}_{jm}$ in eqs (B.42) and (B.43), which describes the generated magnetic field in the atmosphere. To find four unknowns: $y^{\mathrm{m}}_1(r)$, $y^{\mathrm{m}}_2(r)$, c_1 and ${}^bG^{(i)}_{jm}$, we set up an equation system consisting of four equations given by the interface conditions at top and bottom of the ocean layer (B.44) - (B.47). Substituting for every term in eqs (B.44) - (B.47) by eqs (B.38) - (B.43), we get the following equation system that corresponds to the derivation in subsection 3.2.3

$$\begin{aligned}
\frac{i}{r_{\mathrm{m}-1}}\sqrt{j(j+1)}\; y^{\mathrm{m}-1}_{1,jm}(r_{\mathrm{m}-1}) &= \frac{i}{r_{\mathrm{m}-1}}\sqrt{j(j+1)}\; y^{\mathrm{m}}_{1,jm}(r_{\mathrm{m}-1}) + \frac{1}{\omega\, a}\sqrt{j(j+1)}\; G^j_{jm}(a)\;\left(\frac{r_{\mathrm{m}-1}}{a}\right)^{j-1}\\
\frac{-1}{r_{\mathrm{m}-1}}\; y^{\mathrm{m}-1}_{2,jm}(r_{\mathrm{m}-1}) &= \frac{-1}{r_{\mathrm{m}-1}}\; y^{\mathrm{m}}_{2,jm}(r_{\mathrm{m}-1}) + \frac{i}{\omega\, a}\,(j+1)\; G^j_{jm}(a)\left(\frac{r_{\mathrm{m}-1}}{a}\right)^{j-1}\\
\frac{i}{r_{\mathrm{m}}}\sqrt{j(j+1)}\; y^{\mathrm{m}}_{1,jm}(r_{\mathrm{m}}) + \frac{1}{\omega\, a}\sqrt{j(j+1)}\; G^j_{jm}(a) &= (j+1)\; {}^bG^{(i)}_{jm}\\
\frac{-1}{r_{\mathrm{m}}}\; y^{\mathrm{m}}_{2,jm}(r_{\mathrm{m}}) + \frac{i}{\omega\, a}\,(j+1)\; G^j_{jm}(a) &= -i\;\sqrt{j(j+1)}\; {}^bG^{(i)}_{jm}
\end{aligned} \tag{B.49}$$

which can be simplified as

$$\begin{aligned}
y^{\mathrm{m}-1}_{1,jm}(r_{\mathrm{m}-1}) &= y^{\mathrm{m}}_{1,jm}(r_{\mathrm{m}-1}) - \frac{i}{\omega}\; G^j_{jm}(a)\;\left(\frac{r_{\mathrm{m}-1}}{a}\right)^{j}\\
y^{\mathrm{m}-1}_{2,jm}(r_{\mathrm{m}-1}) &= y^{\mathrm{m}}_{2,jm}(r_{\mathrm{m}-1}) - \frac{i}{\omega}\,(j+1)\; G^j_{jm}(a)\left(\frac{r_{\mathrm{m}-1}}{a}\right)^{j}\\
y^{\mathrm{m}}_{1,jm}(r_{\mathrm{m}}) - \frac{i}{\omega}\; G^j_{jm}(a) &= -\,i\,a\sqrt{\frac{(j+1)}{j}}\;{}^bG^{(i)}_{jm}\\
y^{\mathrm{m}}_{2,jm}(r_{\mathrm{m}}) - \frac{i}{\omega}\,(j+1)\; G^j_{jm}(a) &= i\,a\,\sqrt{j(j+1)}\;{}^bG^{(i)}_{jm}\;.
\end{aligned} \tag{B.50}$$

We denote the particular solution as

$$\begin{aligned}
\boldsymbol{s}_{jm}(r) :=& \begin{pmatrix} \dfrac{-i}{\omega}\; G^j_{jm}(a)\;\left(\dfrac{r}{a}\right)^j \\ \dfrac{-i}{\omega}\;(j+1)\; G^j_{jm}(a)\;\left(\dfrac{r}{a}\right)^j \end{pmatrix}\\
=& \begin{pmatrix} 1 \\ j+1 \end{pmatrix} \frac{-i}{\omega}\; G^j_{jm}(a)\;\left(\frac{r}{a}\right)^j
\end{aligned} \tag{B.51}$$

and introduce, on the atmosphere side, a vector

$$\boldsymbol{C}^0_j := \begin{pmatrix} -\,i\,a\sqrt{\dfrac{(j+1)}{j}} \\ \\ i\,a\,\sqrt{j(j+1)} \end{pmatrix}\;. \tag{B.52}$$

These relations are those introduced by eqs (3.65) and (3.63).

Appendix C

The spherical Bessel functions

This appendix summarizes the relations for the Bessel functions used by the matrix propagator technique in chapter 3. This relations has been published by Pěč et al. (1985). The spherical Bessel functions of the first and the second kind, $j_\ell(z)$ and $n_\ell(z)$, are defined by

$$j_\ell(z) = \sqrt{\frac{\pi}{2z}}\, J_{\ell+\frac{1}{2}}(z) \ , \tag{C.1}$$

$$n_\ell(z) = \sqrt{\frac{\pi}{2z}}\, N_{\ell+\frac{1}{2}}(z) \ . \tag{C.2}$$

where J_ℓ and N_ℓ stand for the cylindrical Bessel functions of the first and the second kind, respectively. Both functions satisfy the differential equation

$$\frac{d^2w}{dz^2} + \frac{2}{z}\frac{dw}{dz} + \left[1 - \frac{\ell(\ell+1)}{z^2}\right] w = 0 \ , \tag{C.3}$$

where $w(z)$ stands for $j_\ell(z)$ or $n_\ell(z)$. Moreover, the spherical Bessel functions $w(z)$ satisfy the recurrence relations of the terms

$$w_{\ell+1}(z) + w_{\ell-1}(z) = \frac{2\ell+1}{z} w_\ell(z) \ , \tag{C.4}$$

$$\frac{dw_\ell(z)}{dz} - \frac{\ell}{z} w_\ell(z) + w_{\ell+1}(z) = 0 \ , \tag{C.5}$$

$$\frac{dw_\ell(z)}{dz} + \frac{\ell+1}{z} w_\ell(z) + w_{\ell-1}(z) = 0 \ . \tag{C.6}$$

The cross-products of the Bessel functions of first and second kind and their derivatives are defined as

$$p_\ell = j_\ell(z_1) n_\ell(z_2) - j_\ell(z_2) n_\ell(z_1) \ , \tag{C.7}$$

$$q_\ell = j_\ell(z_1) n'_\ell(z_2) - j'_\ell(z_2) n_\ell(z_1) \ , \tag{C.8}$$

$$r_\ell = j'_\ell(z_1) n_\ell(z_2) - j_\ell(z_2) n'_\ell(z_1) \ , \tag{C.9}$$

$$s_\ell = j'_\ell(z_1) n'_\ell(z_2) - j'_\ell(z_2) n'_\ell(z_1) \ , \tag{C.10}$$

where $'$ stands for the derivative of functions with respect to argument. The cross-products (C.7) - (C.10) satisfy the following recurrence relations,

$$p_{\ell+1} = s_\ell + \frac{\ell^2}{z_1 z_2}\, p_\ell - \frac{\ell}{z_1}\, q_\ell - \frac{\ell}{z_2}\, r_\ell \ , \tag{C.11}$$

$$q_{\ell+1} = \frac{\ell}{z_1}\, p_\ell - \frac{\ell+2}{z_2}\, p_{\ell+1} - r_\ell \;, \tag{C.12}$$

$$r_{\ell+1} = \frac{\ell}{z_2}\, p_\ell - \frac{\ell+2}{z_1}\, p_{\ell+1} - q_\ell \;, \tag{C.13}$$

$$s_{\ell+1} = p_\ell - \frac{(\ell+2)^2}{z_1 z_2}\, p_{\ell+1} - \frac{\ell+2}{z_1}\, q_{\ell+1} - \frac{\ell+2}{z_2}\, r_{\ell+1} \;. \tag{C.14}$$

The checking relation is

$$p_\ell s_\ell - q_\ell r_\ell = \frac{1}{z_1^2 z_2^2} \;. \tag{C.15}$$

The starting values of recurrences (C.11) - (C.14) are:

$$p_0 = \frac{\sin(z_2 - z_1)}{z_1 z_2} \;, \tag{C.16}$$

$$q_0 = \frac{\cos(z_2 - z_1)}{z_1 z_2} - \frac{\sin(z_2 - z_1)}{z_1 z_2^2} \;, \tag{C.17}$$

$$r_0 = -\frac{\cos(z_2 - z_1)}{z_1 z_2} - \frac{\sin(z_2 - z_1)}{z_1^2 z_2} \;, \tag{C.18}$$

$$s_0 = \frac{\sin(z_2 - z_1)}{z_1 z_2} - \frac{\cos(z_2 - z_1)}{z_1^2 z_2} + \frac{\cos(z_2 - z_1)}{z_1 z_2^2} + \frac{\sin(z_2 - z_1)}{z_1^2 z_2^2} \;. \tag{C.19}$$

Spherical Bessel functions of the first and the second kind of the same argument satisfy the relation

$$j_\ell(z) n_{\ell-1}(z) - j_{\ell-1}(z) n_\ell(z) = z^{-2} \;. \tag{C.20}$$

Let function $\chi_\ell(z)$ be the ratio of the spherical Bessel functions of the first and second kind,

$$\chi_\ell(z) = \frac{z\, j_{\ell+1}(z)}{j_\ell(z)} \;. \tag{C.21}$$

The recurrent relation for $\chi_\ell(z)$ reads as

$$\chi_{\ell+1}(z) = (2\ell + 3) - \frac{z^2}{\chi_\ell(z)} \;. \tag{C.22}$$

The starting value of recurrence (C.21) is

$$\chi_0(z) = 1 - z\ \cot(z) \;. \tag{C.23}$$

Appendix D

Basic relations for spherical harmonics representation

This appendix summarizes some basic relations for spherical harmonics by following Varshalovich et al. (1988) book with the references on the section number and equation number given in this book.

D.1 Definition of scalar spherical harmonics

(*chap. 5.2.1 eq. 6*)

$$Y_{jm}(\vartheta,\varphi) := P_{jm}(\cos\vartheta)e^{im\varphi} \tag{D.1}$$

where $P_{jm}(\cos\vartheta)$ are the associated Legendre functions

$$P_{jm}(\cos\vartheta) := (-1)^m \sqrt{\frac{2j+1}{4\pi}\frac{(j-m)!}{(j+m)!}}\,(\sin\vartheta)^m \frac{d^m}{(d\cos\vartheta)^m}\,P_j(\cos\vartheta) \tag{D.2}$$

and $P_j(\cos\vartheta)$ is the Legendre polynomial, with

$$P_j(\cos\vartheta) := \frac{1}{2^j j!}\frac{d^j(\cos^2\vartheta-1)^j}{d(\cos\vartheta)^j} \tag{D.3}$$

where

$$j = 0,1,2,3,\ldots,\infty \tag{D.4}$$

$$m = -j,\ldots,0,\ldots,j \tag{D.5}$$

The expansion of function F into a series of scalar spherical harmonics is

$$F(r,\vartheta,\varphi) = \sum_{j=1}^{\infty}\sum_{m=-j}^{j} F_{jm}(r)\;Y_{jm}(\vartheta,\varphi) \tag{D.6}$$

The zonal spherical harmonics are

$$Y_{j0}(\vartheta,\varphi) = \sqrt{\frac{2j+1}{4\pi}}\,P_j(\cos\vartheta) \tag{D.7}$$

Orthonormality condition
(*Chap. 5.1.4*)
(*eq. 6*)

$$\int_0^\pi \int_0^{2\pi} Y_{j_1 m_1}(\vartheta,\varphi)\, Y^*_{j_2 m_2}(\vartheta,\varphi)\ \sin\vartheta\ d\vartheta\ d\varphi = \delta_{j_1 j_2}\delta_{m_1 m_2} \tag{D.8}$$

Complex conjugation
(*Chap. 5.4*)
(*eq. 1*)

$$Y^*_{jm}(\vartheta,\varphi) = (-1)^m\, Y_{j\,-m}(\vartheta,\varphi) \tag{D.9}$$

D.2 Vector spherical harmonics

The expansion of a vector function $\boldsymbol{F}$ into a series of vector spherical harmonics

$$\boldsymbol{F}(r,\vartheta,\varphi) = \sum_{j=1}^{\infty}\sum_{m=-j}^{j}\sum_{\ell=j-1}^{j+1} F^{\ell}_{jm}(r)\ \boldsymbol{Y}^{\ell}_{jm}(\vartheta,\varphi) \tag{D.10}$$

(*Chap. 7.3.1*)
(*eq. 6,7*)

$$\boldsymbol{Y}^{(1)}_{jm}(\vartheta,\varphi) = \frac{1}{\sqrt{j(j+1)}}\nabla_\Omega\, Y_{jm}(\vartheta,\varphi) \tag{D.11}$$

$$\boldsymbol{Y}^{(0)}_{jm}(\vartheta,\varphi) = \frac{-i}{\sqrt{j(j+1)}}(\boldsymbol{e}_r \times \nabla_\Omega)\, Y_{jm}(\vartheta,\varphi) \tag{D.12}$$

$$\boldsymbol{Y}^{(-1)}_{jm}(\vartheta,\varphi) = \boldsymbol{e}_r\, Y_{jm}(\vartheta,\varphi) \tag{D.13}$$

(*eq. 10*)

$$\boldsymbol{Y}^{j+1}_{jm}(\vartheta,\varphi) = \sqrt{\frac{j}{2j+1}}\boldsymbol{Y}^{(1)}_{jm}(\vartheta,\varphi) - \sqrt{\frac{j+1}{2j+1}}\boldsymbol{Y}^{(-1)}_{jm}(\vartheta,\varphi) \tag{D.14}$$

$$\boldsymbol{Y}^{j}_{jm}(\vartheta,\varphi) = \boldsymbol{Y}^{(0)}_{jm}(\vartheta,\varphi) \tag{D.15}$$

$$\boldsymbol{Y}^{j-1}_{jm}(\vartheta,\varphi) = \sqrt{\frac{j+1}{2j+1}}\boldsymbol{Y}^{(1)}_{jm}(\vartheta,\varphi) + \sqrt{\frac{j}{2j+1}}\boldsymbol{Y}^{(-1)}_{jm}(\vartheta,\varphi) \tag{D.16}$$

(*eq. 9*)

$$\boldsymbol{Y}^{(1)}_{jm}(\vartheta,\varphi) = \sqrt{\frac{j+1}{2j+1}}\boldsymbol{Y}^{j-1}_{jm}(\vartheta,\varphi) + \sqrt{\frac{j}{2j+1}}\boldsymbol{Y}^{j+1}_{jm}(\vartheta,\varphi) \tag{D.17}$$

$$\boldsymbol{Y}^{(0)}_{jm}(\vartheta,\varphi) = \boldsymbol{Y}^{j}_{jm}(\vartheta,\varphi) \tag{D.18}$$

$$\boldsymbol{Y}^{(-1)}_{jm}(\vartheta,\varphi) = \sqrt{\frac{j}{2j+1}}\boldsymbol{Y}^{j-1}_{jm}(\vartheta,\varphi) - \sqrt{\frac{j+1}{2j+1}}\boldsymbol{Y}^{j+1}_{jm}(\vartheta,\varphi) \tag{D.19}$$

Orthonormality condition
(*Chap. 7.3.13*)
(*eq. 121*)

$$\int_0^\pi \int_0^{2\pi} \boldsymbol{Y}^{\ell_1\,*}_{j_1 m_1}(\vartheta,\varphi)\boldsymbol{Y}^{\ell_2}_{j_2 m_2}(\vartheta,\varphi)\ \sin\vartheta\ d\vartheta\ d\varphi = \delta_{j_1 j_2}\delta_{\ell_1\ell_2}\delta_{m_1 m_2} \tag{D.20}$$

Complex conjugation
(*Chap. 7.3.3*)
(*eq. 39*)

$$\begin{aligned} \boldsymbol{Y}^{\ell\,*}_{jm}(\vartheta,\varphi) &= (-1)^{j+\ell+m+1}\boldsymbol{Y}^{\ell}_{j\,-m}(\vartheta,\varphi) \\ \boldsymbol{Y}^{(\lambda)*}_{jm}(\vartheta,\varphi) &= (-1)^{m+\lambda+1}\boldsymbol{Y}^{(\lambda)}_{j\,-m}(\vartheta,\varphi) \end{aligned} \tag{D.21}$$

The zonal spherical vector harmonics are expressed by the associated Legendre function of order $m = 1$

$$\boldsymbol{Y}^{(0)}_{j0}(\vartheta,\varphi) = -i\,P_{j1}(\vartheta)\,\boldsymbol{e}_{\varphi} \tag{D.22}$$

D.3 Components of vector spherical harmonics

(*Chap. 7.3.2*)
(*eq. 25*)

$$\begin{aligned} \Big[\boldsymbol{Y}^{(1)}_{jm}(\vartheta,\varphi)\Big]_r &= 0 \\ \Big[\boldsymbol{Y}^{(1)}_{jm}(\vartheta,\varphi)\Big]_{\vartheta} &= \frac{1}{\sqrt{j(j+1)}}\,\frac{\partial}{\partial\vartheta}\,Y_{jm}(\vartheta,\varphi) \\ \Big[\boldsymbol{Y}^{(1)}_{jm}(\vartheta,\varphi)\Big]_{\varphi} &= \frac{1}{\sqrt{j(j+1)}}\,\frac{1}{\sin\vartheta}\,\frac{\partial}{\partial\varphi}\,Y_{jm}(\vartheta,\varphi) \end{aligned} \tag{D.23}$$

(*eq. 26*)

$$\begin{aligned} \Big[\boldsymbol{Y}^{(0)}_{jm}(\vartheta,\varphi)\Big]_r &= 0 \\ \Big[\boldsymbol{Y}^{(0)}_{jm}(\vartheta,\varphi)\Big]_{\vartheta} &= \frac{i}{\sqrt{j(j+1)}}\,\frac{1}{\sin\vartheta}\,\frac{\partial}{\partial\varphi}\,Y_{jm}(\vartheta,\varphi) \\ \Big[\boldsymbol{Y}^{(0)}_{jm}(\vartheta,\varphi)\Big]_{\varphi} &= -\frac{i}{\sqrt{j(j+1)}}\,\frac{\partial}{\partial\vartheta}\,Y_{jm}(\vartheta,\varphi) \end{aligned} \tag{D.24}$$

(*eq. 27*)

$$\begin{aligned} \Big[\boldsymbol{Y}^{(-1)}_{jm}(\vartheta,\varphi)\Big]_r &= Y_{jm}(\vartheta,\varphi) \\ \Big[\boldsymbol{Y}^{(-1)}_{jm}(\vartheta,\varphi)\Big]_{\vartheta} &= 0 \\ \Big[\boldsymbol{Y}^{(-1)}_{jm}(\vartheta,\varphi)\Big]_{\varphi} &= 0 \end{aligned} \tag{D.25}$$

D.4 Solution of the Helmholtz equation by vector spherical harmonics

The vector $w_{\ell}(z)\,\boldsymbol{Y}^{\ell}_{jm}(\vartheta,\varphi)$ satisfies the vector Helmholtz equation
(*Chap.7.3.5 Differential Equations c) eq. 49*)

$$(\Delta + k^2)\{w_{\ell}(z)\boldsymbol{Y}^{\ell}_{jm}(\vartheta,\varphi)\} = 0 \tag{D.26}$$

where $w_{\ell}(z)$ is the Bessel function of the first and second kind, and $z = kr$.

D.5 The cross product of vector spherical harmonics used for the source term

The cross product in equation (2.24) is arranged according to the relation given in (*chap.7.3.10 eq. 100 Clebsch-Gordan Series*)

$$\begin{aligned}\boldsymbol{Y}^{\ell_1}_{j_1 m_1}(\vartheta,\varphi)\times\boldsymbol{Y}^{\ell_2}_{j_2 m_2}(\vartheta,\varphi) = i\sqrt{\frac{3}{2\pi}(2j_1+1)(2j_2+1)(2\ell_1+1)(2\ell_2+1)} \\ \times\sum_{j\,\ell}\begin{Bmatrix} j_1 & \ell_1 & 1 \\ j_2 & \ell_2 & 1 \\ j & \ell & 1\end{Bmatrix} C^{\ell 0}_{\ell_1 0 \ell_2 0}\, C^{jm}_{j_1 m_1 j_2 m_2}\, \boldsymbol{Y}^{\ell}_{jm}(\vartheta,\varphi)\,. \end{aligned} \tag{D.27}$$

where the Wigner's $9-j$ symbols are given by (*Chap. 10.9.2 Explicit Forms of the 9j symbols for Special Values of the Arguments*)

$$\begin{Bmatrix} a & b & c \\ d & e & c \\ g & g & 1\end{Bmatrix} = (-1)^{b+d+g+c} 2\frac{(a-d)(a+d+1)-(b-e)(b+e+1)}{[(2g+2)(2g+1)2g(2c+2)(2c+1)2c]^{\frac{1}{2}}}\begin{Bmatrix} a & b & c \\ e & d & g\end{Bmatrix} \tag{D.28}$$

and the $6-j$ symbols are given in table 9.2 Numerical Values of the 6j symbols (*Chap. 9.11 Tables of Algebraic Expressions for the 6j Symbols*). The Glebsch-Gordan coefficients $C^{jm}_{j_1 m_1 j_2 m_2}$ are then numerically solved in (*Chap. 8 The Clebsch-Gordan coefficients*). The first Glebsh-Gordan coefficient for the zonal case is (*Chap. 8.5.2 Spherical Values of Momentum Projections a)*)

$$C^{c0}_{a0b0} = \begin{cases} 0, & \text{if } a+b+c = 2g+1, \\ \frac{(-1)^{g-c}\sqrt{2c+1}\,g!}{(g-a)!(g-b)!(g-c)!}\left[\frac{(2g-2a)!(2g-2b)!(2g-2c)!}{(2g+1)!}\right]^{\frac{1}{2}}, & \text{if } a+b+c = 2g, \end{cases} \tag{D.29}$$

where g is a positive integer. The general form of the Clebsch-Gordan coefficients can be found in (*Chap. 8.2.1 Representations of the Glebsh-Gordan coefficients in the form of algebraic sums 5) Wigner[43]*)

$$\begin{aligned} C^{jm}_{j_1 m_1 j_2 m_2} =& \delta_{m,m_1+m_2}\triangle(j_1 j_2 j)\left[\frac{(j+m)!(j-m)!(2j+1)}{(j_1+m_1)!(j_1-m_1)!(j_2+m_2)!(j_2-m_2)!}\right]^{\frac{1}{2}} \\ &\times\sum_z \frac{(-1)^{j_2+m_2+z}(j+j_2+m_1-z)!(j_1-m_1+z)!}{z!(j-j_1+j_2-z)!(j+m-z)!(j_1-j_2-m+z)!} \end{aligned} \tag{D.30}$$

where

$$\triangle(j_1\,j_2\,j) = \left[\frac{(j_1+j_2-j)!(j_1-j_2+j)!(-j_1+j_2+j)!}{(j_1+j_2+j+1)!}\right]^{\frac{1}{2}} \tag{D.31}$$

and the summation index z assumes integer values for which all the factorial arguments are non-negative.

D.6 Differential operations

(*chap.7.3.6. c) eq. 55*)

1)

$$\operatorname{curl}[f(r)\boldsymbol{Y}_{jm}^{j+1}(\vartheta,\varphi)] = i\sqrt{\frac{j}{2j+1}}\left(\frac{d}{dr}+\frac{j+2}{r}\right)f(r)\boldsymbol{Y}_{jm}^{j}(\vartheta,\varphi) \tag{D.32}$$

2)

$$\begin{aligned}\operatorname{curl}[f(r)\boldsymbol{Y}_{jm}^{j}(\vartheta,\varphi)] &= i\sqrt{\frac{j}{2j+1}}\left(\frac{d}{dr}-\frac{j}{r}\right)f(r)\,\boldsymbol{Y}_{jm}^{j+1}(\vartheta,\varphi)\\ &+ i\sqrt{\frac{j+1}{2j+1}}\left(\frac{d}{dr}+\frac{j+1}{r}\right)f(r)\,\boldsymbol{Y}_{jm}^{j-1}(\vartheta,\varphi)\end{aligned} \tag{D.33}$$

3)

$$\operatorname{curl}[f(r)\boldsymbol{Y}_{jm}^{j-1}(\vartheta,\varphi)] = i\sqrt{\frac{j+1}{2j+1}}\left(\frac{d}{dr}-\frac{j-1}{r}\right)f(r)\boldsymbol{Y}_{jm}^{j}(\vartheta,\varphi) \tag{D.34}$$

D.7 Algebraic relations

(*chap. 7.3.8. b) eq. 71*)

$$\boldsymbol{e}_r\cdot\boldsymbol{Y}_{jm}^{j-1}(\vartheta,\varphi) = \sqrt{\frac{j}{2j+1}}\,Y_{jm}(\vartheta,\varphi) \tag{D.35}$$

$$\boldsymbol{e}_r\cdot\boldsymbol{Y}_{jm}^{j}(\vartheta,\varphi) = 0 \tag{D.36}$$

$$\boldsymbol{e}_r\cdot\boldsymbol{Y}_{jm}^{j+1}(\vartheta,\varphi) = -\sqrt{\frac{j+1}{2j+1}}\,Y_{jm}(\vartheta,\varphi) \tag{D.37}$$

(*chap. 7.3.8 c) eq. 73*)

$$\boldsymbol{e}_r\times\boldsymbol{Y}_{jm}^{j-1}(\vartheta,\varphi) = i\sqrt{\frac{j+1}{2j+1}}\boldsymbol{Y}_{jm}^{j}(\vartheta,\varphi) \tag{D.38}$$

$$\boldsymbol{e}_r\times\boldsymbol{Y}_{jm}^{j}(\vartheta,\varphi) = i\sqrt{\frac{j+1}{2j+1}}\boldsymbol{Y}_{jm}^{j-1}(\vartheta,\varphi) + i\sqrt{\frac{j}{2j+1}}\boldsymbol{Y}_{jm}^{j+1}(\vartheta,\varphi) \tag{D.39}$$

$$\boldsymbol{e}_r\times\boldsymbol{Y}_{jm}^{j+1}(\vartheta,\varphi) = i\sqrt{\frac{j}{2j+1}}\boldsymbol{Y}_{jm}^{j}(\vartheta,\varphi) \tag{D.40}$$

D.8 Operator ∇

(*Chap. 1.3.1*)

$$\nabla = \boldsymbol{e}_r\nabla_r + \boldsymbol{e}_\vartheta\nabla_\vartheta + \boldsymbol{e}_\varphi\nabla_\varphi \tag{D.41}$$

$$\begin{aligned}\nabla_r &= \frac{\partial}{\partial r}\\ \nabla_\vartheta &= \frac{1}{r}\frac{\partial}{\partial\vartheta}\\ \nabla_\varphi &= \frac{1}{r\sin\vartheta}\frac{\partial}{\partial\varphi}\end{aligned} \tag{D.42}$$

and if

$$\nabla = \boldsymbol{e}_r\frac{\partial}{\partial r} + \frac{1}{r}\nabla_\Omega \tag{D.43}$$

then

$$\nabla_\Omega = \boldsymbol{e}_\vartheta\frac{\partial}{\partial\vartheta} + \frac{\boldsymbol{e}_\varphi}{\sin\vartheta}\frac{\partial}{\partial\varphi} \tag{D.44}$$

D.9 Special case: zonal toroidal vector spherical harmonics $Y_{j0}^{(0)}(\vartheta, \varphi)$

The derivation of Y_{jm} with respect to longitude φ
(*Chap. 5.8.2*)
(*eq. 4*)

$$\frac{\partial}{\partial\varphi} Y_{jm}(\vartheta, \varphi) = im\, Y_{jm}(\vartheta, \varphi)\ . \tag{D.45}$$

For $m = 0$

$$\frac{\partial}{\partial\varphi} Y_{j0}(\vartheta, \varphi) = 0\ . \tag{D.46}$$

The derivation with respect to co-latitude ϑ
(*eq. 5*)

$$\begin{aligned} \frac{\partial}{\partial\vartheta} Y_{jm}(\vartheta, \varphi) &= \frac{1}{2}\sqrt{j(j+1) - m(m+1)}\, Y_{jm+1}(\vartheta, \varphi) e^{-i\varphi} \\ &\quad - \frac{1}{2}\sqrt{j(j+1) - m(m-1)}\, Y_{jm-1}(\vartheta, \varphi) e^{i\varphi}\ . \end{aligned} \tag{D.47}$$

In addition, the relation for $m = \pm 1$:
(*Chap. 5.13.2*)
(*eq. 8*)

$$Y_{j\pm1}(\vartheta, \varphi) = \mp \frac{e^{\pm i\varphi}}{\sin\vartheta}\sqrt{\frac{j(j+1)}{4\pi(2j+1)}}\left[P_{j-1}(\cos\vartheta) - P_{j+1}(\cos\vartheta)\right]\ . \tag{D.48}$$

Eq. (D.47) for $m = 0$ now reads as

$$\begin{aligned} \frac{\partial}{\partial\vartheta} Y_{j0}(\vartheta, \varphi) &= -\frac{1}{2}\sqrt{j(j+1)}\,\frac{e^{i\varphi}}{\sin\vartheta}\sqrt{\frac{j(j+1)}{4\pi(2j+1)}}\left[P_{j-1}(\cos\vartheta) - P_{j+1}(\cos\vartheta)\right] e^{-i\varphi} \\ &\quad - \frac{1}{2}\sqrt{j(j+1)}\,\frac{e^{-i\varphi}}{\sin\vartheta}\sqrt{\frac{j(j+1)}{4\pi(2j+1)}}\left[P_{j-1}(\cos\vartheta) - P_{j+1}(\cos\vartheta)\right] e^{i\varphi} \\ &= -\sqrt{j(j+1)}\,\frac{1}{\sin\vartheta}\sqrt{\frac{j(j+1)}{4\pi(2j+1)}}\left[P_{j-1}(\cos\vartheta) - P_{j+1}(\cos\vartheta)\right] \\ &= -\frac{1}{\sin\vartheta}\,\frac{j(j+1)}{\sqrt{4\pi(2J+1)}}\left[P_{j-1}(\cos\vartheta) - P_{j+1}(\cos\vartheta)\right] \end{aligned} \tag{D.49}$$

and using relations (D.24); the components of the zonal toroidal vector spherical harmonics take the form

$$\begin{aligned} \left[\boldsymbol{Y}_{j0}^{(0)}(\vartheta, \varphi)\right]_r &= 0\,, \\ \left[\boldsymbol{Y}_{j0}^{(0)}(\vartheta, \varphi)\right]_\vartheta &= 0\,, \\ \left[\boldsymbol{Y}_{j0}^{(0)}(\vartheta, \varphi)\right]_\varphi &= \frac{i}{\sqrt{j(j+1)}}\,\frac{j(j+1)}{\sin\vartheta}\,\frac{1}{\sqrt{4\pi(2j+1)}}\left[P_{j-1}(\cos\vartheta) - P_{j+1}(\cos\vartheta)\right]\,, \\ &= \frac{i}{\sin\vartheta}\sqrt{\frac{j(j+1)}{4\pi(2j+1)}}\left[P_{j-1}(\cos\vartheta) - P_{j+1}(\cos\vartheta)\right]\ . \end{aligned} \tag{D.50}$$

Eidesstattliche Erklärung

Hiermit versichere ich, die vorliegende Dissertation selbstständig und ohne unerlaubte Hilfe angefertigt zu haben. Es wurden keine anderen als die im Text aufgeführten Hilfsmittel und Quellen verwendet. Ein Promotionsverfahren wurde zu keinem früheren Zeitpunkt an einer anderen Hochschule oder bei einem anderen Fachbereich beantragt.

Jan Dostal
Berlin, Januar 2014